

EDITED BY: Fei Ye, Chao Sun, Yi Xie, Lu Cai and Bing Wang
PUBLISHED IN: *Frontiers in Public Health*

EDITED BY: Fei Ye, Chao Sun, Yi Xie, Lu Cai and Bing Wang
PUBLISHED IN: *Frontiers in Public Health*





frontiers

Frontiers eBook Copyright Statement

The copyright in the text of individual articles in this eBook is the property of their respective authors or their respective institutions or funders. The copyright in graphics and images within each article may be subject to copyright of other parties. In both cases this is subject to a license granted to Frontiers.

The compilation of articles constituting this eBook is the property of Frontiers.

Each article within this eBook, and the eBook itself, are published under the most recent version of the Creative Commons CC-BY licence.

The version current at the date of publication of this eBook is CC-BY 4.0. If the CC-BY licence is updated, the licence granted by Frontiers is automatically updated to the new version.

When exercising any right under the CC-BY licence, Frontiers must be attributed as the original publisher of the article or eBook, as applicable.

Authors have the responsibility of ensuring that any graphics or other materials which are the property of others may be included in the CC-BY licence, but this should be checked before relying on the CC-BY licence to reproduce those materials. Any copyright notices relating to those materials must be complied with.

Copyright and source acknowledgement notices may not be removed and must be displayed in any copy, derivative work or partial copy which includes the elements in question.

All copyright, and all rights therein, are protected by national and international copyright laws. The above represents a summary only. For further information please read Frontiers' Conditions for Website Use and Copyright Statement, and the applicable CC-BY licence.

ISSN 1664-8714

ISBN 978-2-88976-841-7

DOI 10.3389/978-2-88976-841-7

About Frontiers

Frontiers is more than just an open-access publisher of scholarly articles: it is a pioneering approach to the world of academia, radically improving the way scholarly research is managed. The grand vision of Frontiers is a world where all people have an equal opportunity to seek, share and generate knowledge. Frontiers provides immediate and permanent online open access to all its publications, but this alone is not enough to realize our grand goals.

Frontiers Journal Series

The Frontiers Journal Series is a multi-tier and interdisciplinary set of open-access, online journals, promising a paradigm shift from the current review, selection and dissemination processes in academic publishing. All Frontiers journals are driven by researchers for researchers; therefore, they constitute a service to the scholarly community. At the same time, the Frontiers Journal Series operates on a revolutionary invention, the tiered publishing system, initially addressing specific communities of scholars, and gradually climbing up to broader public understanding, thus serving the interests of the lay society, too.

Dedication to Quality

Each Frontiers article is a landmark of the highest quality, thanks to genuinely collaborative interactions between authors and review editors, who include some of the world's best academicians. Research must be certified by peers before entering a stream of knowledge that may eventually reach the public - and shape society; therefore, Frontiers only applies the most rigorous and unbiased reviews.

Frontiers revolutionizes research publishing by freely delivering the most outstanding research, evaluated with no bias from both the academic and social point of view. By applying the most advanced information technologies, Frontiers is catapulting scholarly publishing into a new generation.

What are Frontiers Research Topics?

Frontiers Research Topics are very popular trademarks of the Frontiers Journals Series: they are collections of at least ten articles, all centered on a particular subject. With their unique mix of varied contributions from Original Research to Review Articles, Frontiers Research Topics unify the most influential researchers, the latest key findings and historical advances in a hot research area! Find out more on how to host your own Frontiers Research Topic or contribute to one as an author by contacting the Frontiers Editorial Office: frontiersin.org/about/contact

MEDICAL APPLICATION AND RADIOBIOLOGY RESEARCH OF PARTICLE RADIATION

Topic Editors:

Fei Ye, Institute of Modern Physics, Chinese Academy of Sciences (CAS), China

Chao Sun, Institute of Modern Physics, Chinese Academy of Sciences (CAS), China

Yi Xie, Institute of Modern Physics, Chinese Academy of Sciences (CAS), China

Lu Cai, University of Louisville, United States

Bing Wang, National Institute of Radiological Sciences (NIRS), Japan

Citation: Ye, F., Sun, C., Xie, Y., Cai, L., Wang, B., eds. (2022). Medical Application and Radiobiology Research of Particle Radiation. Lausanne: Frontiers Media SA. doi: 10.3389/978-2-88976-841-7

Table of Contents

- 05 Editorial: Medical Application and Radiobiology Research of Particle Radiation**
Fei Ye, Chao Sun, Yi Xie, Bing Wang and Lu Cai
- 08 Carbon Ion Therapy Inhibits Esophageal Squamous Cell Carcinoma Metastasis by Upregulating STAT3 Through the JAK2/STAT3 Signaling Pathway**
Hongtao Luo, Zhen Yang, Qiuning Zhang, Lihua Shao, Shihong Wei, Ruifeng Liu, Zheng Li, Yichao Geng, Chengcheng Li and Xiaohu Wang
- 19 China's Particle Therapy Equipment Market: Opportunities Outweigh Challenges**
Zhongying Dai, Yuanyuan Ma and Qiang Li
- 23 Protective Effects of p53 Regulatory Agents Against High-LET Radiation-Induced Injury in Mice**
Akinori Morita, Bing Wang, Kaoru Tanaka, Takanori Katsube, Masahiro Murakami, Takashi Shimokawa, Yuichi Nishiyama, Shintaro Ochi, Hidetoshi Satoh, Mitsuru Neno and Shin Aoki
- 29 Carbon Ion Irradiation Enhances the Anti-tumor Efficiency in Tongue Squamous Cell Carcinoma via Modulating the FAK Signaling**
Qingzong Si, Qian Ye, Zhitong Bing, Ruihong Fan, Xiaoli Hu, Bin Liu, Jizeng Wang, Yang Liu and Xiaoli An
- 38 Design of Beam Shaping Assemblies for Accelerator-Based BNCT With Multi-Terminals**
Guangru Li, Wei Jiang, Lu Zhang, Weiqiang Chen and Qiang Li
- 48 Irradiation-Induced Changes in the Immunogenicity of Lung Cancer Cell Lines: Based on Comparison of X-rays and Carbon Ions**
Juntao Ran, Jiangtao Wang, Ziyang Dai, Yandong Miao, Jian Gan, Chengpeng Zhao and Quanlin Guan
- 59 Dosimetric Deviations of Bragg-Peak Position Shifts in Uniform Magnetic Fields for Magnetic Resonance Imaging-Guiding Proton Radiotherapy: A Monte Carlo Study**
Xiaowa Wang, Hailun Pan, Qinqin Cheng, Xufei Wang and Wenzhen Xu
- 69 Dose-Effects Models for Space Radiobiology: An Overview on Dose-Effect Relationships**
Lidia Strigari, Silvia Strolin, Alessio Giuseppe Morganti and Alessandro Bartoloni
- 83 Combined Effects of Proton Radiation and Simulated Microgravity on the Cell Viability and ALP Activity of Murine Osteoblast Cells**
Liqu Ma, Fuquan Kong, Yihao Gong, Qiaojuan Wang, Jiancheng Liu and Li Sui
- 90 Radioactivity and Space Range of Ultra-Low-Activity for in vivo Off-line PET Verification of Proton and Carbon Ion Beam—A Phantom Study**
Fuquan Zhang, Junyu Zhang, Yan Lu, Yixiangzi Sheng, Yun Sun, Jiangang Zhang, Jingyi Cheng and Rong Zhou

- 97** *Carbon Ion Radiotherapy Evokes a Metabolic Reprogramming and Individualized Response in Prostate Cancer*
Renli Ning, Yulei Pei, Ping Li, Wei Hu, Yong Deng, Zhengshan Hong, Yun Sun, Qing Zhang and Xiaomao Guo
- 106** *Carbon Ion Radiotherapy Acts as the Optimal Treatment Strategy for Unresectable Liver Cancer During the Coronavirus Disease 2019 Crisis*
Zheng Li, Qiang Li, Xiaohu Wang, Sha Li, Weiqiang Chen, Xiaodong Jin, Xinguo Liu, Zhongying Dai, Xiongxiang Liu, Xiaogang Zheng, Ping Li, Hui Zhang, Qiuning Zhang, Hongtao Luo and Ruifeng Liu
- 118** *From Classical Radiation to Modern Radiation: Past, Present, and Future of Radiation Mutation Breeding*
Liqu Ma, Fuquan Kong, Kai Sun, Ting Wang and Tao Guo
- 129** *From Photon Beam to Accelerated Particle Beam: Antimetastasis Effect of Combining Radiotherapy With Immunotherapy*
Liqu Ma
- 137** *Artificial Intelligence Radiotherapy Planning: Automatic Segmentation of Human Organs in CT Images Based on a Modified Convolutional Neural Network*
Guosheng Shen, Xiaodong Jin, Chao Sun and Qiang Li



OPEN ACCESS

EDITED AND REVIEWED BY
Dariusz Leszczynski,
University of Helsinki, Finland

*CORRESPONDENCE

Fei Ye
yefe@impcas.ac.cn
Lu Cai
lu.cai@louisville.edu

SPECIALTY SECTION

This article was submitted to
Radiation and Health,
a section of the journal
Frontiers in Public Health

RECEIVED 28 May 2022
ACCEPTED 06 July 2022
PUBLISHED 22 July 2022

CITATION

Ye F, Sun C, Xie Y, Wang B and Cai L
(2022) Editorial: Medical Application
and Radiobiology Research of Particle
Radiation.
Front. Public Health 10:955116.
doi: 10.3389/fpubh.2022.955116

COPYRIGHT

© 2022 Ye, Sun, Xie, Wang and Cai.
This is an open-access article
distributed under the terms of the
[Creative Commons Attribution License](#)
(CC BY). The use, distribution or
reproduction in other forums is
permitted, provided the original
author(s) and the copyright owner(s)
are credited and that the original
publication in this journal is cited, in
accordance with accepted academic
practice. No use, distribution or
reproduction is permitted which does
not comply with these terms.

Editorial: Medical Application and Radiobiology Research of Particle Radiation

Fei Ye^{1*}, Chao Sun¹, Yi Xie¹, Bing Wang² and Lu Cai^{3*}

¹Institute of Modern Physics (CAS), Lanzhou, China, ²National Institute of Radiological Sciences, National Institutes for Quantum Science and Technology, Chiba, Japan, ³Department of Pediatrics, Radiation Oncology, Pharmacology and Toxicology, Pediatric Research Institute, University of Louisville School of Medicine, Louisville, KY, United States

KEYWORDS

particle therapy, radiation protection, radiation breeding, personalized medicine, BNCT

Editorial on the Research Topic

Medical Application and Radiobiology Research of Particle Radiation

Applications of particle radiation technology in the medical and biological fields are focused on disease treatment, radiation protection and radiation biology research related to plants and microorganisms. With the continuous improvement of cancer treatment technologies such as protons, heavy ions and boron neutron capture therapy (BNCT) (1), more and more medical centers have installed and used related equipment in recent years (2). However, due to the different policies of the medical industries, the development speed of particle therapy in various countries varies significantly. Charged ion therapy could offer advantages of biological and physical dose distributions, and higher relative biological effectiveness over conventional photon therapy for treatment of X-ray resistant and hypoxic tumors (3). BNCT, on the other hand, is the hope of radiation therapy for diffuse or irregularly shaped tumors (4). Improving the accuracy and efficiency of treatment remains major challenges for medical physicists (5).

Meanwhile, the worst nightmare for radiation oncologists was the accelerated metastasis and spread of tumors after radiation therapy (6). In addition, although the doctor will make a radiotherapy plan for physical dose delivery for each patient before radiation therapy (7), personalized medicine based on the radiation response of individual patients will be the future trend. The treatment based on individual radiation response now has two promising directions, combination of radiation therapy with immunotherapy and combination of radiation therapy with metabolic therapy.

Radiation protection has been a top priority ever since the recognition of the harmful effects of radiation on the human. For particle radiation protection, the most important research object is the radiation of high-energy charged particles in space.

Although gene editing technology (8) has developed rapidly in the past decade, radiation breeding is still an important way to cultivate crop seed lines, especially the development of particle accelerator technology and the continuous deepening

of aerospace research, which has made the research of particle radiation breeding more in-depth.

In this Research Topic, we invited scientists studying high-energy charged particles either for cancer treatment or for radiobiology research. The Research Topics accepted 15 articles including a total of 92 authors, demonstrating the high interest in several of the topics described above. As of this writing, the Research Topics have been viewed over 25000 times. The articles can be categorized into the following topics.

Medical physics technology

Four articles are dedicated to the improvement of dose delivery accuracy and treatment efficiency in particle therapy. In a highly viewed article, [Li et al.](#) reported a beam shaping assemblies (BSAs) design for accelerator based BNCT with multi terminals. The design of this beam shaping assembly allows one proton accelerator to be used to produce both epithermal and thermal neutrons. The latter is suitable for the treatment of superficial tumors, such as melanoma, and for preclinical experiments in small animals. The combination of MRI and proton therapy system transforms the traditional radiotherapy process (localization-treatment) into an adaptive workflow (MRI scan-plan optimization-treatment implementation), to allow timely adjustment of the treatment plan according to tumor volume changes and realizes real-time individualization of each fractionation for each patient, which is important for improving tumor control rate and reducing toxic side effects. Proton trajectories have deflection in the magnetic field, and the paper by Wang et al. calculates the dose deviation in the dose calculation of the proton therapy system when combined with MRI. PET can detect the induced radioactivity of charged particle streams *in vivo* to monitor information such as Bragg peak location and dose distribution. [Zhang et al.](#) found that off-line PET can detect ultra-low radioactivity down to 30 Bq/ml, this property allows off-line PET to be used to evaluate the completion of particle treatment plans. In the traditional radiotherapy workflow, organ segmentation depends heavily on physician expertise (9). [Shen et al.](#) automatically segmented 17 human organs using a neural network algorithm, which improved the accuracy and speed of organ segmentation.

Basic research related to cancer treatment

Whether radiotherapy promotes tumor metastasis is a controversial topic. In this issue, two studies on carbon ion irradiation of gastrointestinal tract cancer cell lines reveal the metastasis inhibitory effect of carbon ions. [Si et al.](#) found that carbon ion irradiation not only increased the growth inhibition of CAL27 cell line (tongue squamous cell

carcinoma) through FAK signaling pathway, but also decreased the metastatic ability of cancer cells. [Luo et al.](#) found that carbon radiation inhibited the metastatic ability of ECA109 and KYSE150 cell lines (esophageal squamous cell carcinoma) by modulating the JAK2/STAT3 signaling pathway. In addition, [Ma](#) reviewed the research progress on the anti-metastatic effects and mechanisms of photon or particle beam radiotherapy combined with immunotherapy, followed by the prediction of the future of this research area. Regarding individualized medicine in radiotherapy, currently it seemed only applied in the customization of dose delivery schedules. Apparently, it is a limitation because differences in metabolic capacity and levels of immune activation among different individuals may make the same treatment plan with different prognoses. In fact, this notion is supported by the following studies under different conditions. [Ning et al.](#) investigated metabolic end products in the urine of prostate cancer patients treated with carbon ion radiation, and they found that metabolic reprogramming and inhibition are involved in response to carbon ion radiotherapy in patients with prostate cancers. Therefore, they suggested the potential application of examining urine metabolites timely to assess individual response to carbon ion radiotherapy. Using single cell transcriptome technology to compare immunogenic molecular markers produced after X-ray and carbon ion irradiation of lung cancer cell lines, [Ran et al.](#) revealed a stronger immune response of these cancer cells in response to carbon ion irradiation than X-ray.

It is well-known that the COVID-19 pandemic has significantly disrupted the normal treatment of patients with cancer. [Li et al.](#) have re-evaluated the safety and efficacy of carbon ion radiation therapy for unresectable liver cancer and also compared with transarterial chemoembolization under such unexpected and undesirable condition. Consequently, carbon ion radiation therapy was able to achieve superior overall survival, local control, and relative hepatic protection since it can maximize the utilization of inpatient and outpatient treatment for patients with unresectable liver cancer due to shorter hospital stays (due to a shorter treatment course) and reduced care needs (due to low normal tissue toxicity). In addition, carbon ion radiation therapy allows in-hospital telemedicine to maintain sufficient person-to-person physical distance throughout the treatment of unresectable liver cancer, which is significant for cutting off the transmission route of the virus.

Particle radiation protection

In addition to artificial manufacturing, particle radiation is generally found in radon gas and in space. By comparing data from space missions and ground-based experiments, [Bartoloni et al.](#) compiled dose-effect relationships for several particle radiation health risk events. In a ground-based experiment simulating a space environment, [Ma et al.](#) evaluated the effects of

proton radiation combined with microgravity effects on mouse embryonic osteoblast precursor cells (MC3T3-E1) and showed that cell proliferation and differentiation capacity were reduced in a dose-dependent manner. After demonstrating the protective effect of transcription factor P53 modulators against low-energy X-ray or gamma radiation-induced damage, [Morita et al.](#) further demonstrated that P53 modulators were also effective in protecting the hematopoietic system and mitigating intestinal damage during high-energy carbon or iron ion beam irradiation.

Others

Food supply is of common international concern. With increasing populations and rapid climate change, increasing food production has become an imperative. Although advanced technologies such as gene editing provide an effective way to breed varieties, radiation is able to mutate to improve germplasm diversity because it can bring about more random mutations throughout the genome. [Ma et al.](#) reviewed the achievements and progress of traditional photon radiation breeding and described the developments in seed production research brought by particle radiation based on particle accelerator and cosmic radiation received on space stations that have emerged in recent years.

Particle accelerator is the largest medical device, which is expensive and occupies a large area, and the industrialization process of particle therapy is greatly influenced by the industrial policy of each country. [Dai et al.](#) shared the industrial policy of particle therapy in China and the difficulties encountered in the industrialization process. This article has the highest number of views, which indicates that readers have a strong interest in this topic.

References

1. Malouff TD, Seneviratne DS, Ebner DK, Stross WC, Waddle MR, Trifiletti DM, et al. Boron neutron capture therapy: a review of clinical applications. *Front Oncol.* (2021) 11:601820. doi: 10.3389/fonc.2021.601820
2. Durante M, Cucinotta FA, Loeffler JS. Editorial: charged particles in oncology. *Front Oncol.* (2017) 7:301. doi: 10.3389/fonc.2017.00301
3. Byun HK, Han MC, Yang K, Kim JS, Yoo GS, Koom WS, et al. Physical and biological characteristics of particle therapy for oncologists. *Cancer Res Treat.* (2021) 53:611–20. doi: 10.4143/crt.2021.066
4. Matsumoto Y, Fukumitsu N, Ishikawa H, Nakai K, Sakurai H, Fang J, et al. A critical review of radiation therapy: from particle beam therapy (Proton, Carbon, and BNCT) to beyond. *J. Personalized Med.* (2021) 11:825. doi: 10.3390/jpm11080825
5. Yap J, De Franco A, Sheehy S. Future developments in charged particle therapy: improving beam delivery for efficiency

and efficacy. *Front Oncol.* (2021) 11:780025. doi: 10.3389/fonc.2021.780025

In summary, this special issue reviews past and current works, and provides new findings in researches and applications related to particle radiation, with an emphasis on the particle therapy in cancer treatment. We also collected articles on topics related to particle radiation protection, radiation seeding and the industrialization of particle therapy devices. We hope that this special issue could present the readers with a big picture of particle radiation applications and bring new ideas to researchers.

Author contributions

FY drafted the manuscript. BW, CS, and YX revised the manuscript. LC finalized the manuscript. All authors contributed to the article and approved the submitted version.

Conflict of interest

The authors declare that the research was conducted in the absence of any commercial or financial relationships that could be construed as a potential conflict of interest.

Publisher's note

All claims expressed in this article are solely those of the authors and do not necessarily represent those of their affiliated organizations, or those of the publisher, the editors and the reviewers. Any product that may be evaluated in this article, or claim that may be made by its manufacturer, is not guaranteed or endorsed by the publisher.

6. Blyth BJ, Cole AJ, MacManus MP, Martin OA, et al. Radiation therapy-induced metastasis: radiobiology and clinical implications. *Clin Exp Metastasis.* (2018) 35:223–36. doi: 10.1007/s10585-017-9867-5
7. Schaub L, Harrabi SB, Debus J. Particle therapy in the future of precision therapy. *Br J Radiol.* (2020) 93:20200183. doi: 10.1259/bjr.20200183
8. Tan Y, Du H, Wu X, Liu Y, Jiang M, Song S, et al. Gene editing: an instrument for practical application of gene biology to plant breeding. *J Zhejiang Univ Sci B.* (2020) 21:460–73. doi: 10.1631/jzus.B1900633
9. Coates J, Souhami L, El Naqa I. Big data analytics for prostate radiotherapy. *Front Oncol.* (2016) 6:149. doi: 10.3389/fonc.2016.00149



Carbon Ion Therapy Inhibits Esophageal Squamous Cell Carcinoma Metastasis by Upregulating STAT3 Through the JAK2/STAT3 Signaling Pathway

OPEN ACCESS

Edited by:

Bing Wang,
National Institutes for Quantum and
Radiological Science and Technology
(Japan), Japan

Reviewed by:

Tomisato Miura,
Hirosaki University, Japan
Peramaiyan Rajendran,
King Faisal University, Saudi Arabia
Ming Chen,
Zhejiang Cancer Hospital, China

*Correspondence:

Xiaohu Wang
xhwang@impcas.ac.cn

† These authors have
contributed equally to this work

Specialty section:

This article was submitted to
Radiation and Health,
a section of the journal
Frontiers in Public Health

Received: 03 July 2020

Accepted: 28 October 2020

Published: 20 November 2020

Citation:

Luo H, Yang Z, Zhang Q, Shao L,
Wei S, Liu R, Li Z, Geng Y, Li C and
Wang X (2020) Carbon Ion Therapy
Inhibits Esophageal Squamous Cell
Carcinoma Metastasis by
Upregulating STAT3 Through the
JAK2/STAT3 Signaling Pathway.
Front. Public Health 8:579705.
doi: 10.3389/fpubh.2020.579705

Hongtao Luo^{1,2,3†}, Zhen Yang^{4†}, Qiuning Zhang^{1,3}, Lihua Shao⁵, Shihong Wei⁵,
Ruifeng Liu^{1,3}, Zheng Li¹, Yichao Geng², Chengcheng Li² and Xiaohu Wang^{1,2,3,4*}

¹ Institute of Modern Physics, Chinese Academy of Sciences, Lanzhou, China, ² The First Clinical Medical College of Lanzhou University, Lanzhou, China, ³ Lanzhou Heavy Ion Hospital, Lanzhou, China, ⁴ The Basic Medical College of Lanzhou University, Lanzhou, China, ⁵ Gansu Provincial Cancer Hospital, Lanzhou, China

Radiation therapy is an important component of the comprehensive treatment of esophageal cancer. However, conventional radiation resistance is one of the main reasons for treatment failure. The superiority of heavy ion radiation in physics and biology has been increasingly highlighted in radiation therapy research. The Janus Kinase 2/Signal Transducer and Activator of Transcription 3 (JAK2/STAT3) pathway plays an important role in the occurrence, development and metastasis of esophageal squamous cell carcinoma (ESCC) and is related to the development of resistance to ionizing radiation in ESCC. Therefore, the aim of the present study was to investigate the relationship between carbon ion inhibition of the proliferation and metastasis of esophageal carcinoma cells and the JAK2/STAT3 signaling pathway. The results demonstrated that carbon ion beams significantly reduced cell viability and stimulated apoptosis in human ESCC cells in a dose-dependent manner. In addition, carbon ion beams induced G2/M phase cell cycle arrest in ESCC cells and inhibited tumor metastasis in a dose-dependent manner. Additionally, poorly differentiated KYSE150 cells were more sensitive to the same carbon ion beam dose than moderately differentiated ECA109 cells. Carbon ion beam exposure regulated the relative expression of metastasis-related molecules at the transcriptional and translational levels in ESCC cells. Carbon ion beams also regulated *CDH1* and *MMP2* downstream of the STAT3 pathway and inhibited ESCC cell metastasis, which activated the STAT3 signaling pathway. This study confirmed the inhibition of cell proliferation and the metastatic effect of carbon ion beam therapy in ESCC cells.

Keywords: carbon ion beam, esophageal squamous cell carcinoma, apoptosis, metastasis, JAK2/STAT3 pathway

INTRODUCTION

Esophageal cancer is the eighth most prevalent cancer worldwide and is the sixth leading cause of tumor-related death (1). Radiation therapy is one of the mainstays of treatment for esophageal cancer, but in China, 95% of esophageal cancers are esophageal squamous cell carcinomas (ESCCs) (2). ESCC is relatively resistant to traditional X-ray radiotherapy and has poor clinical outcomes, and the main causes of failure are local uncontrolled growth or/and recurrence. Studies have shown that when high linear energy transfer (LET) ray-carbon ion irradiation is applied, cell damage primarily involves DNA double-strand breaks (DSBs). Clinical studies have shown that carbon ion radiotherapy has a good clinical effect on refractory or recurrent tumors treated with conventional photon radiotherapy. At present, not many mechanisms by which carbon ion radiation induces tumor cell apoptosis and inhibits metastasis have been established. Signal transducer and activator of transcription 3 (STAT3) was recognized as an oncogene for its role in the malignant transformation of cells and tumorigenesis (3, 4). STAT3 protein is activated by tyrosine phosphorylation at residue 705, and p-STAT3 (Tyr705) is able to upregulate the transcription of genes involved in cell proliferation, apoptosis, angiogenesis, invasion and metastasis. Carbon ion beams can alter the biological characteristics of tumor cells. However, the mechanisms by which carbon ion beams function remain unclear, especially in terms of how they regulate the JAK2/STAT3 signaling pathway.

MATERIALS AND METHODS

Cell Culture and Irradiation Conditions

Human ESCC cells (ECA109, KYSE150) were obtained from the Shanghai Genechem Co., Ltd. The cells were maintained in RPMI1640 medium supplemented with 10% (v/v) fetal bovine serum (FBS), 100 U/mL penicillin and 100 mg/mL streptomycin (Life Technologies) in a humidified atmosphere of 5% (v/v) CO₂ and 95% (v/v) air at 37°C. The medium was changed every other day, and cells in the logarithmic growth phase (1×10^7 cells were harvested at 70% confluence) were used for subsequent experiments. Heavy ions were obtained from the Cooling Storage Ring Project of the Heavy Ion Research Facility in Lanzhou (HIRFL-CSR) (Ray parameters: energy of 100 MeV, dose rate of 1 Gy/min, broadened Bragg peak of 5 mm, radiation field of 5×5 cm). For cell irradiation, heavy ions were obtained from the carbon ion ($^{12}\text{C}^{6+}$) beam of the Deep Therapy Terminal, Institute of Modern Physics, Chinese Academy of Sciences (HIRFL-CSR). Irradiation doses were 0, 1, 2, and 4 Gy. This experiment was repeated three times.

Colony Formation Assay

Cells in the logarithmic growth phase were detached with 0.25% trypsin and then triturated into single cells and centrifuged. The number of cells was counted with a counting board. After they were resuspended in culture medium containing 10% FBS, ECA109 and KYSE150 cells were inoculated separately into a

6-well plate after, as follows: 0 Gy group, 200 cells/well; 1 Gy group, 1,000 cells/well; 2 Gy group, 2,000 cells/well; and 4 Gy group, 4,000 cells/well. Three replicate wells were used for each group. After an overnight inoculation, the cells were exposed to 0, 1, 2, or 4 Gy carbon ion rays and cultured in a cell incubator for 12 days. When the cell colonies were visible to the naked eye, approximately 50 cells were counted under the microscope, and the experiment was terminated. Next, the cells were fixed in 4% polyformaldehyde (500 μL) for 15 min, stained with a crystal violet solution (500 μL) for 15 min and observed by microscopy. The plating efficiency (PE) = colony number/inoculation number \times 100%, and the survival fraction (SF) = colony rate in the experimental group/colony rate in the control group \times 100%. The cell dose survival curve was generated using the formula $S = 1 - (1 - e^{-KD})^N$ and GraphPad Prism 6 software. This experiment was repeated three times.

Cell Counting Kit-8 (CCK-8) Assay

ECA109 and KYSE150 cells cultured in individual wells were detached with trypsin and resuspended in a small volume of culture medium, after which the cells were counted. Next, 100 μL ($\sim 10,000$ cells) of the cell suspension was added to each well of a 96-well plate. Six replicate wells were used for each group, and the culture plate was placed in an incubator for a 24-h pre-culture (37°C, 5% CO₂) to allow the cells to adhere. To avoid the influence of water volatilization on cell growth and the experimental results, 200 μL PBS was added to each well of the culture plate. When the cells reached 50–60% confluence, they were exposed to 0, 1, 2, or 4 Gy carbon ion rays. Cell proliferation was detected at 24, 48, and 72 h after irradiation. Cells in each well were then incubated with 10 μL CCK-8 solution for 2 h. The optical density (OD) value of each well was detected by a microplate reader (450 nm). The cell survival rate = (OD value in each irradiation group - OD value in each blank group) / (OD value in the non-irradiation group - OD value in each blank group) \times 100%. This experiment was repeated three times.

Cell Cycle and Apoptosis Analysis

Cells were seeded into $\Phi 60$ plates for 24 h and exposed to 0, 1, 2, or 4 Gy carbon ion radiation when they reached 50–60% confluence. Next, the cells were prepared by trypsin digestion after which 1×10^3 cells/ml were collected for the detection of cell cycle distribution. The cell cycle distribution was detected at 24 h. Cells were then labeled with propidium iodide (PI), and 1×10^4 cells were collected by flow cytometry for cell cycle analysis (BD Biosciences, San Jose, CA, USA). ECA109 and KYSE150 cells were irradiated with 0, 1, 2, or 4 Gy of carbon ion beams and then cultured for 24 h. The cells were detached with EDTA-free trypsin and then washed with pre-cooled PBS. The dead cells floating in the medium were also collected. The cells were suspended in 100 μL of $1 \times$ binding buffer and prepared as a single cell suspension with a density of 1×10^6 cells/ml. After treatment, the cells were harvested with trypsin and washed twice with cold PBS. The cells were then stained with Annexin V for 10 min in the dark and then stained with PI for 5 min. Annexin V-binding buffer was then added to the mixture before fluorescence was

measured on a FACSCalibur flow cytometer (BD Biosciences; Baltimore, MD, USA). In all, 2×10^4 cells were collected by flow cytometry for apoptosis analysis. The data were analyzed using Flow Jo software.

Wound-Healing Assay

Wound-healing assays were performed according to a routine protocol, as follows: 3×10^5 ECA109 and KYSE150 cells were seeded in each well of a 6-well plate in RPMI 1640 medium with 10% FBS and cultured at 37°C with 5% CO₂ for 24 h until a monolayer was formed. A scratch wound was generated at the bottom of the plate using a sterile 10-μL pipette tip. After three washes in PBS, the cells were irradiated with 0, 1, 2, or 4 Gy carbon ion beams and then cultured for 24 h, which allowed examination of cell migration in the absence of cell growth. Wound closure was measured in three random fields in each well using an inverted microscope and was compared with that of the control group. Each group was assayed in triplicate.

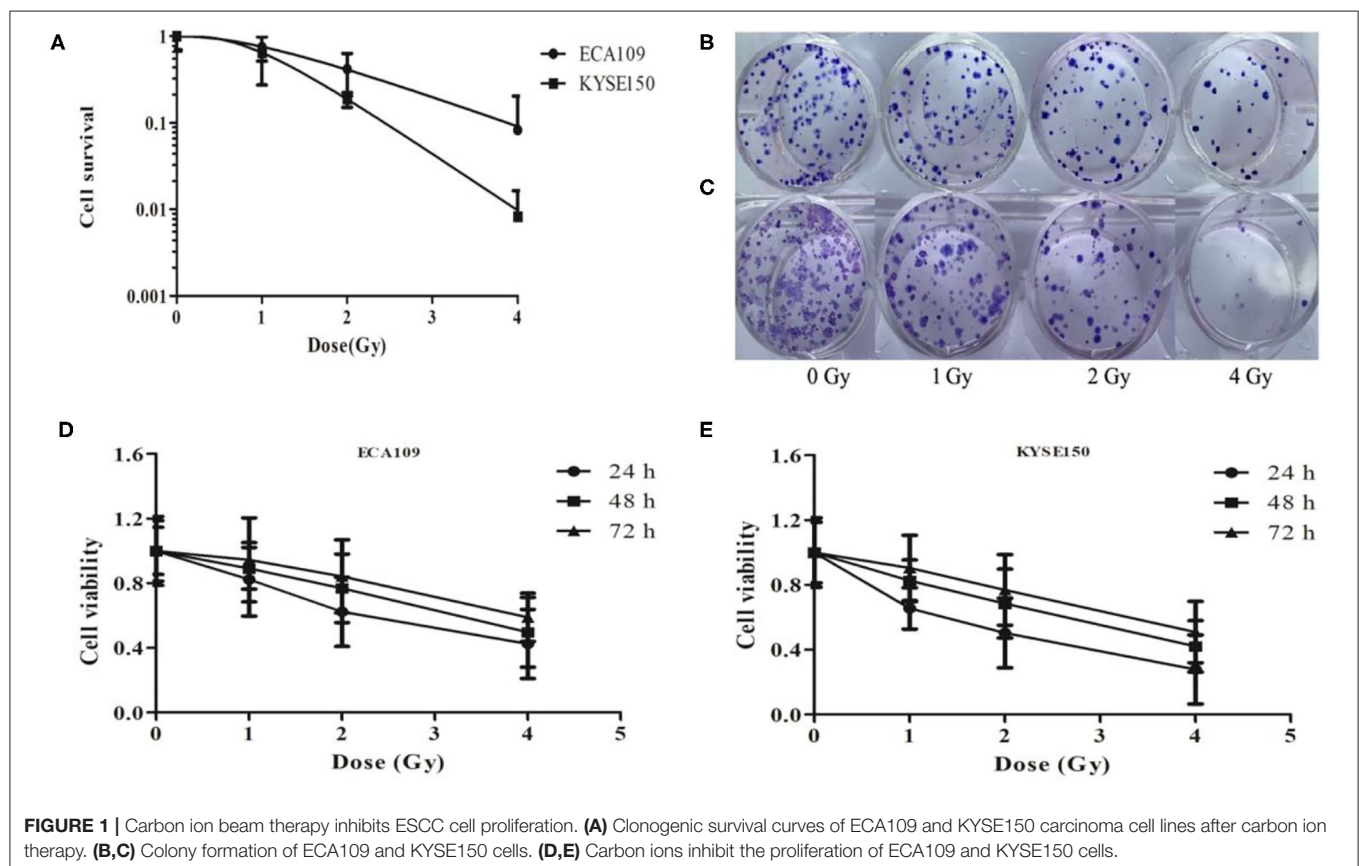
Transwell Assay

A Transwell assay to determine cell invasion was performed according to the following protocol. Polycarbonate membranes with an 8-μm pore (Corning, USA) were placed in 24-well Transwell plates (Corning, USA). Briefly, the polycarbonate filters were coated with Matrigel at a concentration of 1 μg/mL and placed in a modified Boyden chamber. The irradiated cells

were prepared by trypsin digestion after which cells (3×10^4) resuspended in RPMI 1640 medium containing 1% (v/v) FBS were added to the top chamber. Culture medium containing 5% (v/v) FBS was then added to the bottom chamber. Cell motility/migration was measured as the number of cells that migrated from a defined area on the uncoated microfilter through micropores over a given time (24 h). The cells that migrated to the lower surface of the membrane were fixed in methanol for 10 min and stained with 0.5% (w/v) crystal violet for 30 min. All experiments were performed in triplicate, and a minimum of five fields per filter was counted.

RNA Isolation and Quantification

Total RNA was extracted from cells using TRIzol (Takara Co., Ltd., Dalian, China), after which the concentration and purity of the RNA were determined. For the detection of *STAT3*, *MMP2* and *CDH1* mRNA, reverse transcription primers (synthesized by Suzhou GENEWIZ Co., Ltd., Suzhou, China) and a reverse transcription kit (Takara Co., Ltd., Dalian, China) were used to reverse-transcribe cDNA. SYBR Green Real-Time PCR Master Mix was used for real-time polymerase chain reaction (PCR) assays, which were performed in an ABI 7500 real-time PCR system. The following primer sequences were used for real-time PCR: *STAT3*-F: 5'-ACCAGCAGTATAGCCGCTTC-3'; *STAT3*-R: 5'-GCCACAATCCGGCAATCT-3'; *MMP2*-F: 5'-GATGGCATCGCTCAGATCCG-3'; *MMP2*-R: 5'-TCAG GCCA

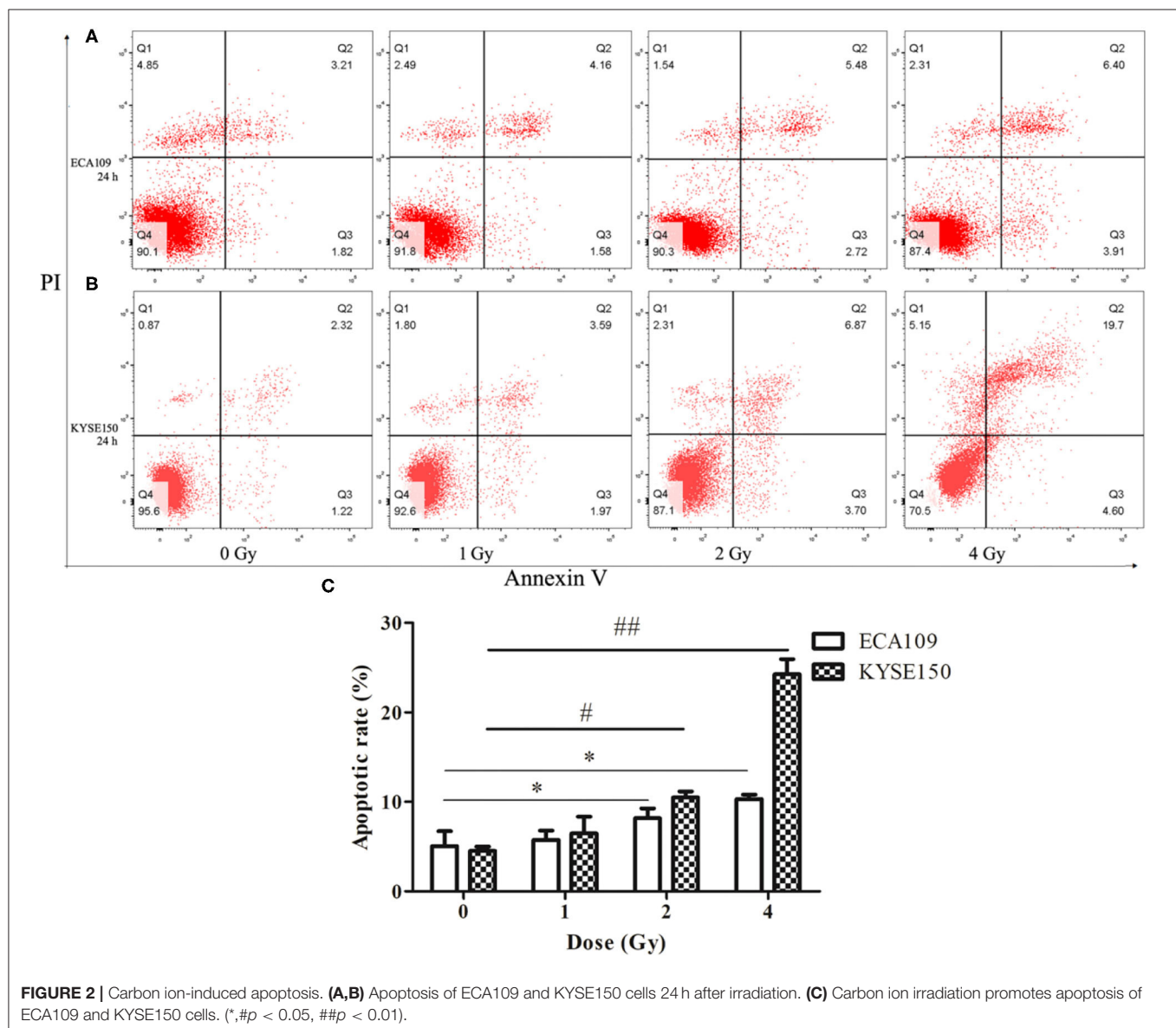


GAATGTGGCCAC-3'; *CDH1*-F: 5'-AGAGGTGGGTGACTAC AAA-3'; *CDH1*-R: 5'-TCTCTCCGAAGAAACAG-3'; JAK2-F: 5'-GCTCAGTGGCGGCATGAT-3'; 5'-CACTGCCATCCCAA GACATTC-3'; *ACTB*-F: 5'-CGGGAAATCGTGC GTGAC-3'; *ACTB*-R: 5'-GAAGGAAGGCTGGAAGAGT-3'. *ACTB* was used as an internal control, and $2^{-\Delta\Delta C_t}$ was used to calculate gene expression. This experiment was repeated three times.

Western Blot Analysis

Cells were washed with ice-cold PBS and total proteins were extracted in lysis buffer (Solarbio, Beijing). The protein concentrations were determined by a Bradford assay. The cell lysates were mixed with 5x sodium dodecyl sulfate (SDS) sample buffer, boiled for 5 min, and then separated by 10% (w/v) SDS-PAGE. After electrophoresis, the proteins were transferred to polyvinylidene difluoride (PVDF) membranes, which were blocked in 5% (w/v) non-fat dry milk or BSA for 30 min.

Membranes were rinsed and incubated with the following specific antibodies against MMP2 (mouse monoclonal, 1:2,000) (GTX27033, GeneTex, USA), ACTB (mouse monoclonal, 1:2,000) (GTX26272, GeneTex, USA), JAK2 (YT2429, rabbit, Immunoway, 1:1000), STAT3 (rabbit polyclonal, 1:1,000) (cat. no. 9139T, CST, USA), Phospho-Stat3 (Tyr705) (rabbit polyclonal, 1:1,000) (cat. no. 9145, CST, USA), and CDH1 (mouse monoclonal, 1:2,000) (GTX629691, GeneTex, USA) in Tris-buffered saline containing 5% (w/v) non-fat dry milk and Tween-20 (0.1% (v/v)) (TBST) overnight at 4°C. After washing, the signals were detected with a horseradish peroxidase-conjugated secondary antibody (1:1,000, cat. no. ZDR-5307, ZSGB. BIO, China) for 1 h and were washed three times in TBST. Finally, immunopositive bands were visualized using an enhanced chemiluminescence (ECL) system (Amersham Pharmacia Biotech) and were exposed using Image Lab 3.0 (Bio-Rad, USA).



Statistical Analyses

The statistical significance between groups was determined using either the ANOVA test followed by the Bonferroni post-test when applicable or the Mann-Whitney *U*-test. Data are presented as the mean \pm SD. All experiments were performed at least three times using new frozen batches of cells to maintain independence among replicates. Analysis was performed and graphs were generated using GraphPad Prism software 5.0.

RESULTS

Carbon Ion Beams Inhibit Cell Colony Formation and Cell Proliferation

We analyzed the radiosensitivity of two differentiated esophageal cancer cell lines (ECA109 and KYSE150) to carbon ions. The results confirmed that colony formation ability was significantly

lower in cells treated with 1, 2, and 4 Gy compared with cells treated with 0 Gy (**Figure 1A**). A positive correlation was observed between the colony formation inhibition rate and the carbon ion irradiation dose. The survival of both cell lines decreased after treatment with 1 Gy irradiation compared with treatment with 0 Gy, but the difference was not significant (**Figures 1B,C**); however, after 2 and 4 Gy irradiation, cell survival decreased significantly ($p = 0.031$). Taken together, these data clearly demonstrate that carbon ions can effectively inhibit ESCC cell proliferation.

The CCK-8 assay results revealed different growth changes after 24, 48, and 72 h. After 1 Gy irradiation, ECA109 and KYSE150 cell proliferation was significantly inhibited at 24 h, and this inhibition increased in a dose-dependent manner; ECA109 cell proliferation inhibition showed a decreasing trend at different times after irradiation, but no significant differences

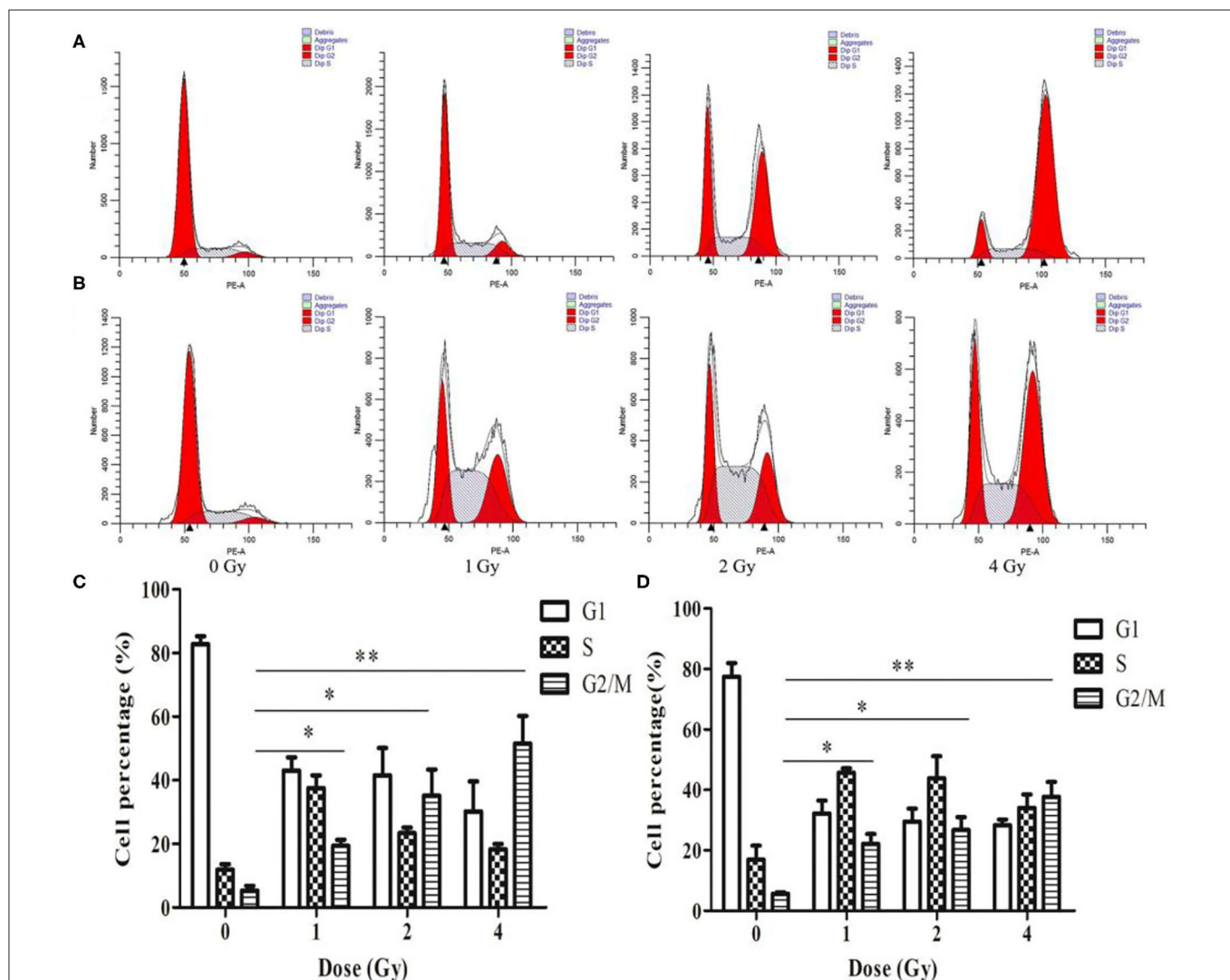


FIGURE 3 | Changes in cell cycle arrest 24 h after irradiation of ECA109 and KYSE150 cells with carbon ion rays. **(A,B)** Cell cycle distribution of ECA109 and KYSE150 cells 24 h after irradiation. **(C,D)** Inhibition of cell cycle arrest in ECA109 and KYSE150 cells by carbon ions. * $p < 0.05$, ** $p < 0.01$.

were found among the various time points (Figures 1D,E). Compared with ECA109 cells, KYSE150 cells were more sensitive to heavy ion irradiation, and KYSE150 cell proliferation was significantly inhibited 24 h after 1 Gy irradiation ($p = 0.042$). However, cell proliferation inhibition was not significant at 48 and 72 h. In contrast, KYSE150 cell proliferation was significantly inhibited after 2 and 4 Gy irradiation.

Carbon Ion Beams Induce Apoptosis in Human ESCC Cells

Compared with the 0 Gy group, the 2 and 4 Gy groups exhibited enhanced inhibition of cell viability in the tested cell lines. At 24 h after irradiation, more dead ECA109 cells were observed

(Figure 2A) than after 0 Gy; the apoptosis rate was significantly higher after 1, 2 and 4 Gy irradiation, and the apoptosis rates were highest in KYSE150 cells after 2 and 4 Gy irradiation ($p = 0.048$, $p = 0.027$, Figure 2B). The number of apoptotic cells was positively correlated with the irradiation dose. The apoptosis rates of ECA109 cells and KYSE150 cells were different after the same dose of carbon ion irradiation, as KYSE150 cells were more sensitive to carbon ion beams (Figure 2C).

Carbon Ion Beams Induce G2/M Cell Cycle Arrest in Human ESCC Cells

The cell cycle involves a series of cellular events that lead to cell division and eventually proliferation. After 0, 1, 2 and

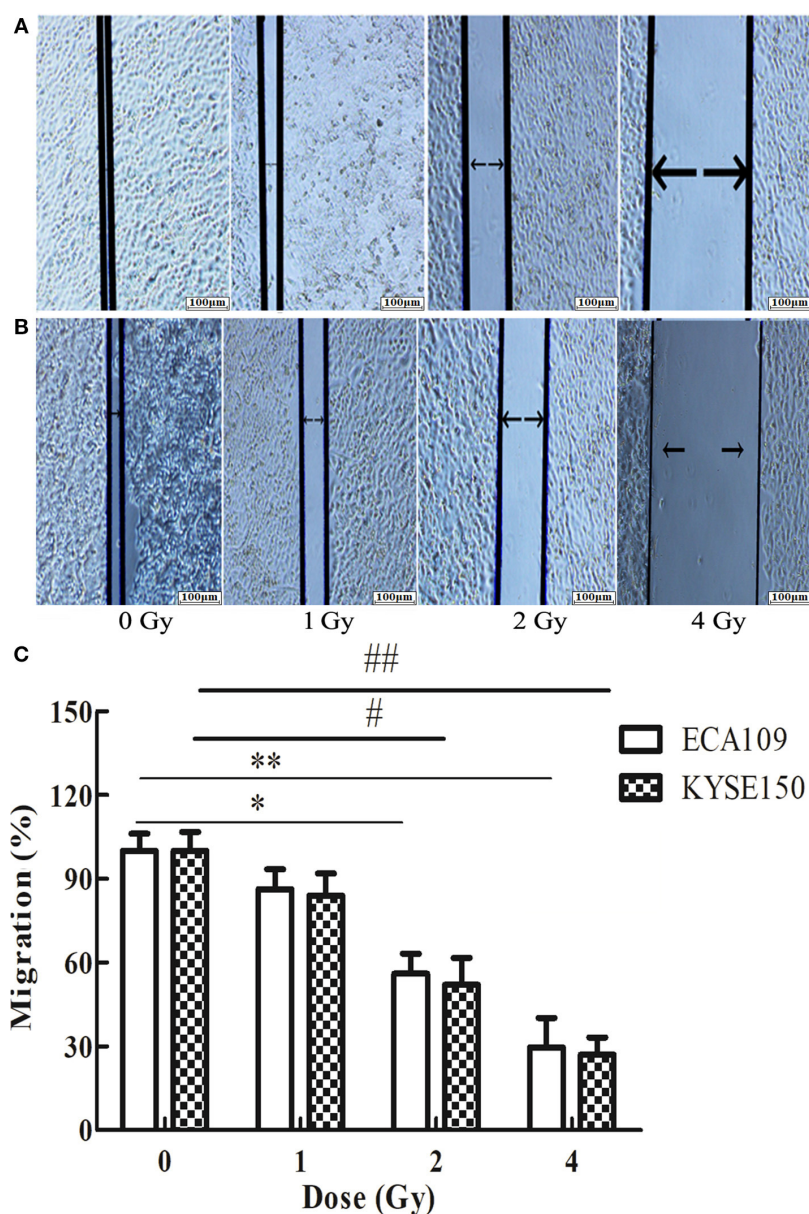


FIGURE 4 | The effect of carbon ion beam irradiation on ECA109 and KYSE150 cell migration as shown by a wound-healing assay. (A,B) Scratch area of ECA109 and KYSE150 cells 24 h after irradiation. (C) Inhibition of ECA109 and KYSE150 cell migration by carbon ions (*, $p < 0.05$, **, $p < 0.01$).

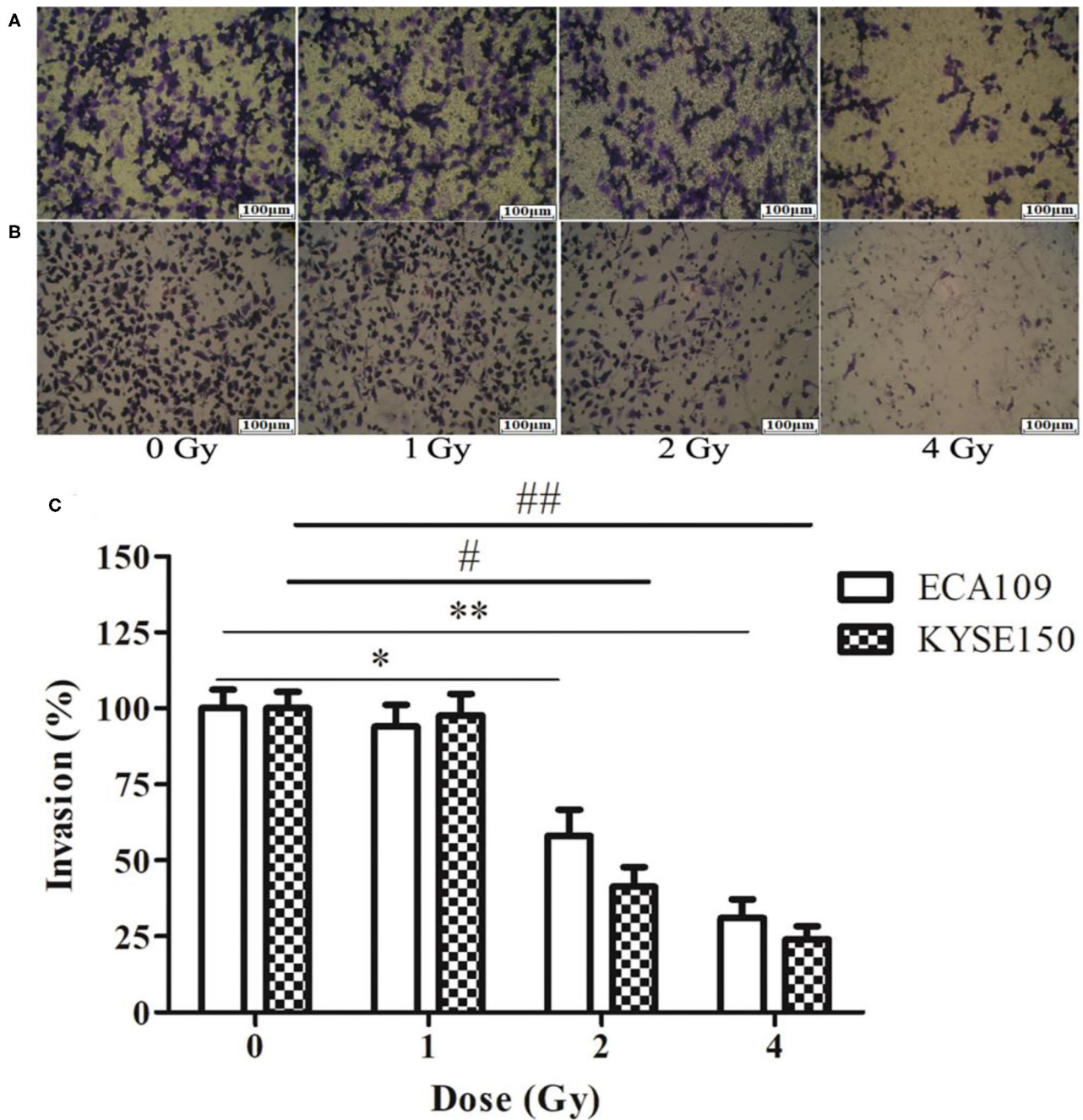
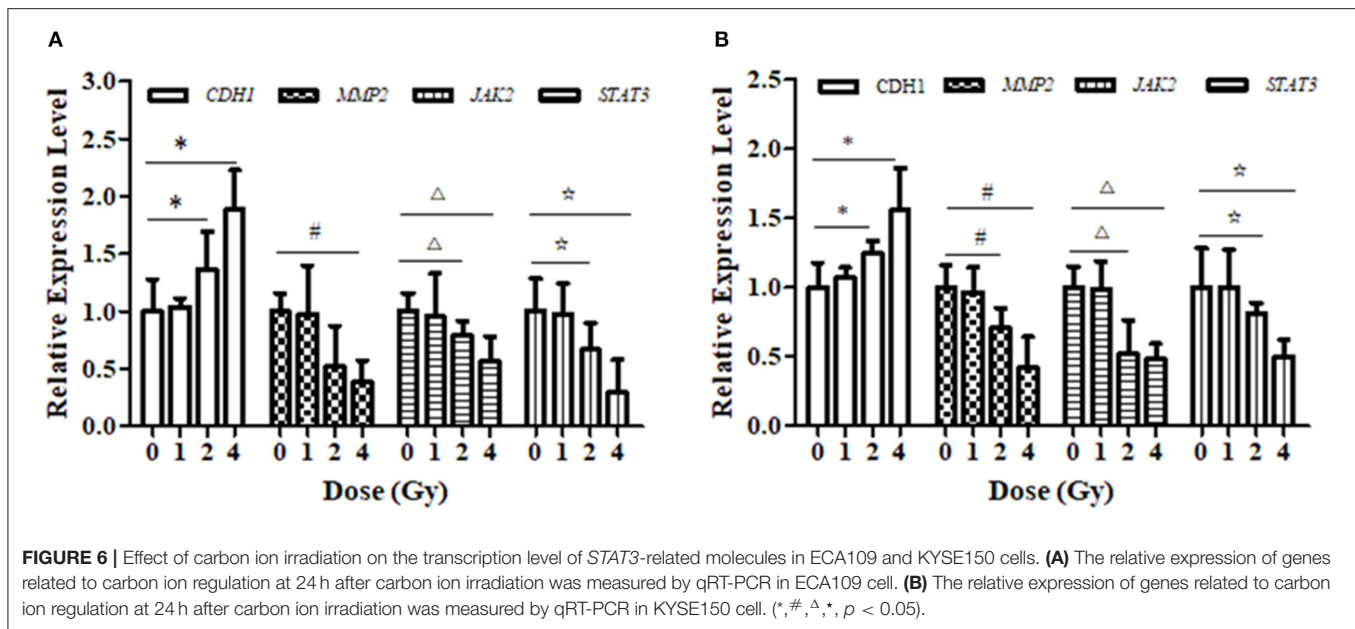


FIGURE 5 | The effect of carbon ion beam irradiation on ECA109 and KYSE150 cell invasiveness by Transwell assay. **(A)** Number of invasive ECA109 cells after irradiation. **(B)** Number of invasive KYSE150 cells after irradiation. **(C)** Inhibition of ECA109 and KYSE150 cell invasion by carbon ions (*, # $p < 0.05$, **, ## $p < 0.01$).

4 Gy irradiation, the number of ECA109 and KYSE150 cells in G2/M phase arrest increased in a dose-dependent manner within 24 h compared with after 0 Gy irradiation (**Figures 3A,B**). Twenty-four hours after carbon ion irradiation, significantly more KYSE150 cells were in S phase arrest after 1, 2 and 4 Gy irradiation, whereas the number of cells in S phase arrest was

decreased after 4 Gy (**Figure 3B**). S phase arrest increased after 1 Gy irradiation, but G2/M phase arrest was not significantly different ($p = 0.69$), while G2/M phase arrest was significant after 2 and 4 Gy irradiation ($p = 0.025$, $p = 0.013$, **Figure 3C**). G2/M arrest also increased in a dose-dependent manner, and the increase was most significant after 4 Gy ($p = 0.010$, **Figure 3D**).



Carbon Ion Beams Inhibit Migration and Invasiveness of ECA109 and KYSE150 Cells

The wound-healing assay showed that the relative migration and invasiveness of ECA109 cells was significantly lower 24 h after 2 and 4 Gy irradiation than 24 h after 0 Gy irradiation ($p = 0.045$, $p = 0.028$, **Figure 4A**). A positive correlation was observed between the number of KYSE150 cells that had migrated and invaded and the irradiation dose (**Figures 4B,C**). However, migration and invasion in the 1 Gy group were not significantly different ($p = 0.960$, **Figures 5A,B**). At 24 h after irradiation, the number of migrating and invading KYSE150 cells was significantly lower ($p = 0.031$, $p = 0.010$, **Figure 5C**) after 2 and 4 Gy irradiation than after 0 Gy irradiation but was not significantly different after irradiation with 1 Gy ($p = 1.25$).

Carbon Ion Beams Regulate Metastasis-Related Expression of Proteins in the JAK2/STAT3 Signaling Pathway

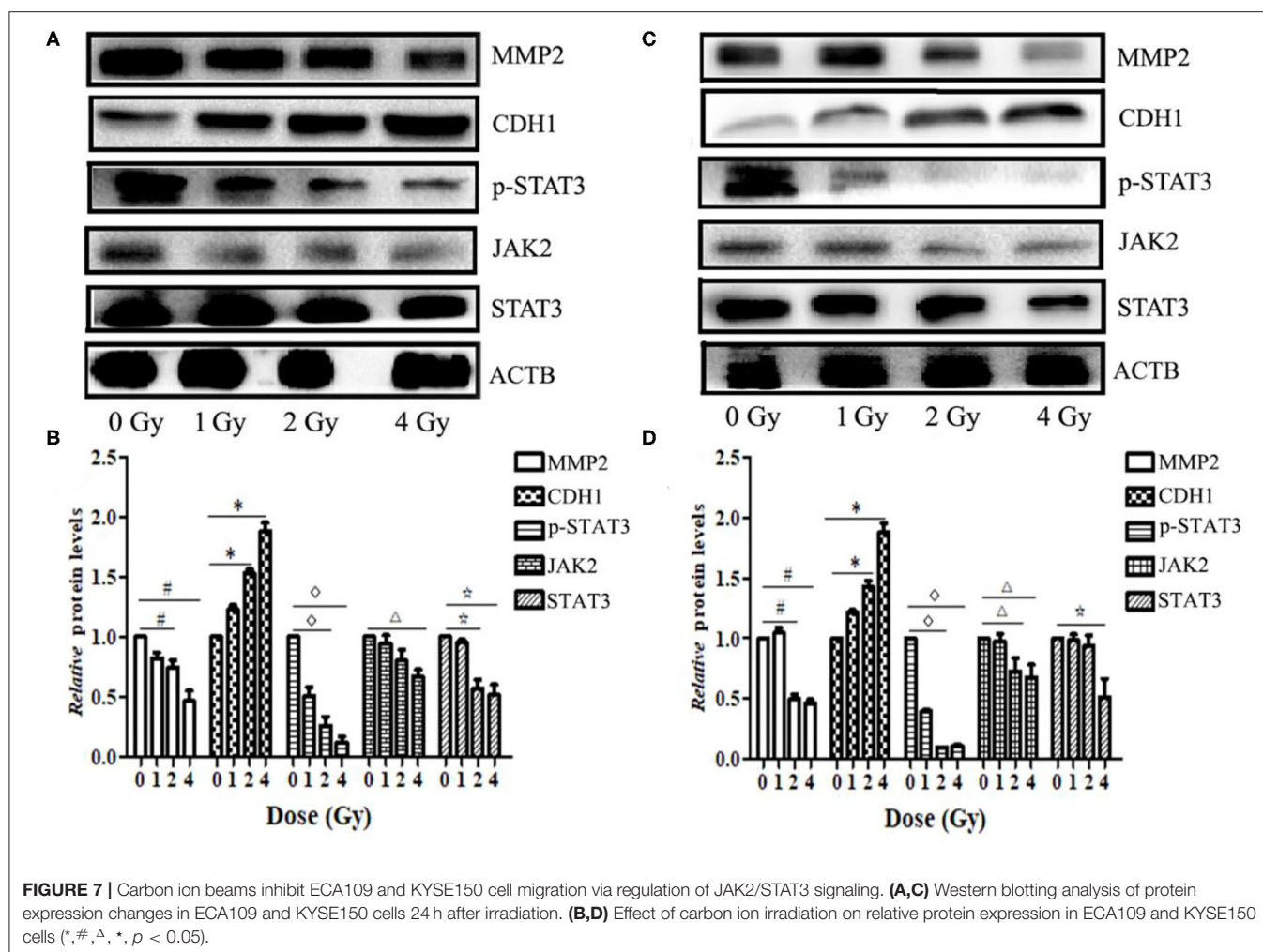
The relative expression levels of *CDH1*, *JAK2*, and *STAT3* mRNA in ECA109 cells were significantly different ($p = 0.027$, $p = 0.034$ and $p = 0.015$, **Figure 6A**) after 2 and 4 Gy carbon ion irradiation compared with those in the 0 Gy group. *MMP2* mRNA was differentially expressed after 4 Gy and was not significantly expressed after 1 Gy irradiation ($p = 0.081$). At 24 h, *CDH1* expression was upregulated and *MMP2*, *JAK2* and *STAT3* mRNA expression was downregulated after 2 and 4 Gy irradiation in KYSE150 cells, and these differences were significant ($p = 0.017$, $p = 0.042$, and $p = 0.29$, **Figure 6B**); in contrast, the expression levels were not significantly altered after 1 Gy irradiation ($p = 0.076$, $p = 0.052$, and $p = 0.108$).

Western blotting results showed that the expression levels of *MMP2* and *STAT3* proteins in ECA109 and KYSE150 cells

were reduced at 24 h after different doses of carbon ion beam irradiation (**Figures 7A,B**), and the expression levels of both proteins were lower after 2 and 4 Gy irradiation than after 0 Gy irradiation ($p = 0.136$ and $p = 0.265$, $p > 0.05$). Carbon ion irradiation of 2 and 4 Gy significantly reduced the expression of *JAK2* in KYSE150 cells, while in ECA109 cells, the expression of *JAK2* was significantly downregulated after 4 Gy irradiation (**Figures 7C,D**). The expression level of *CDH1* (E-cadherin) protein was increased, with the highest protein expression observed after 4 Gy irradiation (**Figure 7C**). No significant difference was seen in the expression levels of these three proteins after 1 Gy irradiation. In KYSE150 cells, the expression levels of *MMP2*, *STAT3* and p-*STAT3*(Tyr705) were significantly altered after 4 Gy irradiation (**Figure 7D**).

DISCUSSION

ESCC is a common cancer type worldwide and accounts for an estimated 90% of the most malignant esophageal tumors (5). The treatment of ESCC is generally limited to surgical resection, chemotherapy and radiotherapy approaches, but the results are often largely unsatisfactory (6). Surgery is the treatment of choice for EC, but 80% of patients with EC are no longer candidates for radical surgery at the time of diagnosis (7), and thus, radiotherapy is the primary treatment for patients with advanced EC (8). Recent studies have indicated that ESCC progression occurs as a result of synergy among multiple genes (9). In recent years, with the continuous development of radiotherapy equipment and technology, carbon ion beams with high-energy transmission of linear density rays not only have the physical advantages of Bragg peak dose distributions compared with photons, but they also have greater radiobiological effects. The relative biological effectiveness (RBE) value of the Bragg peak area (tumor target area) is high, and clustered DNA damage is predominant in



damaged and dying cancer cells. This damage is not dependent on the cell cycle or on the oxygen enhancement ratio where the cells are located and cannot easily be repaired (10, 11). Inhibition of the JAK2/STAT3 signal transduction pathway is expected to be an effective way to inhibit tumor growth and promote tumor cell apoptosis. It has been shown that STAT3 can be used as a marker of ESCC cell proliferation (12, 13). According to the results of this study, after carbon ion irradiation was applied to moderately differentiated cells (ECA109) and poorly differentiated cells (KYSE150), proliferation was inhibited after 2 and 4 Gy irradiation, and the primary effect of ionizing radiation was to induce DNA molecule breakage in the cells, thereby inhibiting cell proliferation. Cells subjected to ionizing radiation, which initiates protein repair at DSBs (14, 15), demonstrate a clear time-dependent linear relationship with the radiation dose (16, 17). A small effect of oxygen is also observed during heavy ion beam irradiation with a LET of more than 200 keV/μm (18).

In this study, we found that the cell cycle in two ESCC cell lines with different degrees of differentiation was arrested at the G2/M phase after carbon ion irradiation and that the

number of cells in cell cycle arrest was positively correlated with the irradiation dose. Furthermore, KYSE150 cells were more sensitive than ECA109 cells to carbon ion radiation. Over time, the radiation effect caused by the release of powerful energy from the heavy ion beam at the end of the range causes the double-stranded DNA of the target gene to become irreparably damaged (19), which leads to apoptosis. In recent years, *in vitro* studies have shown that heavy ion beam ($^{12}\text{C}^{6+}$) irradiation of lung cancer cells induces G2/M arrest, increases the rate of apoptosis and inhibits tumor cell invasion and metastasis (20, 21). The results showed that heavy ion irradiation could induce G2/M phase arrest and that heavy ion beams caused DNA DSBs, which cause irreparable lethal damage and effects on downstream signaling (22–24); this in turn initiates apoptotic mechanisms (25). In our study, a correlation was found between the migration rate of both cell lines and the irradiation dose, and poorly differentiated KYSE150 cells were more sensitive to carbon ion radiation. The effect of carbon ion rays on cell mobility was not correlated with the length of time after irradiation. Heavy ion beams can exert anti-tumor effects by upregulating the pro-apoptotic gene *BAX* and inhibiting the anti-apoptotic

gene *BCL2*, which inhibits *MMP2* and *MMP9* expression and angiogenesis in tumors (26). We discovered that 24 h after carbon ion irradiation of two ESCC cell lines with different degrees of differentiation, *CDH1* expression was upregulated, while that of *MMP2* and *STAT3* was downregulated at the transcriptional level in ECA109 cells; these changes consequently inhibited the metastasis of tumor cells. The upregulated expression of *CDH1* may be related to epithelial-mesenchymal transition (EMT), and we suspect that the transition between *CDH2* and *CDH1* expression occurs after carbon ion irradiation. The core function of *CDH1* is undoubtedly determined by multiple forms of regulation, such as promoter methylation, histone methylation, transcriptional inhibition, and post-transcriptional modification-mediated endocytosis (27–29). Tumor metastasis may be the result of the joint action of these molecules, and specific experiments have confirmed this in follow-up studies. The relative expression of *CDH1*, *MMP2* and *STAT3* mRNA in poorly differentiated KYSE150 cells was correlated with the irradiation dose. The expression levels of these proteins are possibly altered through downregulation of the relative *MMP2*, p-*STAT3*(Tyr705) and *STAT3* expression at the transcriptional and translational levels, upregulation of *CDH1* expression, and co-regulation of EC cell metastasis by carbon ion beams. It has been shown that phosphorylation of *STAT3* can increase cell-cell contact, and thus, *STAT3* may be an essential gene for the migration and invasiveness of tumor cells (30–32).

It has been shown that *STAT3* protein binds to a high-affinity binding site in the promoter region of the *MMP2* gene, which upregulates *MMP2* expression. Inhibition of *STAT3* inhibits its target gene *MMP2* and inhibits tumor cell invasion (33). In malignant tumors, E-cadherin, an epithelial marker, is downregulated, and vimentin, an interstitial marker, is upregulated; moreover, cell adhesion is decreased, migration is enhanced, and tumor cells are more susceptible to invasion and metastasis (34). In various human malignancies, aberrant activation of the *STAT3* signaling pathway is closely associated with tumor EMT, invasion and metastasis (35). Many studies have shown that inducing the inactivation of *JAK2* can inhibit *STAT3* activation and can thus inhibit *STAT3* signaling, which then regulates apoptosis of cancer cells. The elevated expression of p-*STAT3*(Tyr705) is the result of sustained activation of the *STAT3* signaling pathway, which affects the energy needed for cell proliferation and invasion (36). In addition, many studies have shown that *STAT3* over-expression significantly decreases the expression of *CDH1* and that inhibition of *STAT3* expression significantly increases *CDH1*

expression (37, 38). Activation of *STAT3* signaling leads to the decreased expression of *CDH1*, which encodes E-cadherin, an epithelial marker in ESCC cells that promotes cell invasion and metastasis (39). In melanoma cells, the *STAT3* signaling pathway can promote *MMP2* expression, while inhibition of phosphorylated *STAT3* expression can significantly inhibit *MMP2* expression *in vivo*, which inhibits tumor cell growth and invasion (40).

In conclusion, our findings indicate that carbon ions inhibit the sustained activation of *STAT3* through the *JAK2/STAT3* pathway, which inhibits the migration and invasiveness of esophageal cancer cells. We also found that high doses of carbon ions prolonged G2/M cell cycle arrest, promoted apoptosis and significantly inhibited cell proliferation.

DATA AVAILABILITY STATEMENT

The raw data supporting the conclusions of this article will be made available by the authors, without undue reservation.

CONSENT FOR PUBLICATION

Written informed consent for publication was obtained from each participant.

AUTHOR CONTRIBUTIONS

HL, XW, and QZ: conception and design. XW, HL, and SW: administrative support. HL, ZY, LS, SW, RL, YG, and CL: experimental testing. HL, QZ, ZY, ZL, and SW: data analysis and interpretation. All authors contributed to the article and approved the submitted version.

FUNDING

This work was supported by grants from the 2017 Lanzhou Talent Innovation and Entrepreneurship Project Funding, Key Technologies for the Basic and Clinical Application of Domestic Heavy Ion Accelerator for Tumor Treatment (grant number 2017-RC-23); the Science and Technology Support Program of the Gansu Provincial Science and Technology Department (grant number [2016] 1604FKCA109), the Health Industry Scientific Research Program of Gansu Province in 2019 (grant number GWSKY-2019-91) and the Lanzhou heavy Ion Accelerator High-end user Project (HIR20GY007).

REFERENCES

- Okuda M, Inoue J, Fujiwara N, Kawano T, Inazawa J. Subcloning and characterization of highly metastatic cells derived from human esophageal squamous cell carcinoma KYSE150 cells by *in vivo* selection. *Oncotarget*. (2017) 8:34670–7. doi: 10.18632/oncotarget.16668
- Wu J, Gao FX, Wang C, Qin M, Han F, Xu T, et al. IL-6 and IL-8 secreted by tumour cells impair the function of NK cells via the *STAT3* pathway in oesophageal squamous cell carcinoma. *J Exp Clin Cancer Res*. (2019) 38:321. doi: 10.1186/s13046-019-1310-0
- Johnson DE, O'Keefe RA, Grandis JR. Targeting the IL-6/*JAK/STAT3* signalling axis in cancer. *Nat Rev Clin Oncol*. (2018) 15:234–48. doi: 10.1038/nrclinonc.2018.8
- Huynh J, Chand A, Gough D, Ernst M. Therapeutically exploiting *STAT3* activity in cancer - using tissue repair as a road map. *Nat Rev Cancer*. (2019) 19:82–96. doi: 10.1038/s41568-018-0090-8

5. Wang X, Gao Z, Liao J, Shang M, Li X, Yin L, et al. lncRNA UCA1 inhibits esophageal squamous-cell carcinoma growth by regulating the Wnt signaling pathway. *J Toxicol Environ Health A*. (2016) 79:407–18. doi: 10.1080/15287394.2016.1176617
6. Nakajima M, Kato H. Treatment options for esophageal squamous cell carcinoma. *Expert Opin Pharmacother*. (2013) 14:1345–54. doi: 10.1517/14656566.2013.801454
7. Tu CC, Hsu PK. The frontline of esophageal cancer treatment: questions to be asked and answered. *Ann Transl Med*. (2018) 6:83. doi: 10.21037/atm.2017.10.31
8. Kimura M, Ishiguro H, Tanaka T, Takeyama H. Advanced esophageal cancer with tracheobronchial fistula successfully treated by esophageal bypass surgery. *Int J Surg Case Rep*. (2015) 9:115–18. doi: 10.1016/j.ijscr.2015.02.053
9. Shigeoka M, Urakawa N, Nishio M, Takase N, Utsunomiya S, Akiyama H, et al. Cyr61 promotes CD204 expression and the migration of macrophages via MEK/ERK pathway in esophageal squamous cell carcinoma. *Cancer Med*. (2015) 4:437–46. doi: 10.1002/cam4.401
10. Shiochiro K, Hideaki N, Makoto A, Kei I, Yoshihiro Y, Noriko S, et al. AT Cells Show Dissimilar Hypersensitivity to Heavy-Ion and X-rays Irradiation. *J Radiat Res*. (2010) 51:251–55. doi: 10.1269/jrr.09069
11. Jingu K, Tsujii H, Mizoe JE, Hasegawa A, Bessho H, Takagi R, et al. Carbon ion radiation therapy improves the prognosis of unresectable adult bone and soft-tissue sarcoma of the head and neck. *Int J Radiat Oncol Biol Phys*. (2012) 82:2125–31. doi: 10.1016/j.ijrobp.2010.08.043
12. Wu J, Feng X, Zhang B, Li J, Xu X, Liu J, et al. Blocking the bFGF/STAT3 interaction through specific signaling pathways induces apoptosis in glioblastoma cells. *J Neurooncol*. (2014) 120:33–41. doi: 10.1007/s11060-014-1529-8
13. Huang W, Dong Z, Chen Y, Wang F, Wang CJ, Peng H, et al. Small-molecule inhibitors targeting the DNA-binding domain of STAT3 suppress tumor growth, metastasis and STAT3 target gene expression *in vivo*. *Oncogene*. (2016) 35:783–92. doi: 10.1038/onc.2015.215
14. MacPhail SH, Banath JP, Yu TY, Chu EH, Lambur H, Olive PL. Expression of phosphorylated histone H2AX in cultured cell lines following exposure to X-rays. *Int J Radiat Biol*. (2003) 79:351–8. doi: 10.1080/0955300032000093128
15. Pilch DR, Sedelnikova OA, Redon C, Celeste A, Bonner WMJB, Biology C. Characteristics of -H2AX foci at DNA double-strand breaks sites. *Biochem Cell Biol*. (2003) 81:123–29. doi: 10.1139/o03-042
16. Bonner WM. Low-dose radiation: thresholds, bystander effects, and adaptive responses. *Proc Natl Acad Sci USA*. (2003) 100:4973–5. doi: 10.1073/pnas.1031538100
17. Liu SZ. Nonlinear dose-effect relationship of different parameters in cancer cell lines. *Crit Rev Toxicol*. (2005) 35:595–7. doi: 10.1080/10408440500246843
18. Furusawa Y, Fukutsu K, Aoki M, Itsukaichi H, Eguchi-Kasai K, Ohara H, et al. Inactivation of aerobic and hypoxic cells from three different cell lines by accelerated (3)He-, (12)C- and (20)Ne-ion beams. *Radiat Res*. (2000) 154:485–96. doi: 10.1667/0033-7587(2000)154[0485:IOAAHC]2.0.CO;2
19. Lorat Y, Brunner CU, Schanz S, Jakob B, Taucher-Scholz G, Rube CE. Nanoscale analysis of clustered DNA damage after high-LET irradiation by quantitative electron microscopy—the heavy burden to repair. *DNA Repair (Amst)*. (2015) 28:93–06. doi: 10.1016/j.dnarep.2015.01.007
20. Xu H, Gao L, Che T, Du W, Li Q, Gao Q, et al. The effects of 12C6+ irradiation on cell cycle, apoptosis, and expression of caspase-3 in the human lung cancer cell line h1299. *Cancer Biother Radiopharm*. (2012) 27:113–18. doi: 10.1089/cbr.2011.1037
21. Akino Y, Teshima T, Kihara A, Kodera-Suzumoto Y, Inaoka M, Higashiyama S, et al. Carbon-ion beam irradiation effectively suppresses migration and invasion of human non-small-cell lung cancer cells. *Int J Radiat Oncol Biol Phys*. (2009) 75:475–81. doi: 10.1016/j.ijrobp.2008.12.090
22. Bae Y, Jung SH, Kim GY, Rhim H, Kang S. Hip2 ubiquitin-conjugating enzyme overcomes radiation-induced G2/M arrest. *Biochim Biophys Acta*. (2013) 1833:2911–21. doi: 10.1016/j.bbamer.2013.07.023
23. Ghorai A, Bhattacharyya NP, Sarma A, Ghosh U. Radiosensitivity and induction of apoptosis by high LET carbon ion beam and low LET gamma radiation: a comparative study. *Scientifica (Cairo)*. (2014) 2014:438030. doi: 10.1155/2014/438030
24. Ogata T, Teshima T, Kagawa K, Hishikawa Y, Takahashi Y, Kawaguchi A, et al. Particle irradiation suppresses metastatic potential of cancer cells. *Cancer Res*. (2005) 65:113–20.
25. Ghosh S, Narang H, Sarma A, Krishna M. DNA damage response signaling in lung adenocarcinoma A549 cells following gamma and carbon beam irradiation. *Mutat Res*. (2011) 716:10–19. doi: 10.1016/j.mrfmmm.2011.07.015
26. Liu Y, Liu Y, Sun C, Gan L, Zhang L, Mao A, et al. Correction: carbon ion radiation inhibits glioma and endothelial cell migration induced by secreted VEGF. *PLoS ONE*. (2015) 10:e0135508. doi: 10.1371/journal.pone.0135508
27. Ciriello G, Gatza ML, Beck AH, Wilkerson MD, Rhie SK, Pastore A, et al. Comprehensive molecular portraits of invasive lobular breast cancer. *Cell*. (2015) 163:506–19. doi: 10.1158/1538-7445.SABCS14-S2-04
28. Aiello NM, Kang Y. Context-dependent EMT programs in cancer metastasis. *J Exp Med*. (2019) 216:1016–26. doi: 10.1084/jem.20181827
29. Padmanaban V, Krol I, Suhail Y, Szczerba BM, Aceto N, Bader JS, et al. E-cadherin is required for metastasis in multiple models of breast cancer. *Nature*. (2019) 573:1–6. doi: 10.1038/s41586-019-1526-3
30. Vultur A, Cao J, Arulanandam R, Turkson J, Jove R, Greer P, et al. Cell-to-cell adhesion modulates Stat3 activity in normal and breast carcinoma cells. *Oncogene*. (2004) 23:2600–16. doi: 10.1038/sj.onc.1207378
31. Suiling C, Min Z, Lirong C. Overexpression of phosphorylated-STAT3 correlated with the invasion and metastasis of cutaneous squamous cell carcinoma. *J Dermatol*. (2005) 32:354–60. doi: 10.1111/j.1346-8138.2005.tb00906.x
32. Wang B, Liu T, Wu J-C, Luo S-Z, Biomedicine M-YXJ, Biomedicine P, et al. STAT3 aggravates TGF- β 1-induced hepatic epithelial-to-mesenchymal transition and migration. *Biomed Pharmacother*. (2017) 98:214–21. doi: 10.1016/j.biopha.2017.12.035
33. Wang G, Jing Y, Cao L, Gong C, Gong Z, Cao X. A novel synthetic Asiatic acid derivative induces apoptosis and inhibits proliferation and mobility of gastric cancer cells by suppressing STAT3 signaling pathway. *Oncotargets Ther*. (2017) 10:55–66. doi: 10.2147/OTT.S121619
34. Gou Y, Zhai F, Zhang L, Cui L. RUNX3 regulates hepatocellular carcinoma cell metastasis via targeting miR-186/E-cadherin/EMT pathway. *Oncotarget*. (2017) 8:61475–86. doi: 10.18632/oncotarget.18424
35. Hajimoradi M, Hassan ZM, Ebrahimi M, Soleimani M, Samani FSCJ. STAT3 is overactivated in gastric cancer stem-like cells. *Cell J*. (2016) 17:617–28. doi: 10.22074/cellj.2016.3834
36. Yang S, Sun D, Wang L, Wang X, Shi M, Jiang X, et al. The role of STAT3/mTOR-regulated autophagy in angiotensin II-induced senescence of human glomerular mesangial cells. *Cell Signal*. (2019) 53:327–38. doi: 10.1016/j.cellsig.2018.10.021
37. Zhang C, Guo F, Xu G, Ma J, Shao F. STAT3 cooperates with twist to mediate epithelial-mesenchymal transition in human hepatocellular carcinoma cells. *Oncol Rep*. (2015) 33:1872–82. doi: 10.3892/or.2015.3783
38. Yue X, Zhao Y, Zhang C, Li J, Hu WJO. Leukemia inhibitory factor promotes EMT through STAT3-dependent miR-21 induction. *Oncotarget*. (2015) 7:3777–90. doi: 10.18632/oncotarget.6756
39. Sulkowska U, Wincewicz A, Kanczuga-Koda L, Koda M, Sulkowski S. Comparison of CDH1 with STAT3 and apoptosis regulators: Bak and Bcl-xL in endometrioid adenocarcinomas of different ER-alpha immunoprofile. *Gynecol Endocrinol*. (2018) 34:171–74. doi: 10.1080/09513590.2017.1379494
40. Xie TX, Wei D, Liu M, Gao AC, Ali-Osman F, Sawaya R, et al. Stat3 activation regulates the expression of matrix metalloproteinase-2 and tumor invasion and metastasis. *Oncogene*. (2004) 23:3550–60. doi: 10.1038/sj.onc.1207383

Conflict of Interest: The authors declare that the research was conducted in the absence of any commercial or financial relationships that could be construed as a potential conflict of interest.

Copyright © 2020 Luo, Yang, Zhang, Shao, Wei, Liu, Li, Geng, Li and Wang. This is an open-access article distributed under the terms of the Creative Commons Attribution License (CC BY). The use, distribution or reproduction in other forums is permitted, provided the original author(s) and the copyright owner(s) are credited and that the original publication in this journal is cited, in accordance with accepted academic practice. No use, distribution or reproduction is permitted which does not comply with these terms.



China's Particle Therapy Equipment Market: Opportunities Outweigh Challenges

Zhongying Dai, Yuanyuan Ma and Qiang Li*

Department of Radiation Medical Physics, Institute of Modern Physics, Chinese Academy of Sciences, Lanzhou, China

OPEN ACCESS

Edited by:

Lu Cai,

University of Louisville, United States

Reviewed by:

Weihai Zhuo,

Fudan University, China

Marko Markov,

Independent Researcher, Sofia,

Bulgaria

*Correspondence:

Qiang Li

liqiang@impcas.ac.cn

Specialty section:

This article was submitted to

Radiation and Health,

a section of the journal

Frontiers in Public Health

Received: 04 September 2020

Accepted: 13 October 2020

Published: 01 December 2020

Citation:

Dai Z, Ma Y and Li Q (2020) China's Particle Therapy Equipment Market: Opportunities Outweigh Challenges.

Front. Public Health 8:602776.

doi: 10.3389/fpubh.2020.602776

Since 2019, China has been the second largest medical device market in the world. At present, high-end radiotherapy equipment such as particle therapy system has a huge market potential due to the grim situation of cancer prevention and control and the growth of people's wealth in China. However, China's MedTech industry, especially the particle therapy equipment field, still faces the influence of policy, fluctuation of market demand, strengthening of industry supervision, and even geopolitical realities. This paper reviews the market prospect of particle therapy medical devices from the perspective of China's medical device policy and demand information analysis, which is conducive to the research on the industrial layout of particle therapy medical physics, and also helps high-performance medical device manufacturers to expand their business visions. MedTech manufacturers should actively adjust their business strategy and implement scientific and technological innovation on the basis of compliance with industry regulatory requirements in order to seize opportunities from challenges and gain profits growth.

Keywords: particle therapy, Chinese particle therapy equipment, medical device market, medical device industry innovation, medical device regulation (MDR)

INTRODUCTION

The Chinese medical device market is fostered by the burgeoning demand from the increasingly affluent and a rapidly aging population and the rising prevalence of chronic diseases, such as diabetes, heart disease, and cancer.

Today, the market for medical devices in China is rapidly developing, far exceeding the country's economic growth rate. Currently it is increasing in value by around 20% a year, and it was worth an estimated value of \$96.3 billion in 2019, making it the second largest medical device market in the world after the United States¹. Among them, China's radiotherapy equipment market increased from 5.83 billion yuan in 2008 to 26.9 billion yuan in 2015, with a compound annual growth rate of 24.42% (1, 2).

Particle therapy equipment in particular is in great need in China.

From 2015 to 2020, a total of 77 proton and heavy ion center projects have been reported in China, including two heavy ion (Wuwei and Shanghai) and four proton therapy projects in operation, 26 proton projects under construction, and 60 proposed items. Many hospitals in China have signed purchase agreements for proton heavy ion radiotherapy equipment. Enthusiasm for investment presents the potentially attractive and capacious market future of particle therapy equipment.

¹ Available online at: <https://ibc-static.broad.msu.edu/sites/globaleedge/medc/industry-mpi/pdfs/medical-devices-MPI-Insights-and-Rankings-2017.pdf>

However, profit growth in China's MedTech industry still faces the influence of policy, shifting of market demand, strengthening of industry supervision, and even geopolitics. Specifically, the shifting of domestic demand, regional share, and strict supervision are the challenges faced by the high-end medical equipment industry, especially the particle therapy equipment field.

SEEKING OPPORTUNITIES FROM CHALLENGES

Challenges: Localization of Market Demand

China's "made in China 2025" initiative calls on China's top hospitals to increase the use of domestically produced equipment by 50% by 2020, focusing on the development of high-performance equipment, such as diagnostic imaging equipment, robotic surgical instruments, etc. (3). The trend of medical device market demand is obviously affected by the policies and incline to be localized.

The state pushes forward the implementation of demand localization strategy through centralized bidding policy and governmental procurement redirection. Those technology roadmap and business strategy of medical device products with access to the Chinese market need to adapt to the shifting demand (4).

The state-owned public and private hospitals respond quickly for the localization strategy in China. In 2019, six quotas of proton therapy equipment were obtained by large-scale regional public hospitals, at least half of which are to be locally made. Although Chinese medical device manufacturers are the leaders in the domestic market, hospitals and healthcare providers nationwide prefer imported devices, especially when purchasing innovative and high-tech devices. Significant scale of demand for foreign-made, high-end devices is also fueled by continuous growth of China's aging population, and driving forces to improve the quality of care by the Chinese government. Obviously, the strategy of using legal commercial means to transform foreign brand products into local-made ones helps to cope with the changes in market demand trend.

Challenges: Regionalization of Market Share

Due to the worry that hospitals introduce large-scale medical equipment blindly, resulting in waste of resources, the state has strengthened the market-oriented demand management of this equipment (5). With regard to large radiotherapy equipment such as particle therapy system, linear accelerator, and PET, the state has planned the allocation area according to the actual situation of the coverage capacity of medical service and the diagnosis and treatment level of medical institutions, especially the carbon ion proton treatment system. In 2018, the authority of the China medical device in central government came up with a medical equipment quota management policy, in which the basic market share of proton therapy systems in China was allocated

macroscopically, with at least 10 proton therapy systems to be disposed by the end of 2020 (6).

For those medical equipment companies that really want to maximize profits by utilizing market demand, it is time to adjust their product, supply chain, and commercial settings flexibly. In this way, medical equipment manufacturers have the chance to seek out high profits in the value chain by providing unique high-quality equipment that meets both the market demand and market regulatory requirements.

Challenges: Internationalization of Market Supervision

The concept of China's medical device regulation also helps to standardize the medical device market. In recent years, the supervision notion has gradually integrated with the international mainstream regulatory mechanism, laying stress on ensuring the safety and effectiveness of public use of medical devices through strengthening the awareness of subject responsibility (7, 8). Since 2014, China has implemented the policy of "registration before production license" and paid more attention to the supervision of medical devices after marketing (9). The system of medical device marketing license holder (MAH) defines the responsibilities of product marketing holders from the perspective of "responsibility"; China's "Internet +" plan of action has sped up the realization of information traceability of medical device products, through the construction and implementation of medical device market license information supervision and device unique identification systems (10). To seize market opportunities and make huge profits, the enterprises who develop particle therapy system with complex components should focus on the following aspects: internally, improving information management level and product quality control system, cutting down on time and energy wasting; externally, strengthening industry self-discipline, complying with regulatory requirements spontaneously and saving cost of market access, capturing new development opportunities, and seizing market opportunities.

The market supervision principle of Chinese government requires that MedTech manufacturers must comply with obscure requirements. In view of this industry and market trend, the medical device industry tends to adopt a localization strategy, which helps to win purchase orders on the one hand and has the additional benefits of reducing costs and enhancing market familiarity on the other hand. The foreign medical device enterprise, which occupy the high position of the value chain, also needs to be adjusted to maintain brand advantage and earn high profits. MedTech companies from the developed world should find other ways to enter China such as finding OEM partners, licensing technology, establishing factories, etc.

Opportunity: Medical Device Industry Innovation Encouraged

Despite many challenges, both foreign and domestic medical device manufacturers still have many opportunities to make profits under the innovation strategy. In order to achieve its goal of promoting China's economy up the value chain,

creating “national champions” and lowering dependence on foreign imports, China has made the development of the country's biomedical and high-end medical device manufacturing sector a key priority (11, 12). Incentive policies such as the special plans of medical equipment and technical innovation have been formulated. The medical device industry is required to make breakthroughs in frontier and common technology, especially large-scale medical devices with intensive high-tech applications, wide interdisciplinary cross-sections, and significant technology integration, such as particle therapy systems, nuclear magnetic resonance instrument, CT, and 10 other categories of advanced medical equipment.

MedTech innovation was encouraged with a series of policies intensively promulgated throughout the development process of China's medical equipment industry. In 2013, the National Health Commission of China launched the application development and promotion plan of domestic large-scale equipment; in 2015, China grouped medical devices into the key realm of the medical industry, and was determined to accelerate the localization of medical device manufacturing during the 13th Five Year Plan period (13).

The government's “Made in China 2025” initiative for improving industry efficiency, product quality, and brand reputation will further boost the development of domestic medical device manufacturing. The revision of NMPA (the National Medical Products Administration) regulations has listed medical device innovation as a priority, which speeds up the market access of innovative products. By the end of 2019, NMPA has approved the market access of 73 innovative medical device products, including the carbon ion therapy system independently developed by China (14).

In addition, domestic medical device manufacturers are encouraged to increase investment in technology and technological innovation to enhance long-term competitiveness and move up the value chain. Some local manufacturers are growing stronger and more competitive with foreign suppliers, such as Lanzhou Kejin Taiji, Shanghai Lianying, Beijing Guoke ion, Shenzhen Aowo, Xinhua medical and Neusoft Medical Co etc., which have been competitive in CT, gamma knife, linac, carbon ion therapy system, and other products in recent years.

REFERENCES

1. Wang BT, Gong HW. Annual report on the development of medical device industry in China (2018) [M]. Beijing: Social Sciences Academic Press(BEIJING, CHINA) (2018).
2. Lang JY, Wang P, Wu DK, Zhong HL, Lu B, Deng XW, et al. An investigation of the basic situation of radiotherapy in mainland China in (2015). *Chinese J Rad Oncol*. (2016) 25:541–5. doi: 10.3760/CMA.J.ISSN.1004-4221.2016.06.001
3. State Council of the People's Republic of China. “Made in China 2025” initiative. [EB/OL]. Available online at: http://www.gov.cn/zhengce/content/2015-05/19/content_9784.htm (accessed May 08, 2015).
4. Li B, Wang L, Cao H, et al. Improvement of medical device “Made in China” based on ten-year data of the Shanghai medical device market survey. *China Med Dev*. (2018) 033:23–6. doi: 10.3969/j.issn.1674-1633.2018.02.007
5. Chu SZ, Wang EN, Du LN. Analysis on the development trend and problems of medical device industry in China [J]. *Chinese J Pharm*. (2017). 48:930–5. doi: 10.16522/j.cnki.cjph.2017.06.026
6. National Health Commission of the People's Republic of China. Notice on Issue of Management Catalogue for Configuration License of Large Medical Equipment (2018). [EB/OL]. Available online at: <http://www.nhc.gov.cn/guihuaxxs/s3585/201804/7a698cead5524960bcf5f435fba33eee.shtml> (accessed April 09, 2018).

DISCUSSION

At present, China's medical device market is full of uncertainty. In addition to being associated with the outbreak of a new coronavirus disease (officially known as COVID-19), the medical device industry market is expected to be alert to the impact and consequences of the trade war between the United States and China.

However, opportunities outweigh challenges in China's high-end medical device market nowadays accordingly.

Specifically, the influence of policy, fluctuation of market demanding, industry supervision enhancement, and even geopolitical realities are the challenges faced by the high-end medical equipment industry, especially the particle therapy equipment field. The opportunity comes from the flexible adaptation of policy and market demand fluctuation through technological innovation and product improvement.

In the next national planning cycle, China's 14th Five year plan (2021–2025), the national intellectual property system will be further strengthened, and the more mature supervision mode of the medical technology market, such as two vote system and GMP (Good Manufacturing Practice) / GSP (Good Supply Practice) management evaluation system, will be improved. With the rapid development of a highly digital medical device ecosystem, the market access path of innovative products is expected to be shortened.

In view of this, the opportunities for localized innovative medical devices are greater, compared with the fierce market competitive pattern of China's medical device market, especially in high-end equipment.

AUTHOR CONTRIBUTIONS

ZD: data collection and drafting papers. YM: make important revisions to the paper. QL: approval of final papers to be published. All authors contributed to the article and approved the submitted version.

FUNDING

This work was jointly supported by the National Key Research and Development Program of China (No. 2018YFC0115702), and the Youth Innovation Promotion Association of the Chinese Academy of Sciences (No. 2017454).

7. Boyer P, Morshed B I, Mussivand T. Medical device market in China[J]. *Artif. Organs*. (2015) 39:520–5. doi: 10.1111/aor.12427
8. Cai TZ, Discussion on the internationalization trend of china's medical device Industry [J](in Chinese). *Chinese Med Device Inform*. (2016) 7:21–2.
9. Liu XL, Zhang JJ, Liu HY. Problems and countermeasures in medical device supervision [J](in Chinese). *China Manage Informat*. (2016). 19:187–8. doi: 10.12092/j.issn.1009-2501.2018.08.001
10. Chen L, Li M, Discussion on informatization of medical device supervision in China [J] (in Chinese). *Chinese J Med Instrum*. (2017). 41:275–8. doi: 10.3969/j.issn.1671-7104.2017.04.011
11. Yip GS, McKern B. *China's Next Strategic Advantage: From Imitation to Innovation*. Massachusetts: MIT Press (2016).
12. Ministry of Science and Technology of the People's Republic of China. *Thirteenth Five-Year Special Plan for Medical Device Technology Innovation*. [EB/OL]. Available online at: http://www.most.gov.cn/tztg/201706/t20170612_133477.htm (accessed June 12, 2017).
13. State Council of China. “Healthy China 2030” Outline [EB/OL]. (2016-10-15). Available online at: http://www.gov.cn/xinwen/2016-10/25/content_5124174.htm (accessed July 23, 2019).
14. Ministry of Science and Technology of the People's Republic of China. Catalogue of innovative medical devices. [EB/OL]. http://www.most.gov.cn/tztg/201812/t20181205_143991.htm (accessed May 05, 2018).

Conflict of Interest: The authors declare that the research was conducted in the absence of any commercial or financial relationships that could be construed as a potential conflict of interest.

Copyright © 2020 Dai, Ma and Li. This is an open-access article distributed under the terms of the Creative Commons Attribution License (CC BY). The use, distribution or reproduction in other forums is permitted, provided the original author(s) and the copyright owner(s) are credited and that the original publication in this journal is cited, in accordance with accepted academic practice. No use, distribution or reproduction is permitted which does not comply with these terms.



Protective Effects of p53 Regulatory Agents Against High-LET Radiation-Induced Injury in Mice

Akinori Morita^{1*}, Bing Wang^{2*}, Kaoru Tanaka², Takanori Katsube², Masahiro Murakami², Takashi Shimokawa², Yuichi Nishiyama¹, Shintaro Ochi¹, Hidetoshi Satoh³, Mitsuru Neno² and Shin Aoki³

¹ Department of Biomedical Science and Technology, Graduate School of Biomedical Sciences, Tokushima University, Tokushima, Japan, ² National Institute of Radiological Sciences, National Institutes for Quantum and Radiological Science and Technology, Chiba, Japan, ³ Department of Medicinal and Life Science, Faculty of Pharmaceutical Sciences, Tokyo University of Science, Chiba, Japan

OPEN ACCESS

Edited by:

Olga Zeni,

National Research Council (CNR), Italy

Reviewed by:

Joel S. Greenberger,

University of Pittsburgh Medical

Center, United States

Lorenzo Manti,

University of Naples Federico II, Italy

*Correspondence:

Akinori Morita

morita@tokushima-u.ac.jp

Bing Wang

wang.bing@qst.go.jp

Specialty section:

This article was submitted to

Radiation and Health,

a section of the journal

Frontiers in Public Health

Received: 31 August 2020

Accepted: 12 November 2020

Published: 03 December 2020

Citation:

Morita A, Wang B, Tanaka K,

Katsube T, Murakami M,

Shimokawa T, Nishiyama Y, Ochi S,

Satoh H, Neno M and Aoki S (2020)

Protective Effects of p53 Regulatory

Agents Against High-LET

Radiation-Induced Injury in Mice.

Front. Public Health 8:601124.

doi: 10.3389/fpubh.2020.601124

Radiation damage to normal tissues is one of the most serious concerns in radiation therapy, and the tolerance dose of the normal tissues limits the therapeutic dose to the patients. p53 is well known as a transcription factor closely associated with radiation-induced cell death. We recently demonstrated the protective effects of several p53 regulatory agents against low-LET X- or γ -ray-induced damage. Although it was reported that high-LET heavy ion radiation (>85 keV/ μ m) could cause p53-independent cell death in some cancer cell lines, whether there is any radioprotective effect of the p53 regulatory agents against the high-LET radiation injury *in vivo* is still unclear. In the present study, we verified the efficacy of these agents on bone marrow and intestinal damages induced by high-LET heavy-ion irradiation in mice. We used a carbon-beam (14 keV/ μ m) that was shown to induce a p53-dependent effect and an iron-beam (189 keV/ μ m) that was shown to induce a p53-independent effect in a previous study. Vanadate significantly improved 60-day survival rate in mice treated with total-body carbon-ion ($p < 0.0001$) or iron-ion ($p < 0.05$) irradiation, indicating its effective protection of the hematopoietic system from radiation injury after high-LET irradiation over 85 keV/ μ m. 5CHQ also significantly increased the survival rate after abdominal carbon-ion ($p < 0.02$), but not iron-ion irradiation, suggesting the moderate relief of the intestinal damage. These results demonstrated the effectiveness of p53 regulators on acute radiation syndrome induced by high-LET radiation.

Keywords: p53, radioprotector, cell death, hematopoietic syndrome, gastrointestinal syndrome

INTRODUCTION

In recent years, several molecular target drugs have been developed for reducing acute radiation toxicities (1–8). Although the effects of these radioprotectors have been demonstrated by experiments with low-LET radiation, we speculated that such cell death-regulating agents were also effective for protection against particle beam injury, because their radioprotective efficacies do not depend on a radical scavenging action, which is mainly effective for radiation injury caused by indirect action (9).

Although particle therapy has characteristic advantages by the superior dose distribution, the risks of radiation injury in normal tissues still determine the limits of a tolerable

dose, thus cell death-regulating agents are expected as one of the non-invasive measures to reduce adverse events from occurring in organs at risk (OAR). This is especially necessary to protect OAR close to the tumor and to further improve hypofractionated regimens to increase the dose per fraction while suppressing the side effects of acute injury (10–13). In addition, although the estimated exposure dose is not quite high, it will be useful as a basic study for the development of protective agents against cosmic rays. The potential health risk in a manned interplanetary mission with a long duration up to 3 years should be reduced by proper countermeasures and the absorbed doses estimated for the largest solar particle events would be higher than 1 Gy and could reach 10 Gy in a thinly shielded spacecraft (14). Our knowledge from radiobiology indicates clearly that a dose at this latitude of even low-LET photon radiation could definitely cause significant detrimental biological effects. There are two major radiation sources of space radiation: galactic cosmic rays (GCRs) and solar particle events. GCRs consist of 85% low LET protons, 14% helium ions and 1% high atomic number and energy (HZE) particles including iron particles (15). Although these HZE particles make up only 1% of GCRs, they are high-LET particle radiations. They contribute to 21% of the estimated ionizing dose equivalent from GCR exposure during interplanetary missions in deep space and contribute significantly to the overall biological impact of cosmic rays (16).

p53 regulatory agents are expected to be applied as a normal tissue-selective radioprotective agent, because these agents selectively suppress apoptosis of OAR having normal p53 function and do not protect cancer cells that lost p53 functions (17). Furthermore, when the suppression of p53 is transient, unlike constitutive p53-knockout, p53 suppression does not promote carcinogenesis (18). On the other hand, it has been demonstrated by using tumor-derived cultured cells that particle beam-induced cell death does not show a p53 dependency on the LET of 85 keV/μm or more (19). It is unclear whether particle beam injuries in the bone marrow and intestinal epithelium, which are highly radiosensitive among OAR, are p53-dependent events.

We have already found sodium orthovanadate (vanadate) as an effective “p53 inhibitor” for bone marrow death and 5-chloro-8-quinolinol (5CHQ) as an effective “p53 modulator” for intestinal death (4, 7). Our previous work with low-LET radiations had demonstrated that vanadate is the strongest p53 inhibitor with many other biological functions; it is significantly effective against bone marrow death and partially works against intestinal death in total-body irradiation (TBI) tests, and 5CHQ is basically a p53 modulator playing important roles in modulating p53 functions, in particular, activation; it could markedly protect the intestinal death in abdominal irradiation (ABI) tests but has a weak radioprotective activity against bone marrow death in TBI tests. The difference of the spectra against acute radiation syndrome (ARS) is attributed to that p53 plays distinct roles in ARS between bone marrow death and intestinal death, in brief, p53 functions as a promoting factor that induces apoptosis in bone marrow death and as a resistance factor that prevents mitotic death in intestinal death (20). In particular, to demonstrate the protective role of p53, it is necessary to evaluate

the effects of these compounds on the radiation-injured intestine using the ABI technique to avoid bone marrow death. In general, this ABI system requires more than twice the dose used in the TBI test to achieve a lethal effect. In this study, to evaluate the efficacy of these compounds, mice were irradiated systemically or abdominally with particle beams and evaluated using 60-day survival test. Regarding the radiation quality, we used a carbon-beam (14 keV/μm) that was shown to induce a p53-dependent effect and an iron-beam (189 keV/μm) that was shown to induce a p53-independent effect in a previous study (19).

MATERIALS AND METHODS

All animal experiments were performed at National Institute of Radiological Sciences (NIRS), National Institutes for Quantum and Radiological Science and Technology (QST). All experimental protocols (Experimental Animal Research Plans No. 09-1042 and No. 17-2006) involving mice were reviewed and approved by The Institutional Animal Care and Use Committee of the NIRS, QST. The experiments were performed in strict accordance with the NIRS, QST Guidelines for the Care and Use of Laboratory Animals.

Animals

Seven weeks-old ICR strain female mice were purchased from SLC Inc. (Shizuoka, Japan) and maintained in a conventional animal facility under a 12 h light–12 h dark photoperiod and controlled temperature (22–24°C) and humidity (50 ± 5%). The animals were housed in autoclaved aluminum cages with sterilized wood chips and allowed to access standard laboratory chow (MB-1, Funabashi Farm Co., Japan) and acidified water (pH = 3.0 ± 0.2) *ad libitum*. The animals were acclimatized to the laboratory conditions for 1 week before use. To avoid possible effects from the developmental condition of the animals, 6 weeks-old mice with a significantly different body weight (more or less than the mean ± 2 SD) were omitted from this study.

Irradiation

For high LET heavy ion irradiation, the monoenergetic ion beam of carbon and iron particles was generated and accelerated by a synchrotron, the Heavy Ion Medical Accelerator in Chiba (HIMAC) at NIRS, QST, Japan (21, 22). The beam energy was 290 MeV/nucleon and 500 MeV/nucleon for carbon- and iron-beams, and the ion beams were expanded by wobbler magnets to a 10 cm irradiation field with homogeneous irradiation dose. Samples were irradiated at the entrance (plateau) region of the ion beams corresponding to a dose averaged LET value of about 14 and 189 keV/μm, respectively. The dose rate for TBI and ABI was at about 2.7 (C-ion)/3.6 (Fe-ion) and 6.1(C-ion)/5.1(Fe-ion) Gy/min, respectively. For TBI, the mice were held in a special Lucite columnar container, which was with an outer diameter of 10 cm and 3 individual cells of the same size (each mouse in each cell). The mice were in an air-breathing condition (there were six holes 5 mm in diameter in the wall of each cell). The containers were set on the beam track and the focused 10 cm diameter carbon- or iron-beam was delivered to the animals at room temperature without anesthesia. For

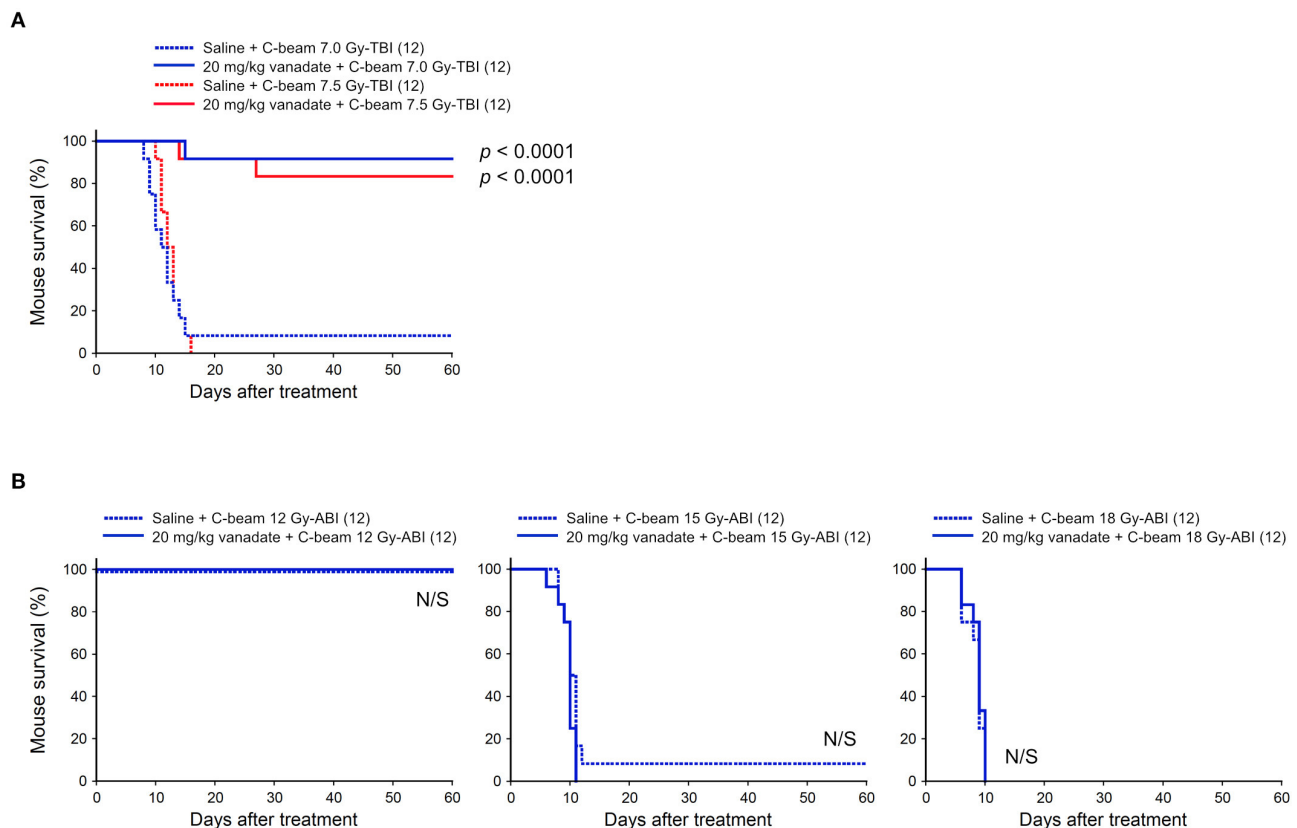


FIGURE 1 | Effect of vanadate on total-body or abdominally irradiated mice with carbon-beam. ICR female mice were i.p. injected with vanadate 30 min before irradiation. Numbers in parenthesis denote the number of mice. **(A)** Sixty-day survival tests after 7.0 or 7.5 Gy-TBI of ICR mouse subgroups of vehicle alone or 20 mg/kg vanadate. By chi-square test, $p < 0.0001$, respectively. **(B)** Sixty-day survival tests after 12, 15, or 18 Gy-ABI of ICR mouse subgroups of vehicle alone or 20 mg/kg vanadate. By chi-square test, $p =$ not significant (N/S), respectively.

ABI, the animals were anesthetized by a combination anesthetic (0.3 mg/kg of medetomidine, 4.0 mg/kg of midazolam, and 5.0 mg/kg of butorphanol), fixed on a special Lucite plate using medical adhesive tapes, and then set on the beam track. The 10 cm diameter carbon- or iron-beam was further collimated to a 2 cm slit by 5 cm brass collimators and delivered locally to the whole abdominal area of the mouse. Irradiation was performed at room temperature.

Sodium Orthovanadate (Vanadate) and 5-chloro-8-quinolinol (5CHQ)

Vanadate was purchased from Sigma-Aldrich (Sigma-Aldrich, St. Louis, MO, USA). The physiological normal saline (NS) (Otsuka Pharmaceutical Co., Ltd., Japan) was used as a solvent to make vanadate solution (2 mg/mL in NS solution). Vanadate at dose of 20 mg/kg body weight or vehicle (NS solution) was administered to the mouse 30 min before irradiation by a single intraperitoneal injection. 5CHQ was purchased from Wako Pure Chemical Industry (Wako Pure Chemical Industry, Co., Ltd., Japan) and recrystallized from ethanol for reducing possible cytotoxicity. Injection solution was prepared using dimethyl sulfoxide (DMSO) (Sigma-Aldrich, St. Louis, MO, USA) and olive oil (Wako Pure Chemical Industry, Co., Ltd., Japan) as solvents. Animals were given a single intraperitoneal injection of

5CHQ at a dose of 60 mg/kg body weight or vehicle (20% DMSO in olive oil) 30–60 min before irradiation.

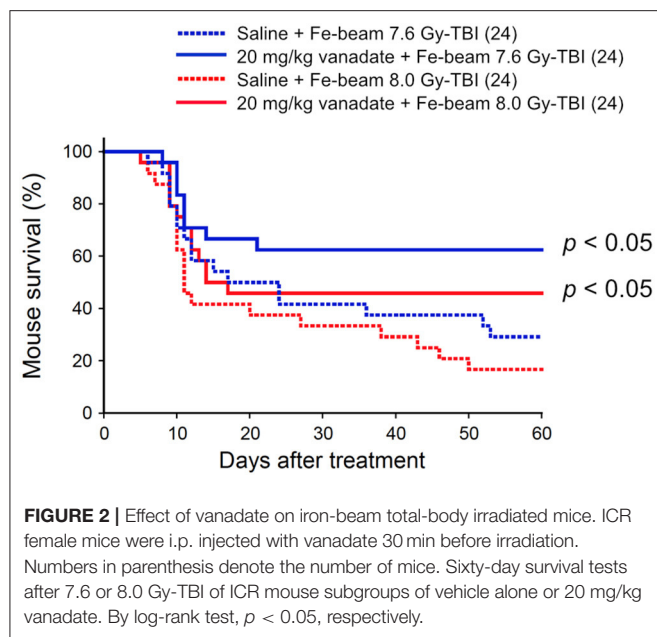
Survival Test

Survival of the animals was monitored daily up to 60 days after irradiation. For statistical analysis, log-rank test was performed when the number of animals per group was 20 or more, and chi-square test was performed when the number animals was <20 using Microsoft Excel with the add-in software Statcel 4 (OMS publisher Ltd, Saitama, Japan).

RESULTS

Vanadate Is Highly Effective in Protection of Carbon-Beam TBI-Induced Death, but Not Protective Against ABI-Induced Death

At first, the protective effect of vanadate was examined in carbon-beam irradiation experiments (290 MeV/nucleon, mono-beam, LET 14 keV/ μm). In the TBI experiments, 7.0, and 7.5 Gy were delivered to 8-week-old female ICR mice (12 mice in each irradiation group), and the survival rate was observed for 60 days (**Figure 1A**). In 7.0 and 7.5 Gy-TBI mice, the survival rate at 60 days was 8.3 and 0% in the vehicle-administered group, whereas the survival rate in the vanadate-administered group was



92 and 83%, respectively, showing a significant radioprotective effect of vanadate ($p < 0.0001$). In order to show the killing effect for carbon-beam ABI, we delivered 12, 15, and 18 Gy to mice, and the survival rate was observed for 60 days (Figure 1B). At the administered doses, a dose at 12 Gy-ABI was not lethal and no protective effect of vanadate was observed in 15 Gy or 18 Gy-ABI mice. These data clearly demonstrate that vanadate has a protective effect against the bone marrow death induced by carbon-beam TBI, while that it is ineffective against the intestinal death induced by carbon-beam ABI.

Vanadate Is Also Effective in Protection of Iron-Beam TBI-Induced Death

Second, the protective effect of vanadate was examined in iron-beam TBI experiments (500 MeV/nucleon, mono-beam, LET 189 keV/ μ m). In the TBI experiments, 7.6 and 8.0 Gy were delivered to 8-week-old female ICR mice (24 mice in each irradiation group), and the survival rate was observed for 60 days (Figure 2). In 7.6 and 8.0 Gy-TBI mice, the survival rate at 60 days was 29 and 17% in the vehicle-administered group, whereas the survival rate in the vanadate-administered group was 63 and 46%, respectively, showing a statistically significant protective effect of vanadate ($p < 0.05$), although the surviving rates were lower than those of carbon-beam experiments. These findings suggest that p53 inhibition could also suppress bone marrow death induced by high LET radiation with LET value exceeding 85 keV/ μ m.

5CHQ Is Effective in Carbon-Beam ABI-Induced Death, but Not Protective Against Carbon-Beam TBI-Induced Death and Iron-Beam ABI-Induced Death

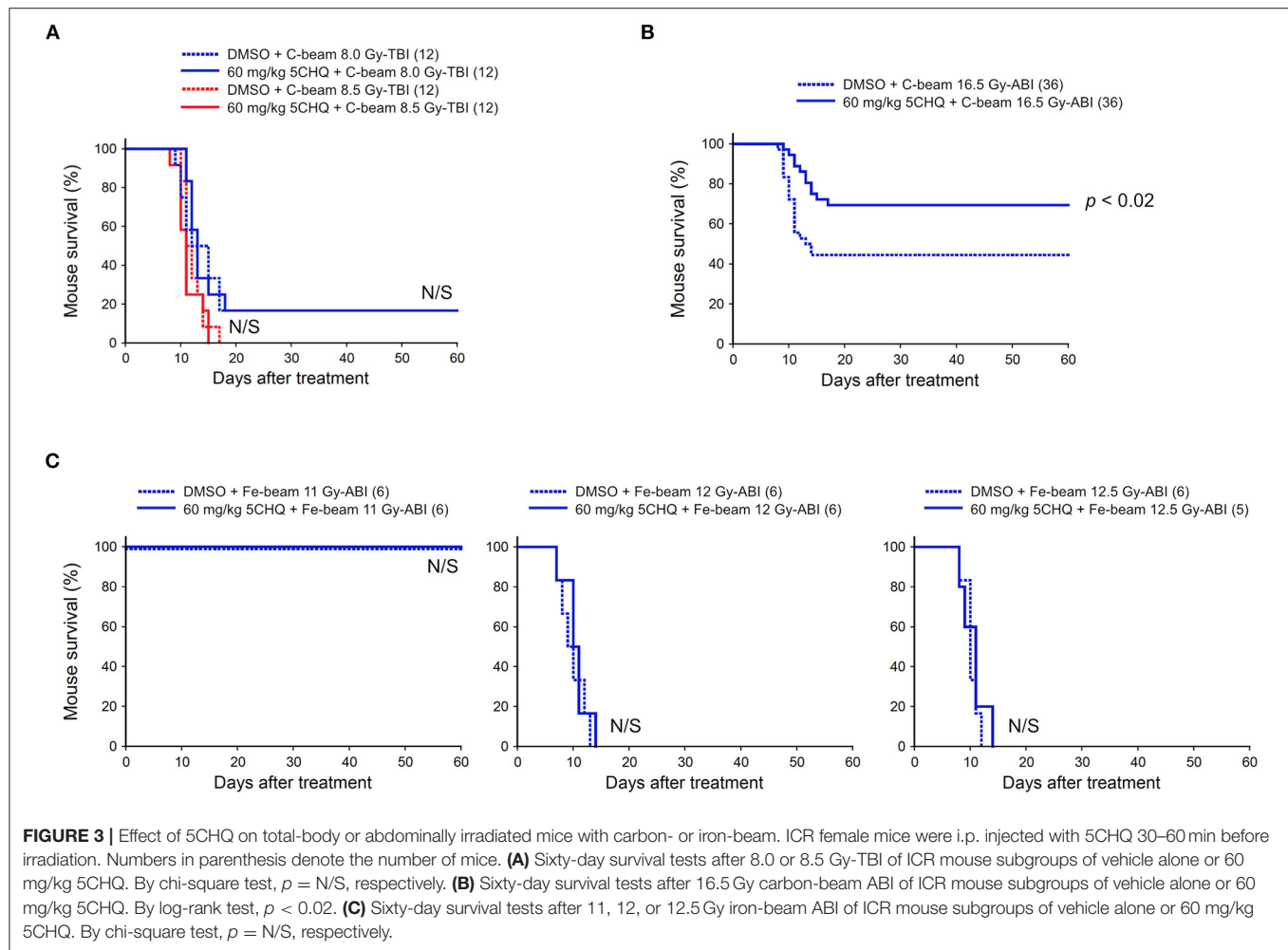
We also investigated the protective effect of 5CHQ, a p53 modulator which has an agonistic activity of activating

radioprotective functions of p53, on the particle beam-irradiated mice. As previously reported, 5CHQ is more protective against ABI-induced intestinal death than in TBI-induced bone marrow death in mice, albeit in low-LET radiation experiments (7). Firstly, we examined the carbon-beam TBI experiments and 8.0 and 8.5 Gy were delivered to 8-week-old female ICR mice (12 mice in each irradiation group) (Figure 3A). In the TBI experiments with vehicle DMSO, a slightly higher dose than those with vehicle saline was required to achieve a lethal effect and no protective effect of 5CHQ was observed in any group of systemically irradiated mice. Next, the particle beam protective effect of 5CHQ was evaluated using abdominally irradiated mice. In the carbon-beam ABI experiment, a dose at 16.5 Gy was delivered to 8-week-old female ICR mice (36 mice in each irradiation group) (Figure 3B). As a result, the survival rate at 60 days was 44% in the vehicle-administered group, whereas the survival rate in the 5CHQ-administered group was 70%, showing a statistically significant protective effect of 5CHQ ($p < 0.02$). We also examined the protective effect of 5CHQ in the iron-beam ABI experiments (Figure 3C). At the administered doses, a dose at 11 Gy-ABI was not lethal and no protective effect of vanadate was observed in 12 Gy or 12.5 Gy-ABI mice. These data demonstrate that 5CHQ has a protective effect against the intestinal death induced by carbon-beam ABI, while that it is ineffective against that induced by iron-beam ABI.

DISCUSSION

In this study, we evaluated the protective activity of p53 regulatory agents against bone marrow death by particle beam TBI and intestinal death by particle beam ABI in the mouse models. At first, considering that iron-beam causes more severe damage to cells than carbon-beam at the same dose and saving animal lives whenever potentially applicable, tests for “vanadate vs. Fe-beam ABI” and “5CHQ vs. Fe-beam TBI” had not been performed as these agents showed ineffective against carbon-beam in the corresponding tests (Figures 1B, 3A).

Considering that vanadate inhibits p53, the results that vanadate was highly effective in the TBI experiments, and no protective effect was observed in the ABI experiments are appropriate. The ineffectiveness of vanadate against intestinal death by ABI was also confirmed by low-LET X-ray ABI experiments (Nishiyama et al., manuscript in preparation). Because these results are consistent with reports of p53's tissue response that promotes cell death in the bone marrow and is protective in the intestine upon radiation injury (20). Of note, when comparing the mouse survival after carbon- and iron-beam injuries, iron-beam injury is characterized by the late occurrence of deaths even 30–60 days after irradiation (Figures 1, 2). This delayed iron-beam damage was suppressed by vanadate. The cause of delayed death is not clear, it may not be due to the bone marrow suppression when taking into account the short life span of the hematopoietic lineage cells. As such a late fatal radiation injury, radiation angiopathy caused by a delayed cell death of endothelial cells is well known (23). Further studies are needed to explore the cause of death using different approaches such



as pathological examinations or bone marrow transplantation. In any case, it is clear that there are cell populations that can avoid the fate of cell death even after exposure to particle beams with an LET value higher than 85 keV/ μm by pharmaceutically regulating cell death machinery. The dense lesions induced by these high-LET radiations are considered to be too severe to be regulated by p53 (19). Our data demonstrate that even in such a circumstance, at least some cells are rescued by p53 regulatory agent. It is also considered that vanadate has various activities such as protein tyrosine phosphatase inhibition (24, 25) and activates radioresistant factors other than p53 to exert its radioprotective activity. We will focus our next research on solving these research issues.

As shown in **Figure 3**, 5CHQ was effective against carbon-beam intestinal injury, but ineffective against carbon-beam bone marrow injury and iron-beam intestinal injury. The ineffectiveness of 5CHQ for iron-beam intestinal injury may suggest its activity was not strong enough as a p53 modulator rather than the limit of therapeutic strategies for suppressing intestinal death by p53 modulators. The discovery of a p53 modulator with a stronger activity than 5CHQ might improve the protective effect. Considering that the current clinical heavy ion

radiotherapy is performed using carbon beams for the treatment of tumors in the pelvic region, suppression of radiation intestinal disorders by application of p53 modulators is expected to be a useful therapeutic strategy.

DATA AVAILABILITY STATEMENT

The raw data supporting the conclusions of this article will be made available by the authors, without undue reservation.

ETHICS STATEMENT

The animal study was reviewed and approved by Animal Care and Use Committee of the National Institute of Radiological Sciences, National Institutes for Quantum and Radiological Science and Technology.

AUTHOR CONTRIBUTIONS

AM, BW, YN, TS, and MN designed research. AM, BW, KT, TK, MM, and SO performed research. AM, BW, and SO analyzed data. HS and SA contributed a purification of 5CHQ

by recrystallization. AM, BW, YN, TS, and MN wrote the manuscript. All authors contributed to manuscript revision, read, and approved the submitted version.

FUNDING

This study was partially supported by KAKENHI (19H03604) from the Japan Society for the Promotion of Science, MEXT Grant-in-Aid for Scientific Research on Innovative Areas Living in Space (Grant Numbers: 15H05944 and 15H05935) and two HIMAC Research Project Grants (17J327 and 20J327).

REFERENCES

- Komarov PG, Komarova EA, Kondratov RV, Christov-Tselkov K, Coon JS, Chernov MV, et al. A chemical inhibitor of p53 that protects mice from the side effects of cancer therapy. *Science*. (1999) 285:1733–7. doi: 10.1126/science.285.5434.1733
- Strom E, Sathe S, Komarov PG, Chernova OB, Pavlovskaya I, Shyshynova, et al. Small-molecule inhibitor of p53 binding to mitochondria protects mice from gamma radiation. *Nat Chem Biol*. (2006) 2:474–9. doi: 10.1038/nchembio809
- Burdelya LG, Krivokrysenko VI, Tallant TC, Strom E, Gleiberman AS, Gupta D, et al. An agonist of toll-like receptor 5 has radioprotective activity in mouse and primate models. *Science*. (2008) 320:226–30. doi: 10.1126/science.1154986
- Morita A, Yamamoto S, Wang B, Tanaka K, Suzuki N, Aoki S, et al. Sodium orthovanadate inhibits p53-mediated apoptosis. *Cancer Res*. (2010) 70:257–65. doi: 10.1158/0008-5472.CAN-08-3771
- Saha S, Bhanja P, Liu L, Alfieri AA, Yu D, Kandimalla ER, et al. TLR9 agonist protects mice from radiation-induced gastrointestinal syndrome. *PLoS ONE*. (2012) 7:e29357. doi: 10.1371/journal.pone.0029357
- Wang X, Wei L, Cramer JM, Leibowitz BJ, Judge C, Epperly M, et al. Pharmacologically blocking p53-dependent apoptosis protects intestinal stem cells and mice from radiation. *Sci Rep*. (2015) 5:8566. doi: 10.1038/srep08566
- Morita A, Takahashi I, Sasatani M, Aoki S, Wang B, Ariyasu S, et al. A chemical modulator of p53 transactivation that acts as a radioprotective agonist. *Mol Cancer Ther*. (2018) 17:432–42. doi: 10.1158/1535-7163.MCT-16-0554
- Pant V, Xiong S, Wasylshen AR, Larsson CA, Aryal NK, Chau G, et al. Transient enhancement of p53 activity protects from radiation-induced gastrointestinal toxicity. *Proc Natl Acad Sci USA*. (2019) 116:17429–37. doi: 10.1073/pnas.1909550116
- Hall EJ, Giaccia AJ. *Radiobiology for the Radiologist*. 7th ed. Philadelphia: Lippincott Williams & Wilkins (2012).
- Tsuji H, Yanagi T, Ishikawa H, Kamada T, Mizoe J, Kanai T, et al. Hypofractionated radiotherapy with carbon ion beams for prostate cancer. *Int J Radiat Oncol Biol Phys*. (2005) 63:1153–60. doi: 10.1016/j.ijrobp.2005.04.022
- Okada T, Tsuji H, Kamada T, Akakura K, Suzuki H, Shimazaki J, et al. Carbon ion radiotherapy in advanced hypofractionated regimens for prostate cancer: from 20 to 16 fractions. *Int J Radiat Oncol Biol Phys*. (2012) 84:968–72. doi: 10.1016/j.ijrobp.2012.01.072
- Nomiya T, Tsuji H, Maruyama K, Toyama S, Suzuki H, Akakura K, et al. Phase I/II trial of definitive carbon ion radiotherapy for prostate cancer: evaluation of shortening of treatment period to 3 weeks. *Br J Cancer*. (2014) 110:2389–95. doi: 10.1038/bjc.2014.191
- Nomiya T, Tsuji H, Kawamura H, Ohno T, Toyama S, Shinomiya Y, et al. A multi-institutional analysis of prospective studies of carbon ion radiotherapy for prostate cancer: a report from the Japan Carbon ion Radiation Oncology Study Group (J-CROS). *Radiother Oncol*. (2016) 121:288–93. doi: 10.1016/j.radonc.2016.10.009
- Townsend LW, Stephens Jr. DL, Hoff JL, Zapp EN, Moussa HM, Miller TM, et al. The Carrington event: possible doses to crews in space from a comparable event. *Adv Space Res*. (2006) 38:226–31. doi: 10.1016/j.asr.2005.01.111
- Bourdarie S, Xapsos M. The near-Earth space radiation environment. *IEEE Trans Nucl Sci*. (2008) 55:1810–32. doi: 10.1109/TNS.2008.2001409
- Sato T, Nagamatsu A, Ueno H, Kataoka R, Miyake S, Takeda K, et al. Comparison of cosmic-ray environments on earth, moon, mars and in spacecraft using PHITS. *Radiat Prot Dosi*. (2018) 180:146–49. doi: 10.1093/rpd/ncx192
- Ochi S, Nishiyama Y, Morita A. Development of p53-targeting drugs that increase radioresistance in normal tissues. *J Med Invest*. (2019) 66:219–23. doi: 10.2152/jmi.66.219
- Christophorou MA, Ringshausen I, Finch AJ, Swigart LB, Evan GI. The pathological response to DNA damage does not contribute to p53-mediated tumour suppression. *Nature*. (2006) 443:214–7. doi: 10.1038/nature05077
- Takahashi A, Matsumoto H, Furusawa Y, Ohnishi K, Ishioka N, Ohnishi T. Apoptosis induced by high-LET radiations is not affected by cellular p53 gene status. *Int J Radiat Biol*. (2005) 81:581–6. doi: 10.1080/09553000500280484
- Kirsch DG, Santiago PM, di Tomaso E, Sullivan JM, Hou WS, Dayton T, et al. p53 controls radiation-induced gastrointestinal syndrome in mice independent of apoptosis. *Science*. (2010) 327:593–6. doi: 10.1126/science.1166202
- Kanai T, Endo M, Minohara S, Miyahara N, Koyama-ito H, Tomura H, et al. Biophysical characteristics of HIMAC clinical irradiation system for heavy-ion radiation therapy. *Int J Radiat Oncol Biol Phys*. (1999) 44:201–10. doi: 10.1016/S0360-3016(98)00544-6
- Bolst D, Tran LT, Guatelli S, Matsufuji N, Rosenfeld AB. Modelling the biological beamline at HIMAC using Geant4. *J Phys Conf Ser*. (2019) 1154:012003. doi: 10.1088/1742-6596/1154/1/012003
- Lee CL, Daniel AR, Holbrook M, Brownstein J, Silva Campos LD, Hasapis S. Sensitization of vascular endothelial cells to ionizing radiation promotes the development of delayed intestinal injury in mice. *Radiat Res*. (2019) 192:258–66. doi: 10.1667/RR15371.1
- Gordon JA. Use of vanadate as protein-phosphotyrosine phosphatase inhibitor. *Methods Enzymol*. (1991) 201:477–82. doi: 10.1016/0076-6879(91)01043-2
- Korbecki J, Baranowska-Bosiacka I, Gutowska I, Chlubek D. Biochemical and medical importance of vanadium compounds. *Acta Biochim Pol*. (2012) 59:195–200. doi: 10.18388/abp.2012_2138

ACKNOWLEDGMENTS

The content of this manuscript has been presented in part at the 57th Annual Meeting of the Biology Group of the Japanese Society for Radiation Oncology, 2nd Technological Competency as Caring in the Health Sciences 2018, and the 61st Annual Meeting of the Japanese Radiation Research Society. The authors would like to thank Ms. Hiromi Arai, Mr. Sadao Hirobe, Ms. Mikiko Nakajima, Ms. Chianing Hsieh, and Ms. Yasuko Morimoto for their expert technical assistance and administrative support.

Conflict of Interest: The authors declare that the research was conducted in the absence of any commercial or financial relationships that could be construed as a potential conflict of interest.

Copyright © 2020 Morita, Wang, Tanaka, Katsube, Murakami, Shimokawa, Nishiyama, Ochi, Satoh, Neno and Aoki. This is an open-access article distributed under the terms of the Creative Commons Attribution License (CC BY). The use, distribution or reproduction in other forums is permitted, provided the original author(s) and the copyright owner(s) are credited and that the original publication in this journal is cited, in accordance with accepted academic practice. No use, distribution or reproduction is permitted which does not comply with these terms.



Carbon Ion Irradiation Enhances the Anti-tumor Efficiency in Tongue Squamous Cell Carcinoma via Modulating the FAK Signaling

Qingzong Si¹, Qian Ye¹, Zhitong Bing², Ruihong Fan¹, Xiaoli Hu², Bin Liu¹, Jizeng Wang³, Yang Liu^{2*} and Xiaoli An^{1*}

¹ School of Stomatology, Lanzhou University, Lanzhou, China, ² Institute of Modern Physics, Chinese Academy of Sciences, Lanzhou, China, ³ Institute of Solid Mechanics, School of Civil Engineering and Mechanics, Lanzhou University, Lanzhou, China

OPEN ACCESS

Edited by:

Lu Cai,
University of Louisville, United States

Reviewed by:

Xin Duan,
Cincinnati Children's Hospital Medical
Center, United States
Qiang Liu,
Chinese Academy of Medical
Sciences and Peking Union Medical
College, China

*Correspondence:

Yang Liu
liuy@impcas.ac.cn
Xiaoli An
anxl@lzu.edu.cn

Specialty section:

This article was submitted to
Radiation and Health,
a section of the journal
Frontiers in Public Health

Received: 19 November 2020

Accepted: 05 January 2021

Published: 03 February 2021

Citation:

Si Q, Ye Q, Bing Z, Fan R, Hu X, Liu B,
Wang J, Liu Y and An X (2021)
Carbon Ion Irradiation Enhances the
Anti-tumor Efficiency in Tongue
Squamous Cell Carcinoma via
Modulating the FAK Signaling.
Front. Public Health 9:631118.
doi: 10.3389/fpubh.2021.631118

Oral cancer is a very aggressive disease with high rates of recurrence and metastasis. This study aimed at addressing how efficiently tongue cancer is suppressed after carbon ion irradiation. Here, the close relationship between upregulated expression of focal adhesion kinase (FAK) and high metastatic status in tongue squamous cell carcinoma patients was validated using bioinformatics and immunohistochemical analyses. Our data indicated that FAK suppression significantly enhanced the killing effect induced by irradiation in the tongue cancer cell line CAL27, as evidenced by increased apoptotic induction and reduced colony formation. More importantly, in FAK-deficient cells, carbon ion irradiation was shown to remarkably inhibit migration and invasion by delaying wound healing and slowing down motility. Further studies revealed that irradiation exposure caused disorganization of the actin cytoskeleton and reduced cell adhesive energy in FAK-deficient cells. Moreover, carbon ion treatment, in combination with FAK silencing, markedly blocked the phosphorylation levels of FAK, and paxillin, which partly contributed to the reduced motility of tongue squamous cell carcinoma CAL27 cells. Collectively, these results suggest that the prominent obstructing role of carbon ion irradiation in the growth inhibition and metastatic behavior of tumors, including attenuation of cell adhesiveness, motility, and invasiveness, could be distinctly modulated by FAK-mediated downstream pathways.

Keywords: carbon ion irradiation, FAK, metastatic potential, tongue squamous cell carcinoma, cell growth

INTRODUCTION

Oral squamous cell carcinoma (OSCC) is the most lethal head and neck squamous cell carcinoma, with an increasing incidence among younger subjects (1, 2). Over the past decades, the prognosis of OSCC patients has remained dismally poor despite remarkable improvements in surgery, chemotherapy, and radiotherapy (3–5). A retrospective review of clinical outcomes showed that the 5-year survival rate of patients with OSCC who underwent postoperative radiation therapy (PORT) using cobalt 60 photons was prominently lower than those who did not undergo PORT (6). Moreover, approximately one-third of patients with OSCC experience locoregional recurrence or

distant metastases after multimodality management, including PORT (7). Hence, the development of more effective radiation treatment for OSCC therapy is imperative.

Growing evidence indicates that radiotherapy with heavy ions is advantageous in clinical trials compared to conventional irradiation with photons, such as γ -rays or X-rays, owing to the unique characteristics of improved dose deposition and higher relative biological effectiveness (8, 9). Carbon ion irradiation is more efficient in inducing cell killing than X-ray irradiation (10). Multiple lines of evidence from *vitro* and *in vivo* studies have shown that conventional radiotherapy can enhance the formation of metastasizing cells (11–13). In contrast, heavy ion irradiation has mostly been found to suppress the migratory and invasive potential of cancer cells (14–17). Our previous data also demonstrated that cell motility was more suppressed after carbon ion irradiation than after X-ray irradiation in glioma cells (18), lung cancer cells (19), and tongue squamous cell carcinoma (TSCC) (20).

Focal adhesion kinase (FAK) is frequently overexpressed in various tumors and is a crucial signaling component that is activated by numerous stimuli and functions as a biosensor or integrator for regulating cell motility, adhesion, and growth (21). FAK amplification in OSCC was reported to correlate with lymph node metastasis (22). Knockdown of FAK has been found to inhibit the survival, invasion, and metastasis of oral cancer (2, 23). Hence, the control of growth and metastatic processes will lead to promising therapies for the clinical treatment of OSCC by targeting FAK.

This study aimed to unravel the influence and possible mechanisms of carbon ion irradiation on metastatic potential in TSCC, one of the most common oral cancers (24). Moreover, we explored the contribution of FAK signaling as a modulator of behavior in cancer cells receiving carbon ion irradiation.

MATERIALS AND METHODS

Clinical Data Collection and Processing

The genomic and clinical data of squamous cell carcinoma of the patients with oral cancer were extracted from head and neck squamous cell carcinoma data in The Cancer Genome Atlas (TCGA) database (<http://xena.ucsc.edu/>). The TCGA dataset included 124 primary tumors samples and 13 normal samples. To analyze the relationship between FAK and metastasis in oral TSCC, we extracted stage I ($n = 9$) and IV ($n = 47$) cancer samples from clinical data. The area of the receiver operating characteristic curve (AUC) represents the performance of each gene.

Cell Culture and Treatment

The human TSCC cell line (CAL27) was purchased from BeNa Culture Collection (BNCC, Beijing, China). Lentiviral particles designed to silence human FAK (5-GATAGTGGACAGTCACA

AA-3) and control lentiviral vectors were produced by Shanghai GeneChem Co. Ltd., China.

Carbon ion irradiation was conducted at the Heavy Ion Research Facility, Lanzhou of the Institute of Modern Physics, Chinese Academy of Sciences, using an 80 MeV/u carbon ion beam, with an LET 50 Kev/ μ m (18, 25).

Colony Formation Assay

We measured the colony forming ability of the irradiated CAL27 cells with or without FAK modification. The fixed colonies with chilled methanol were stained with 0.4% crystal violet (Sigma-Aldrich). Colonies of >50 cells were used to analyze the cloning efficiency.

Apoptosis Analysis by Flow Cytometry

Apoptosis was detected in irradiated CAL27 cells with or without FAK downregulation using a commercial kit (BD Biosciences, San Jose, CA, USA) according to the manufacturer's protocol. The apoptotic population was measured using a Flowsight imaging flow cytometer (Amnis/Merck Millipore, Darmstadt, Germany).

Wound Healing Assay

We determined the migratory ability via wound assays using IBIDI culture-inserts (ibidi, Martinsried, Germany). The cells at the logarithmic growth stage were incubated at 37°C in a humidified atmosphere containing 5% CO₂. When the cells were adherent to the wall in a single layer, a circular wound was scratched using a sterile 200 μ L pipette tip. Cells migrated into the wounded area, and photographs were captured immediately (0 h) and at 6, 12, 24, and 48 h using an optical microscope. The wound area and migration velocity were analyzed using ImageJ software (National Institute of Health, USA).

Transwell Assay

Cell invasion was assessed using BD Matrigel invasion chambers (BD Biosciences). Following FAK silencing and/or irradiation, CAL27 cells were seeded into the upper culture compartments supplemented with serum-free medium. The lower culture compartments were filled with DMEM containing 10% fetal bovine serum. Cells that invaded through the pores were fixed and stained with crystal violet after 24 h incubation.

AFM for Imaging and Mechanical Measurements

Single-cell topographical and mechanical characteristics of living CAL27 cells were measured by a AFM nano-indentation method (JPK Instruments AG, Germany), as described previously (26, 27). Adhesion energy in the cytoplasmic regions was obtained using the JPK data processing software (Version spm-4.2.50, JPK, Germany) (28, 29).

Immunofluorescence/Immunohistochemical Staining Assay

For F-actin staining, the fixed cells were stained with fluorescein isothiocyanate-phalloidin (Sigma-Aldrich, St. Louis, MO). The

Abbreviations: AFM, Atomic Force Microscope; CK, control check; CIR, carbon ion radiotherapy; FAK, focal adhesion kinase; JCT, juxta-cancerous tissue; OSCC, oral squamous cell carcinoma; PORT, postoperative radiation therapy; PTK2, protein tyrosine kinase 2; TSCC, tongue squamous cell carcinoma.

slides were mounted in VECTASHIELD with DAPI (Vector Laboratories, Burlingame, CA) and were viewed using a confocal microscope. The cytoskeleton obtained by immunofluorescence staining can be extracted using ImageJ software (NIH, USA), and the cytoskeleton structure was lined and analyzed. The cytoskeleton was marked with different colors according to the complexity of its connections, and the complexity of the cytoskeleton can be determined according to the distribution of colors.

Tissue microarray chips containing 20 tissues of TSCC were obtained from Shanghai Biochip Co., Ltd (H0raC060PG01 and H0raC080PG01, and the ID of ethics approval was T20-0361). FAK expression was detected in cancer and juxtacancerous tissue (JCT) using immunohistochemical staining.

Western Blot Analysis

Protein samples were extracted from cells in RIPA buffer (Solarbio, Beijing, China) and analyzed in cells 24 h after irradiation with or without FAK knockdown. Total protein samples were blotted with the following antibodies: anti-FAK, anti-phospho-FAK (Y397), anti-phospho-paxillin (Y118), and anti- β -actin (GeneTex, Irvine, CA).

Statistical Analysis

Three independent experiments were carried out to obtain the quantitative data. Statistical analysis was performed using SPSS 16.0 (SPSS Inc., Chicago, IL, USA). Comparisons between two groups were performed with one-way analysis of variance (ANOVA) followed by LSD *post hoc* test. A *P*-value of <0.05 was considered statistically significant.

RESULT

Screening and Validation of TSCC Biomarkers Based on Bioinformatics Analysis

Based on previous literature, 12 transcriptomic biomarkers that are OSCC diagnostic biomarkers were screened in our study (30). As displayed in **Figure 1A**, the diagnosis and classification of primary (N0) and metastatic (\geq N1) tumors using receiver operating characteristic curves were tested. The results showed that MMP-1, DUSP1, and ITGA3 were downregulated in OSCC, with AUC values of 0.536, 0.527, and 0.599, respectively. Conversely, SAT1, CXCL8, ITGA4, EGFR, and PTK2/FAK were upregulated in OSCC. More importantly, EGFR and PTK2/FAK had the highest AUC value (0.715) among all genes, indicating that EGFR and PTK2/FAK could be suitable biomarker candidates associated with cancer progression.

Considering the different locations of the primary oral tumor, **Figure 1B** shows a higher PTK2/FAK expression in oral cavity or oral tongue cancer. Boxplot analysis of stage I and IV samples indicated that PTK2/FAK was more prominently upregulated in stage IV than in stage I samples in the TSCC patients ($P = 0.032$, **Figure 1C**). Moreover, there was increased expression of FAK protein in the late stage of the tumor compared to the adjacent normal tissue in the TSCC patients using the tissue chip technique (**Figures 1D,E**). Taken together, these findings

imply that PTK2/FAK is highly associated with the metastasis progression of TSCC patients.

Target Effects of FAK Signaling in TSCC Cells Exposed to Carbon Ion Irradiation

To test the contribution of FAK signaling in tumor inhibition during carbon ion radiation therapy, we knocked down FAK expression in CAL27 cells using lentivirus carrying FAK shRNA. Reduced expressions of FAK, FAK-pY397, and paxillin-pY118 were observed in the irradiated cells, FAK shRNA-infected cells, and cells treated with combined treatment compared to control shRNA-infected cells (**Figure 2A**). Moreover, a diminished trend was more prominent in the FAK shRNA combined with irradiation treatment group. Additionally, the proportion of apoptotic cells was up to 7.86, 13.51, and 20.13% in the FAK shRNA, irradiation, and FAK shRNA combined with irradiation groups, respectively, compared to the control shRNA group (1.11%) (**Figure 2B** and **Supplementary Figure 3**).

To validate the long-term effect of cell growth, colony formation was evaluated in CAL27 cells exposed to carbon ions in the presence or absence of FAK. Compared to the irradiation alone treatment, the relative number of colonies formed by CAL27 cells after treatment with irradiation plus FAK knockdown was reduced by 47.2% (**Figures 2C,D**).

Alterations in Cellular Motility Abilities Induced by FAK Silencing and Carbon Ion Irradiation

The motility abilities of CAL27 cells following FAK deletion before carbon ion irradiation were evaluated via wound healing and Transwell invasion assays. The moving paths of circular wound recovery showed a decreased migration velocity of collective cells within 48 h in every treatment group compared to that in the shRNA-control group (**Figure 3A**). Moreover, the quantitative results of cells taken at 24 h after scratching indicated a markedly significant decline in the wound area by 44.6, 52.4, and 77.2% in irradiated, FAK-/-, and FAK-/- irradiated cells compared to that in control cells (**Figure 3D**). Further data revealed that a reduction in wound healing ability was significantly found in the FAK silencing and irradiation groups compared to the irradiation group ($P < 0.01$).

The Transwell invasion assay showed that the invasiveness capacity of CAL27 cells in irradiated cells ($P < 0.05$), FAK shRNA-infected cells ($P < 0.05$), and cells treated with FAK shRNA combined with irradiation ($P < 0.01$) was remarkably lower than that of control cells (**Figure 3C**). The number of invaded cells subjected to irradiation alone was 4.83-fold higher than that of cells treated with the combination of FAK shRNA infection and carbon ion irradiation (**Figure 3E**).

Modulation of Cytoskeletal Rearrangement and Biomechanical Properties via FAK Downregulation

As shown in **Figure 4A** and immunofluorescence staining in **Supplementary Figure 2**, an unordered actin filament arrangement accompanied by decreased intensity of actin

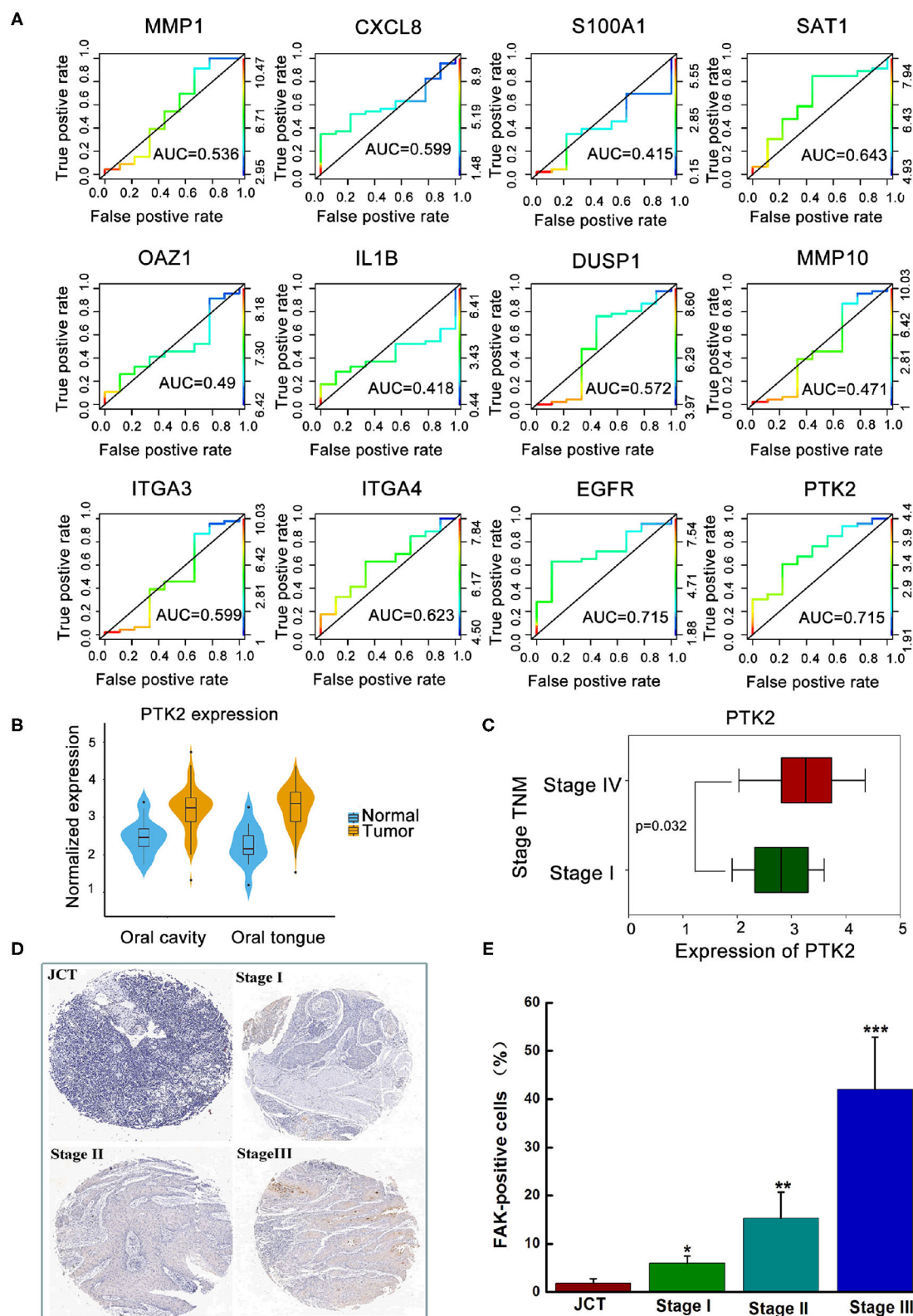
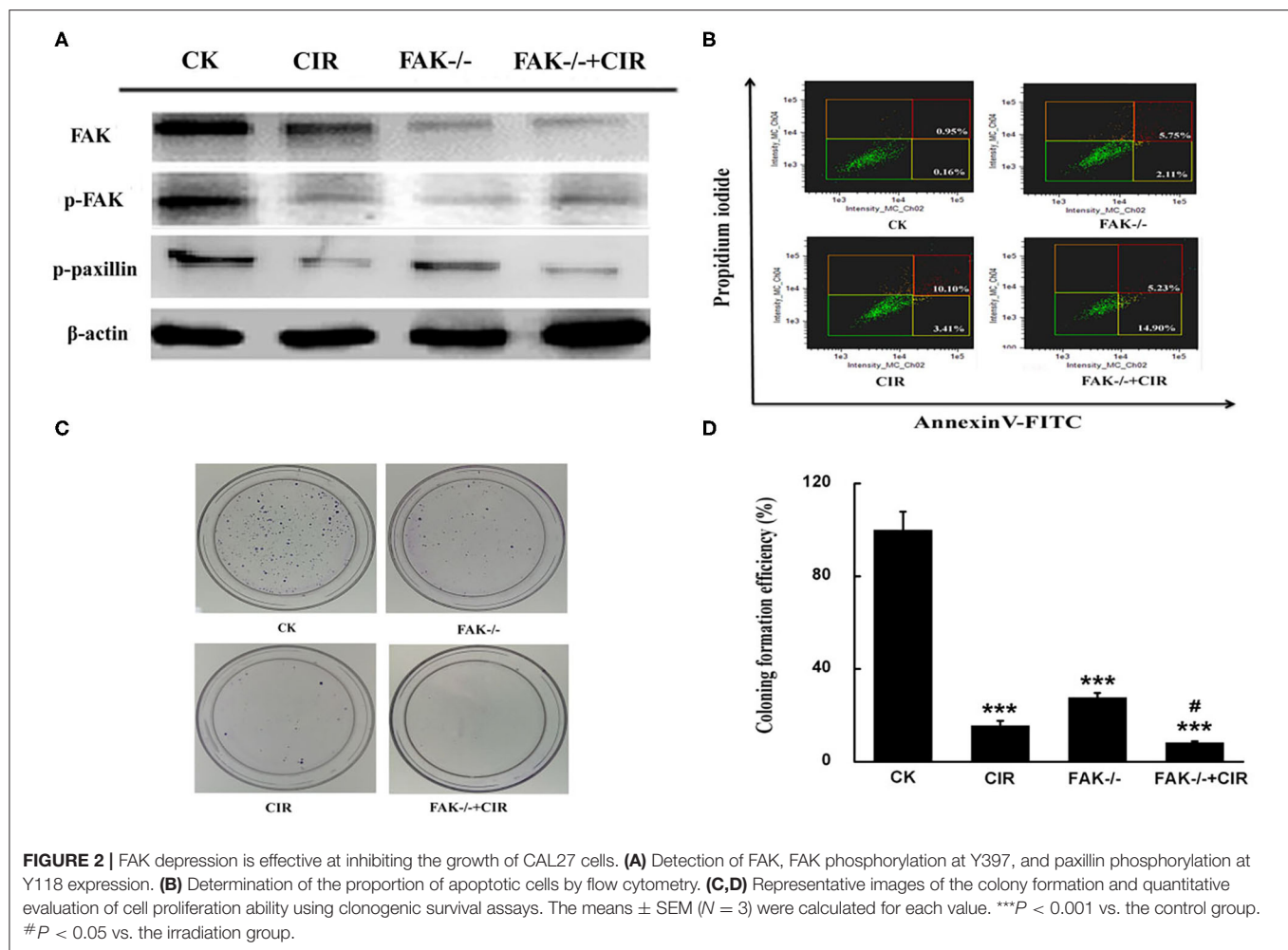


FIGURE 1 | The clinical analysis between the expression of FAK and oral cancer progression. **(A)** Exploration of key genes involved in primary (N0) and metastatic (\geq N1) tumors via the ROC curve test. **(B)** Higher expression of PTK2/FAK in the oral cavity or oral tongue cancer. **(C)** Difference between PTK2/FAK expression in stages I and IV tongue squamous cell carcinoma. **(D)** Detection of the expression of FAK in the tissue chip. **(E)** Quantitative analysis of FAK positive cell proportion. * $P < 0.05$, ** $P < 0.01$, and *** $P < 0.001$ vs. the juxtacancerous tissue (JCT) group.



fibers was observed in CAL27 cells with different treatments. In particular, actin staining exhibited an obvious ring-like distribution around the membrane protrusion structures of cells in the combination treatment group with FAK inhibition and irradiation. Moreover, in contrast to the control cells, FAK inhibition remarkably disrupted the formation of lamellipodia, filopodia, and membrane protrusions in the irradiated cells. Moreover, the abundance of the extracted cytoskeleton decreased in all treatment groups compared to that in the control group, but this trend was not significant.

The topography and deflection images are displayed in **Figure 4C**. Compared to the control group, there was a relatively rough plasma membrane in the combined treatment group. At this point, the variations in cytoplasmic adhesion energy from force-displacement curves acquired by the AFM indentations were decreased in the irradiated cells, FAK shRNA-infected cells, and cells treated with FAK shRNA combined with irradiation compared to the control cells (**Figure 4D**).

DISCUSSION

More aggression is found in TSCC than in other forms of OSCC because of its propensity for rapid local invasion and spread (31). As shown in **Supplementary Figure 1**, from

the TCGA database, FAK/PTK2 was identified as one of the valuable diagnostic biomarkers in OSCC. Our data from nine patients with stage I TSCC (N0) and 47 patients with stage IV TSCC ($\geq N1$) using public databases showed that genomic alteration of FAK closely modulated the malignant progression of TSCC, including histological differentiation, TNM stage, and lymph node metastasis (**Figure 1**). FAK is a critical non-receptor tyrosine kinase involved in many aspects of the metastatic process, including adhesion, migration, and invasion (32). Therefore, FAK could be a more suitable candidate for predicting the metastatic status of TSCCs than other existing biomarkers. Here, we propose that targeting FAK may present a feasible approach for improving the efficacy of radiotherapy for TSCC.

In previous studies, carbon ion irradiation as a promising therapy has been proven to efficiently induce cell death in X-ray-resistant OSCC by modulating diverse signaling molecules, such as AKT and SPHK1 (33, 34). Analogously, FAK has been reported to exert an anti-apoptotic action against ionizing radiation in HL-60 cells by inhibiting the mitochondrial apoptosis pathway (35). Our data showed that carbon ion irradiation remarkably repressed the expression of FAK and phosphorylation of FAK on Tyr³⁹⁷ and paxillin on Tyr¹¹⁸ in CAL27 cells. Furthermore, when cells were exposed to the combination of FAK downregulation

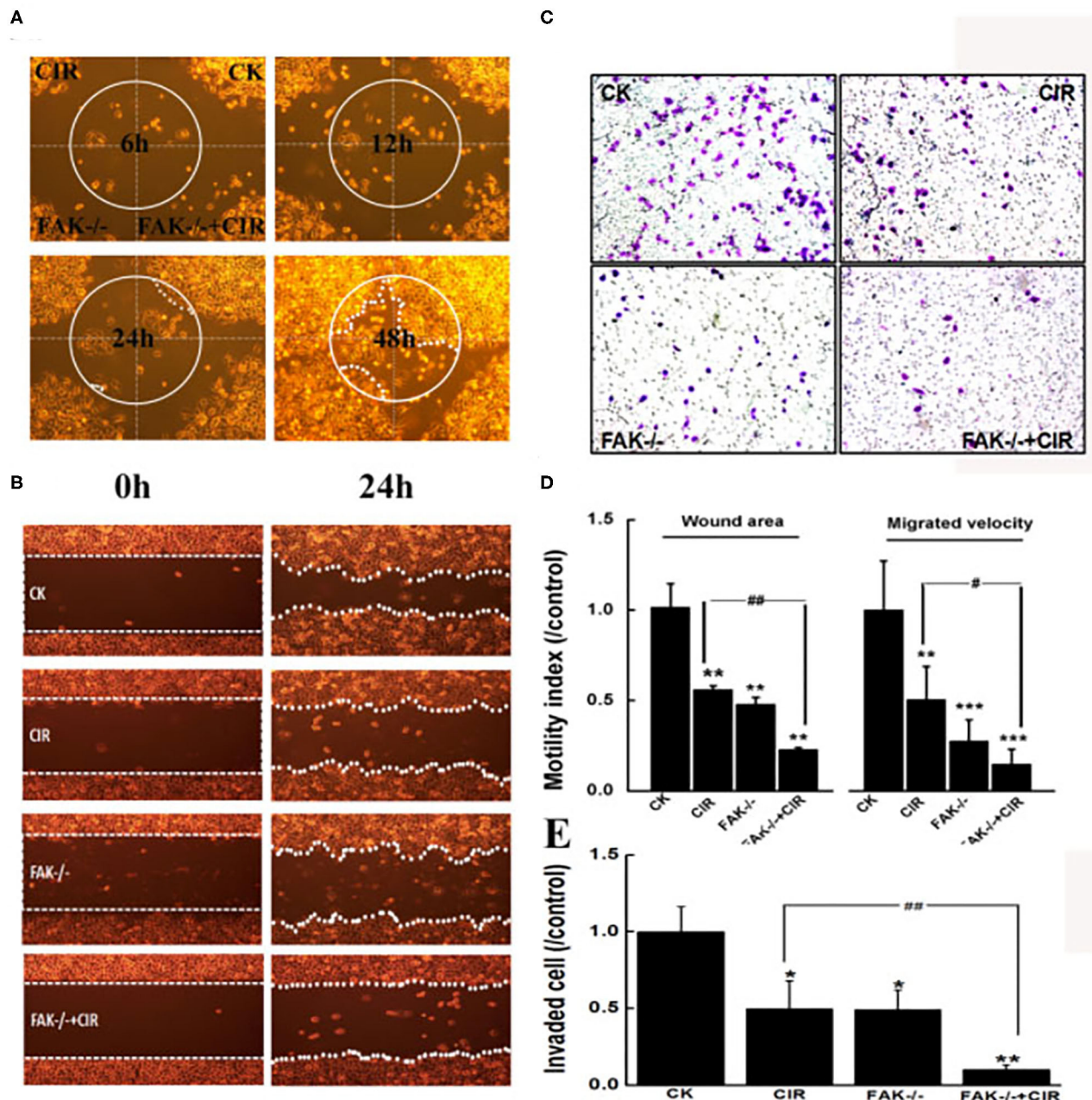


FIGURE 3 | Inhibition of FAK reduces migration and invasion in CAL27 cells after carbon ion irradiation. **(A)** Monitoring of moving paths of the circular wound of cells up to 48 h. **(B)** Typical images of cells taken at 0 h and 24 h after scratching. **(C)** Representative images of cells invaded through the matrigel-coated membrane. **(D)** Quantitative analyses of cell migration signatures. **(E)** Quantitative evaluation of cell invasion ability. * $P < 0.05$, ** $P < 0.01$, and *** $P < 0.001$ compared to the control group. # $P < 0.05$ and ## $P < 0.01$ vs. the irradiation group.

by shRNA and irradiation, the clonogenic formation assay revealed a strong inhibitory effect on cell survival, along with a higher proportion of apoptotic cells (Figure 2). In agreement with previous findings, glioblastoma (36), colon cancer (37), and head and neck cancer cells (38) showed enhanced cell-killing effects in response to ionizing radiation by FAK deletion.

The activation of the FAK-paxillin signaling pathway has been considered a crucial index for tumor metastasis (39). In the current study, carbon ions distinctly limited the area and speed of wound healing cell migration as well as the number of invading cells through the invasion chamber (Figure 3). It is worth noting that, after FAK knockdown, the migratory and invasive abilities of CAL27 cells were more prominently inhibited when compared

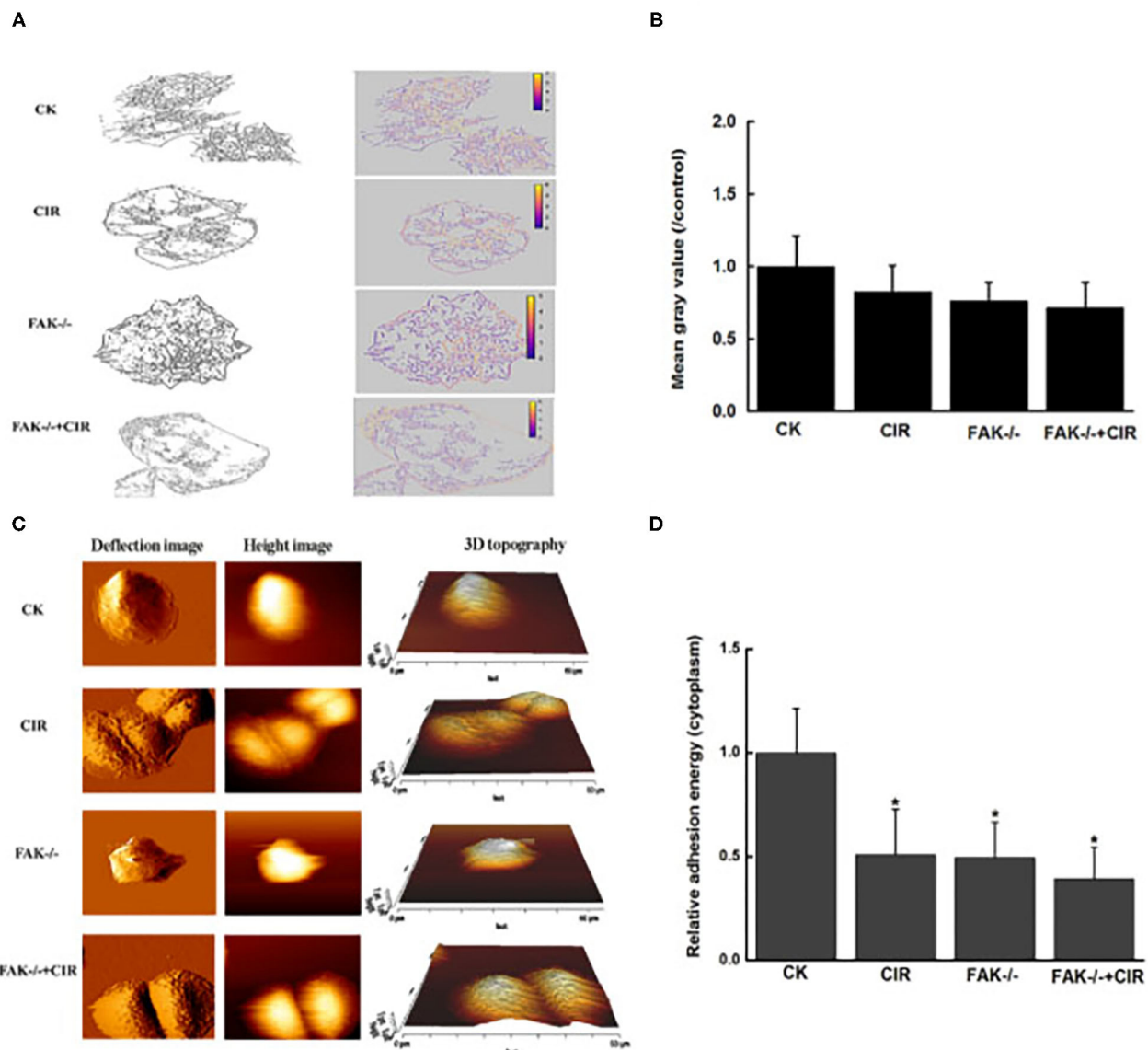


FIGURE 4 | Modulation of cytoskeletal structure and cellular adhesion after treatment with carbon ion irradiation in the presence or absence of FAK activity. **(A)** Characteristic extraction of cytoskeletal structure. **(B)** Measurement of the relative mean gray value of cells in images. **(C)** Representative examples of vertical deflection, height, and 3D images in a single cell. **(D)** Quantitative analysis of adhesion energy in the cytoplasmic region. The mean \pm SEM ($N = 3$) were calculated for each value. * $P < 0.05$ vs. the control group.

to cells treated with radiation alone. Here, the precise role of the combination of FAK knockdown and carbon ion irradiation was confirmed to suppress the high-motility capability of the TSCC cell line CAL27. Moreover, our findings suggest that FAK activity helps to elucidate the molecular mechanisms underlying motility reduction caused by carbon ion beams in TSCC. In this regard, previous findings have also demonstrated that heavy ion radiotherapy is more effective than conventional photon beam therapy in preventing metastasis in preclinical studies (40).

To provide further evidence for FAK knockdown-mediated cell motility repression, alterations in cytoskeletal structure

and cell adhesion were determined in irradiated CAL27 cells. Cell movement relies on changes in the dynamics of actin filaments (41). **Figure 4** shows that a certain decrease in the mean actin density was observed in each treatment group. However, as expected, as shown in **Supplementary Figure 2**, obvious disorganization of actin distribution and reduction of cell protrusion occurred in the combined FAK shRNA plus irradiation group, indicating that there is a lack of cell polarization and can limit cell motility potential. Furthermore, compared to control cells, FAK silencing resulted in reduced adhesion energy to the substrates in

the irradiated cells, FAK shRNA-infected cells, or cells treated with FAK shRNA combined with irradiation, which was consistent with changes in cell motility and phosphorylation of adhesion proteins.

This study demonstrated that carbon ion irradiation and FAK inhibition, especially their combined application, can effectively inhibit OSCC, providing a basis for further *in vivo* experiments and clinical trials.

In addition, the detection of cytoskeletal structure and cell adhesion illustrated the relationship between their variation and cell motor ability. In future studies, we will further study the effects of heavy ions and FAK on cell properties, such as shape, elasticity, rigidity, and viscosity, as well as the relationship between cell properties and their migration and invasion ability, to find a more appropriate way to inhibit the metastasis of OSCC.

CONCLUSION

Mechanistically, we have provided evidence that carbon ion irradiation significantly blocked the FAK-related signal pathway, which partially explains the anti-tumor mechanisms of carbon ions. Furthermore, combining FAK downregulation with carbon ion irradiation could synergistically offer comparable therapeutic benefits for TSCC patients regarding the inhibition of metastatic potential.

DATA AVAILABILITY STATEMENT

The raw data supporting the conclusions of this article will be made available by the authors, without undue reservation.

REFERENCES

- Hsing EW, Shiah SG, Peng HY, Chen YW, Chuu CP, Hsiao JR, et al. TNF- α -induced miR-450a mediates TMEM182 expression to promote oral squamous cell carcinoma motility. *PLoS ONE*. (2019) 14:e0213463. doi: 10.1371/journal.pone.0213463
- Xi WH, Yang LY, Cao ZY, Qian Y. Tivantinib (ARQ-197) exhibits anti-tumor activity with down-regulation of FAK in oral squamous cell carcinoma. *Biochem Biophys Res Commun*. (2015) 457:723–9. doi: 10.1016/j.bbrc.2015.01.062
- Almangush A, Heikkinen I, Makitie AA, Coletta RD, Laara E, Leivo I, et al. Prognostic biomarkers for oral tongue squamous cell carcinoma: a systematic review and meta-analysis. *Br J Cancer*. (2017) 117:856–66. doi: 10.1038/bjc.2017.244
- van Dijk BA, Brands MT, Geurts SM, Merckx MA, Roodenburg JL. Trends in oral cavity cancer incidence, mortality, survival and treatment in the Netherlands. *Int J Cancer*. (2016) 139:574–83. doi: 10.1002/ijc.30107
- Yen CJ, Tsou HH, Hsieh CY, Chu CY, Chiu CF, Chen CC, et al. Sequential therapy of neoadjuvant biochemotherapy with cetuximab, paclitaxel, and cisplatin followed by cetuximab-based concurrent bioradiotherapy in high-risk locally advanced oral squamous cell carcinoma: Final analysis of a phase 2 clinical trial. *Head Neck*. (2019) 41:1703–12. doi: 10.1002/hed.25640
- Garzino-Demo P, Dell'Acqua A, Dalmaso P, Fasolis M, La Terra Maggiore GM, Ramieri G, et al. Clinicopathological parameters and outcome of 245 patients operated for oral squamous cell carcinoma. *J Craniomaxillofac Surg*. (2006) 34:344–50. doi: 10.1016/j.jcms.2006.04.004

ETHICS STATEMENT

The studies involving human participants were reviewed and approved by Tissue microarray chip containing oral squamous cell carcinoma were obtained from Shanghai Biochip Co. The ID of ethics approval is T20-0361, submitted in this system. The patients/participants provided their written informed consent to participate in this study.

AUTHOR CONTRIBUTIONS

QS: designed the experiment, executed the research and wrote the original draft. QY, ZB, RF, and XH: executed the research and interpreted the data. BL and JW: discussed reviewed the manuscript. XA and YL: acquired the data, analyzed the data and interpreted the data, and reviewed the manuscript. All authors contributed to the article and approved the submitted version.

FUNDING

This study was supported by grants from Talent Innovation and Entrepreneurship Project of Lanzhou City (2018-RC-36), Clinical Research Center of Shanxi Province for Dental and Maxillofacial Diseases, College of Stomatology, Xi'an Jiaotong University (2019YHJB10), and Natural Science Foundation of Gansu Province (20JR5RA264).

SUPPLEMENTARY MATERIAL

The Supplementary Material for this article can be found online at: <https://www.frontiersin.org/articles/10.3389/fpubh.2021.631118/full#supplementary-material>

- Hosni A, Huang SH, Chiu K, Xu W, Su J, Bayley A, et al. Predictors of early recurrence prior to planned postoperative radiation therapy for oral cavity squamous cell carcinoma and outcomes following salvage intensified radiation therapy. *Int J Radiat Oncol Biol Phys*. (2019) 103:363–73. doi: 10.1016/j.ijrobp.2018.09.013
- Jin X, Li F, Liu B, Zheng X, Li H, Ye F, et al. Different mitochondrial fragmentation after irradiation with X-rays and carbon ions in HeLa cells and its influence on cellular apoptosis. *Biochem Biophys Res Commun*. (2018) 500:958–65. doi: 10.1016/j.bbrc.2018.04.214
- Wang Y, Guan H, Xie DF, Xie Y, Liu XD, Wang Q, et al. Proteomic analysis implicates dominant alterations of RNA metabolism and the proteasome pathway in the cellular response to carbon-ion irradiation. *PLoS ONE*. (2016) 11:e0163896. Epub 2016/10/07. doi: 10.1371/journal.pone.0163896
- Sato K, Azuma R, Imai T, Shimokawa T. Enhancement of mTOR signaling contributes to acquired X-ray and C-ion resistance in mouse squamous carcinoma cell line. *Cancer Sci*. (2017) 108:2004–10. doi: 10.1111/cas.13323
- Blyth BJ, Cole AJ, MacManus MP, Martin OA. Radiation therapy-induced metastasis: radiobiology and clinical implications. *Clin Exp Metastas*. (2018) 35:223–36. doi: 10.1007/s10585-017-9867-5
- Moncharmont C, Levy A, Guy JB, Falk AT, Guilbert M, Trone JC, et al. Radiation-enhanced cell migration/invasion process: a review. *Crit Rev Oncol Hematol*. (2014) 92:133–42. doi: 10.1016/j.critrevonc.2014.05.006
- Vilalta M, Rafat M, Graves EE. Effects of radiation on metastasis and tumor cell migration. *Cell Mol Life Sci*. (2016) 73:2999–3007. doi: 10.1007/s00018-016-2210-5

14. Konings K, Vandevoorde C, Belmans N, Vermeesen R, Baselet B, Walleghem MV, et al. The combination of particle irradiation with the hedgehog inhibitor GANT61 differently modulates the radiosensitivity and migration of cancer cells compared to X-ray irradiation. *Front Oncol.* (2019) 9:391. doi: 10.3389/fonc.2019.00391
15. Moncharmont C, Guy JB, Wozny AS, Gilormini M, Battiston-Montagne P, Ardail D, et al. Carbon ion irradiation withstands cancer stem cells' migration/invasion process in Head and Neck Squamous Cell Carcinoma (HNSCC). *Oncotarget.* (2016) 7:47738–49. doi: 10.18632/oncotarget.10281
16. Stahler C, Roth J, Cordes N, Taucher-Scholz G, Mueller-Klieser W. Impact of carbon ion irradiation on epidermal growth factor receptor signaling and glioma cell migration in comparison to conventional photon irradiation. *Int J Radiat Biol.* (2013) 89:454–61. doi: 10.3109/09553002.2013.766769
17. Wozny AS, Vares G, Alphonse G, Lauret A, Monini C, Magne N, et al. ROS production and distribution: a new paradigm to explain the differential effects of X-ray and carbon ion irradiation on cancer stem cell migration and invasion. *Cancers.* (2019) 11:4. doi: 10.3390/cancers11040468
18. Liu Y, Liu Y, Sun C, Gan L, Zhang L, Mao A, et al. Carbon ion radiation inhibits glioma and endothelial cell migration induced by secreted VEGF. *PLoS ONE.* (2014) 9:e98448. doi: 10.1371/journal.pone.0098448
19. Liu Y, Liu Y, Zhang H, Sun C, Zhao Q, Di C, et al. Effects of carbon-ion beam irradiation on the angiogenic response in lung adenocarcinoma A549 cells. *Cell Biol Int.* (2014) 38:1304–10. doi: 10.1002/cbin.10327
20. Zheng Q, Liu Y, Zhou HJ, Du YT, Zhang BP, Zhang J, et al. X-ray radiation promotes the metastatic potential of tongue squamous cell carcinoma cells via modulation of biomechanical and cytoskeletal properties. *Hum Exp Toxicol.* (2015) 34:894–903. doi: 10.1177/0960327114561664
21. Mitra SK, Hanson DA, Schlaepfer DD. Focal adhesion kinase: in command and control of cell motility. *Nat Rev Mol Cell Biol.* (2005) 6:56–68. doi: 10.1038/nrm1549
22. de Vicente JC, Rosado P, Lequerica-Fernandez P, Allonca E, Villallain L, Hernandez-Vallejo G. Focal adhesion kinase overexpression: correlation with lymph node metastasis and shorter survival in oral squamous cell carcinoma. *Head Neck.* (2013) 35:826–30. doi: 10.1002/hed.23038
23. Xiao W, Jiang M, Li H, Li C, Su R, Huang K. Knockdown of FAK inhibits the invasion and metastasis of Tca8113 cells *in vitro*. *Mol Med Rep.* (2013) 8:703–7. doi: 10.3892/mmr.2013.1555
24. Camisasca DR, Honorato J, Bernardo V, da Silva LE, da Fonseca EC, de Faria PAS, et al. Expression of Bcl-2 family proteins and associated clinicopathologic factors predict survival outcome in patients with oral squamous cell carcinoma. *Oral Oncology.* (2009) 45:225–33. doi: 10.1016/j.oraloncology.2008.05.021
25. Fushimi K, Uzawa K, Ishigami T, Yamamoto N, Kawata T, Shibahara T, et al. Susceptible genes and molecular pathways related to heavy ion irradiation in oral squamous cell carcinoma cells. *Radiother Oncol.* (2008) 89:237–44. doi: 10.1016/j.radonc.2008.04.015
26. Dufrene YF, Ando T, Garcia R, Alsteens D, Martinez-Martin D, Engel A, et al. Imaging modes of atomic force microscopy for application in molecular and cell biology. *Nat Nanotechnol.* (2017) 12:295–307. doi: 10.1038/nnano.2017.45
27. Li QS, Lee GY, Ong CN, Lim CT. AFM indentation study of breast cancer cells. *Biochem Biophys Res Commun.* (2008) 374:609–13. doi: 10.1016/j.bbrc.2008.07.078
28. Trache A, Xie L, Huang H, Glinsky VV, Meininger GA. Applications of atomic force microscopy for adhesion force measurements in mechanotransduction. *Methods Mol Biol.* (2018) 1814:515–28. doi: 10.1007/978-1-4939-8591-3_30
29. Zhang BP, Li L, Li ZQ, Liu Y, Zhang H, Wang JZ. Carbon ion-irradiated hepatoma cells exhibit coupling interplay between apoptotic signaling and morphological and mechanical remodeling. *Sci Rep-Uk.* (2016) 6:35131. doi: 10.1038/srep35131
30. Yakob M, Fuentes L, Wang MB, Abemayor E, Wong DT. Salivary biomarkers for detection of oral squamous cell carcinoma - current state and recent advances. *Curr Oral Health Rep.* (2014) 1:133–41. doi: 10.1007/s40496-014-0014-y
31. Liu X, Wang A, Lo Muzio L, Kolokythas A, Sheng S, Rubini C, et al. Deregulation of manganese superoxide dismutase (SOD2) expression and lymph node metastasis in tongue squamous cell carcinoma. *BMC Cancer.* (2010) 10:365. doi: 10.1186/1471-2407-10-365
32. Sparano A, Quesnelle KM, Kumar MS, Wang Y, Sylvester AJ, Feldman M, et al. Genome-wide profiling of oral squamous cell carcinoma by array-based comparative genomic hybridization. *Laryngoscope.* (2006) 116:735–41. doi: 10.1097/01.mlg.0000205141.54471.7f
33. Higo M, Uzawa K, Kawata T, Kato Y, Kouzu Y, Yamamoto N, et al. Enhancement of SPHK1 *in vitro* by carbon ion irradiation in oral squamous cell carcinoma. *Int J Radiat Oncol Biol Phys.* (2006) 65:867–75. doi: 10.1016/j.ijrobp.2006.02.048
34. Takahashi A, Ma H, Nakagawa A, Yoshida Y, Kanai T, Ohno T, et al. Carbon-ion beams efficiently induce cell killing in X-ray resistant human squamous tongue cancer cells. *Int J Med.* (2014) 3:133–42. doi: 10.4236/ijmpcero.2014.33019
35. Storch K, Sagerer A, Cordes N. Cytotoxic and radiosensitizing effects of FAK targeting in human glioblastoma cells *in vitro*. *Oncol Rep.* (2015) 33:2009–16. doi: 10.3892/or.2015.3753
36. Luo CW, Wu CC, Ch'ang HJ. Radiation sensitization of tumor cells induced by shear stress: the roles of integrins and FAK. *Biochim Biophys Acta.* (2014) 1843:2129–37. doi: 10.1016/j.bbamcr.2014.06.007
37. Skinner HD, Giri U, Yang L, Woo SH, Story MD, Pickering CR, et al. Proteomic profiling identifies PTK2/FAK as a driver of radioresistance in hpv-negative head and neck cancer. *Clin Cancer Res.* (2016) 22:4643–50. doi: 10.1158/1078-0432.CCR-15-2785
38. Kasahara T, Koguchi E, Funakoshi M, Aizu-Yokota E, Sonoda Y. Antiapoptotic action of focal adhesion kinase (FAK) against ionizing radiation. *Antioxid Redox Signal.* (2002) 4:491–9. doi: 10.1089/15230860260196290
39. Chen C, Wang Y, Chen S, Ruan X, Liao H, Zhang Y, et al. Genistein inhibits migration and invasion of cervical cancer HeLa cells by regulating FAK-paxillin and MAPK signaling pathways. *Taiwan J Obstet Gynecol.* (2020) 59:403–8. doi: 10.1016/j.tjog.2020.03.012
40. Ogata T, Teshima T, Kagawa K, Hishikawa Y, Takahashi Y, Kawaguchi A, et al. Particle irradiation suppresses metastatic potential of cancer cells. *Cancer Res.* (2005) 65:113–20. Available online at: <https://cancerres.aacrjournals.org/content/65/1/113>
41. Lorch JH, Thomas TO, Schmoll HJ. Bortezomib inhibits cell-cell adhesion and cell migration and enhances epidermal growth factor receptor inhibitor-induced cell death in squamous cell cancer. *Cancer Res.* (2007) 67:727–34. doi: 10.1158/0008-5472.CAN-06-2162

Conflict of Interest: The authors declare that the research was conducted in the absence of any commercial or financial relationships that could be construed as a potential conflict of interest.

Copyright © 2021 Si, Ye, Bing, Fan, Hu, Liu, Wang, Liu and An. This is an open-access article distributed under the terms of the Creative Commons Attribution License (CC BY). The use, distribution or reproduction in other forums is permitted, provided the original author(s) and the copyright owner(s) are credited and that the original publication in this journal is cited, in accordance with accepted academic practice. No use, distribution or reproduction is permitted which does not comply with these terms.



Design of Beam Shaping Assemblies for Accelerator-Based BNCT With Multi-Terminals

Guangru Li^{1,2,3,4}, Wei Jiang¹, Lu Zhang¹, Weiqiang Chen^{1,2,3,4} and Qiang Li^{1,2,3,4*}

¹ Institute of Modern Physics, Chinese Academy of Sciences, Lanzhou, China, ² College of Life Sciences, University of Chinese Academy of Sciences, Beijing, China, ³ Key Laboratory of Heavy Ion Beam Radiation Biomedicine, Chinese Academy of Sciences, Lanzhou, China, ⁴ Gansu Provincial Key Laboratory of Heavy Ion Beam Radiation Medical Application, Lanzhou, China

To moderate fast neutrons produced by accelerator to appropriate therapeutic energies for boron neutron capture therapy (BNCT), beam shaping assembly (BSA) is required definitely. In this work, based on a model of 2.5 MeV/30mA proton accelerator, the Monte Carlo simulation software MCNPX was employed to design multi-terminal BSAs. All parameters for both the thermal and epithermal neutron beams at the exit ports of the designed BSAs meet the treatment recommendation values proposed by the International Atomic Energy Agency (IAEA). The clinical parameters of the thermal and epithermal neutron beams were also calculated for clinical indication consideration.

Keywords: accelerator-based BNCT, beam shaping assembly, thermal neutron, epithermal neutron, multi-terminal

OPEN ACCESS

Edited by:

Lu Cai,

University of Louisville, United States

Reviewed by:

Xingcai Guan,

Lanzhou University, China

Jacob Fantidis,

International Hellenic

University, Greece

*Correspondence:

Qiang Li

liqiang@impcas.ac.cn

Specialty section:

This article was submitted to

Radiation and Health,

a section of the journal

Frontiers in Public Health

Received: 16 December 2020

Accepted: 08 February 2021

Published: 11 March 2021

Citation:

Li G, Jiang W, Zhang L, Chen W and

Li Q (2021) Design of Beam Shaping

Assemblies for Accelerator-Based

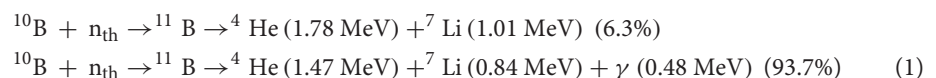
BNCT With Multi-Terminals.

Front. Public Health 9:642561.

doi: 10.3389/fpubh.2021.642561

INTRODUCTION

Boron neutron capture therapy (BNCT) is a novel modality of radiation cancer therapy. Boron compounds are administered to tumor cells, then the tumor is irradiated with neutrons, inducing the $^{10}\text{B} (n, \alpha)^7\text{Li}$ nuclear reaction:



Both α particles and ${}^7\text{Li}$ nuclei deposit their energies along their very short paths, which are comparable to the size of cells. As a result, tumor cells are destroyed accurately without harming healthy tissues (1).

BNCT was firstly proposed by G. Locher in 1936 (2) and firstly practiced by W. Sweet in 1951 for the clinical trial of glioma (3). Over the past two decades, many research groups around the world have continued the work of W. Sweet and the others, particularly the pioneering clinical work of Hatanaka (4). Subsequently, clinical trials of BNCT were conducted in the United States, Sweden, Finland, the Czech Republic, Argentina, the European Union (centered on Finland) and Japan.

Nuclear reactors were firstly used to produce neutrons for BNCT. However, although they could provide high-intensity neutron beam, they have numerous shortcomings: most of them are located far from hospitals, and are also very expensive. Besides, nuclear reactors have too huge size to be suitable for being used in hospital. Accelerator-based BNCT (AB-BNCT) facilities therefore are being developed to replace nuclear reactors. In AB-BNCT, fast neutrons are obtained by bombarding lithium or beryllium target with protons. However, the fast neutrons produced by this method cannot be used for BNCT treatment directly and need to be moderated by beam shaping assembly (BSA). The functions of BSA are: (1) slow fast neutrons down to thermal neutrons

TABLE 1 | Neutron beam parameters and IAEA recommended values.

Thermal neutron beam parameters	Recommended values	Epithermal neutron beam parameters	Recommended values
Thermal neutron flux Φ_{th} ($\text{cm}^{-2}\text{s}^{-1}$)	$\geq 1 \times 10^9$	Epithermal neutron flux Φ_{epith} ($\text{cm}^{-2}\text{s}^{-1}$)	$\geq 1 \times 10^9$
Thermal neutron ratio Φ_{th}/Φ_{total}	>0.9	Thermal neutron ratio Φ_{th}/Φ_{epith}	≤ 0.05
Epithermal and fast neutron component $D_{epi-fast}/\Phi_{th}$ (Gy cm^2)	$\leq 2 \times 10^{-13}$	Fast neutron component D_{fast}/Φ_{epith} (Gy cm^2)	$\leq 2 \times 10^{-13}$
Gamma component D_{γ}/Φ_{th} (Gy cm^2)	$\leq 2 \times 10^{-13}$	Gamma component D_{γ}/Φ_{epith} (Gy cm^2)	$\leq 2 \times 10^{-13}$
J/Φ	>0.7	J/Φ	>0.7
Thermal energy group Φ_{th}		$E < 0.5 \text{ eV}$	
Epithermal energy group Φ_{epith}		$0.5 \text{ eV} \leq E \leq 10 \text{ keV}$	
Fast energy group Φ_{fast}		$E > 10 \text{ keV}$	

(< 0.5 eV) or epithermal neutrons (0.5 eV–10 keV), (2) reduce the composition of fast neutron, thermal neutron and γ ray as much as possible, and (3) collimate neutron beam. The thermal neutron is suitable for treating superficial lesions while the epithermal neutron is for treating deep ones. BSA is mainly composed of the following components: moderator, reflector, gamma filter, collimator, etc., and thermal neutron filters are also required if neutrons need to be moderated to the energy range of epithermal neutrons.

Currently, the proposed BSA designs around the world mainly focus on generating epithermal neutrons which are essential for the treatment of deep-seated tumors, such as the BSAs in Tsukuba University (5), Nagoya University (6, 7), and Kyoto University (8). However, thermal neutron beam cannot be ignored anyway. It is applicable to the treatment of superficial tumors, such as melanoma, as well as cell and animal pre-clinical experiments. Therefore, multiple BSAs were designed for the generation of thermal and epithermal neutrons, respectively, and both of them fulfill the IAEA recommended values (9) which are listed in **Table 1**. In this work, the Monte Carlo simulation program MCNPX was used to design multiple BSAs based on an AB-BNCT model and the clinical parameters of the thermal and epithermal neutrons generated from the multiple BSAs were calculated, aiming at providing reference for the construction of AB-BNCT facility.

METHODS AND MATERIALS

Initial BSA Model

An initial BSA model was proposed and shown in **Figure 1**. The whole BSA has a cylinder structure with lithium target and beam channel located in the central axis of the cylinder. The lithium target is 10 cm in diameter and 100 μm in thickness, and there is a copper holder of 2.3 cm in thickness below the target, which plays a role in heat dissipation and structure support. Thirty milliamper proton beams would generate lots of heat in target indeed and Li target has a low melt pointing. So, it is necessary to consider a cooling system for the Li target. In this work, copper

was used to roughly represent the cooling system for target. The beam pipe is made of 316L stainless steel with a thickness of 1 cm for 2.5 MeV proton transport, and the thickness of the stainless steel above the target is 4 cm. In this way, the radiation damage of recoiling neutrons and protons can be reduced. Boron containing polyethylene (10 wt% natural B) is used in the outer side of the BSA as an absorption shield for neutrons. On the bottom of the collimator, a gamma shield is designed in the inner side of the collimator to further reduce the gamma component in the beam. The diameter of the BSA beam port is set to 14 cm. Finally, we used the MCNPX software to calculate the physical and clinical parameters of thermal and epithermal neutrons.

In addition, in the optimization process of BSA for thermal neutrons, the energy of thermal neutron is close to the kinetic energy of nuclear thermal motion in materials of reflector, moderator etc. So, the library of the thermal scattering law data S (α , β) may be required. This library plays an important role in describing the transport of thermal neutrons (10). This work used the ENDF/B-VII.0 cross section library for the simulation of thermal neutron scattering.

Neutron Source

The neutron beam generated from bombarding lithium target by 2.5 MeV protons was simulated using the MCNPX software, whose spectrum and angular distribution are shown in **Figure 2**. The neutron beam was made as a dumb data file, which acted as a neutron source used in the BSA optimization. In this way, the computation time was greatly reduced.

Moderator and Reflector

The most important part of BSA is moderator. Its role is to moderate the energy of neutrons produced by protons into the energy range of thermal or epithermal neutrons without producing excessive gamma rays. Thus, the moderator should have a high scattering cross section at desired energies (thermal or epithermal energy), low one for undesired energies (thermal or fast energy) and absorption cross section, avoiding loss of neutron intensity and producing large quantities of gamma-rays (11). In the optimization process, different moderator materials (Fluential, TiF_3 , CaF_2 , Al, AlF_3 and MgF_2 for epithermal neutron beam BSA, and D_2O , normal polyethylene and graphite for thermal neutron BSA, respectively) were considered (12–14).

Another important part is reflector which is used to reflect scattered neutrons back into the beam. Reflector should have a low absorption cross section, a high elastic scattering cross section for thermal or epithermal neutrons and also a large mass number in which less loss of energy with elastic collision. We considered Teflon, Pb, 316L stainless steel, BeO, and Al_2O_3 for thermal neutron beam BSA, and Teflon, Al_2O_3 , Pb for epithermal neutron beam BSA, respectively.

Neutron and Gamma Filters

To minimize the damage to healthy tissue around the tumor, beam filters are necessary for reducing contaminations of fast neutrons, thermal neutrons and gamma rays. For the thermal neutron beam BSA, Pb, and Bi were compared as gamma filter.

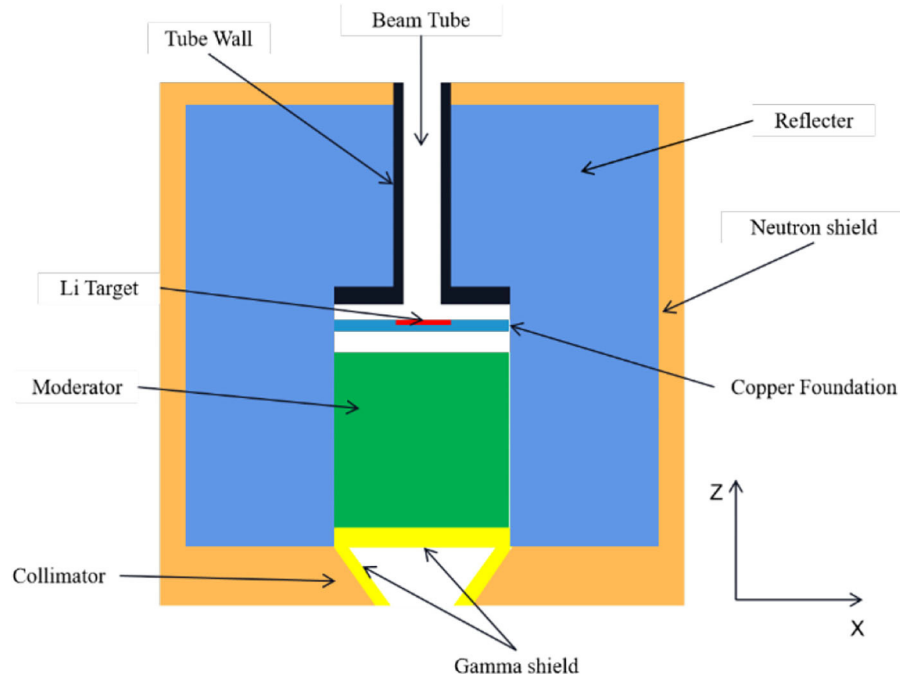


FIGURE 1 | Structure of initial design of BSA.

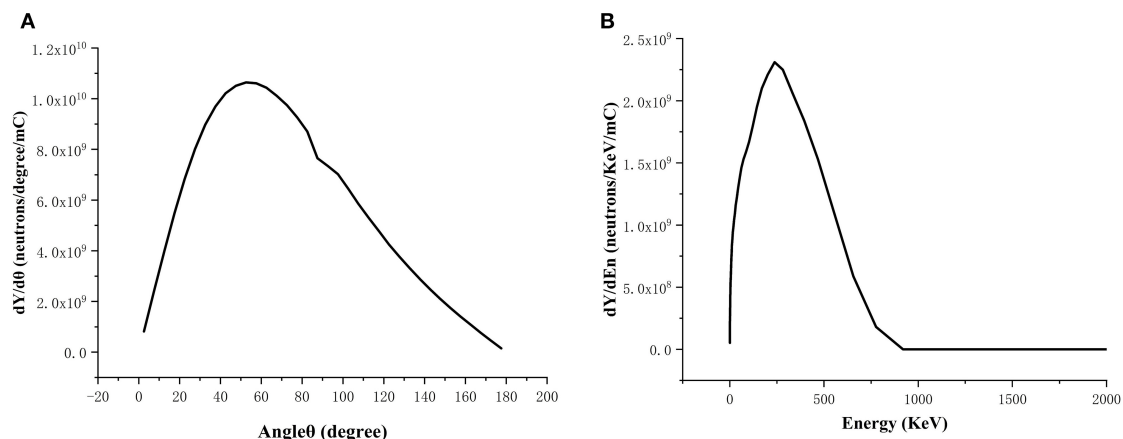


FIGURE 2 | Spectrum (A) and angular distribution (B) of the neutron beam generated from bombarding Li target by 2.5 MeV/30 mA protons.

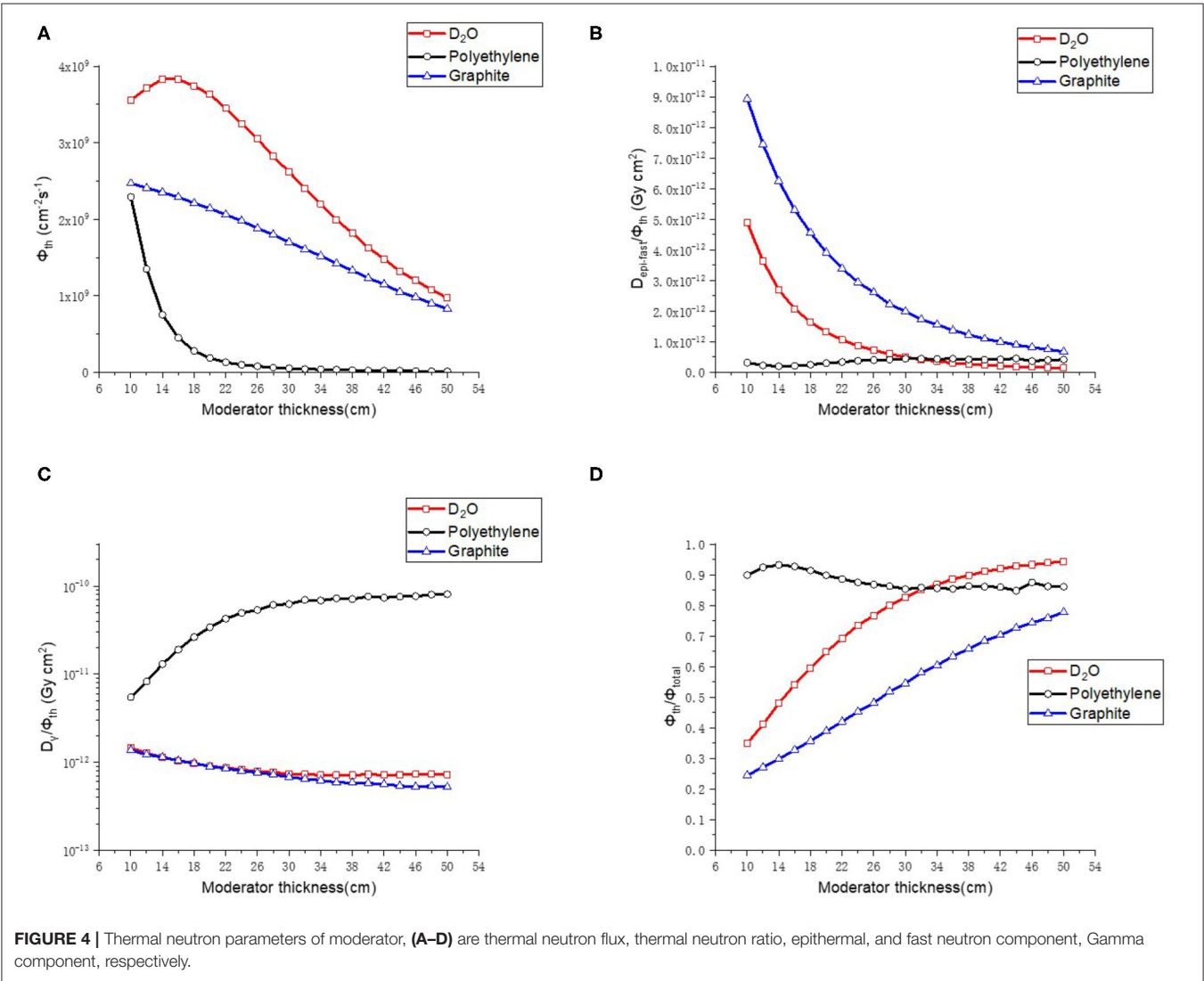
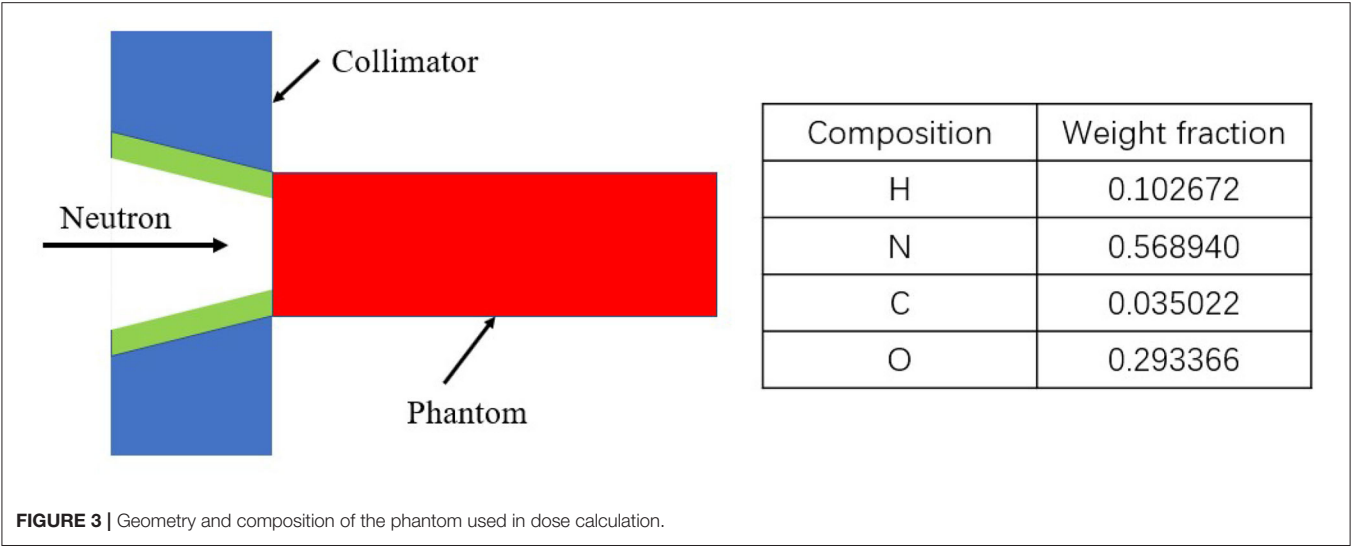
As for the epithermal neutron beam BSA, Ni, and ^7LiF were used as fast neutron filter and thermal neutron filter, respectively.

Collimator

The collimator can limit divergence of the neutron beam and, reduce undesired irradiation and focus neutrons to patient position. And we calculated J/Φ to measure the beam divergence variation. A high ratio means that the neutron beam is close to the beam port and change slightly with distance from the port. A target value for this ratio should be > 0.7 (9).

Clinical Parameters

Under clinical conditions, it is vital to investigate the dosimetry performance in the patients. So, in-phantom parameters were calculated. These parameters are advantage depth (AD), advantage ratio (AR), AD dose rate (ADDR), and treatment time (TT), where AD is the depth in phantom at which the total therapeutic dose in tumor equals the maximum dose of the normal tissue. AD indicates the depth of effective beam penetration. The AR is the ratio of the total therapeutic dose in tumor to the total normal tissue dose over a given depth (usually from the surface to AD). It is a measure of the therapeutic gain.



ADDR is defined as the maximum dose rate for the normal tissue (15, 16).

Four components contributing to the absorbed dose in BNCT as follows:

- (1) The gamma dose D_γ : the dose due to gamma rays in the neutron beam as well as gamma rays induced in the tissue from nuclear reactions, like $^1\text{H} (n, \gamma) ^2\text{H}$ reaction;
- (2) The hydrogen dose D_H : the dose due to recoil protons from $^1\text{H} (n, n') ^1\text{H}$ reaction;
- (3) The nitrogen dose D_N : the dose due to energetic proton and the recoiling ^{14}C nucleus from $^{14}\text{N} (n, p) ^{14}\text{C}$ reaction;
- (4) The boron dose D_B : the dose due to α particles and the recoiling ^7Li nuclei from $^{10}\text{B} (n, \alpha) ^7\text{Li}$ reaction.

The total RBE-weighted dose, D_T is expressed in the unit of RBE-Gy, as a sum of physical dose components multiplied by appropriate weighting-factors (RBE or CBE) for each dose component. It can be calculated using Equation (2) as below:

$$D_T = C_B \times D_B + \omega_N \times D_N + \omega_H \times D_H + \omega_\gamma \times D_\gamma \quad (2)$$

where ω_γ , ω_H , ω_N , and C_B are the weighting factors for gamma rays, hydrogen, nitrogen and boron, respectively. The values of ω_H and ω_N were taken as 3.0, ω_γ was considered as 1, while ω_B was 1.35 for boron in the normal tissue and 3.8 for boron in the tumor. A simple phantom was considered to be a cylinder with a simplified composition of soft tissue as shown in **Figure 3**. The elemental compositions for the material of the cylinder phantom were also listed in **Figure 3** (17). ^{10}B was added to the phantom directly at the tumor concentration, as B_T , of 30 ppm. The normal tissue concentration, B_N , was chosen as 9 ppm, so that the ratio of B_T to B_N , or T/N was 3.33 (18).

RESULTS AND DISCUSSION

Optimization Design of the Thermal Neutron Beam BSA

Moderator for the Thermal Neutron Beam BSA

The thickness of the material varied from 10 to 50 cm with a step of 2 cm in the calculations, and the radius of the moderator was set to be 22 cm. The results are shown in **Figure 4**. D_2O

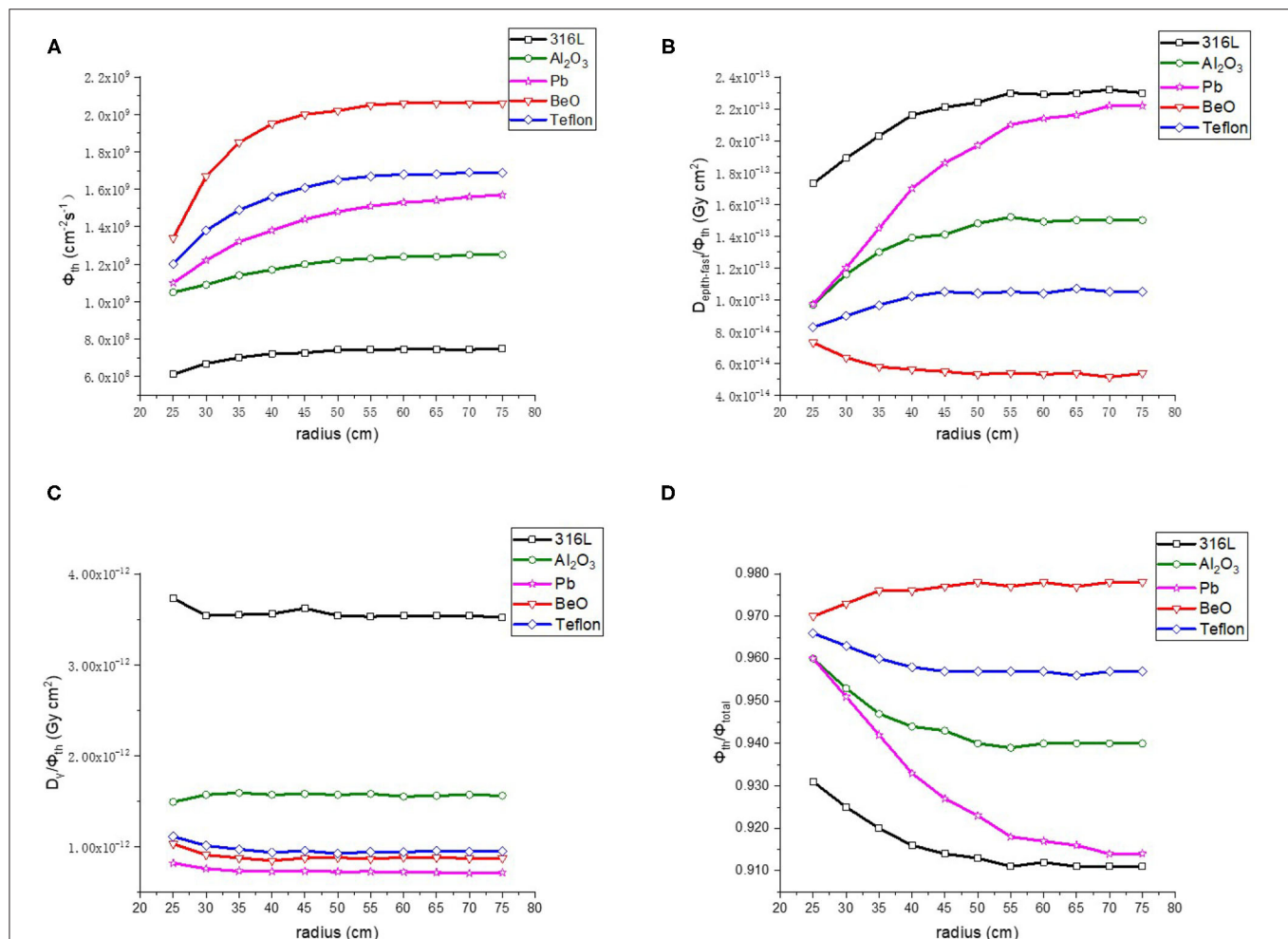


FIGURE 5 | Thermal neutron parameters of reflector, (A–D) are thermal neutron flux, thermal neutron ratio, epithermal, and fast neutron component, Gamma component, respectively.

gave the highest thermal neutron flux (Φ_{th}), and when the thickness exceeded 30 cm, it gave low epithermal and fast neutron component ($D_{epi-fast}/\Phi_{th}$), low γ ray component (D_γ/Φ_{th}), and high proportion of thermal neutron (Φ_{th}/Φ_{total}). Therefore, D_2O was chosen as the moderator for the thermal neutron beam BSA with a thickness of 40 cm.

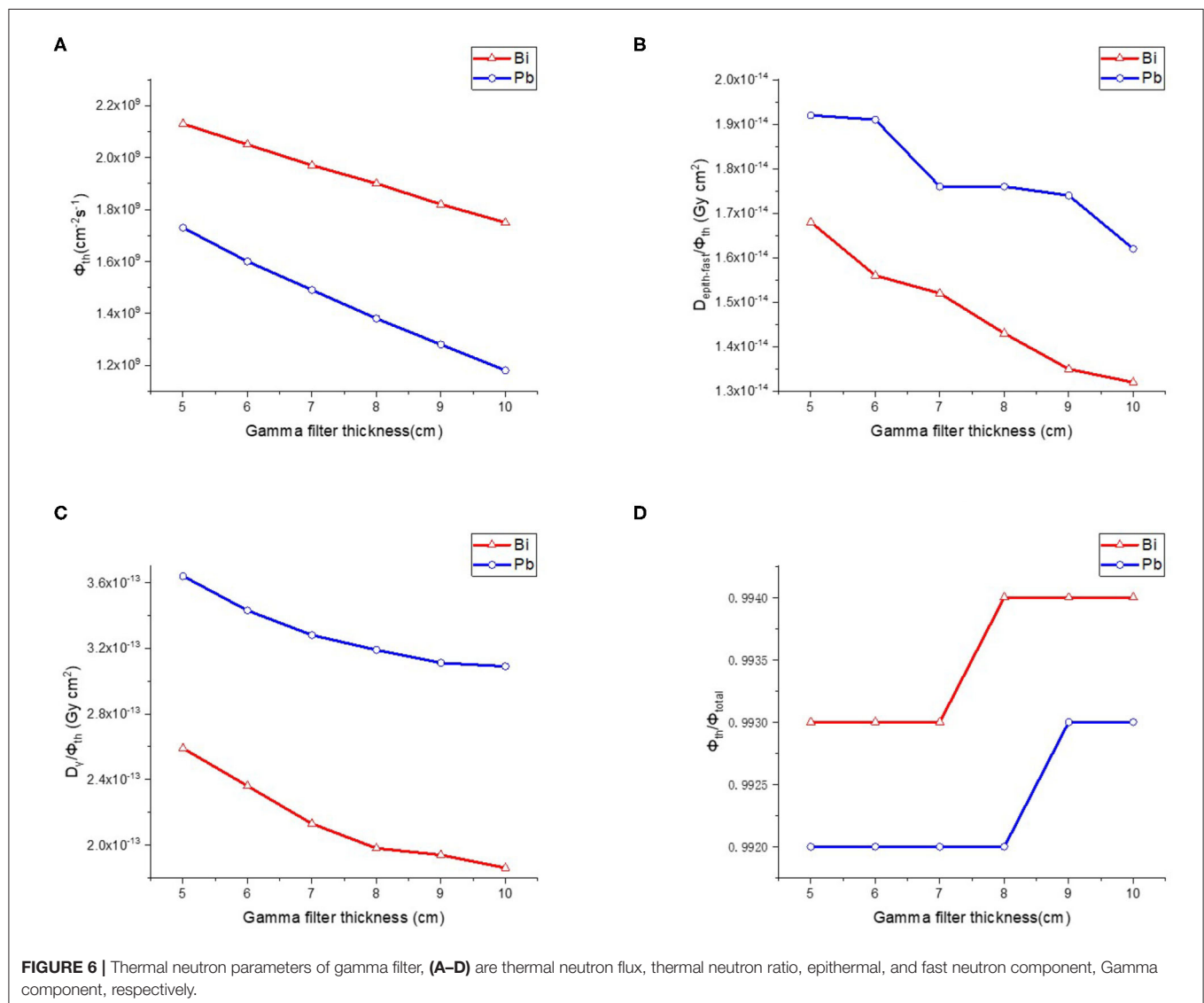
Reflector for the Thermal Neutron Beam BSA

As the next step of the optimization, BeO, Al_2O_3 , 316L stainless steel, Teflon and Pb were compared for the reflector. The radius of the reflector was changed with a range of 25–75 cm and a step length of 5 cm. The results are shown in **Figure 5**. First of all, among the five kinds of materials, BeO presented the highest thermal neutron flux (Φ_{th}), the lowest epithermal and fast neutron component ($D_{epi-fast}/\Phi_{th}$) and the highest proportion of thermal neutron (Φ_{th}/Φ_{total}). The γ ray component is also lower than 316L Stainless steel, Al_2O_3 and Teflon, so BeO was selected as the reflector material. In addition, it shows that when the

radius is > 45 cm, the reflector radius has no significant influence on the neutron beam parameters. Considering the purpose of saving material and reducing the size of BSA, the reflector radius is chosen as 50 cm.

Gamma Filter for Thermal Neutron Beam BSA

After determining the materials and sizes of the moderator and reflector, it is necessary to optimize the design of gamma filter to reduce γ rays' component because that γ rays which produced during moderation process cause unnecessary dose to normal tissue. The commonly used gamma filter materials are Pb and Bi. We made a comparison between these two materials. The thickness of gamma filter varied from 5–10 cm and the step length was 1 cm. Results as shown in **Figure 6**, Bi is a better choice for BNCT because it provides high photon elimination and low loss of thermal neutron flux. Therefore, we choose 9 cm Bi as gamma filter.



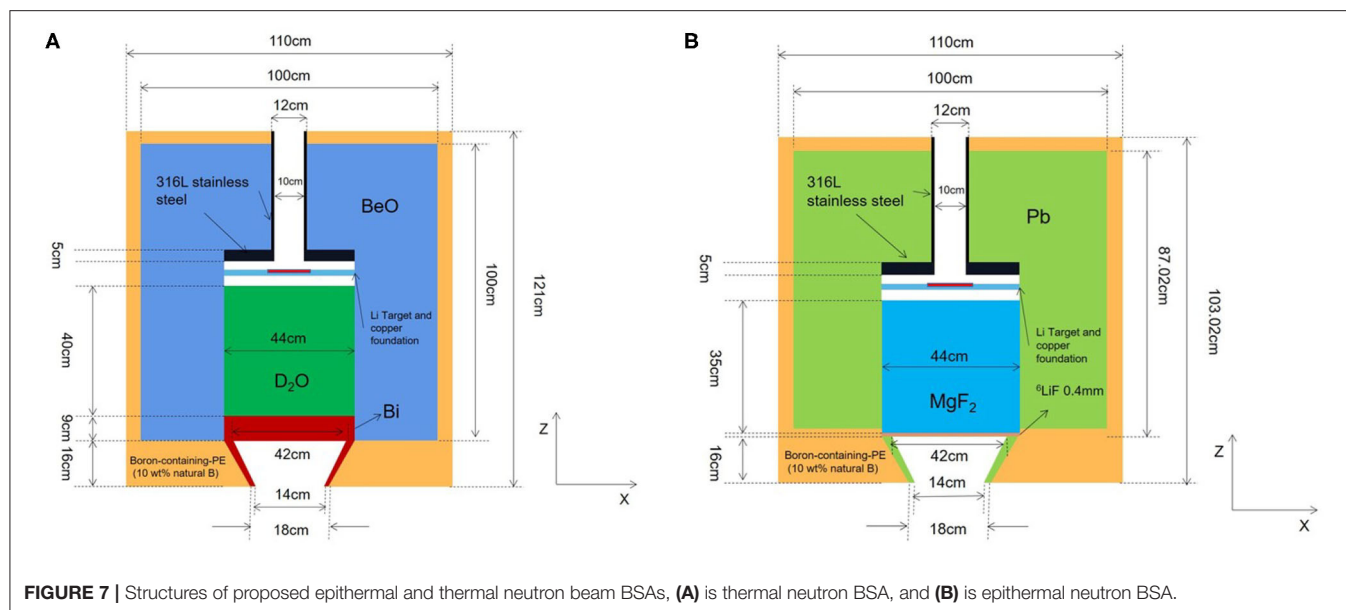


FIGURE 7 | Structures of proposed epithermal and thermal neutron beam BSAs, **(A)** is thermal neutron BSA, and **(B)** is epithermal neutron BSA.

TABLE 2 | Thermal neutron beam parameters of proposed design and other designs in the world.

Thermal neutron beam	Thermal neutron flux Φ_{th} ($\text{cm}^{-2}\text{s}^{-1}$)	Epithermal and fast neutron components $D_{epi-fast}/\Phi_{th}$ (Gy cm^2)	Thermal neutron ratio Φ_{th}/Φ_{total}	Gamma component D_{γ}/Φ_{th} (Gy cm^2)	J/Φ
Proposed design	1.82×10^9	1.35×10^{-14}	0.994	1.94×10^{-13}	0.654
Hospital neutron irradiator IHNI (12)	2.14×10^9	1.70×10^{-13}	—	9.73×10^{-14}	0.798
Italian INFN (4 MeV protons on beryllium) (14)	$1.17 \pm 0.003 \times 10^9$	$8 \pm 2 \times 10^{-16}$	0.99	$1.38 \pm 0.003 \times 10^{-13}$	—
The IAEA recommended values	$\geq 1 \times 10^9$	$\leq 2 \times 10^{-13}$	> 0.9	$\leq 2 \times 10^{-13}$	> 0.7

TABLE 3 | Epithermal neutron beam parameters of proposed design and other designs in the world.

Epithermal neutron beam	Epithermal flux Φ_{epith} ($\text{cm}^{-2}\text{s}^{-1}$)	Fast neutron component D_{fast}/Φ_{epith} (Gy cm^2)	Thermal neutron ratio Φ_{th}/Φ_{epith}	Gamma component D_{γ}/Φ_{th} (Gy cm^2)	J/Φ
Proposed design	1.26×10^9	1.85×10^{-13}	0.033	1.48×10^{-13}	0.715
Kyoto University (8)	1.2×10^9	5.8×10^{-13}	—	7.8×10^{-14}	—
Nagoya University (7)	1.05×10^9	2×10^{-13}	0.058	2.19×10^{-13}	0.71
Montagnini et al. (19)	1.226×10^9	1.7×10^{-13}	0.0096	1.7×10^{-13}	0.61
Kim et al. (20)	1.01×10^9	0.09×10^{-13}	0.048	0.09×10^{-13}	—
Kim et al. (20)	1.03×10^9	0.08×10^{-13}	0.047	0.08×10^{-13}	—
Fantidis. (21)	1.096×10^9	1.40×10^{-13}	0.0056	1.40×10^{-13}	—
Fantidis. (21)	0.523×10^9	1.77×10^{-13}	0.0098	1.77×10^{-13}	—
The IAEA recommended values	$\geq 1 \times 10^9$	$\leq 2 \times 10^{-13}$	< 0.05	$\leq 2 \times 10^{-13}$	> 0.7

Collimator

We choose Bi as material of collimator. And it is designed as a cone. It is 16 cm long (in height), and radius of bottoms are 22 and 7 cm. The J/Φ is 0.654 which is basically meets

the target value. The details of collimator are shown in Figure 7A.

In conclusion, the final design of thermal neutron beam BSA can be obtained by using D_2O as moderator, BeO as reflector,

and Bi as gamma filter. The structure of thermal neutron beam BSA is shown in **Figure 7A**, and the neutron beam parameters were listed in **Table 2** with other designs in the world. The flux of proposed thermal neutron beam BSA is higher than INFN and not much less than IHNI. However, IHNI is based on reactor, so it's difficult to build in hospital. So, the proposed thermal neutron beam BSA has its advantages.

Optimization Design of Epithermal Neutron Beam BSA

The process of the optimization design is basically the same as that of the thermal neutron beam BSA, so we show the final optimization results directly. We choose 45 cm MgF_2 as moderator, 50 cm Pb as reflector, 0.4 mm ^6LiF as the thermal neutron filter. The collimator is as same as thermal neutron BSA except its material is Pb. The structure of epithermal neutron

beam BSA is shown in **Figure 7B**, and the parameters are listed in **Table 3** with other designs in the world.

It is obvious that all the parameters of proposed BSAs fulfill the IAEA recommended values. And the flux of proposed epithermal neutron beam BSA is higher than other designs.

Calculation of Clinical Parameters

Firstly, we calculated neutron flux distribution in the phantom of thermal neutron beam and epithermal neutron beam generated by proposed BSAs, respectively. As shown in **Figures 8A,B**, the maximum depth of flux in the phantom of thermal neutron beam is 5 cm, and the maximum depths of thermal and epithermal flux of epithermal neutron beam are 12 and 8 cm, respectively. The components of epithermal and fast neutron are too low so that they are not shown in the **Figure 8A**.

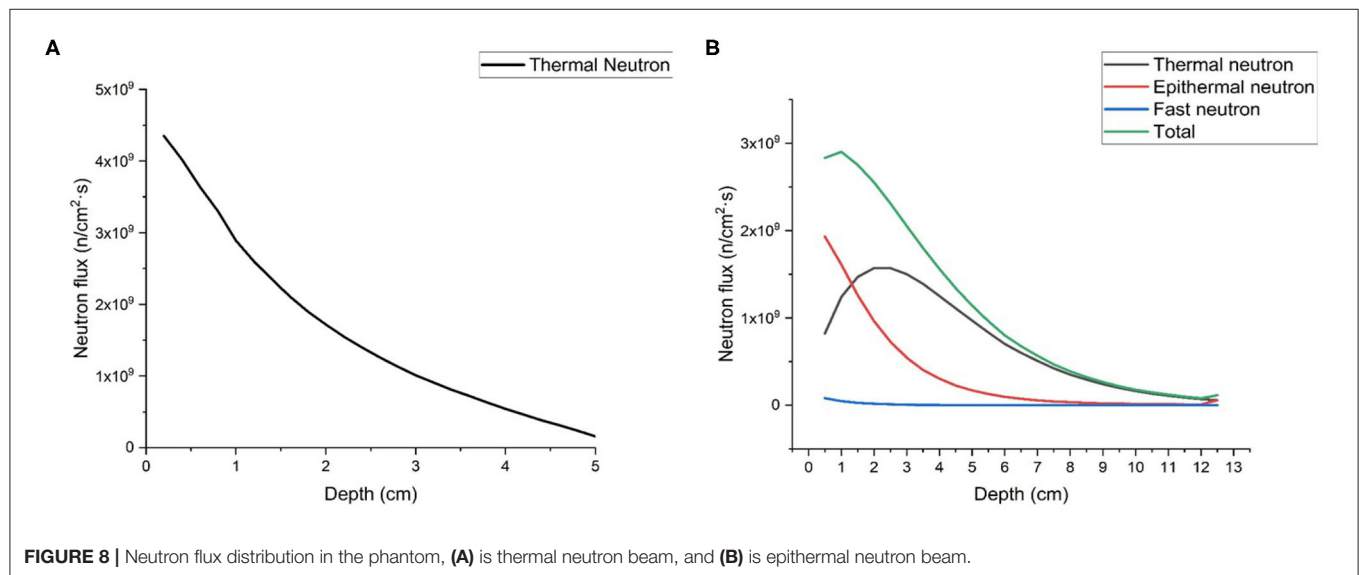


FIGURE 8 | Neutron flux distribution in the phantom, (A) is thermal neutron beam, and (B) is epithermal neutron beam.

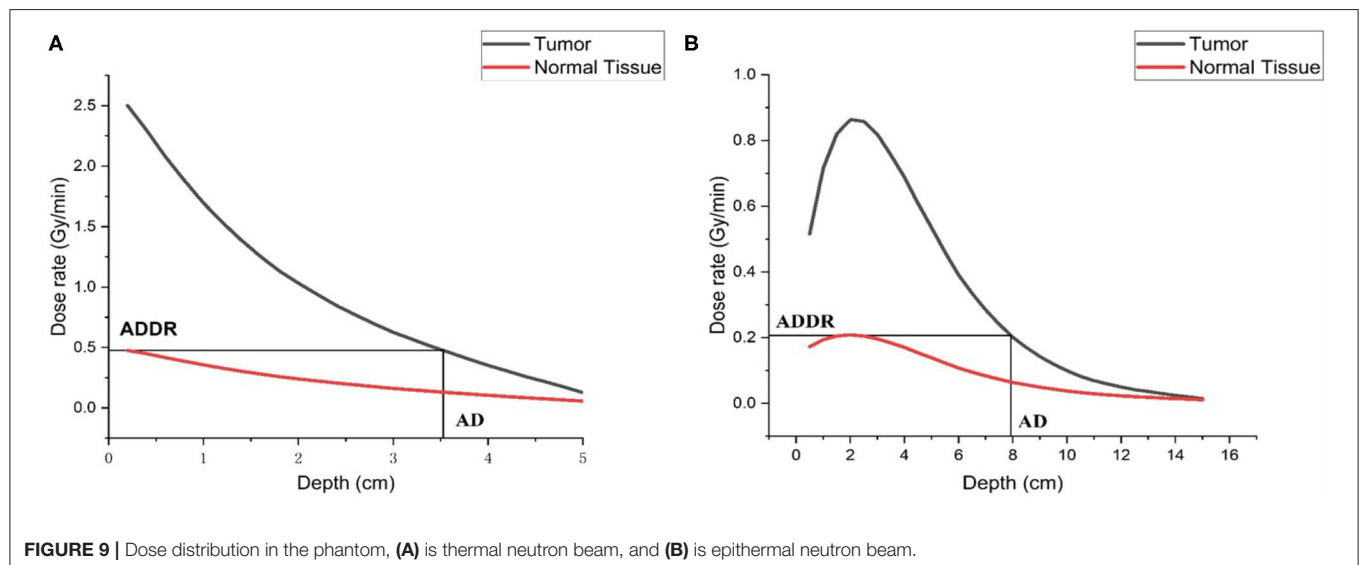


FIGURE 9 | Dose distribution in the phantom, (A) is thermal neutron beam, and (B) is epithermal neutron beam.

As for the dose in tumor and normal tissue, we also calculated them in the phantom. As shown in **Figure 9**, the AD is 7.93 cm for epithermal neutron beam and 3.52 cm for thermal neutron beam. The ADDR for thermal neutron beam is 0.476RBE-Gy/min, and for epithermal neutron beam it is 0.208RBE-Gy/min. According to the results, we found that the large amount of dose was delivered to skin and superficial normal tissue. If we defined the time that dose delivered to normal tissue exceed the maximum tolerated dose (12.5RBE-Gy) as the treatment time (TT) which is the maximum value. Then, TTs are 60.1 min for epithermal neutron beam and 26.3 min for thermal neutron beam. During this time, the maximum D_T s of tumor are 51.87 RBE-Gy for epithermal neutron beam and 65.75 RBE-Gy for epithermal neutron beam. And maximum DRs are 0.863RBE-Gy/min for epithermal neutron beam and 2.5 RBE-Gy/min for thermal neutron beam, respectively.

CONCLUSIONS

In this paper, MCNPX is used to design the BSAs of an AB-BNCT using $^7\text{Li}(p,n)^7\text{Be}$ reaction. The optimized BSAs for thermal and epithermal neutron beams can ensure that the beam parameters at the exit all meet the recommended values of IAEA. And the clinical parameters are also calculated so that it can give a reference for clinical condition. So the final optimal design of thermal and epithermal BSA can be an important reference for the BSA engineering scheme of multi-terminal AB-BNCT device. In the follow-up work, the accelerator-based multi-terminal BSA conversion device will be further designed to facilitate the flexible switching and replacement of BSA, ensure the safe operation

of the device, and give better play to the advantages of multi-terminal devices, which will promote the development of AB-BNCT in China.

DATA AVAILABILITY STATEMENT

The raw data supporting the conclusions of this article will be made available by the authors, without undue reservation.

AUTHOR CONTRIBUTIONS

GL adapted the neutron source in the Li target (with WJ), performed the simulations on BSA, calculated clinical parameters, and wrote the manuscript. WJ and LZ helped execute MCNP and adjust the input files. WC participated in the study design and reviewed the results. QL supervised this work and contributed to the study design. All authors contributed to the article and approved the submitted version.

FUNDING

This study was funded by National Key R&D Program of China (2018YFC0115700), National Natural Science Foundation of China (11875299), Major science and technology project of Gansu Province (1602FKDA005), The key research program of the Chinese Academy of Sciences (KFZD-SW-222), West Light Foundation of The Chinese Academy of Sciences (29Y86205), and the project of Youth Innovation Promotion Association, CAS (2017454).

REFERENCES

- Barth RF, Soloway AH. Boron neutron capture therapy of primary and metastatic brain tumors. *Mol Chem Neuropathol.* (1994) 21:139–54. doi: 10.1007/BF02815348
- Locher GL. Biological effects and therapeutic possibilities of neutrons. *Am J Roentgenol Radium Ther.* (1936) 36:1–13.
- Sweet WH. The uses of nuclear disintegration in the diagnosis and treatment of brain tumor. *N Engl J Med.* (1951) 245:875–8. doi: 10.1056/NEJM195112062452301
- Hatanaka H, Nakagawa Y. Clinical results of long-surviving brain tumor patients who underwent boron neutron capture therapy. *Int J Radiat Oncol.* (1994) 28:1061–6. doi: 10.1016/0360-3016(94)90479-0
- Kumada H, Naito F, Hasegawa K, Kobayashi H, Kurihara T, Takada K, et al. Development of LINAC-based neutron source for boron neutron capture therapy in University of Tsukuba. *Plasma Fusion Res.* (2018) 13:2406006. doi: 10.1585/pfr.13.2406006
- Uritani A, Menjo Y, Watanabe K, Yamazaki A, Kiyanagi Y, Tsuchida K. Design of beam shaping assembly for an accelerator-driven BNCT system in Nagoya University. *J Phys Soc Jpn.* (2018) 011002:1–7. doi: 10.7566/JPSCP.22.011002
- Sato K, Uritani A, Watanabe K, Yoshihashi S, Yamazaki A, Kiyanagi Y, et al. Improved design of the exit of a beam shaping assembly for an accelerator-driven BNCT system in Nagoya University. *J Phys Soc Jpn.* (2018) 011003:1–7. doi: 10.7566/JPSCP.22.011003
- Tanaka H, Sakurai Y, Suzuki M, Masunaga S, Mitsumoto T, Fujita K, et al. Experimental verification of beam characteristics for cyclotron-based epithermal neutron source (C-BENS). *Appl Radiat Isot.* (2011) 69:1642–5. doi: 10.1016/j.apradiso.2011.03.020
- IAEA. *Current Status of Neutron Capture Therapy.* Vienna (2001).
- Chadwick MB, Herman M, Obložinský P, Dunn ME, Danon Y, Kahler AC, et al. ENDF/B-VII.1 nuclear data for science and technology: cross sections, covariances, fission product yields and decay data. *Nucl Data Sheets.* (2011) 112:2887–996. doi: 10.1016/j.nds.2011.11.002
- Zaidi L, Belgaid M, Taskaev S, Khelifi R. Beam shaping assembly design of $^7\text{Li}(p,n)^7\text{Be}$ neutron source for boron neutron capture therapy of deep-seated tumor. *Appl Radiat Isot.* (2018) 139:316–24. doi: 10.1016/j.apradiso.2018.05.029
- Ke G, Sun Z, Shen F, Liu T, Li Y, Zhou Y. The study of physics and thermal characteristics for in-hospital neutron irradiator (IHNI). *Appl Radiat Isot.* (2009) 67:S234–7. doi: 10.1016/j.apradiso.2009.03.117
- Sakurai Y, Kobayashi T. Characteristics of the KUR heavy water neutron irradiation facility as a neutron irradiation field with variable energy spectra. *Nucl Instruments Methods Phys Res Sect A Accel Spectrometers Detect Assoc Equip.* (2000) 453:569–96. doi: 10.1016/S0168-9002(00)00465-4
- Ceballos C, Esposito J, Agosteo S, Colautti P, Conte V, Moro D, et al. Towards the final BSA modeling for the accelerator-driven BNCT facility at INFN LNL. *Appl Radiat Isot.* (2011) 69:1660–3. doi: 10.1016/j.apradiso.2011.01.032
- Rasouli FS, Masoudi FS, Kasesaz Y. Design of a model for BSA to meet free beam parameters for BNCT based on multiplier system for D-T neutron source. *Ann Nucl Energy.* (2012) 39:18–25. doi: 10.1016/j.anucene.2011.08.025
- Rasouli FS, Masoudi SF. Simulation of the BNCT of brain tumors using MCNP code: Beam designing and dose evaluation. *Iran J Med Phys.* (2012) 9:183–92. doi: 10.22038/ijmp.2012.150

17. McConn RJ, Gesh CJ, Pagh RT, Rucker RA, Williams R III. *Compendium of Material Composition Data for Radiation Transport Modeling*. Richland, WA (2011) doi: 10.2172/1023125
18. Seki R, Wakisaka Y, Morimoto N, Takashina M, Koizumi M, Toki H, et al. Physics of epi-thermal boron neutron capture therapy (epi-thermal BNCT). *Radiol Phys Technol.* (2017) 10:387–408. doi: 10.1007/s12194-017-0430-5
19. Montagnini B, Cerullo N, Esposito J, Giusti V, Mattioda F, Varone R. Spectrum shaping of accelerator-based neutron beams for BNCT. *Nucl Instruments Methods Phys Res Sect A Accel Spectrometers Detect Assoc Equip.* (2002) 476:90–8. doi: 10.1016/S0168-9002(01)01398-5
20. Kim KO, Kim JK, Kim SY. Optimized therapeutic neutron beam for accelerator-based BNCT by analyzing the neutron angular distribution from ${}^7\text{Li}(p,n){}^7\text{Be}$ reaction. *Appl Radiat Isot.* (2009) 67:1173–9. doi: 10.1016/j.apradiso.2009.02.004
21. Fantidis JG. Beam shaping assembly study for BNCT facility based on a 2.5 MeV proton accelerator on Li target. *J Theor Appl Phys.* (2018) 12:249–56. doi: 10.1007/s40094-018-0312-1

Conflict of Interest: The authors declare that the research was conducted in the absence of any commercial or financial relationships that could be construed as a potential conflict of interest.

Copyright © 2021 Li, Jiang, Zhang, Chen and Li. This is an open-access article distributed under the terms of the Creative Commons Attribution License (CC BY). The use, distribution or reproduction in other forums is permitted, provided the original author(s) and the copyright owner(s) are credited and that the original publication in this journal is cited, in accordance with accepted academic practice. No use, distribution or reproduction is permitted which does not comply with these terms.



Irradiation-Induced Changes in the Immunogenicity of Lung Cancer Cell Lines: Based on Comparison of X-rays and Carbon Ions

Juntao Ran^{1†}, Jiangtao Wang^{2†}, Ziyang Dai¹, Yandong Miao², Jian Gan², Chengpeng Zhao³ and Quanlin Guan^{2,4*}

¹ Department of Radiation Oncology, The First Hospital of Lanzhou University, Lanzhou, China, ² The First Clinical Medical College of Lanzhou University, Lanzhou, China, ³ Department of Oncology, The First Hospital of Lanzhou University, Lanzhou, China, ⁴ Department of Oncology Surgery, The First Hospital of Lanzhou University, Lanzhou, China

OPEN ACCESS

Edited by:

Lu Cai,
University of Louisville, United States

Reviewed by:

Emily Li,
Royal Adelaide Hospital, Australia
Qifeng Wang,
Sichuan Cancer Hospital, China

*Correspondence:

Quanlin Guan
guanquanlin@yeah.net

[†]These authors have contributed
equally to this work

Specialty section:

This article was submitted to
Radiation and Health,
a section of the journal
Frontiers in Public Health

Received: 10 February 2021

Accepted: 29 March 2021

Published: 22 April 2021

Citation:

Ran J, Wang J, Dai Z, Miao Y, Gan J,
Zhao C and Guan Q (2021)
Irradiation-Induced Changes in the
Immunogenicity of Lung Cancer Cell
Lines: Based on Comparison of X-rays
and Carbon Ions.
Front. Public Health 9:666282.
doi: 10.3389/fpubh.2021.666282

Increasing the immunogenicity of tumors is considered to be an effective means to improve the synergistic immune effect of radiotherapy. Carbon ions have become ideal radiation for combined immunotherapy due to their particular radiobiological advantages. However, the difference in time and dose of immunogenic changes induced by Carbon ions and X-rays has not yet been fully clarified. To further explore the immunogenicity differences between carbon ions and X-rays induced by radiation in different “time windows” and “dose windows.” In this study, we used principal component analysis (PCA) to screen out the marker genes from the single-cell RNA-sequencing (scRNA-seq) of CD8⁺ T cells and constructed a protein-protein interaction (PPI) network. Also, ELISA was used to test the exposure levels of HMGB1, IL-10, and TGF- β under different “time windows” and “dose windows” of irradiation with X-rays and carbon ions for A549, H520, and Lewis Lung Carcinoma (LLC) cell lines. The results demonstrated that different marker genes were involved in different processes of immune effect. HMGB1 was significantly enriched in the activated state, while the immunosuppressive factors TGF- β and IL-10 were mainly enriched in the non-functional state. Both X-rays and Carbon ions promoted the exposure of HMGB1, IL-10, and TGF- β in a time-dependent manner. X-rays but not Carbon ions increased the HMGB1 exposure level in a dose-dependent manner. Besides, compared with X-rays, carbon ions increased the exposure of HMGB1 while relatively reduced the exposure levels of immunosuppressive factors IL-10 and TGF- β . Therefore, we speculate that Carbon ions may be more advantageous than conventional X-rays in inducing immune effects.

Keywords: irradiation, immunogenicity, lung cancer, X-rays, carbon ions

INTRODUCTION

Radiotherapy (RT) is the primary treatment for lung cancer, which first-line treatment accounts for ~30% of all newly diagnosed patients (1). Nevertheless, lung cancer treatment is still tricky, and a new treatment method is urgently needed (2). Relevant studies have shown that immunotherapy has a positive impact on the treatment endpoint of lung cancer and has changed lung cancer treatment. Immunotherapy has become the most promising and effective treatment for

lung cancer (3). The effectiveness of RT is explained as reasonable local tumor control and practical immune activation effect (4, 5). However, in addition to activating immunity, radiation also has an immunosuppressive effect (6), including the recruitment or polarization of immunosuppressive cytokines, immune checkpoint molecules, and suppressive immune cell subtypes (7). Therefore, it is necessary to understand the immunomodulatory properties of radiation to enhance the immune synergy of radiotherapy. Carbon ions have significant radiobiological advantages over conventional X-rays (8, 9), and the direct killing effect on radiation-resistant tumor cells is stronger than conventional X-rays 2–3 times (5, 10). Therefore, it is essential to analyze the immunogenic changes induced by two kinds of radiation in tumor cells to improve radioimmunity.

Immunogenic cell death (ICD) is a form of cell death that can be recognized by the immune system and induce a specific anti-tumor immune response (11). ICD relies on the specific stimuli while provoking the temporal and spatial coordinated immunogenic signals (12, 13), including tumor-associated antigens (TAAs) and damage-associated molecular patterns (DAMPs) related to the activation of dangerous signals pathways (14, 15). Various stimuli, including radiotherapy, chemotherapy, and oncolytic viruses (OVs), can induce ICD (16, 17). In theory, the advantage of enhancing ICD is that it can stimulate the immune system.

CD8⁺T cells are the primary effector cells involved in the anti-tumor immune response, especially during the immune response process caused by radiation (18). The T cell receptor (TCR) on the surface of T cells binds to the antigen-MHC complex and then establishes the immune response by clonal expansion (19). Due to the heterogeneity and difference between cells, the expression of differential genes in CD8⁺ T cells may play different roles in the process of participating in immune effects in the activated or resting state (20). RT combined with immunotherapy has become an effective treatment for NSCLC (21, 22). The immune regulation mechanism induced by radiation has also become an essential aspect of forming the abscopal effect and improving the prognosis. However, the effect of different radiation on the immune response is poorly understood. The change of tumor immunogenicity induced by radiation is an essential mechanism for improving tumor microenvironment (TME) and immune synergism (23). Among them, HMGB1, TGF- β , and IL-10 are important cytokines in radiation-induced ICD and then participate in the process of immune regulation (24–26). As one of the critical DAMPs, HMGB1 plays an essential role in the immune effect stage (27). As classic immunosuppressive factors, the increase of TGF- β and IL-10 is often accompanied by immune effector cell function inhibition and the increase of tumor-associated macrophage (TAMs) infiltration (28, 29).

In this study, based on the scRNA-seq results of CD8⁺T cell clusters in lung cancer tissues in the GEO database, we performed PCA and Cluster analysis on the distribution of the differential genes, which were screened out by bioinformatics methods. What is essential, we compared the effects of X-rays and carbon-ions radiation on the change trends of HMGB1, IL-10, and TGF- β

under different doses and times by ELISA and further explored the role in the immune process of CD8⁺ T cells.

MATERIALS AND METHODS

Data Retrieval and Processing

In this research, scRNA-seq of CD8⁺ T Cell clusters isolated from human lung and lung tumor samples with flow cytometry was downloaded from Gene Expression Omnibus (GEO, <https://www.ncbi.nlm.nih.gov/geo/>) datasets. GSE111894, with 1,084 human lung samples and GPL16791 platform, was selected (30).

Principal Component Analysis (PCA), TSNE Cluster Analysis, and Marker Gene Annotation

Use R language to perform PCA dimensionality reduction processing on the downloaded scRNA-seq data of lung cancer CD8⁺T cell clusters and screen out the relevant genes of each principal component. On this basis, perform TSNE cluster analysis and visualization to find differential expression genes (DEGs) and draw the scatter diagram and violin diagram of the marker genes in each cluster.

Construction of Protein-Protein Interaction Network and Protein Co-Expression Analysis

The marker genes of the different principal components were submitted to the STRING database (<http://www.string-db.org/>) to clarify the information of protein-protein interaction (PPI) (31). The protein co-expression network was constructed and visualized by Cytoscape 3.7.1 software. The number of nodes adjacent to each protein was calculated and sorted by the Molecular Complex Detection (MCODE) plug-in with an MCODE score of more than two (32). Besides, the selected high-risk proteins were analyzed for protein co-expression and visualization (33). $P < 0.05$ was considered to have statistical significance.

Cell Lines

Human LUAD cell lines A549 and LUSC cell lines NCI-H520 were purchased from the Cell Bank, Type Culture Collection, Chinese Academy of Sciences (CBTCCAS). Mouse Lewis lung cancer cells (LLC) was purchased from Cellcook Co, Ltd, Guangzhou, China. Cells were cultured in Dulbecco's Modified Eagle Medium (GIBCO, US) containing 10% fetal bovine serum (BIOWEST, France) and 1% penicillin/streptomycin (HyClone) and were incubated at 37°C in 5% CO₂.

Irradiation Conditions

X-Rays

The cells were inoculated in T25 culture flasks 24 h before irradiation, which was subsequently irradiated on X-ray instruments dedicated to radiobiological experiments at the Institute of Modern Physics, Chinese Academy of Sciences. The X-rays were operated at 100 Kev, with a dose rate of 1.0 Gy/min, which source was 0.5 meters away from the sample surface. The cells were irradiated at room temperature.

Carbon Ions

The samples were irradiated with the 80 MeV/u carbon ions beam provided by the external tumor treatment terminal of the Lanzhou Heavy Ion Research Facility (HIRFL), and the carbon ions beam provided by HIRFL was calibrated before the irradiation to make sure the LET of the carbon ions irradiated to the sample surface was 30 keV/ μm , and the dose rate was 2.0 Gy/min. Irradiation was performed at room temperature. The control samples were sham-irradiated.

Enzyme-Linked Immunosorbent Assay

The A549/H520/LLC cells in the exponential growth phase were irradiated with 0 Gy, 2 Gy, 4 Gy, 6 Gy X-rays, and Carbon ions irradiation, and the cell culture supernatant was collected at different time points (6, 18, 24, 36, and 48 h), which stored at -4°C for later use. TGF- β , IL-10, HMGB1 ELISA kits were purchased from Neobioscience Technology Co, Ltd. The experimental operation was strictly performed under the instructions.

Annexin V/PI Double Staining to Detect Cell Apoptosis

Use flow cytometry to detect changes in cell apoptosis after radiation. Collect the overall sample size of 10,000 cells, detect and collect FL-1 (Annexin V-FITC green fluorescence signal) and FL-2 (PI red fluorescence signal) channel information, and use IDEAS Version 6.0 software for analysis. The apoptosis kit was purchased from BD Biosciences Pharmingen.

Statistical Analysis

The statistical analysis was performed using one-way analysis of variance and an unpaired Student's *t*-test with a 2-tailed distribution, and multiple comparisons have been made. $P < 0.05$ was considered statistically significant. All statistical analyses were performed using IBM's SPSS software (version 20.0).

RESULTS

Construction of PPI Network Based on Significantly DEGs in PCA

Based on the CD8⁺T cell scRNA-seq in lung cancer, we used PCA to screen out the DEGs expressed in the resting state (PC_0), activated state (PC_1), and non-functional state (PC_2) clusters. The larger the absolute value of the numerical value, the more pronounced the gene significance. Interestingly, as a Marker gene in the TME, HMGB1 was significantly enriched in the activated state (Figure 1A), while the immunosuppressive factors TGF- β and IL-10 were significantly enriched in the non-functional state (Figure 1B). In the resting state, these differential genes lacked noticeable distribution differences (Figure 1C). To further clarify the co-expression relationship of marker genes in lung cancer, we constructed a co-expression network based on differential genes from the STRING database and found that almost all independent marker genes have coordinated regulation in the network (Figure 1D).

The Distribution of Marker Genes in CD8⁺ T Cell Single-Cell Clusters

Several marker genes, FOXP3, STAT3, PDCD1, TGF β 1, IL10, HMGB1, which are significantly related to the tumor microenvironment induced by radiation, had significant functional differences in the distribution of CD8⁺T cells clusters. Irradiation causes the immunogenic death of dying cells, among which the accumulation of HMGB1 was pronounced in the resting state and the activated state, while the related inhibitors IL10, TGF β 1, FOXP3 (marker genes of Tregs), STAT3 (FOXP3 transcriptional cofactor), and PDCD1 (PD-1 related genes) were significantly enriched in the non-functional state (Figure 2A). We analyzed the distribution trend of the above marker genes in CD8⁺ T cell clusters in the activated state. Interestingly, this phenomenon was still apparent. HMGB1 became the most apparent gene enriched in the activated state of CD8⁺ T cell clusters. The opposite was true for FOXP3 and IL10 (Figure 2B).

Both X-Rays and Carbon Ions Promoted the Exposure of HMGB1, IL-10, and TGF- β in a Time-Dependent Manner

Given the above CD8⁺ T cell cluster scRNA-seq analysis, we found that different immune responses present different immune-related factors. Based on this, we irradiated three different lung cancer cell lines, including human (A549/H520) and murine (LLC), with different physical doses (0, 2, 4, and 6 Gy) X-rays and Carbon ions irradiation, aiming to explore the changing trend of main DAMPs or TAAs after different radiation exposure. Take the exposure levels of HMGB1, IL-10, and TGF- β at different times (6–48 h) in the three cell lines after 4 Gy radiation as an example. It is not difficult to find that the exposure levels of HMGB1, IL-10, and TGF- β in the three cell lines all increased with time in both X-rays and Carbon ions. Interestingly, the exposure level within 18 h after irradiation only slightly increased and reached a peak after 24–36 h, while the main DAMPs and TAAs increased into a plateau after 48 h of irradiation (Figures 3A–I, Table 1). Also, after 48 h of irradiation with 4 Gy X-rays and carbon ions, we analyzed the differences in apoptosis of A549, H520, and LLC cell lines and found that carbon ions can significantly promote cell apoptosis at the same physical dose (Figures 3J–O).

X-Rays but Not Carbon Ions Increased the HMGB1 Exposure Level in a Dose-Dependent Manner

As one of the DAMPs that significantly enhance the anti-tumor immune effect after radiation, the exposure level of HMGB1 is of great significance for the immune surveillance of the tumor microenvironment. After X-rays and Carbon ions irradiation with the same physical dose (2–6 Gy), the exposure of HMGB1 showed different trends. For X-rays, the exposure level of HMGB1 showed a dose-dependent increase, but the increase was limited in the low dose (0–2 Gy) range, and a substantial increase was showed after 4 Gy. Interestingly, the exposure level of HMGB1 caused by Carbon ions irradiation peaked at a

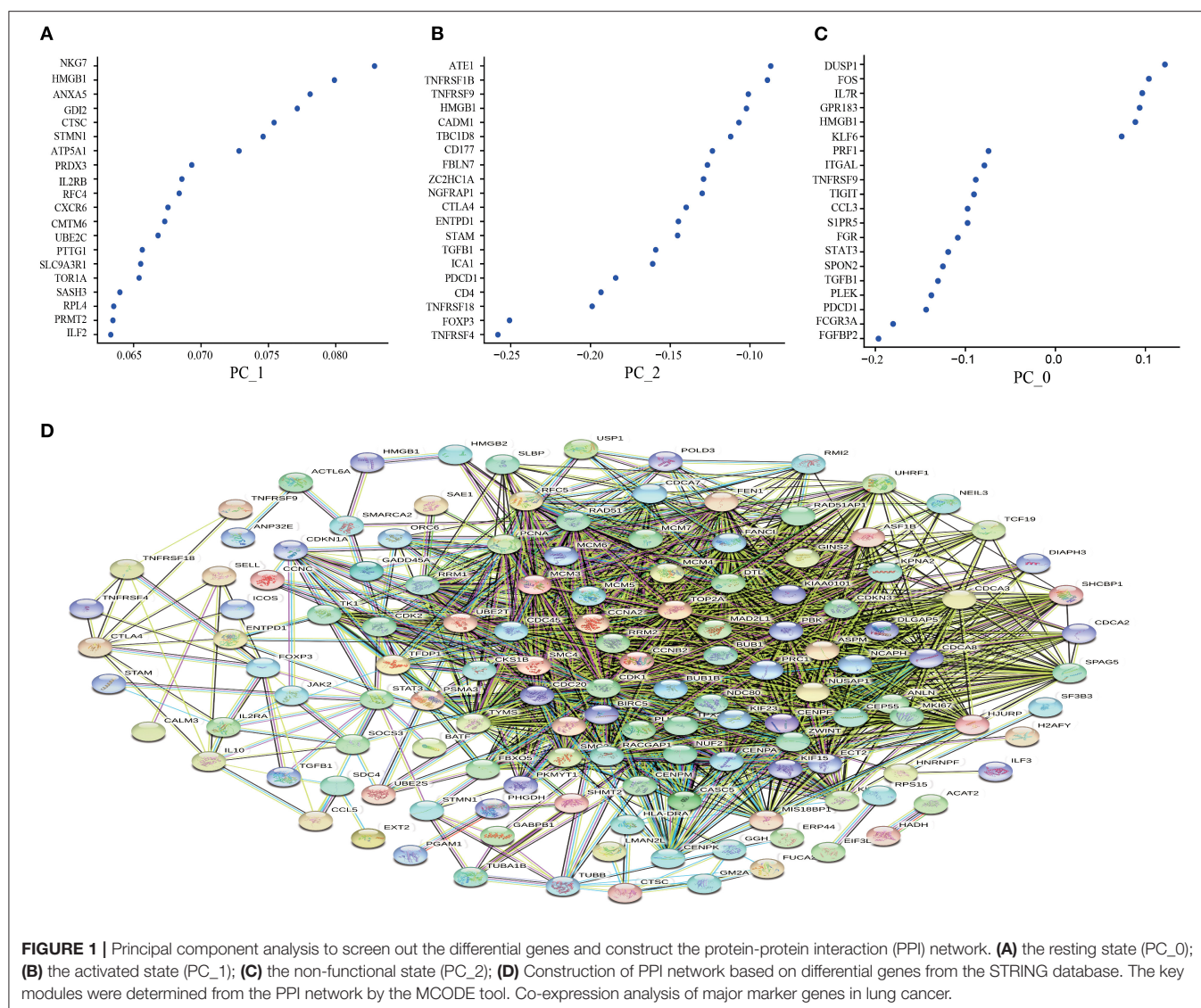


FIGURE 1 | Principal component analysis to screen out the differential genes and construct the protein-protein interaction (PPI) network. **(A)** the resting state (PC_0); **(B)** the activated state (PC_1); **(C)** the non-functional state (PC_2); **(D)** Construction of PPI network based on differential genes from the STRING database. The key modules were determined from the PPI network by the MCODE tool. Co-expression analysis of major marker genes in lung cancer.

physical dose of 4 Gy and then slowly decreased. Besides, under the same physical dose, the exposure level of HMGB1 caused by Carbon ions irradiation was significantly higher than that of X-rays. There was no significant difference in the above trend among the three lung cancer cell lines (Figure 4, Table 2).

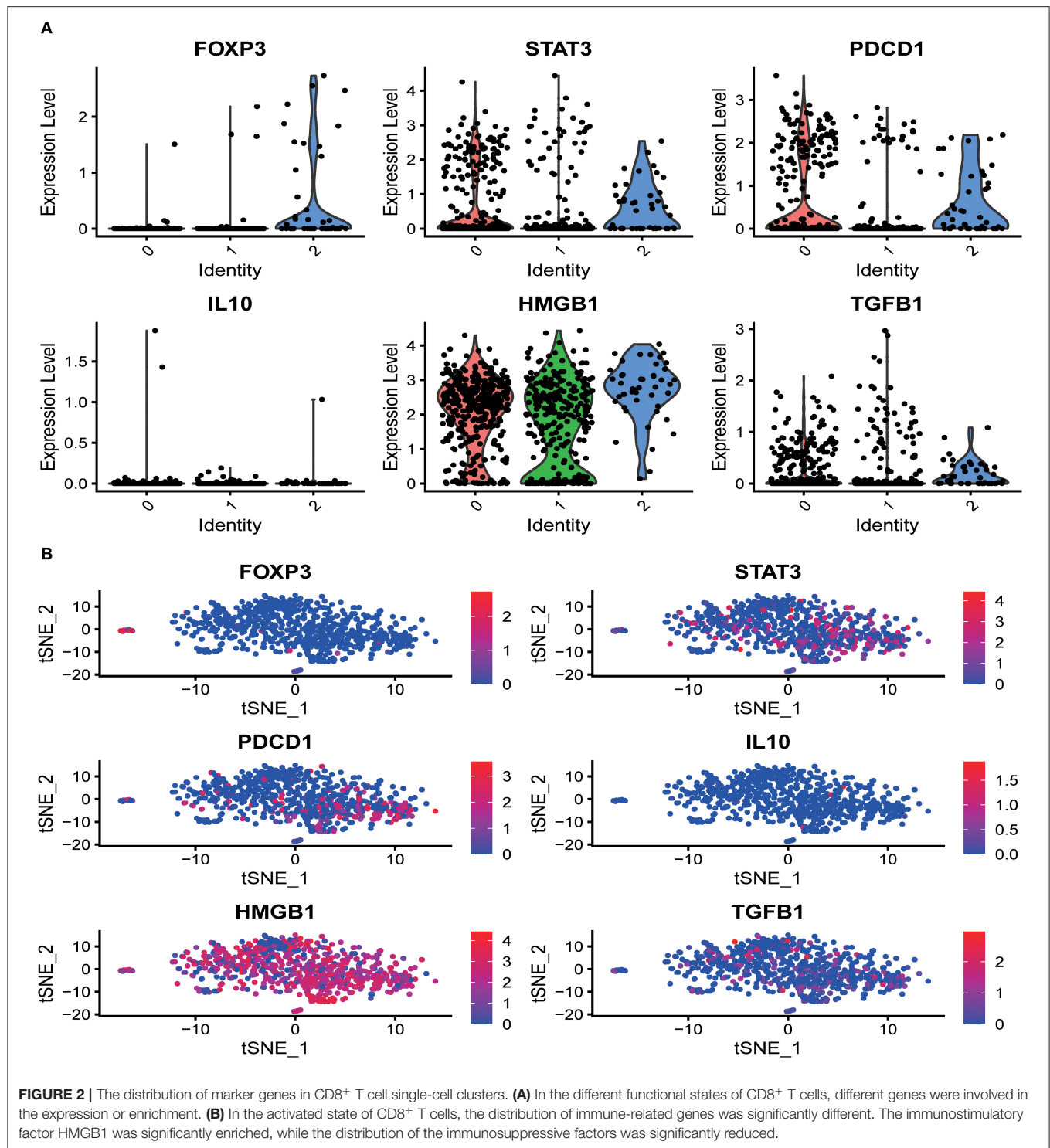
Low-Dose Irradiation Is More Likely to Cause the Enrichment of Immunosuppressive Factors

DAMPs or TAAs released by dying tumor cells caused by radiation include not only immune enhancing elements such as calreticulin and HMGB1 but also immunosuppressive factors such as IL-10 and TGF- β . In this study, we focused on analyzing the changing trends of IL-10 and TGF- β caused by X-rays and Carbon ions radiation. For X-rays, compared with the non-irradiated group, the physical dose at which the IL-10 exposure level reaches the peak was 4 Gy. As the dose increases, the

exposure gradually decreased. The above trend also existed in the changes in TGF- β exposure levels. However, the peak exposure of IL-10 and TGF- β in the Carbon ions radiation group was a physical dose of 2 Gy. Interestingly, this trend was consistent with the RBE value of Carbon ions radiation (Figure 5, Table 3).

DISCUSSION

Nowadays, more and more studies on radiotherapy causing abscopal effects and participating in anti-tumor immune response indicate that inducing immunogenic changes has become one of the essential mechanisms for radiotherapy to exert immune synergy (34). Based on this, a variety of approaches to enhance the immunogenicity of apoptotic cells have been developed (7, 35). Conventional X-rays-induced immunogenicity changes in tumor cells have been reported. However, due to the limitations of radiotherapy resistance, the



immune synergy of radiotherapy needs to be further improved (36). Heavy ions have become definitive radiation therapy due to their superior radiobiological effects (23, 37). However, the advantages and specific mechanisms of the immunogenic changes induced by heavy ions in dying tumor cells are still unclear.

Tumor immunotherapy is an anti-tumor immune response driven by T cells (38). Since the induction of cytotoxic T cells depends on the activation and maturation of DC (39), the research on ICD mainly focuses on the DC-T cell axis and the primary markers for detecting ICD (14, 19). In this study, based on the PCA of scRNA-seq data of lung cancer CD8⁺ T cell

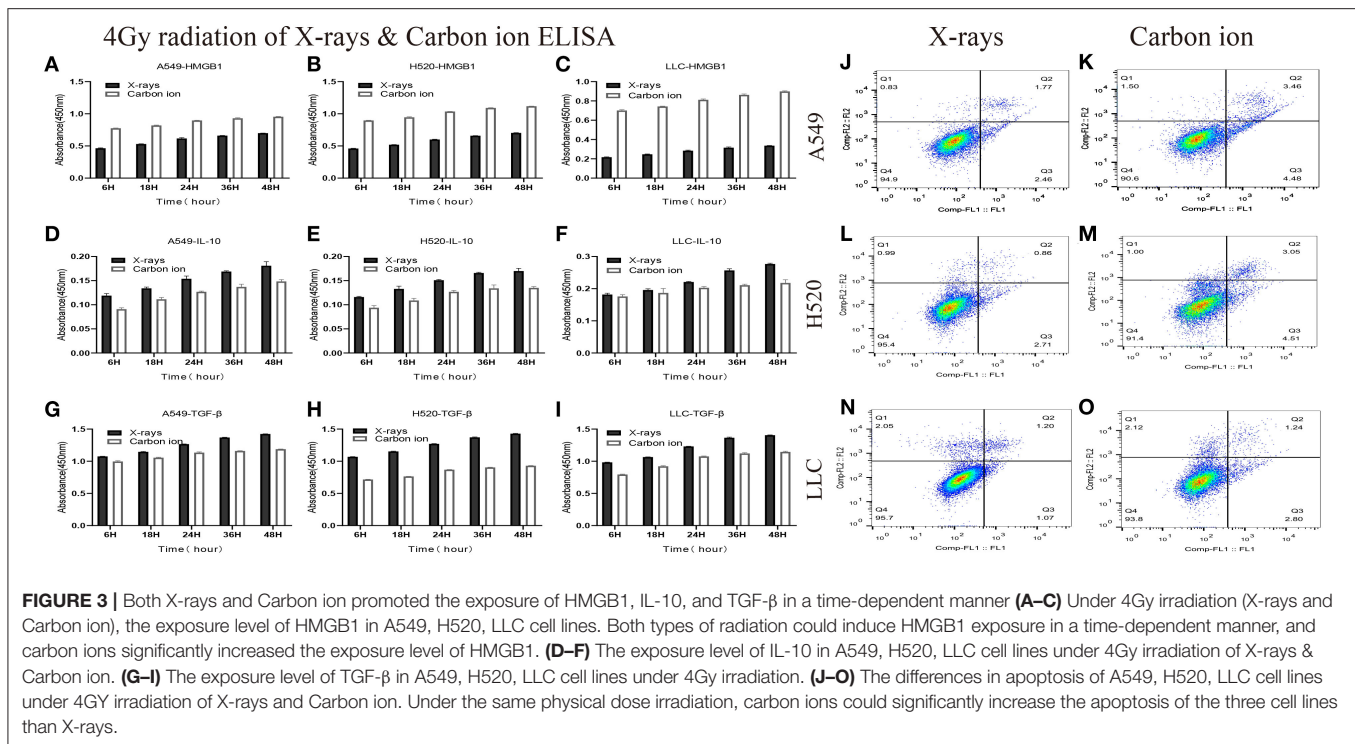


TABLE 1 | Time-dependent expression analysis of HMGB1, IL-10 and TGF-β under 4 Gy physical dose radiation (Carbon ions and X-rays) (ng/ml).

Cells	DAMPs	6h	18h	24h	36h	48h	F _{time}	P _{time}
A549	HMGB1 ^a	4.093 ± 0.077	4.836 ± 0.032	5.838 ± 0.153	6.372 ± 0.035	6.846 ± 0.018	399.403	<0.001
	HMGB1 ^b	7.730 ± 0.037 [▼]	8.299 ± 0.076 [▼]	9.375 ± 0.040 [▼]	9.863 ± 0.103 [▼]	10.199 ± 0.063 [▼]	472.807	<0.001
H520	HMGB1 ^a	4.06 ± 0.031	4.7 ± 0.032	5.647 ± 0.034	6.348 ± 0.017	6.897 ± 0.054	2157.176	<0.001
	HMGB1 ^b	9.375 ± 0.04 [▼]	10.082 ± 0.104 [▼]	11.445 ± 0.022 [▼]	12.338 ± 0.069 [▼]	12.766 ± 0.024 [▼]	1153.562	<0.001
LLC	HMGB1 ^a	19.43 ± 0.39	22.75 ± 0.41	27.07 ± 0.60	30.56 ± 0.91	33.04 ± 0.35	379.061	<0.001
	HMGB1 ^b	78.789 ± 1.120 [▼]	84.575 ± 0.506 [▼]	94.233 ± 1.187 [▼]	101.484 ± 1.265 [▼]	106.657 ± 0.858 [▼]	557.110	<0.001
A549	IL-10 ^a (pg/ml)	0.84 ± 0.045	0.992 ± 0.028	1.182 ± 0.052	1.317 ± 0.012	1.421 ± 0.073	51.193	<0.001
	IL-10 ^b (pg/ml)	0.490 ± 0.033 [*]	0.715 ± 0.036 [*]	0.868 ± 0.014 [*]	0.962 ± 0.052 [*]	1.224 ± 0.254	10.790	0.011
H520	IL-10 ^a (pg/ml)	0.808 ± 0.015	0.982 ± 0.056	1.154 ± 0.013	1.29 ± 0.013	1.325 ± 0.05	76.558	<0.001
	IL-10 ^b (pg/ml)	0.525 ± 0.049 [*]	0.689 ± 0.044 [*]	0.868 ± 0.027 [▼]	0.934 ± 0.066 [*]	0.944 ± 0.026 [*]	32.368	0.001
LLC	IL-10 ^a (pg/ml)	48.689 ± 1.397	53.736 ± 1.297	62.972 ± 0.612	76.737 ± 1.935	84.595 ± 0.971	527.955	<0.001
	IL-10 ^b (pg/ml)	47.170 ± 1.859	51.085 ± 4.925	56.809 ± 1.326 [▼]	59.729 ± 1.08 [▼]	62.32 ± 3.594 [▼]	17.788	<0.001
A549	TGF-β ^a	0.583 ± 0.002	0.635 ± 0.004	0.728 ± 0.002	0.812 ± 0.004	0.860 ± 0.001	3258.027	<0.001
	TGF-β ^b	0.512 ± 0.008 [▼]	0.553 ± 0.005 [▼]	0.609 ± 0.008 [▼]	0.628 ± 0.003 [▼]	0.649 ± 0.002 [▼]	190.477	<0.001
H520	TGF-β ^a	0.578 ± 0.002	0.640 ± 0.004	0.731 ± 0.002	0.815 ± 0.005	0.864 ± 0.004	1874.740	<0.001
	TGF-β ^b	0.338 ± 0.003 [▼]	0.363 ± 0.001 [▼]	0.428 ± 0.002 [▼]	0.450 ± 0.003 [▼]	0.471 ± 0.002 [▼]	1550.763	<0.001
LLC	TGF-β ^a	0.836 ± 0.004	0.924 ± 0.003	1.110 ± 0.002	1.270 ± 0.013	1.321 ± 0.005	4117.563	<0.001
	TGF-β ^b	0.686 ± 0.007 [▼]	0.821 ± 0.009 [▼]	0.993 ± 0.008 [▼]	1.048 ± 0.012 [▼]	1.077 ± 0.011 [▼]	1134.538	<0.001

^aX-rays, ^bCarbon ion, **p* < 0.05, [▼]*p* < 0.01, [▼]*p* < 0.001 (Represents the comparison between Carbon ion and the X-rays radiation group at the same physical dose and time point).

clusters, the DEGs involved in different immune response stages were analyzed, and the main marker genes were screened out. In this study, we evaluated and compared the exposure levels of the relevant antigens of the three lung cancer cell lines under conventional X-rays and carbon ions radiation, which provided a reference for future heavy ion-induced immunogenicity changes and immune regulation.

HMGB1 plays a vital role in ICD and inducing an anti-tumor immune response (40). HMGB1 binds to TLR-4 and receptors to form advanced glycosylation end products, which promote the production of cytokines, cross-presentation of related antigens, and the maturation and activation of DC cells, thereby activating helper T cells and effector T cells (41, 42). Based on the scRNA-seq data of CD8⁺T cell clusters, we found that the accumulation

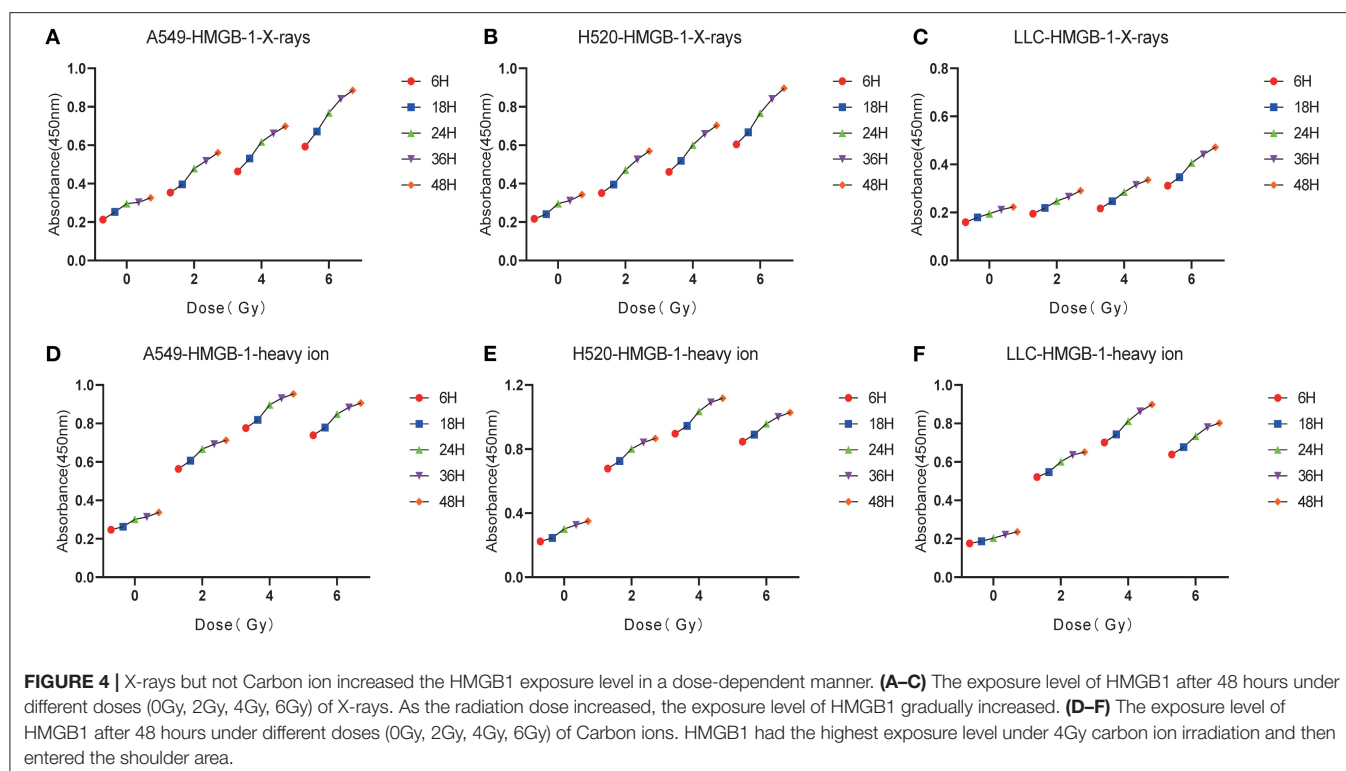


TABLE 2 | Dose-dependent expression analysis of HMGB1 after 48 h of carbon ions and X-rays radiation (ng/ml).

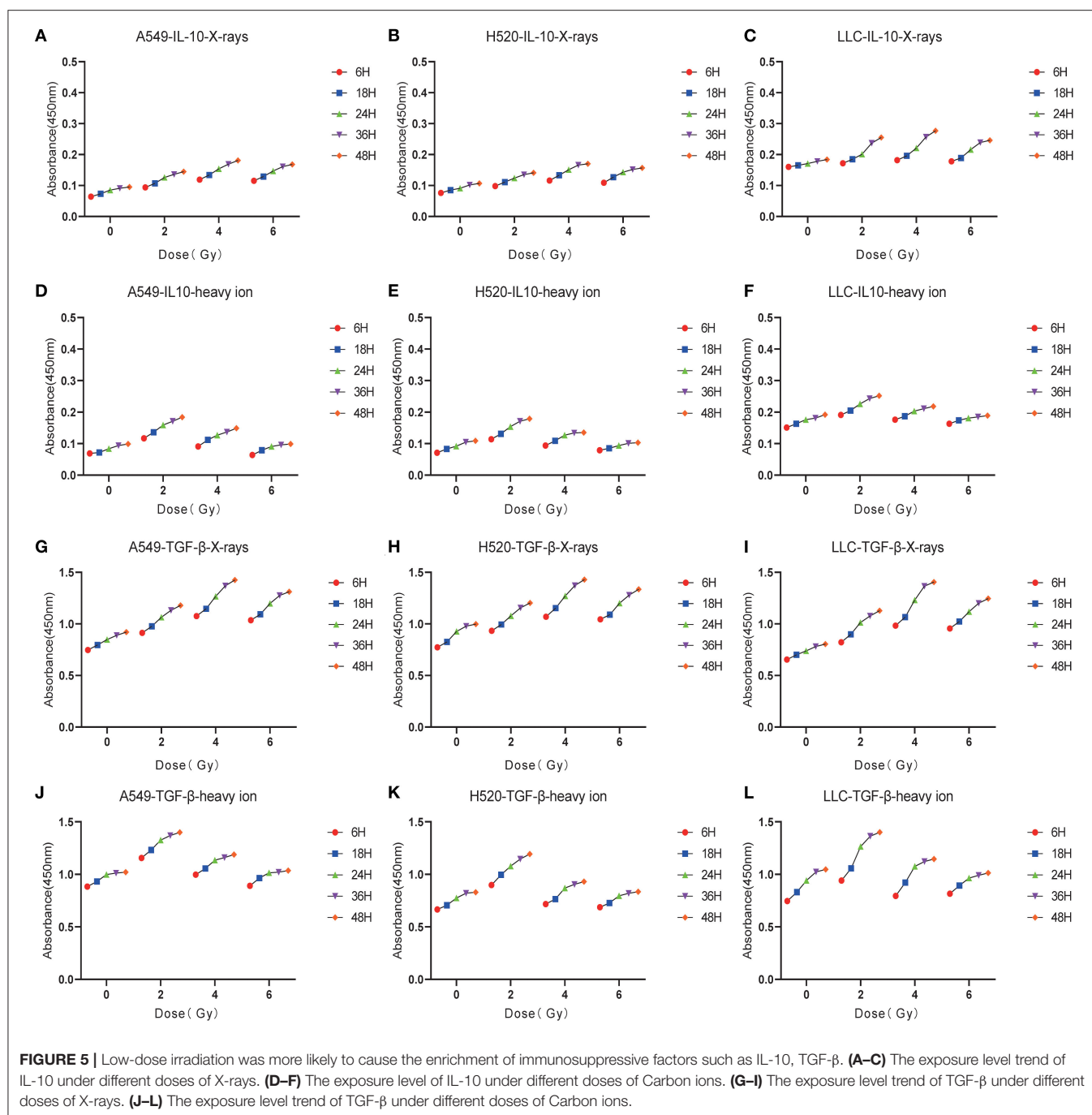
Cells	Radiation	0 Gy	2 Gy	4 Gy	6 Gy	F_{dose}	P_{dose}
A549	X-rays	2.664 ± 0.014	5.173 ± 0.089	6.846 ± 0.018	9.338 ± 0.120	2732.034	<0.001
	C-ion	2.764 ± 0.055	6.925 ± 0.071 [▽]	10.201 ± 0.062 [▼]	9.503 ± 0.020	7326.635	<0.001
H520	X-rays	2.832 ± 0.028	5.283 ± 0.016	6.897 ± 0.054	9.494 ± 0.002	14377.758	<0.001
	C-ion	2.901 ± 0.014	8.954 ± 0.039 [▼]	12.765 ± 0.023 [▼]	11.336 ± 0.063 [▼]	22818.361	<0.001
LLC	X-rays	20.08 ± 0.40	27.76 ± 0.21	33.04 ± 0.35	49.77 ± 0.64	3442.307	<0.001
	C-ion	20.69 ± 0.46	71.99 ± 0.63 [▼]	106.66 ± 0.86 [▼]	92.82 ± 0.36 [▼]	15343.844	<0.001

[▽] $p < 0.01$, [▼] $p < 0.001$ (Represents the comparison between Carbon ion and the X-rays radiation group at the same physical dose and time point).

of HMGB1 was particularly significant in the immune effector clusters of CD8⁺T cells. In contrast, the accumulation of TGF- β , IL-10, FOXP3, and STAT3 were mainly concentrated in the immunosuppressive state (43). During tumorigenesis and progression, the uptake of apoptotic cells by surrounding macrophages is accompanied by the release of anti-inflammatory signals such as TGF- β (44). Therefore, apoptosis can promote tumor tolerance (45). To a certain extent, the exposure of these immunosuppressive factors also provides a basis for explaining radiotherapy resistance or tolerance (46). As we know, the form of cell death caused by carbon ions is different from X-rays, and its higher LET and unique brag peak have become one of the advantages of replacing traditional X-rays (47). Research by Onishi et al. showed that the exposure level of HMGB1 increased with the linear energy transfer (LET) value (48). Yutaka Takahashi et al. found that the exposure level of HMGB-1 in the cell culture supernatant collected 48 h after carbon ions irradiation increased by more than three times compared with

untreated cells (5). Also, the effect of carbon ion radiation on ICD can spread to the peripheral blood (49). Although previous studies have shown that X-ray irradiation and chemotherapy can induce ICD (50), there are few studies on the exposure differences and trends of related antigens that play different roles in the tumor immune response stage under different irradiations.

Similar to the increase in other DAMPs, such as calreticulin after irradiation, the exposure of HMGB1 showed a time and dose-dependent relationship to a certain extent. Under the same physical dose of X-ray and carbon ion irradiation, the exposure level of HMGB1 showed a time-dependent trend, which was different in X-rays and carbon ions. Specifically, the exposure level of HMGB1 induced by carbon ions was higher than that of X-rays, especially in mouse Lewis cells. Interestingly, the exposure level of HMGB1 increased insignificantly within 18 h after irradiation but increased significantly within 24–36 h, and the shoulder area appeared within 48 h. Similar to our research, Yangle Huang et al. found that the three types of



irradiation of photons, protons, and carbon ions also increased the exposure of surface-exposed calreticulin (ecto-CRT) in a time-dependent manner (51). At 48 h after irradiation, ecto-CRT exposure increased significantly but only slightly increased in various tumor cell lines at 12 h after irradiation.

At the same time, after irradiation, the exposure level of HMGB1 induced by X-rays but not carbon ions irradiation was dose-dependent. Under the 6 Gy physical dose of carbon ions irradiation, the exposure level of HMGB1 tended to be flat or even lower, which was similar to the research conclusions of Yangle Huang et al. Cell death caused by apoptosis may be highly

immunogenic. In contrast, the immunogenicity of necrotic cells may be lower than that of cells undergoing immune apoptosis (41, 52). Based on this, we speculate that carbon ions irradiation with 6 Gy physical dose may cause some other types of death pattern, and the specific mechanism that needs to be further studied. Also, studies (24) have shown that even in normal cells, radiation with a dose between 4 and 12 Gy can induce cytoplasmic HMGB1 translocation and stimulate the time and dose-dependent release of HMGB1 *in vivo* and *in vitro*. In the dose range of 4 to 8 Gy, the release of HMGB1 was induced as early as 6 h after stimulation.

TABLE 3 | Dose-dependent expression analysis of IL-10&TGF- β after 48 h of carbon ions and X-rays radiation (ng/ml).

Cells	DAMPs	0Gy	2Gy	4Gy	6Gy	F_{dose}	P_{dose}
A549	IL-10 ^a (pg/ml)	0.568 \pm 0.035	1.098 \pm 0.013	1.421 \pm 0.073	1.308 \pm 0.013	166.986	<0.001
	IL-10 ^b (pg/ml)	0.582 \pm 0.031	1.370 \pm 0.047*	1.067 \pm 0.032*	0.581 \pm 0.063 ∇	19.547	0.007
H520	IL-10 ^a (pg/ml)	0.709 \pm 0.032	1.060 \pm 0.027	1.325 \pm 0.05	1.209 \pm 0.026	117.103	<0.001
	IL-10 ^b (pg/ml)	0.689 \pm 0.029	1.329 \pm 0.024 ∇	0.944 \pm 0.026*	0.625 \pm 0.031 ∇	268.125	<0.001
LLC	IL-10 ^a (pg/ml)	49.402 \pm 0.773	75.958 \pm 1.383	84.595 \pm 0.971	72.477 \pm 1.75	554.724	<0.001
	IL-10 ^b (pg/ml)	48.928 \pm 1.553	75.108 \pm 2.387	62.32 \pm 3.594 \blacktriangledown	51.768 \pm 1.268 \blacktriangledown	88.973	<0.001
A549	TGF- β^a	0.476 \pm 0.003	0.659 \pm 0.003	0.86 \pm 0.001	0.765 \pm 0.002	6896.873	<0.001
	TGF- β^b	0.474 \pm 0.004	0.818 \pm 0.003 \blacktriangledown	0.649 \pm 0.002 \blacktriangledown	0.537 \pm 0.001 \blacktriangledown	7207.095	<0.001
H520	TGF- β^a	0.528 \pm 0.001	0.678 \pm 0.002	0.864 \pm 0.005	0.784 \pm 0.005	3219.170	<0.001
	TGF- β^b	0.532 \pm 0.001	0.653 \pm 0.006*	0.468 \pm 0.002 \blacktriangledown	0.406 \pm 0.001 \blacktriangledown	1908.329	<0.001
LLC	TGF- β^a	0.655 \pm 0.002	0.993 \pm 0.002	1.321 \pm 0.005	1.126 \pm 0.007	14028.502	<0.001
	TGF- β^b	0.652 \pm 0.002	1.401 \pm 0.007 \blacktriangledown	1.077 \pm 0.011 \blacktriangledown	0.922 \pm 0.008 \blacktriangledown	6552.511	<0.001

^aX-Rays, ^bCarbonion, * $p < 0.05$, $\nabla p < 0.01$, $\blacktriangledown p < 0.001$ (Represents the comparison between Carbon ion and the X-rays radiation group at the same physical dose and time point).

Radiation induces ICD of tumor cells to activate M2 macrophages and then secrete various cytokines, including TGF- β and IL-10 (29, 53). TGF- β is a potent immunosuppressive factor in TME, which can damage the function of DCs and inhibit the activation of T cells and promote the transformation of naive CD4⁺T cells into Treg cells (54). TGF- β is usually secreted in the form of inactivation in the extracellular matrix and is released from the latency-related peptide (LAP) by external stimuli such as radiation. Besides, the production of reactive oxygen species (ROS) after radiation can also promote the release of TGF- β , thus increasing the immunosuppressive effect (25). Similarly, IL-10, an important immunosuppressive factor, induces an immunosuppressive pathway by promoting S100A9 nuclear localization and MDSC maturation (55). Consistent with HMGB1, the exposure levels of IL-10 and TGF- β under X-rays and carbon ions irradiation were also time-dependent. Interestingly, the exposure levels of IL-10 and TGF- β induced by different physical doses of X-rays and carbon ions showed different trends. Under 4 Gy X-rays irradiation, the exposure level of IL-10 and TGF- β reached a peak and then entered a plateau or decline phase. However, this trend appeared under 2 Gy carbon ions irradiation. Studies have shown that low-dose radiation may increase the expression of immunosuppressive factors or immune checkpoint molecules. Besides, low-dose radiation may also activate immune suppression and angiogenesis (46) and promote M2 macrophages to inhibit the anti-tumor response and promote metastasis by producing arginase and cytokines TGF- β and IL-10 (56). Therefore, the above data also provided a reference for immune tolerance induced by low-dose irradiation. This study also found that carbon ions above 4 Gy could significantly reduce the exposure level of immunosuppressive factors IL-10 and TGF- β . Interestingly, at this dose, carbon ions radiation-induced the peak exposure level of HMGB1, which suggested that 4 Gy radiation of carbon ions may reach an ideal balance point in promoting immune effects and reducing immune tolerance since this study was only carried out on lung cancer cell lines *in vitro*, which needs to be further verified by animal-related experiments and clinical experiments.

In summary, by comparing the exposure levels of X-rays and carbon ions radiation to DAMPs or TAAs involved in the immune response, we found that both X-rays and carbon ions can change the immunogenicity of lung cancer cells in a time-dependent manner. Based on further analysis of the “time window” and “dose window” of carbon ions radiation, it was found that carbon ions may be more advantageous than traditional X-rays in terms of inducing immunogenic changes. Based on this finding, further exploration of two kinds of radiation-induced immunogenicity and TME changes in mouse tumor-bearing models will be our next task.

DATA AVAILABILITY STATEMENT

The original contributions presented in the study are included in the article/supplementary material, further inquiries can be directed to the corresponding author/s.

AUTHOR CONTRIBUTIONS

JR: conceptualization, methodology, software, formal analysis, validation, data curation, writing—original draft, writing—review and editing, visualization. JW: methodology, software, formal analysis, writing—original draft. YM and CZ: methodology, validation, formal analysis, investigation. ZD and JG: data curation, investigation. QG: conceptualization, writing—review and editing, supervision, project administration. All authors: contributed to the article and approved the submitted version.

FUNDING

This study was supported by grants from the Key R&D Program of Gansu Provincial Department of Science and Technology (20YF3FA028), Gansu Health Industry Scientific Research Project (GSWSKY-2019-79), In-hospital Funded Project of Lanzhou University First Hospital (ldyyyn2018-21), The Science and Technology Project of Chengguan District, Lanzhou City (2020JSCX0044).

REFERENCES

- Uzel EK, Figen M, Uzel Ö. Radiotherapy in lung cancer: current and future role. *Sisli Etfal Hastanesi Tip Bulteni*. (2019) 53:353–60. doi: 10.14744/SEMB.2019.25991
- Steven A, Fisher SA, Robinson BW. Immunotherapy for lung cancer. *Respirology*. (2016) 21:821–33. doi: 10.1111/resp12789
- Corrales L, Scilla K, Caglevic C, Miller K, Oliveira J, Rolfo C. Immunotherapy in lung cancer: a new age in cancer treatment. *Adv Exp Med Biol*. (2018) 995:65–95. doi: 10.1007/978-3-030-02505-2_3
- Falcke SE, Rühle PF, Deloch L, Fietkau R, Frey B, Gaipf US. Clinically relevant radiation exposure differentially impacts forms of cell death in human cells of the innate and adaptive immune system. *Int J Mol Sci*. (2018) 19:3574. doi: 10.3390/ijms19113574
- Takahashi Y, Yasui T, Minami K, Tamari K, Hayashi K, Otani K, et al. Carbon ion irradiation enhances the antitumor efficacy of dual immune checkpoint blockade therapy both for local and distant sites in murine osteosarcoma. *Oncotarget*. (2019) 10:633–46. doi: 10.18632/oncotarget26551
- Wennerberg E, Lhuillier C, Vanpouille-Box C, Pilonis KA, Garcia-Martinez E, Rudqvist NP, et al. Barriers to radiation-induced *in situ* tumor vaccination. *Front Immunol*. (2017) 8:229. doi: 10.3389/fimmu.201700229
- Rückert M, Deloch L, Fietkau R, Frey B, Hecht M, Gaipf US. Immune modulatory effects of radiotherapy as basis for well-reasoned radioimmunotherapies. *Strahlentherapie Onkol*. (2018) 194:509–19. doi: 10.1007/s00066-018-1287-1
- Mohamad O, Sishc BJ, Saha J, Pompos A, Rahimi A, Story MD, et al. Carbon ion radiotherapy: a review of clinical experiences and preclinical research, with an emphasis on DNA damage/repair. *Cancers*. (2017) 9. doi: 10.3390/cancers9060066
- Carvalho HA, Villar RC. Radiotherapy and immune response: the systemic effects of a local treatment. *Clinics*. (2018) 73(Suppl. 1):e557s. doi: 10.6061/clinics/2018/e557s
- Zhang W, Tanaka M, Sugimoto Y, Takigawa T, Ozaki T. Carbon-ion radiotherapy of spinal osteosarcoma with long-term follow. *Eur Spine J*. (2016) 25(Suppl. 1):113–7. doi: 10.1007/s00586-015-4202-9
- Pitt JM, Kroemer G, Zitvogel L. Immunogenic and non-immunogenic cell death in the tumor microenvironment. *Adv Exp Med Biol*. (2017) 1036:65–79. doi: 10.1007/978-3-319-67577-0_5
- Krysko O, Løve Aaes T, Bachert C, Vandenabeele P, Krysko DV. Many faces of DAMPs in cancer therapy. *Cell Death Disease*. (2013) 4:e631. doi: 10.1038/cddis.2013156
- Garg AD, Martin S, Golab J, Agostinis P. Danger signalling during cancer cell death: origins, plasticity and regulation. *Cell Death Differentiation*. (2014) 21:26–38. doi: 10.1038/cdd.201348
- Kepp O, Senovilla L, Vitale I, Vacchelli E, Adjemian S, Agostinis P, et al. Consensus guidelines for the detection of immunogenic cell death. *Oncoimmunology*. (2014) 3:e955691. doi: 10.4161/21624011.2014.955691
- Jiang Q, Zhang C, Wang H, Peng T, Zhang L, Wang Y, et al. Mitochondria-targeting immunogenic cell death inducer improves the adoptive T-cell therapy against solid tumor. *Front Oncol*. (2019) 9:1196. doi: 10.3389/fonc.201901196
- Aurelian L. Oncolytic viruses as immunotherapy: progress and remaining challenges. *Onco Targets Ther*. (2016) 9:2627–37. doi: 10.2147/OTTS63049
- Vanmeerbeek I, Sprooten J, De Ruyscher D, Tejpar S, Vandenberghhe P, Fucikova J, et al. Trial watch: chemotherapy-induced immunogenic cell death in immuno-oncology. *Oncoimmunology*. (2020) 9:1703449. doi: 10.1080/2162402X.20191703449
- Twyman-Saint Victor C, Rech AJ, Maity A, Rengan R, Pauken KE, Stelekati E, et al. Radiation and dual checkpoint blockade activate non-redundant immune mechanisms in cancer. *Nature*. (2015) 520:373–7. doi: 10.1038/nature14292
- van Vloten JB, Workenhe ST, Wootton SK, Mossman KL, Bridle BW. Critical interactions between immunogenic cancer cell death, oncolytic viruses, and the immune system define the rational design of combination immunotherapies. *J Immunol*. (2018) 200:450–8. doi: 10.4049/jimmunol1701021
- Knudson KM, Hicks KC, Ozawa Y, Schlom J, Gameiro SR. Functional and mechanistic advantage of the use of a bifunctional anti-PD-L1/IL-15 superagonist. *J Immunotherapy Cancer*. (2020) 8:e000493. doi: 10.1136/jitc-2019-000493
- Wirsdörfer F, de Leve S, Jendrosseck V. Combining radiotherapy and immunotherapy in lung cancer: can we expect limitations due to altered normal tissue toxicity? *Int J Mol Sci*. (2018) 20:24. doi: 10.3390/ijms20010024
- Agrawal V, Benjamin KT, Ko EC. Radiotherapy and immunotherapy combinations for lung cancer. *Curr Oncol Rep*. (2020) 23:4. doi: 10.1007/s11912-020-00993-w
- Kumari S, Mukherjee S, Sinha D, Abdilsalam S, Krishnan S, Asaithamby A. Immunomodulatory effects of radiotherapy. *Int J Mol Sci*. (2020) 21:8151. doi: 10.3390/ijms21218151
- Wang L, He L, Bao G, He X, Fan S, Wang H. Ionizing radiation induces HMGB1 cytoplasmic translocation and extracellular release. *Guo Ji Fang She Yi Xue He Yi Xue Za Zhi*. (2016) 40:91–9.
- Farhood B, Khodamoradi E, Hoseini-Ghahfarokhi M, Motevaseli E, Mirtavos-Mahyari H, Elejo Musa A, et al. TGF- β in radiotherapy: mechanisms of tumor resistance and normal tissues injury. *Pharmacol Res*. (2020) 155:104745. doi: 10.1016/j.phrs.2020104745
- Kim JY, Kim YS, Kim YK, Park HJ, Kim SJ, Kang JH, et al. The TGF- β dynamics during radiation therapy and its correlation to symptomatic radiation pneumonitis in lung cancer patients. *Radiation Oncol*. (2009) 4:59. doi: 10.1186/1748-717X-4-59
- Solari JIG, Filippi-Chiela E, Pilar ES, Nunes V, Gonzalez EA, Figueiró F, et al. Damage-associated molecular patterns (DAMPs) related to immunogenic cell death are differentially triggered by clinically relevant chemotherapeutics in lung adenocarcinoma cells. *BMC Cancer*. (2020) 20:474. doi: 10.1186/s12885-020-06964-5
- Muppala S, Xiao R, Gajeton J, Krukavets I, Verbovetskiy D, Stenina-Adognrvi O. Thrombospondin-4 mediates hyperglycemia- and TGF- β -induced inflammation in breast cancer. *Int J Cancer*. (2021) 148:2010–22. doi: 10.1002/ijc33439
- Yang L, Dong Y, Li Y, Wang D, Liu S, Wang D, et al. IL-10 derived from M2 macrophage promotes cancer stemness via JAK1/STAT1/NF- κ B/Notch1 pathway in non-small cell lung cancer. *Int J Cancer*. (2019) 145:1099–110. doi: 10.1002/ijc32151
- Clarke J, Panwar B, Madrigal A, Singh D, Gujar R, Wood O, et al. Single-cell transcriptomic analysis of tissue-resident memory T cells in human lung cancer. *J Exp Med*. (2019) 216:2128–49. doi: 10.1084/jem20190249
- Guo Q, Ke XX, Liu Z, Gao WL, Fang SX, Chen C, et al. Evaluation of the prognostic value of STEAP1 in lung adenocarcinoma and insights into its potential molecular pathways via bioinformatic analysis. *Front Genetics*. (2020) 11:242. doi: 10.3389/fgene.202000242
- Tu H, Wu M, Huang W, Wang L. Screening of potential biomarkers and their predictive value in early stage non-small cell lung cancer: a bioinformatics analysis. *Transl Lung Cancer Res*. (2019) 8:797–807. doi: 10.21037/tlcr.2019.1013
- Lu Q, Aon JC. Co-expression for intracellular processing in microbial protein production. *Biotechnol Letters*. (2014) 36:427–41. doi: 10.1007/s10529-013-1379-z
- Kordbacheh T, Honeychurch J, Blackhall F, Faivre-Finn C, Illidge T. Radiotherapy and anti-PD-1/PD-L1 combinations in lung cancer: building better translational research platforms. *Annals Oncol*. (2018) 29:301–10. doi: 10.1093/annonc/mdx790
- Vanpouille-Box C, Alard A, Aryankalayil MJ, Sarfraz Y, Diamond JM, Schneider RJ, et al. DNA exonuclease Trex1 regulates radiotherapy-induced tumour immunogenicity. *Nat Commun*. (2017) 8:15618. doi: 10.1038/ncomms15618
- Aliru ML, Schoenhals JE, Venkatesulu BP, Anderson CC, Barsoumian HB, Younes AI, et al. Radiation therapy and immunotherapy: what is the optimal timing or sequencing? *Immunotherapy*. (2018) 10:299–316. doi: 10.2217/imt-2017-0082
- Spina CS, Tsuruoka C, Mao W, Sunaoshi MM, Chaimowitz M, Shang Y, et al. Differential immune modulation with carbon-ion versus photon therapy. *J Radiat Oncol Biol Phys*. (2021) 109:813–8. doi: 10.1016/j.jrobp.2020.09.053

38. Huang H, Sikora MJ, Islam S, Chowdhury RR, Chien YH, Scriba TJ, et al. Select sequencing of clonally expanded CD8(+) T cells reveals limits to clonal expansion. *Proc Natl Acad Sci USA*. (2019) 116:8995–9001. doi: 10.1073/pnas.1902649116
39. Sprooten J, Ceusters J, Coosemans A, Agostinis P, De Vleeschouwer S, Zitvogel L, et al. Trial watch: dendritic cell vaccination for cancer immunotherapy. *Oncoimmunology*. (2019) 8:e1638212. doi: 10.1080/2162402X.20191638212
40. Ahmed A, Tait SWG. Targeting immunogenic cell death in cancer. *Mol Oncol*. (2020) 14:2994–3006. doi: 10.1002/1878-026112851
41. Green DR, Ferguson T, Zitvogel L, Kroemer G. Immunogenic and tolerogenic cell death. *Nat Reviews Immunol*. (2009) 9:353–63. doi: 10.1038/nri2545
42. Demaria S, Golden EB, Formenti SC. Role of local radiation therapy in cancer immunotherapy. *JAMA Oncol*. (2015) 1:1325–32. doi: 10.1001/jamaoncol.2015.2756
43. Thepmalee C, Panya A, Junking M, Chieochansin T, Yenchitsomanus PT. Inhibition of IL-10 and TGF-beta receptors on dendritic cells enhances activation of effector T-cells to kill cholangiocarcinoma cells. *Hum Vaccin Immunother*. (2018) 14:1423–31. doi: 10.1080/21645515.2018.1431598
44. Willems JJ, Arnold BP, Gregory CD. Sinister self-sacrifice: the contribution of apoptosis to malignancy. *Front Immunol*. (2014) 5:299. doi: 10.3389/fimmu.201400299
45. Maueröder C, Chaurio RA, Platzer S, Muñoz LE, Berens C. Model systems for rapid and slow induction of apoptosis obtained by inducible expression of pro-apoptotic proteins. *Autoimmunity*. (2013) 46:329–35. doi: 10.3109/08916934.2012752463
46. Jarosz-Biej M, Smolarczyk R, Cichoń T, Kułach N. Tumor microenvironment as a “game changer” in cancer radiotherapy. *Int J Mol Sci*. (2019) 20:3212. doi: 10.3390/ijms20133212
47. Chowdhury P, Dey P, Ghosh S, Sarma A, Ghosh U. Reduction of metastatic potential by inhibiting EGFR/Akt/p38/ERK signaling pathway and epithelial-mesenchymal transition after carbon ion exposure is potentiated by PARP-1 inhibition in non-small-cell lung cancer. *BMC Cancer*. (2019) 19:829. doi: 10.1186/s12885-019-6015-4
48. Onishi M, Okonogi N, Oike T, Yoshimoto Y, Sato H, Suzuki Y, et al. High linear energy transfer carbon-ion irradiation increases the release of the immune mediator high mobility group box 1 from human cancer cells. *J Radiat Res*. (2018) 59:541–6. doi: 10.1093/jrr/rry049
49. Ebner DK, Kamada T, Yamada S. Abscopal effect in recurrent colorectal cancer treated with carbon-ion radiation therapy: 2 case reports. *Adv Radiat Oncol*. (2017) 2:333–8. doi: 10.1016/j.adro.2017.06001
50. Fucikova J, Kepp O, Kasikova L, Petroni G, Yamazaki T, Liu P, et al. Detection of immunogenic cell death and its relevance for cancer therapy. *Cell Death Disease*. (2020) 11:1013. doi: 10.1038/s41419-020-03221-2
51. Huang Y, Dong Y, Zhao J, Zhang L, Kong L, Lu JJ. Comparison of the effects of photon, proton and carbon-ion radiation on the ectocalreticulin exposure in various tumor cell lines. *Ann Transl Med*. (2019) 7:542. doi: 10.21037/atm.2019.09128
52. Casares N, Pequignot MO, Tesniere A, Ghiringhelli F, Roux S, Chaput N, et al. Caspase-dependent immunogenicity of doxorubicin-induced tumor cell death. *J Exp Med*. (2005) 202:1691–701. doi: 10.1084/jem.20050915
53. Park HR, Jo SK, Jung U. Ionizing radiation promotes epithelial-to-mesenchymal transition in lung epithelial cells by TGF- β -producing M2 macrophages. *In Vivo*. (2019) 33:1773–84. doi: 10.21873/invivo11668
54. De Martino M, Daviaud C, Vanpouille-Box C. Activin A backs-up TGF- β to promote regulatory T cells. *Oncoimmunology*. (2021) 10:1883288. doi: 10.1080/2162402X.20211883288
55. Bah I, Kumbhare A, Nguyen L, McCall CE, El Gazzar M. IL-10 induces an immune repressor pathway in sepsis by promoting S100A9 nuclear localization and MDSC development. *Cell Immunol*. (2018) 332:32–8. doi: 10.1016/j.cellimm.2018.07003
56. Gandhi S, Chandna S. Radiation-induced inflammatory cascade and its reverberating crosstalks as potential cause of post-radiotherapy second malignancies. *Cancer Metastasis Rev*. (2017) 36:375–93. doi: 10.1007/s10555-017-9669-x

Conflict of Interest: The authors declare that the research was conducted in the absence of any commercial or financial relationships that could be construed as a potential conflict of interest.

Copyright © 2021 Ran, Wang, Dai, Miao, Gan, Zhao and Guan. This is an open-access article distributed under the terms of the Creative Commons Attribution License (CC BY). The use, distribution or reproduction in other forums is permitted, provided the original author(s) and the copyright owner(s) are credited and that the original publication in this journal is cited, in accordance with accepted academic practice. No use, distribution or reproduction is permitted which does not comply with these terms.



Dosimetric Deviations of Bragg-Peak Position Shifts in Uniform Magnetic Fields for Magnetic Resonance Imaging-Guiding Proton Radiotherapy: A Monte Carlo Study

Xiaowa Wang^{1,2,3,4}, Hailun Pan^{1,2}, Qinqin Cheng^{1,2}, Xufei Wang^{1,2*} and Wenzhen Xu⁵

¹ Department of Nuclear Science and Technology, Institute of Modern Physics, Fudan University, Shanghai, China, ² Key Laboratory of Nuclear Physics and Ion-Beam Application (MOE), Fudan University, Shanghai, China, ³ Shanghai Proton and Heavy Ion Center, Shanghai, China, ⁴ Shanghai Engineering Research Center of Proton and Heavy Ion Radiation Therapy, Shanghai, China, ⁵ Shanghai Advanced Research Institute, Chinese Academy of Sciences, Shanghai, China

OPEN ACCESS

Edited by:

Fei Ye,
Institute of Modern Physics
(CAS), China

Reviewed by:

Liang Sun,
Soochow University, China
Wen Chien Hsi,
Baptist Hospital of Miami,
United States

*Correspondence:

Xufei Wang
wangxufei@fudan.edu.cn

Specialty section:

This article was submitted to
Radiation and Health,
a section of the journal
Frontiers in Public Health

Received: 15 December 2020

Accepted: 02 June 2021

Published: 03 August 2021

Citation:

Wang X, Pan H, Cheng Q, Wang X
and Xu W (2021) Dosimetric
Deviations of Bragg-Peak Position
Shifts in Uniform Magnetic Fields for
Magnetic Resonance Imaging-Guiding
Proton Radiotherapy: A Monte Carlo
Study. *Front. Public Health* 9:641915.
doi: 10.3389/fpubh.2021.641915

Objective: To investigate dosimetric deviations in scanning protons for Bragg-peak position shifts, which were caused by proton spiral tracks in an ideal uniform field of magnetic resonance (MRI) imaging-guided proton radiotherapy (MRI-IGPRT).

Methods: The FLUKA Monte-Carlo (MC) code was used to simulate the spiral tracks of protons penetrating water with initial energies of 70–270 MeV under the influence of field strength of 0.0–3.0 Tesla in commercial MRI systems. Two indexes, lateral shift (marked as *WD*) perpendicular to the field and a penetration-depth shift (marked as ΔDD) along the beam path, were employed for the Bragg-peak position of spiral proton track analysis. A comparison was performed between MC and classical analytical model to check the simulation results. The shape of the 2D/3D dose distribution of proton spots at the depth of Bragg-Peak was also investigated. The ratio of Gaussian-fit value between longitudinal and transverse major axes was used to indicate the asymmetric index. The skewness of asymmetry was evaluated at various dose levels by the radius ratio of circumscribed and inscribed circles by fitting a semi-ellipse circle of 2D distribution.

Results: The maximum of *WD* deflection is 2.82 cm while the maximum of shortening ΔDD is 0.44 cm for proton at 270 MeV/u under a magnetic field of 3.0 Tesla. The trend of *WD* and ΔDD from MC simulation was consistent with the analytical model, which means the reverse equation of the analytical model can be applied to determine the proper field strength of the magnet and the initial energy of the proton for the planned dose. The asymmetry of 2D/3D dose distribution under the influence of a magnetic field was increased with higher energy, and the skewness of asymmetry for one proton energy at various dose levels was also increased with a larger radius, i.e., a lower dose level.

Conclusions: The trend of the spiral proton track under a uniform magnetic field was obtained in this study using either MC simulation or the analytical model, which can provide an optimized and planned dose of the proton beam in the clinical application of MRI-IGPRT.

Keywords: proton pencil beam, simulation mode, proton dose changes, magnetic fields intensity, FLUKA simulation

INTRODUCTION

Proton radiotherapy, an advanced form of cancer treatment, can fulfill the aim of radiotherapy to achieve better dose conformity than photons due to the Bragg peak. It results in irradiating the target uniformly with the prescription dose, while sparing the adjacent healthy tissues and critical organs (1) nearby to the target. The treatment modality of proton radiotherapy reduces the integral dose over the body of patients due to a finite penetration of protons. However, proton radiotherapy is more susceptible to uncertainties of the geometrical variations, such as a misalignment of setup, the motion of the target, and also of inter-fractional anatomical changes, due to the limited knowledge of patient anatomy during the initial CT simulation during treatment planning (2, 3). Imaging-guided proton radiotherapy (IGPRT) is implemented to reduce susceptible uncertainties to compensate for any unexpected target changes, thus sparing the healthy tissues (4) with proper safety margins in the treatment planning protocols. Magnetic resonance imaging (MRI) systems provide good contrast of soft tissues between the tumor and organs at risk (OARs) (5–9); it is a prime candidate for IGPRT with several advantages over other imaging modalities. Compared to the computed tomography (CT) imaging, several studies demonstrated the advantages of MRI-based imaging-guided proton radiotherapy (IGRT) (5–13). The MRI-IGPRT using protons can reduce uncertainties in the proton therapy process that result in lower doses to the normal tissues.

However, the spiral track of the proton path from the Lorentz force in a magnetic field of MRI made a dose deviation on the delivered 2D/3D distribution by shifting the Bragg-peak position (14–19), which depends on the gantry angle leading to different incident direction and strength of the magnetic field in MRI. In this study, the characteristics of a tracked spiral proton path and induced 2D/3D dosimetry deviation under an ideal uniform magnetic field were investigated using the FLUKA Monte Carlo (MC) simulation with a built-in magnetic field module (20). The incident energy range was 70–270 MeV/u and perpendicular to the magnetic field of strength of 0.0–3.0 Tesla. The previous study employed an analytical model to evaluate the Bragg-peak position shift in the spiral tracks and performed a comparison with the MC simulation (21). The magnitude of asymmetry of maximum planar dose distributions was also investigated for each energy under the field strength of 3.0 Tesla under different dose levels.

This study was implemented for the clinical application of MRI-IGPRT. Accurate 2D/3D dose distribution of employed energies over different field strengths was generated first, and then the shift of Bragg-peak position in terms of the lateral shift

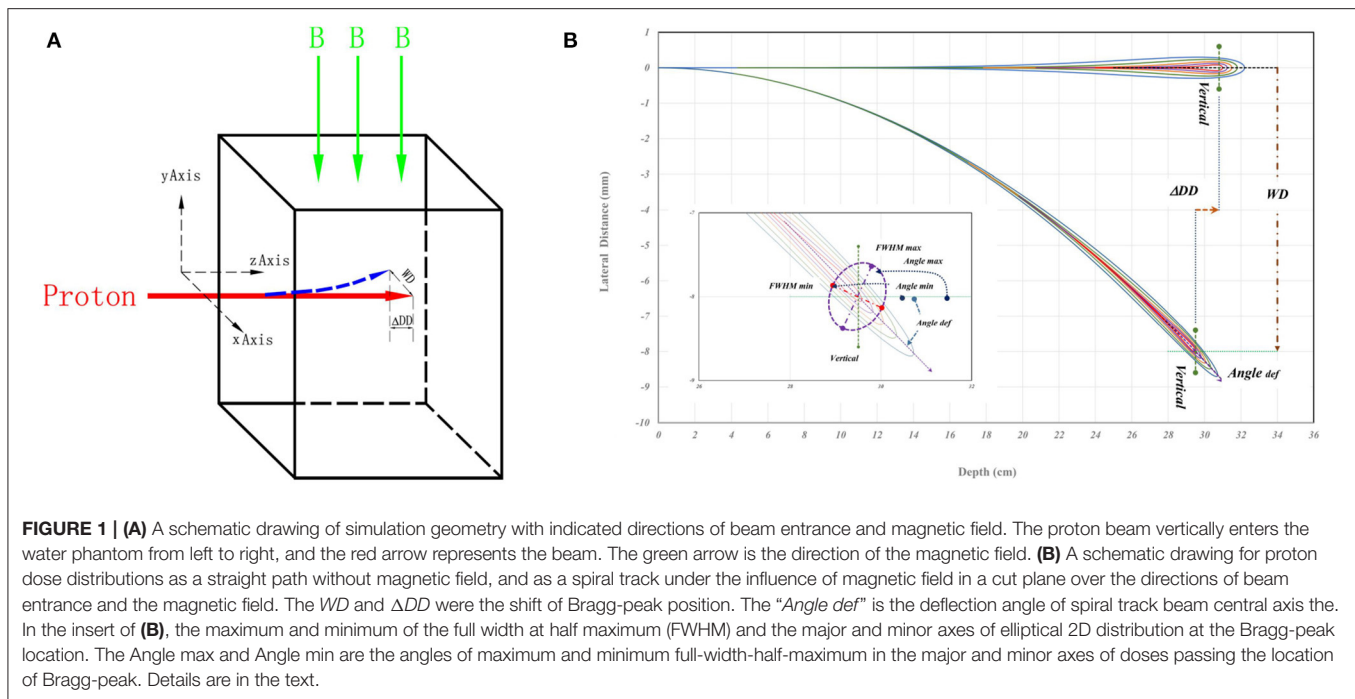
(WD) perpendicular to the field and the penetration-depth shift (ΔDD) along the beam path was evaluated. The values of WD and ΔDD from MC simulation were also compared with that from an analytical model for proton energy over different field strengths. The asymmetric spot shape was investigated by the ratio of Gaussian-fit values between longitudinal and transverse major axes at the planar maximum dose distribution of each proton energy over 3.0 Tesla field strengths. Fitting a semi-ellipse circle of 2D distribution at each dose level, the skewness of asymmetry over various dose levels was also evaluated by the radius ratios of circumscribed and inscribed circles.

MATERIALS AND METHODS

Simulations Used FLUKA Monte-Carlo Code With Shifts of Bragg-Peak Positions

FLUKA (2011.2x) was implemented to simulate the interaction between active pencil-beam-scanning (PBS) proton and the magnetic field (20). Each simulated PBS proton beam entered a water phantom perpendicular to the uniform magnetic field as shown in **Figure 1A**. The red arrow indicates the entering PBS proton, while the green arrow shows the direction of the magnetic field. In **Figure 1B**, a schematic drawing for proton dose distribution, the straight path means without magnetic field and the spiral track means under the influence of a magnetic field in a cut plane over the directions of beam entrance and the magnetic field. The WD and ΔDD were used to evaluate the shift of Bragg-peak position in direction of transverse (i.e., perpendicular) and longitudinal (i.e., along) beam paths for the shifts. The “Angle def” was the deflection of spiral track beam central axis. The insert of **Figure 1B** presents the characteristics for the 3D dose distributions of spiral proton tracks. Details of these parameters will be described later.

In MC simulations, protons were transported in a water phantom with a size of $20 \times 20 \times 35 \text{ cm}^3$ (x, y, and z directions of the phantom geometry, and the distance in z direction is larger than the range of 270 MeV/u incident energy). Parameters of the hadron therapy to a 100 keV limit and cutoff range of transport 0.001458 mm were used in simulation for sufficient accuracy. The water phantom was binned to obtain $0.1 \times 0.02 \times 0.02$ (z, x, and y directions of the phantom geometry) mm^3 voxels. 3D dose distribution was simulated with 1×10^{10} particle histories in each spot with 5 mm sigma of 2D Gaussian lateral distribution at the entrance of the water phantom. The directional divergence of proton space was neglected in simulations because it was minimal in comparison with the lateral scattering spreading in water by the multiple Coulomb scattering (22). The statistical error of each



simulation was $<2\%$ for local maximum value at the depth before the Bragg-peak. The statistical error of the results within 3 mm before and after the Bragg peak was controlled within 0.2%, while that of the low dose beyond 3 mm of Bragg peak was controlled within 4.0%. Simulations were performed with the proton energy of 70, 80, 90, 100, 110, 120, 130, 140, 150, 160, 170, 200, and 270 MeV/u under the magnetic field strength of 0, 0.5, 1.0, 1.5, 2.0, 2.5, and 3 Tesla, which covered the typical parameters used in proton radiotherapy. *WD* and ΔDD of spiral proton tracks were analyzed in each MC simulation.

The Mathematical Formula of an Analytical Model to Calculate *WD* and ΔDD

Following the reference (21), the shift (*WD* or ΔDD) of Bragg-peak position can be calculated by the mathematical formula as shown in Equations (1)–(3). For a proton with kinetic energy E_0 , charge $q = 1$, and rest mass m entering perpendicularly to a magnetic field strength B , the shift of *WD* can be calculated by either Equation (1) or (2), which correspond to non-relativistic and relativistic cases, respectively. For protons with energy of 70, 80, and 90 MeV/u, only Equation (1) was used to calculate the *WD* by considering the energy effect, while both Equations (1) and (2) were used to calculate the *WD* in an interval of 10 MeV for protons with energy 100–170 MeV.

$$WD = \frac{7}{12} \frac{qB\alpha^2}{\sqrt{2m}} E_0^3 \quad (1)$$

$$WD = \frac{7}{12} \frac{qB\alpha^2}{\sqrt{2m}} E_0^3 \left(1 - \frac{3}{8} \left(\frac{E_0}{2mc^2} \right) \right) \quad (2)$$

Where $p \approx 1.75$ and $\alpha \approx 2.43 \times 10^{-3} \text{ MeV}^{-p} \text{ cm}$ in water for the fit parameter of proton stopping power in water.

The shift of ΔDD can be calculated by Equation (3).

$$\Delta DD = \frac{q^2 B^2 \alpha^3 E_0^{3p-1}}{2m} \left(\frac{2p^2}{(4p-1)(3p-1)} \right) \quad (3)$$

The *WD* and ΔDD calculated with the upper equations at certain conditions were compared with corresponding values of MC simulations, and the reverse equations can be used to determine the required energy according to *WD* and ΔDD .

The Asymmetries of 2D/3D Dose Distributions Induced by Magnetic Fields

In addition to the shifts of Bragg-peak position, the 2D spot-shape become asymmetric under the influence of a magnetic field, and the asymmetry especially can be visually seen for the planar dose at the Bragg-peak. To evaluate the skewness of asymmetry of simulated planar 2D distribution, an analysis process using MATLAB (23) platform was used to investigate the referred macroscopic and microscopic aspects in this study. The analysis process includes: (1) Performing a Gaussian fit for obtaining the sigma of 1D distribution in the direction of transverse (x) and longitudinal (y) axes at the plane of the planar dose distributions; (2) Analyzing the ratio of obtained sigma in x/y axes with a field strength of 3.0 Tesla as a function of energy; and (3) Investigating the differences in the area of encompassed ellipse under the magnetic field concerning a standard circle without magnetic field, while the size of each standard circle in the plane depends on the dose level.

The processes of 1 or 2 analyze the data only in the x - or y -axis itself and refer to the macroscopic aspect. Because the minimum/maximum axis of ellipse cannot be on x/y axes, each ellipse can be fitted by minimalizing the area between an

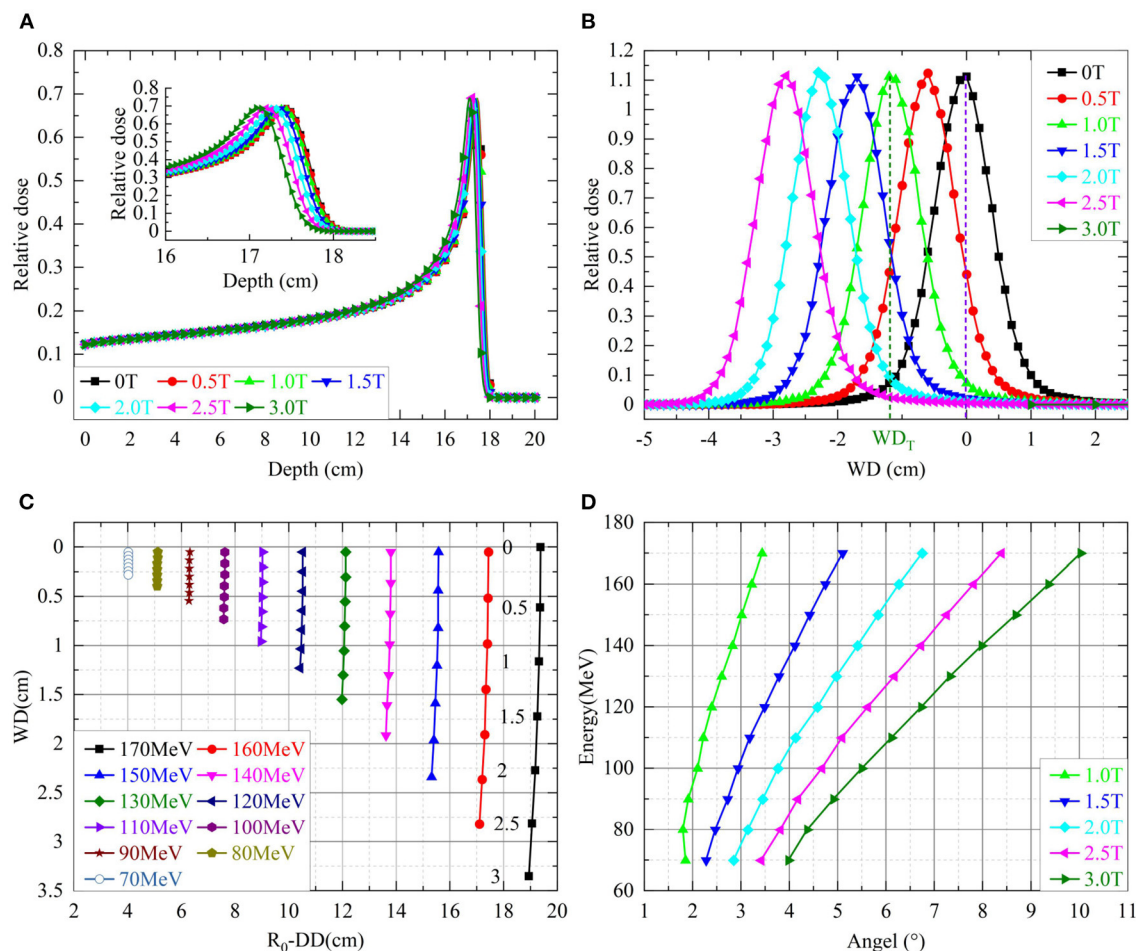


FIGURE 2 | (A) Shows the simulated depth doses of protons with 170 MeV over different field strengths. The insert shows the details of depth doses near the Bragg-peak. **(B)** Shows the shifts of WD for various energies with different field strengths. The numbers next to the shifts of 170 MeV indicated corresponding field strengths. **(C)** Shows the lateral dose profiles of protons with 170 MeV over different field strengths in the axis of WD. **(D)** Shows the beam deflection angles for incidence beam direction.

inscribed circle (IC) and a circumscribed circle (EC) where the IC is the maximum radius with the ellipse and the EC the minimum radius outside the ellipse. The process of 3 refers to the macroscopic aspect by involving the asymmetry at a dose level.

Although the deflection of spiral tracks causing the shifts of Bragg-peak position and the 2D dosimetric deviations in macroscopic and microscopic aspects described above, the major and minor axes of elliptical 2D distribution at the Bragg-peak location may not align with x/y axes related to the beam direction as shown in the insert of **Figure 1B**. The MATLAB code was used to analyze the FWHM of each line passing through the maximum dose point of the Bragg peak in each simulated 3D distribution. It is that the spatial positions of lines having maximum FWHM_{max} and minimum FWHM_{mim} of each simulated 3D dose distribution were located. Based on the orientations of FWHM lines, the rotation angles of FWHM_{max} and FWHM_{mim} lines to the beam incidence are the Angle_{max} and Angle_{min} as indicated in the insert of **Figure 1B**.

RESULTS

The Shifts of Bragg-Peak Positions The MC Simulations and the Analytical Model

Each simulated depth dose was normalized to the maximum dose at the phantom surface. **Figure 2A** shows simulated depth doses for protons with an energy of 170 MeV/u under different field strengths. The insert of **Figure 2A** shows the shifts of ΔDD . **Figure 2B** shows the shifts of WD for various energies with different field strengths. **Figure 2C** shows the lateral profiles shifting under various field strengths. **Figure 2D** shows the beam deflection angles, calculated from WD and ΔDD , concerning the incident beam direction.

Table 1 lists the percentage differences on WD from Equations of (1) or (2) to the simulations over proton energies of 100–170 MeV/u. Both smaller proton energy and a weaker magnetic field would result in a large percentage difference. The mean of percentage differences over listed energies for the Equations of (1)

and (2) were 4.7 and 5.6%, respectively. However, the maximum absolute difference of *WD* between the analytical model and the MC simulation is around 0.5 mm.

Table 2 shows the difference between the analytical model of Equation (3) and the MC simulation for various proton energies under different field strengths. The maximum difference is 0.1 mm.

Applications of Analytical Model for Desired ΔDD and *WD* in the MRI-IGPRT

Based on the position relationship between an OAR and the target, required ΔDD and *WD* can be determined. The Equations of (4) and (5) derived from the revision of Equations (1) and (3) can be used to determine the proton incident energy with a specific field strength to achieve an optimized delivered doses for MRI-IGPRT.

$$E_0 = \left(WD \times \frac{12 \alpha^{-2} \sqrt{2m}}{7 qB} \right)^{\frac{1}{3}} \quad (4)$$

$$E_0 = \left(\Delta DD \times \frac{\alpha^{-3} \bullet 2m (4p-1)(3p-1)}{q^2 B^2} \right)^{\frac{1}{3p-1}} \quad (5)$$

For example, to meet the required position of OARs for avoidance required a *WD* = 2.0 cm or ΔDD = 0.25 cm under a 3.0 Tesla of field strength; calculated incident energy E_0 of the protons by

formula 4 or 5 are 141 MeV/u or 148 MeV/u, respectively. The energy of protons was input to the MC simulation with a 3.0 Tesla of field strength. The MC simulated *WD* and ΔDD outcomes were 2 cm and 0.24 cm, respectively. Similar results validated that Equations (4) and (5) can be used for calculating the incident proton energy of required *WD* and ΔDD . In clinical practice, this approach by proper proton energy under a specified field strength could achieve the desired delivered doses of MRI-IGPRT.

The Asymmetries of 2D/3D Dose Distributions Induced by Magnetic Fields Characteristics of Asymmetric Planar 2D Dose Distributions

Symmetric planar dose distributions at the depth of Bragg-peak without a magnetic field were observed in the top panels of **Figure 3**. However, asymmetric planar distribution for protons of 270 MeV/u appear under a field strength of 3.0 Tesla.

To analyze the characteristics of asymmetric planar distribution, the 1D distribution at the *x*-transverse and *y*-longitudinal axes from each panel of **Figure 3** were extracted and presented in **Figure 4**. Each extracted 1D profile of the *x*- or *y*-axis was fit by Gaussian function. In the absence of a magnetic field, each 1D profile for different energies was symmetrical in comparison to each fit curve. The *x*-transverse profiles for various energies were still symmetrical even under a field strength of 3.0 tesla. However, *y*-longitudinal profiles were visually asymmetric at lower dose levels. These results indicated the unidirectional distortion of proton dose distributions under the magnetic fields.

Although the *x*-transverse profile is symmetric, the *y*-longitudinal profile is asymmetric under the magnetic fields. The changes of sigma widths are also different between *x*- and *y*-profiles under different field strengths. To present the ratio of sigma, widths on the Gaussian fits of *x*- and *y*-profiles were obtained and plotted in **Figure 5** for various proton energies without magnetic field and under 3.0 Tesla. In the absence of a magnetic field, the axis ratios of longitudinal-transverse proton dose distributions were almost identical. Contrastively, in the presence of a magnetic field, the ratios increased with the enhancing energy, especially at energies > 150 MeV/u.

TABLE 1 | The percentage differences of *WD* for formulas 1 and 2 for simulations.

Energy (MeV)	Formula 1 (%)	Formula 2 (%)
100	9.81	11.61
110	6.88	8.93
120	4.92	6.95
130	3.76	5.35
140	3.11	4.08
150	2.93	3.18
160	2.90	2.52
170	3.23	2.10

TABLE 2 | Differences of ΔDD between the analytical model of the Equation (3) and the MC simulation.

Energy (MeV)	B = 1.5T		B = 2.0T		B = 2.5T		B = 3.0T	
	Simulation (mm)	Formula 3 (mm)	Simulation (mm)	Formula 3 (mm)	Simulation (mm)	Formula 3 (mm)	Simulation (mm)	Formula 3 (mm)
100	0.2	0.2	0.2	0.2	0.4	0.4	0.4	0.5
110	0.2	0.2	0.2	0.2	0.4	0.4	0.6	0.6
120	0.2	0.2	0.4	0.4	0.6	0.6	1	1
130	0.4	0.3	0.6	0.6	1	1	1.4	1.4
140	0.4	0.3	0.8	0.8	1.4	1.3	1.8	1.8
150	0.6	0.6	1.2	1.1	1.8	1.8	2.6	2.7
160	1	0.9	1.4	1.5	2.4	2.4	3.4	3.3
170	1.2	1.1	2	1.9	3.2	3.1	4.4	4.4

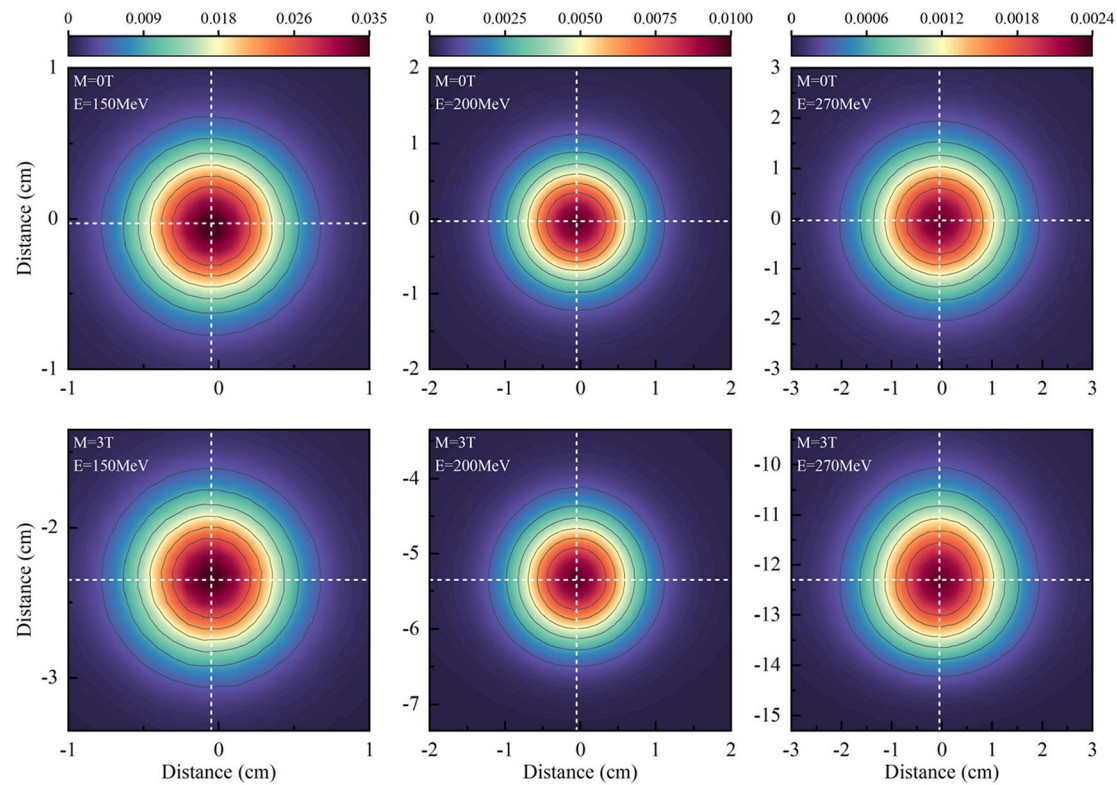


FIGURE 3 | Shows the planar dose distributions at the Bragg-peak positions for protons without magnetic fields at the panels and under a field strength of 3.0 Tesla.

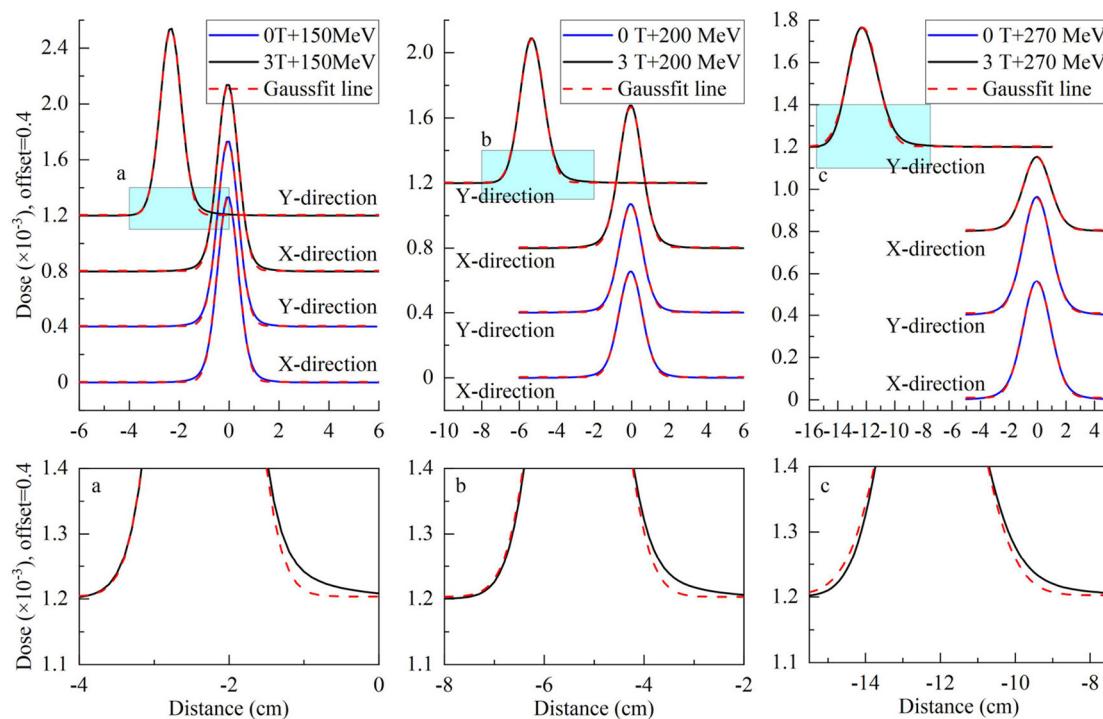


FIGURE 4 | Top panels show extracted x-transverse and y-longitudinal 1D distributions in the solid blue curve with Gaussian fit curves in the dotted red curve for 2D dose distributions in Figure 3. Bottom panels show the detail of y-longitudinal distributions at lower dose levels.

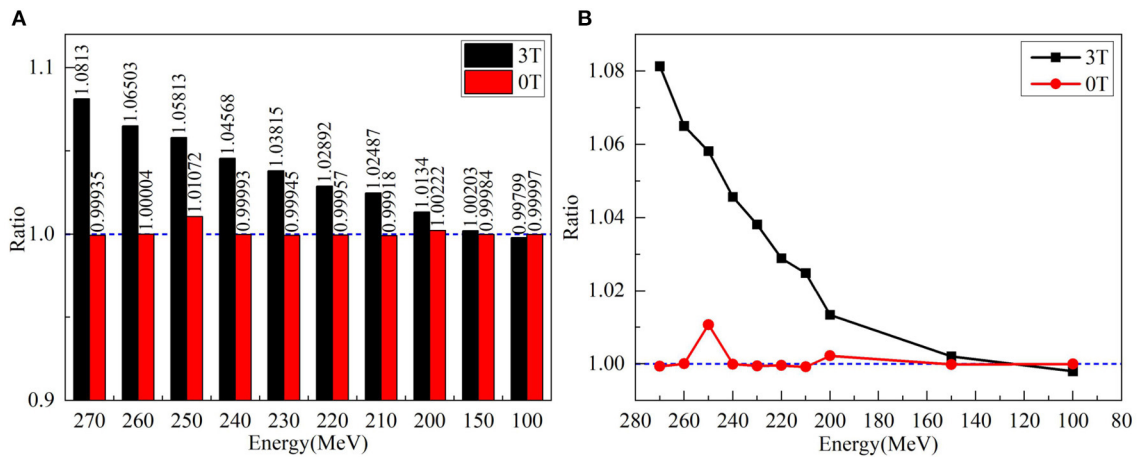


FIGURE 5 | (A) Left panel shows the ratios of sigma widths on the Gaussian fits of x - and y -profiles for various proton energies without a magnetic field and under 3.0 Tesla. **(B)** The right panel showed the ratio of left panel by circles without magnetic field and by squares with a field strength of 3.0 Tesla.

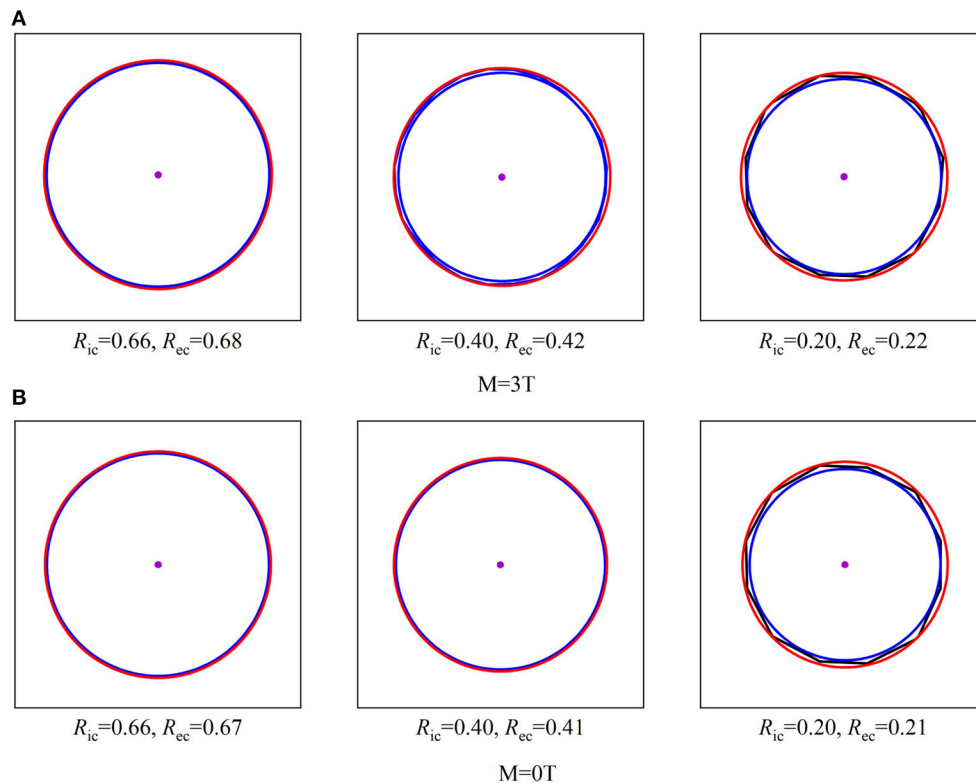


FIGURE 6 | Shows three sizes of isodose curves for 150 MeV protons over three dose levels under a 3.0 Tesla field strength with **(A)** and without a magnetic field **(B)**. The center point of each plot indicates the maximum dose at Bragg-peak position of each simulation. Each isodose curve was fit for a minimized area between the inscribed IC and EC circumscribed circles as described in the text to obtain the radii of IC and EC. When $E = 150\text{MeV}$.

Besides the ratios of sigma widths varying with the proton energy under different field strengths, the changes of sigma widths are different for the isodose curves at different dose levels as shown by the different size of isodose curves in **Figure 6**.

Because the change of sigma width of each isodose curve is different between x and y axes, it results in an elliptical shape for each isodose curve under the influence of the magnetic field. By applying the fit process described above, the radii of IC/EC

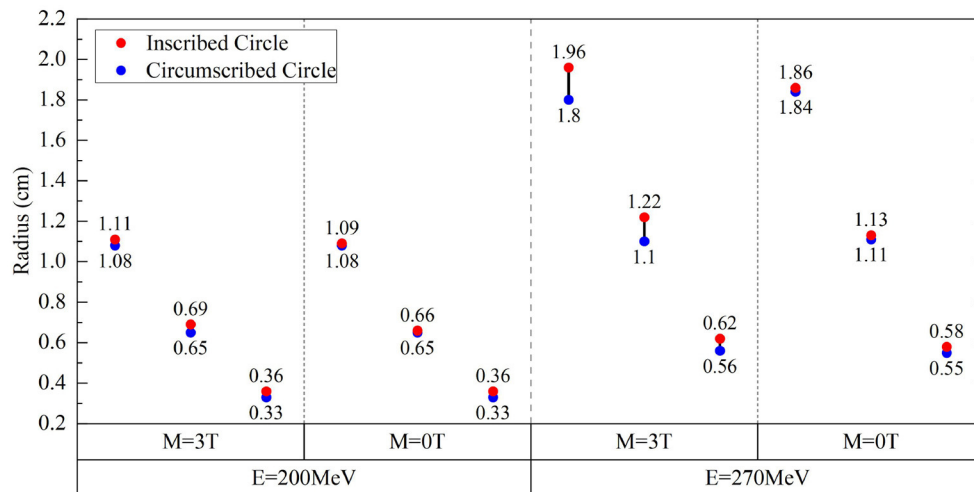


FIGURE 7 | Radius differences of fitted IC/EC circle for isodose curves for protons of 200 and 270 MeV under the field strengths of 0.0 and 3.0 Tesla.

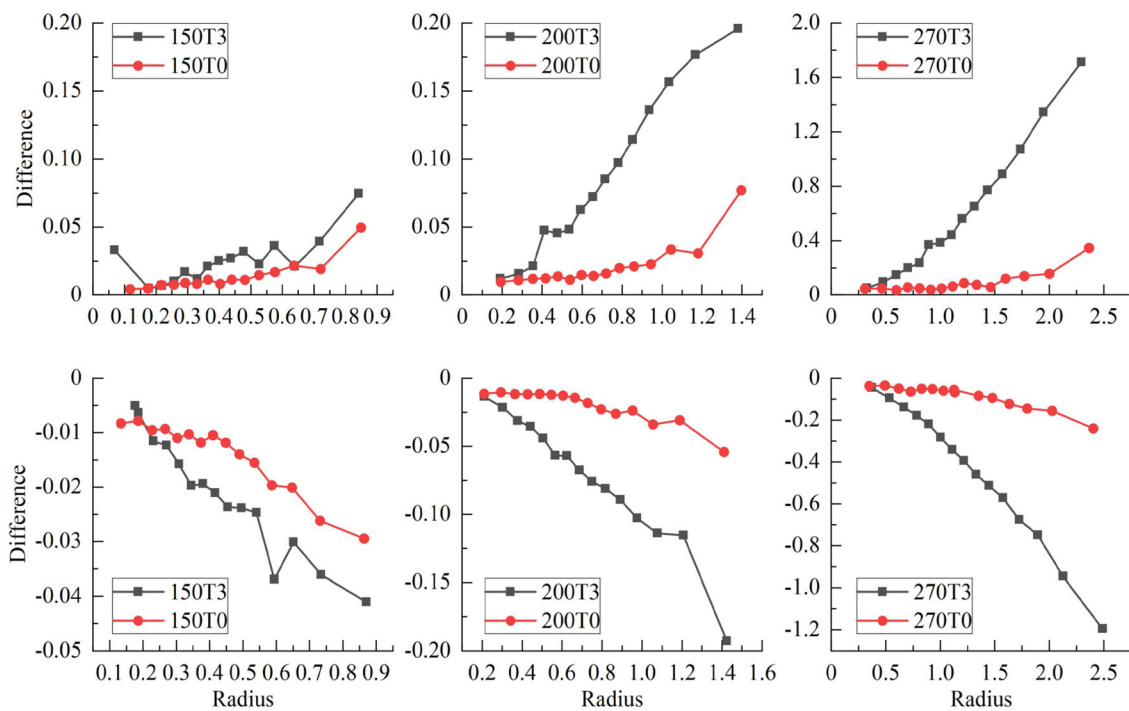


FIGURE 8 | Shows the trend of radius difference between the IC and EC circles as a function of the radius in the standard circle for protons with energies of 150, 200, and 270 MeV.

circles were obtained for each isodose curve to be plotted in **Figure 7**. The area differences of these circles exhibited a certain regularity in the presence of the magnetic field. The average radius differences for a field strength of 3.0 Tesla were twice those without a magnetic field.

Figure 7 shows the radii for fit IC/EC circles of three isodose curves for protons with energies of 200 MeV/u and 270 MeV/u under the field strengths of 0.0 and 3.0 Tesla. The difference

between IC and EC radii increases as the size of the isodose curve increases, i.e., lower dose level. The effect of a magnetic field for 200 and 270 MeV/u protons was three and five times stronger than 150 MeV/u protons, respectively. **Figure 8** shows the trend of radius difference between the IC and EC circles for protons with energies of 150, 200, and 270 MeV/u as a function of radius without a magnetic field. Many standard radii were at the lower dose level. A general trend for larger

TABLE 3 | Dose calculations on different angle profiles.

E (MeV)	FWHM _{max} (cm)	Angle _{max} (degree)	FWHM _{min} (cm)	Angle _{min} (degree)	FWHM _{vertical} (cm)
150	0.8212	1	0.6577	25	0.8122
200	1.3489	81	1.0512	31	1.3141
270	2.3167	83	1.7456	14	2.2304

differences with increased standard radius was seen for all three energies.

The Deflection of Major Axes for Asymmetric 3D Dose Distributions

As shown in the insert of **Figure 1B**, the FWHM of each line passing through the maximum dose point of the Bragg peak were analyzed. The lines passing the maximum and minimum of FWHM were rotated away from its initial orientation; it was initially aligned with the vertical axis as indicated in **Figure 1B**. Due to the re-orientation of major and minor axes of 3D dose distribution for protons passing a magnetic field, the plane formed by the major and minor axes is a certain angle with the beam incident direction as the elliptical circle indicated in the insert of **Figure 1B**. Extracted rotation angles of Angle_{max} and Angle_{min} are listed in **Table 3** for protons with energies of 150, 200, and 270 MeV under a field strength of 3.0 Tesla. The values of FWHM_{max} and FWHM_{min} are also listed in **Table 3** with the FWHM along the vertical axis. Notice that the maximum FWHM is not always along the vertical direction, but can be in a different direction.

DISCUSSION

The MRI-IGRPT can reduce the uncertainties in the radiotherapy process and improve the patient's positioning accuracy. However, the magnetic field significantly alternates the dose distributions of protons passing the magnetic field as shown in our results. In this study, details of the spiral proton track and the asymmetric 2D/3D dose distribution were investigated. The magnetic field not only induces the shift of Bragg-peak position as the spiral proton track, but also varies the 2D/3D dose distributions (11, 12, 14, 15). Induced asymmetric variation of 2D/3D dose distributions were evaluated on the ratio of Gaussian-fit values in the 2D dose distributions. The skewness of asymmetry at different dose levels by the differences between the circumscribed and inscribed circles was also studied. Finally, the rotation angles to the beam incidence for major axes were investigated for maximum and minimum FWHW in the 3D dose distribution.

REFERENCES

1. Baumann M, Krause M, Overgaard J, Debus J, Bentzen SM, Daartz J, et al. Radiation oncology in the era of precision medicine. *Nat Rev Cancer*. (2016) 16:234–9. doi: 10.1038/nrc.2016.18

To validate an analytical model for predicting simulated ΔDD and WD shifts of Bragg-peak position, the mathematic formula derived by Wolf and Bortfeld (21) was used in this study. The validation and verification were successfully conducted using the analytical model. With a validated analytical model, the mathematic formula by reversing the formula was derived. Based on the derived mathematic formula, the anatomical position of the target can be calculated based on the required proton incident energy, which can thus avoid the irradiation of OARs, aiming to achieve the purpose of optimizing proton radiotherapy.

Magnetic fields perturb more on the 2D/3D dose distributions when the energy or/and magnetic field increases. Some existing research on magnetic fields and proton radiotherapy only described the change of proton dose or made preliminary dose calculations (14, 24, 25). Dosimetry deviation in the 2D/3D distribution were performed on the macroscopic to microscopic aspects with parameters such as the angles of deflection and the orientation of major/minor axes of the plane. With the validated analytical model and details of characteristics of dosimetric deviations, the dose perturbation due to the magnetic field can be optimized to deliver desired doses to the treated target.

CONCLUSION

The trend of the spiral proton track under a uniform magnetic field obtained in this study by using either MC simulation or the analytical model can provide optimized doses of the proton beam in the clinical application of MRI-IGPRT. Further developments of the analytical dose calculation algorithm are needed to model the asymmetric dose distribution of protons passing a realistic non-uniform magnetic field.

DATA AVAILABILITY STATEMENT

The original contributions presented in the study are included in the article/supplementary material, further inquiries can be directed to the corresponding author.

AUTHOR CONTRIBUTIONS

XuW and XiW proposed and designed the experiments. XiW and XuW carried out the experiments with the help of HP, QC, and WX. XiW drafted the manuscript and interpreted the data. XuW revised the manuscript. All authors contributed to the article and approved the submitted version.

FUNDING

This work was supported by National Natural Science Foundation of China (Nos. 11375047, 11005019, and 12075063).

2. Moteabbed M, Schuemann J, Paganetti H. Dosimetric feasibility of real-time MRI-guided proton therapy. *Med Phys*. (2014) 41:111713. doi: 10.1118/1.4897570
3. Houweling AC, Crama K, Visser J, Fukata K, Rasch CRN, Ohno T, et al. Comparing the dosimetric impact of interfractional anatomical changes in

- photon, proton and carbon ion radiotherapy for pancreatic cancer patients. *Phys Med Biol.* (2017) 62:3051–64. doi: 10.1088/1361-6560/aa6419
4. Lomax AJ, Bortfeld T, Goitein G, Debus J, Dykstra C, Tercier P-A, et al. A treatment planning inter-comparison of proton and intensity modulated photon radiotherapy. *Radiother Oncol.* (1999) 51:257–71. doi: 10.1016/S0167-8140(99)00036-5
 5. Hartman J, Kontaxis C, Bol GH, Frank SJ, Lagendijk JJW, van Vulpen M, et al. Dosimetric feasibility of intensity modulated proton therapy in a transverse magnetic field of 1.5 T. *Phys Med Biol.* (2015) 60:5955–69. doi: 10.1088/0031-9155/60/15/5955
 6. Paganelli C, Whelan B, Peroni M, Summers P, Fast M, van de Lindt T, et al. MRI-guidance for motion management in external beam radiotherapy: current status and future challenges. *Phys Med Biol.* (2018) 63:22TR03. doi: 10.1088/1361-6560/aaebcf
 7. Brenner DJ, Hall EJ. Computed tomography—an increasing source of radiation exposure. *New Engl J Med.* (2007) 357:22. doi: 10.1056/NEJMr072149
 8. Semelka RC, Armao DM, Elias Junior J, Huda W. Imaging strategies to reduce the risk of radiation in CT studies, including selective substitution with MRI. *J Magn Reson Imaging.* (2007) 25:900–9. doi: 10.1002/jmri.20895
 9. De Schepper AM, De Beuckeleer L, Vandevenne J, Somville J. Magnetic resonance imaging of soft tissue tumors. *Eur Radiol.* (2000) 10:213–23. doi: 10.1007/s003300050037
 10. Rank CM, Tremmel C, Hünemohr N, Nagel AM, Jäkel O, Greilich S. MRI-based treatment plan simulation and adaptation for ion radiotherapy using a classification-based approach. *Radiat Oncol.* (2013) 8:51. doi: 10.1186/1748-717X-8-51
 11. Nguyen N, Nguyen M, Vock J, Lemanski C, Kerr C, Vinh-Hung V, et al. Potential applications of imaging and image-guided radiotherapy for brain metastases and glioblastoma to improve patient quality of life. *Front Oncol.* (2013) 3:284. doi: 10.3389/fonc.2013.00284
 12. Menten MJ, Wetscherek A, Fast MF. MRI-guided lung SBRT: present and future developments. *Phys Med.* (2017) 44:139–49. doi: 10.1016/j.ejmp.2017.02.003
 13. Henke L, Kashani R, Robinson C, Curcuru A, DeWees T, Bradley J, et al. Phase I trial of stereotactic MR-guided online adaptive radiation therapy (SMART) for the treatment of oligometastatic or unresectable primary malignancies of the abdomen. *Radiother Oncol.* (2018) 126:519–26. doi: 10.1016/j.radonc.2017.11.032
 14. Raaymakers BW, Raaijmakers AJE, Lagendijk JJW. Feasibility of MRI guided proton therapy: magnetic field dose effects. *Phys Med Biol.* (2008) 53:5615. doi: 10.1088/0031-9155/53/20/003
 15. Oborn BM, Dowdell S, Metcalfe PE, Crozier S, Mohan R, Keall PJ. Future of medical physics: real-time MRI-guided proton therapy. *Med Phys.* (2017) 44:e77–90. doi: 10.1002/mp.12371
 16. Padilla-Cabal F, Alejandro Fragoso J, Franz Resch A, Georg D, Fuchs H. Benchmarking a GATE/Geant4 Monte Carlo model for proton beams in magnetic fields. *Med Phys.* (2020) 47:223–33. doi: 10.1002/mp.13883
 17. Schellhammer SM, Hoffmann AL. Prediction and compensation of magnetic beam deflection in MR-integrated proton therapy: a method optimized regarding accuracy, versatility and speed. *Phys Med Biol.* (2017) 62:1548–64. doi: 10.1088/1361-6560/62/4/1548
 18. Fuchs H, Moser P, Gröschl M, Georg D. Magnetic field effects on particle beams and their implications for dose calculation in MR-guided particle therapy. *Med Phys.* (2017) 44:1149–56. doi: 10.1002/mp.12105
 19. Oborn BM, Dowdell S, Metcalfe PE, Crozier S, Mohan R, Keall PJ. Proton beam deflection in MRI fields: implications for MRI-guided proton therapy. *Med Phys.* (2015) 42:2113–24. doi: 10.1118/1.4916661
 20. Ferrari A, Sala PR, Fasso A, Ranft J, Siegen U. *FLUKA: A Multi-Particle Transport Code.* CERN 2005-10, INFN/TC_05/11, SLAC-R-773 (2005).
 21. Wolf R, Bortfeld T. An analytical solution to proton Bragg peak deflection in a magnetic field. *Phys Med Biol.* (2012) 57:N329–37. doi: 10.1088/0031-9155/57/17/N329
 22. Grevillot L, Frisson T, Zahra N, Bertrand D, Stichelbaut F, Freud N, et al. Optimization of GEANT4 settings for Proton Pencil Beam Scanning simulations using GATE. *Nucl Instrum Methods Phys Res B.* (2010) 268:3295–305. doi: 10.1016/j.nimb.2010.07.011
 23. MATLAB Release 2015. *The MathWorks, Inc., Natick, MA, United States* (2015).
 24. Ganjeh ZA, Eslami-Kalantari M, Mowlavi AA. Dosimetry calculations of involved and noninvolved organs in proton therapy of liver cancer: a simulation study. *Nucl Sci Tech.* (2019) 30:1–7. doi: 10.1007/s41365-019-0698-8
 25. Raaymakers BW, Raaijmakers AJE, Kotte ANTJ, Jette D, Lagendijk JJW. Integrating a MRI scanner with a 6 MV radiotherapy accelerator: dose deposition in a transverse magnetic field. *Phys Med Biol.* (2004) 49:4109–18. doi: 10.1088/0031-9155/49/17/019

Conflict of Interest: The authors declare that the research was conducted in the absence of any commercial or financial relationships that could be construed as a potential conflict of interest.

Publisher's Note: All claims expressed in this article are solely those of the authors and do not necessarily represent those of their affiliated organizations, or those of the publisher, the editors and the reviewers. Any product that may be evaluated in this article, or claim that may be made by its manufacturer, is not guaranteed or endorsed by the publisher.

Copyright © 2021 Wang, Pan, Cheng, Wang and Xu. This is an open-access article distributed under the terms of the Creative Commons Attribution License (CC BY). The use, distribution or reproduction in other forums is permitted, provided the original author(s) and the copyright owner(s) are credited and that the original publication in this journal is cited, in accordance with accepted academic practice. No use, distribution or reproduction is permitted which does not comply with these terms.



Dose-Effects Models for Space Radiobiology: An Overview on Dose-Effect Relationships

Lidia Strigari¹, Silvia Strolin¹, Alessio Giuseppe Morganti² and Alessandro Bartoloni^{3*}

¹ Department of Medical Physics, Istituto di Ricovero e Cura a Carattere Scientifico (IRCCS) Azienda Ospedaliero-Universitaria di Bologna, Bologna, Italy, ² Radiation Oncology Center, School of Medicine, Department of Experimental, Diagnostic and Specialty Medicine - DIMES, University of Bologna, Bologna, Italy, ³ Istituto Nazionale di Fisica Nucleare (INFN) Sezione di Roma 1, Roma, Italy

OPEN ACCESS

Edited by:

Yi Xie,
Institute of Modern Physics
(CAS), China

Reviewed by:

Nan Ding,
Institute of Modern Physics
(CAS), China
Francis A. Cucinotta,
University of Nevada, Las Vegas,
United States

*Correspondence:

Alessandro Bartoloni
alessandro.bartoloni@cern.ch

Specialty section:

This article was submitted to
Radiation and Health,
a section of the journal
Frontiers in Public Health

Received: 30 June 2021

Accepted: 27 September 2021

Published: 08 November 2021

Citation:

Strigari L, Strolin S, Morganti AG and
Bartoloni A (2021) Dose-Effects
Models for Space Radiobiology: An
Overview on Dose-Effect
Relationships.
Front. Public Health 9:733337.
doi: 10.3389/fpubh.2021.733337

Space radiobiology is an interdisciplinary science that examines the biological effects of ionizing radiation on humans involved in aerospace missions. The dose-effect models are one of the relevant topics of space radiobiology. Their knowledge is crucial for optimizing radioprotection strategies (e.g., spaceship and lunar space station-shielding and lunar/Mars village design), the risk assessment of the health hazard related to human space exploration, and reducing damages induced to astronauts from galactic cosmic radiation. Dose-effect relationships describe the observed damages to normal tissues or cancer induction during and after space flights. They are developed for the various dose ranges and radiation qualities characterizing the actual and the forecast space missions [International Space Station (ISS) and solar system exploration]. Based on a Pubmed search including 53 papers reporting the collected dose-effect relationships after space missions or in ground simulations, 7 significant dose-effect relationships (e.g., eye flashes, cataract, central nervous systems, cardiovascular disease, cancer, chromosomal aberrations, and biomarkers) have been identified. For each considered effect, the absorbed dose thresholds and the uncertainties/limitations of the developed relationships are summarized and discussed. The current knowledge on this topic can benefit from further *in vitro* and *in vivo* radiobiological studies, an accurate characterization of the quality of space radiation, and the numerous experimental dose-effects data derived from the experience in the clinical use of ionizing radiation for diagnostic or treatments with doses similar to those foreseen for the future space missions. The growing number of pooled studies could improve the prediction ability of dose-effect relationships for space exposure and reduce their uncertainty level. Novel research in the field is of paramount importance to reduce damages to astronauts from cosmic radiation before Beyond Low Earth Orbit exploration in the next future. The study aims at providing an overview of the published dose-effect relationships and illustrates novel perspectives to inspire future research.

Keywords: human space exploration, galactic cosmic radiation, galactic cosmic radiation effects, space radiobiology, space radiation doses, dose-effect model

INTRODUCTION

Space radiobiology (SPRB) is a fascinating field that has fostered a growing interest in the recent years, thanks to the increased technological capability to travel and operate in space and the consequent renewed interest from the national space agencies to plan exploratory and colonization space missions.

The space radiation environment is a complex mixture of radiation species dominated by highly penetrating charged particles from different sources (**Figure 1**). In this regard, three different sources of particles are present: particles emitted by the Sun (SPE) due to the solar activities, particles trapped in the magnetic field of the Earth (i.e., Radiation Belt), and galactic cosmic rays (GCRs) coming from outside the solar system.

Planetary magnetic fields and short-term and long-term solar activities modulate the energy spectrum and abundances of radiation species (1). In addition, the presence of shielding on the space stations or spacecraft modifies the incident spectrum and related exposure due to (secondary) particles production resulting from the interaction (spallation) of the space radiation particles with such structures.

Such particles can penetrate several hundreds of centimeters of materials, such as aluminum or tissue/water and fragment before stopping, producing lower Z secondary particles through nuclear interactions. A lower linear energy transfer (LET) characterizes the secondary particles. Such characteristics confer a higher penetration range than the primary particles (2).

Ionizing radiation protection on Earth uses several technical solutions to reduce the exposure of workers: increasing the distance from the radiation source, reducing the exposure time, and implementing *ad hoc* shielding (3).

Distance is not helpful in space since GCRs are mostly isotropically distributed. Time exposure reduction is a valid approach in space, but not practical due to spacecraft velocity or time to perform scientific tasks. Further, it will be significantly longer than what has been experienced so far for the planned exploration and colonization to Moon and Mars. Shielding, either active or passive, is crucial to reduce radiation exposure significantly but cannot fully absorb all space radiation due to the high-energy component and the time-variable contribution of the GCR spectrum. In addition, shielding materials and thickness need to be optimized considering their efficacy and cost to reduce the unavoidable exposures to the minimum acceptable level. Nevertheless, dose- and equivalent dose-rate of the astronauts are around 0.3–0.6 mGy/day, corresponding to 1–1.8 mSv/day, respectively (4).

Both acute and late effects in the space radiation environment are the most frequent and relevant life-threatening adverse events associated with ionizing radiation exposure. Acute radiation syndrome (i.e., short-term effects) is caused by intense and short exposure to SPEs in case of crews unable to reach areas with adequate shielding. Late radiation morbidity [e.g., carcinogenesis or central nervous system (CNS) damage] is associated with continuous exposure to GCR, which is substantially different both qualitatively and quantitatively from the natural background of the radiation of Earth, depending on various above-described factors (i.e., long- or short-term solar activity and magnetic field features).

Mathematical models of dose-effect relationships are developed and are confirmed not only from human studies but also from *in vitro* cell or *in vivo* small animal studies. Such models explain and predict the clinical and subclinical effects recorded during space missions. In addition, it is possible to use clinical diagnostic or radiotherapeutic devices for performing a ground simulation of GCR scenarios and improving the space exposure radiobiological model understanding, due to the similarity of dosage and type of available particles. Moreover, the complete understanding of non-targeted effects induced by charged particles becomes mandatory (5) due to the interaction of secondary particles with several human healthy tissues. Nontargeted effects may dominate cancer risk at space-relevant doses. Furthermore, several investigations are still ongoing to consider the possibility of hibernating astronauts to guarantee additional protection against space radiation effects, given the radioprotective action of hypothermia (6).

Our study aims at reviewing the acute and late adverse effects of space travel to be compared/discussed to the ones currently observed after diagnostic or radiotherapy exposure or through ground simulations to similar dosage/radiations.

MATERIALS AND METHODS

Resource Identification Search Strategy

The performed PubMed search uses the query string reported below to identify the proposed models for acute and late effects related to space mission/exposure and compare these effects with the threshold reported in the diagnostic or therapeutic applications using ionizing radiation. Query search included the following keywords/string: space[title/abstract] model[title/abstract] radiobiol* [title/abstract]. For each detrimental health and tissue effect, an additional search have to be implemented e.g., (model[title/abstract] OR relationship[title/abstract]) AND (radiotherapy[title/abstract] OR space[title/abstract]) AND (radiobiol* [title/abstract] OR dose [title/abstract]).

The research had been restricted to the last 10 years to include only the most recently published studies. The last search was done on August 30, 2021. The authors independently reviewed titles and abstracts to decide study inclusion. Full articles were retrieved when the abstract was considered relevant, and only papers published in English were considered. The bibliographies of retrieved and reviewed papers were also examined to identify other relevant articles to be included and published before 2011. Papers were considered eligible when reporting models and dose-effect correlations.

Analyzed effects included, among others, eye flashes, cataracts, CNS effects, cardiovascular disease (CVD), biomarkers including chromosomal aberrations, cancer induction (including mortality), and other possible risks never evidenced in astronauts but investigated as possible long-term irradiation for future missions to Mars and Moon (**Table 1**). In the last columns of **Table 1**, the overall reliability and research priority rates are reported using a 5-point scoring system from very low (*) to very high (*****) values. The reliability of models has been reported considering the number of revealed effects, statistical

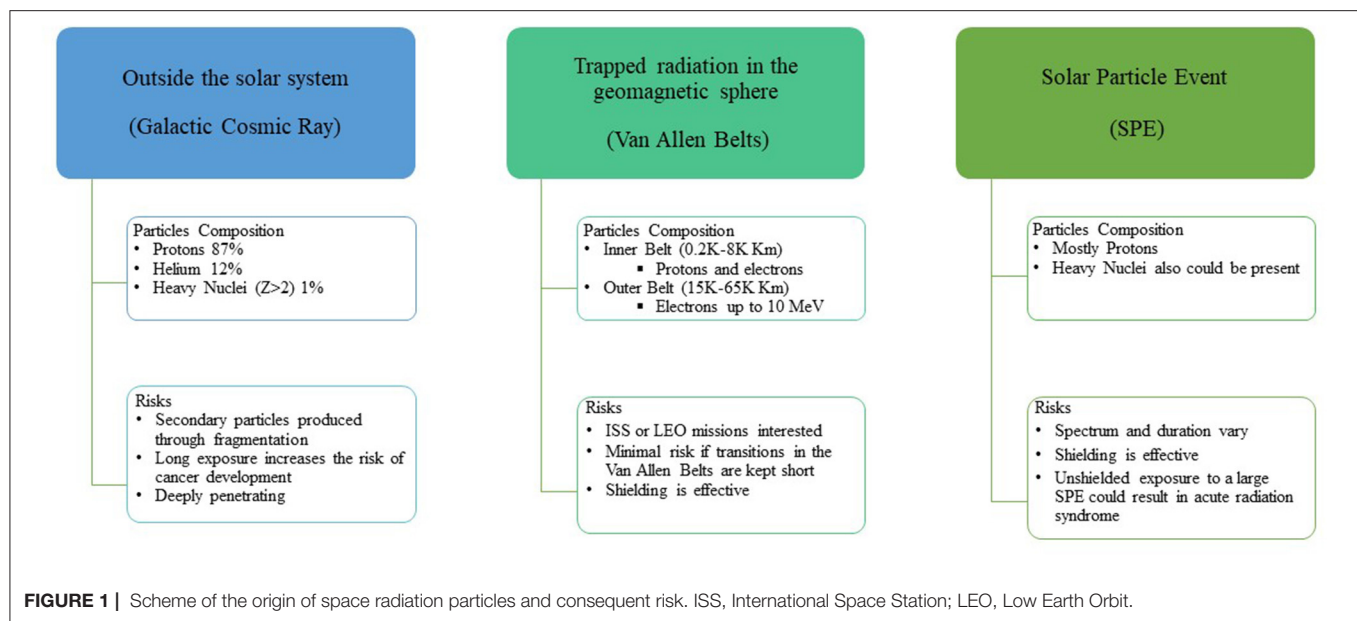


TABLE 1 | Dose-effect relationship for space radiation risk assessment.

Model	Study type	Dose range/threshold or LET	Reference	Reliability	Priority
Eye flashes	Spaceflight	LET > 5–10 keV/μm	(7–10)	****	*
Cataract	Spaceflight	8 mSv	(11–15)	***	***
CNS	Ground/Simulation	100–200 mGy	(16–27)	**	*****
CVD	Spaceflight	1000 mGy	(28–31)	*	***
	Ground/Simulation	(0.1–4,500) mSv	(32–39)		
Cancer	Spaceflight	<100 mGy	(40, 41)	***	*****
	Ground/Simulation	<100 mGy	(42–50)		
Biomarkers or	Spaceflight	5–150 mGy	(51–61)	***	*****
Chromosomal aberrations	Ground/Simulation	<10,000 mGy	(62–65)		
Other Risks	Ground/Simulation	~2,000 mGy	(66, 67)	*	***

* = Very Low, ** = Low, *** = Medium, **** = High, ***** = Very High.

approaches, and information on dose and GCR spectrum and its modification through shielding materials. We also include an attempt to score the priority for future research considering the possible impact on a long-term mission in deep space, the availability of advanced facilities, and the possible synergies with related medical fields using ionizing radiation.

RESULTS

Identified Studies

Based on Pubmed/Medline search, 61 papers have been found. Among this, 54 were original papers reporting/proposing radiobiology or dose-effects models, while 8 were reviews or relevant reports (which were screened for including additional papers). About 24 papers mainly focused on data obtained from astronauts or spaceflight crews, while 37 were generated using ground experiments and/or simulations. Other reports or commentary papers were included in the discussion.

Dose-Effect Relationships

The identified models based on available data from spaceflight missions or ground/simulation data have been described in **Table 1** and more in detail in the subsequent paragraphs. The scores of overall reliability and research priority are also reported in **Table 1**. The scores of overall reliability and research priority are associated with the robustness of identified models and expected doses calculated for long-term missions considering that astronauts are healthy non-smoker subjects. The higher priorities regard cancer, biomarker/sensitivity, and CNS risk, which can potentially affect the duration and quality of life of space crew/astronauts. Regardless of the relevant efforts in the last decades, the reliability of models is still sub-optimal for most of the medium- and long-term effects.

The effects of radiation exposure in space can manifest themselves at different times; short-term (e.g., eye flashes) are observed immediately and are transient, medium-term [e.g., CVD] after several weeks/months depending on the absorbed dose, and long-term (e.g., cancer) can also occur many years

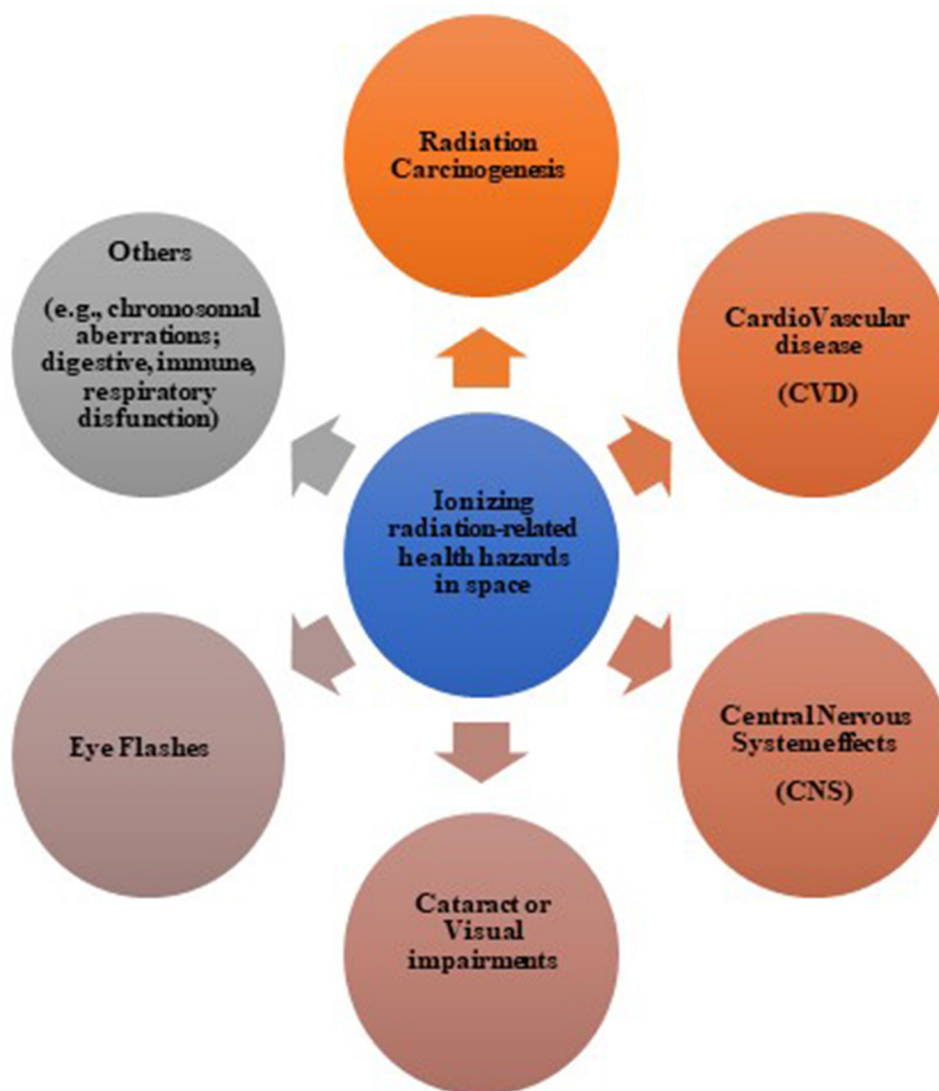


FIGURE 2 | Possible ionizing radiation-related health hazards in space.

(10 to 30) after exposure. The performance, characteristics, limitations, and uncertainties of these dose-effect models are discussed in the following paragraphs.

Figure 2 shows the several possible ionizing radiation-induced effects during and after space missions, including acute and late effects on normal tissues, as well as neurological disease and lens opacification, and cancer risk. **Figure 2** also includes the oral mucositis and CVD, which have never registered at the doses absorbed by astronauts until now but represent a potential risk in case of prolonged exposure as expected after the Mars colonization.

Eye Flashes

Spaceflight-Based Studies

More in detail, the first description of the biological consequences of the space radiation exposure on human cells was the

subjective sensations of lights on eyes, commonly called eye flashes, first observed by Apollo crews (7). The origin of the eye flashes remained unresolved for several years. Geometrical considerations and the Monte Carlo calculations show that, at least in part, the flashes seen by astronauts are correlated with charged particles traversing the retina. Primary or secondary neutrons and possibly heavy ions, rather than mesons, were suspected to cause eye flashes. Observations on the helmets of Apollo astronauts reveal numerous tracks of metallic ions as heavy as zinc and nickel, which are very rare in space, suggesting that the technical environment of spacecraft itself adds extra complexity to the actual spectrum of secondary particles. Secondary particles, generated by the interaction of very high-energy particles with metallic stuff of spacecraft, having the a LET $>5\text{--}10\text{ keV}/\mu\text{m}$ were suspected to cause eye flashes (8, 9). The phenomenon of light flashes in space investigated

onboard Mir space station correlated the data on particles hitting the eye collected with the SilEye detectors with human observations. Likely, a nucleus in the radiation environment of the Mir has roughly a 1% probability of causing eye flashes, whereas the proton probability is almost of three orders of lesser magnitude. The probability of the eye flashes increases above 10 keV/micrometer as a LET function, reaching about 5% at around 50 keV/micrometer (9). Preliminary studies indicate that light ions are the most probable particles for generating eye flashes (10). The measured rate of ions in the eye produced an average rate of 5×10^{-2} eye flashes per minute (20 in about 420 min of observation).

Cataract

Spaceflight-Based Studies

Cataract risk from space radiation seems linear without a threshold caused by genetic damage leading to aberrant cellular differentiation of lens epithelial cells (11, 12). However, questions on the definition of clinical significance and the progression of cataracts with time must still be addressed for risk assessment.

The systematic investigation of lens opacification among US astronauts studied by Cucinotta et al. (13) compares historical data for cataract incidence in the 295 astronauts participated in the Longitudinal Study of Astronaut Health (LSAH) by NASA and individual occupational radiation exposure data. A dose-effect threshold of about 8 mSv, based on epidemiological [corrected] data link an increased risk of cataracts for astronauts with higher lens doses (>8 mSv) of space radiation relative to other astronauts with lower lens doses (<8 mSv). These results remain preliminary because of subjective scoring methods and suggest that relatively low doses of space radiation may predispose crew to an increased incidence and early appearance of cataracts (13).

The NASA Study of Cataract in Astronauts (NASCA) (14, 15) is a 5-year longitudinal study of the effect of space radiation exposure on the severity/progression and risk of lens opacity. The study included 171 consenting astronauts who flew at least one mission in space, and a comparison group made up of three components: (a) 53 astronauts who had not flown in space, (b) 95 military aircrew personnel, and (c) 99 non-aircrew ground-based comparison subjects. Continuous measures of nuclear, cortical, and posterior subcapsular lens opacities were derived from digitized images and were collected for assessing demographic characteristics, medical history, and habits. The variability and median of cortical cataracts were significantly higher for exposed astronauts than for non-exposed astronauts and comparison subjects with similar ages ($P = 0.015$). Cross-sectional data analysis revealed a small deleterious effect of space radiation for cortical and possibly posterior subcapsular cataract lens opacities. These results suggest increased cataract risks at smaller radiation doses than have been reported previously.

Preliminary analyses of 5 years of data with an average of 3.8 exams per subject found no relationship between radiation exposure and progression rates for posterior subcapsular cataracts and nuclear cataracts, e.g., the estimated median progression rate from space radiation being $0.25 \pm 0.13\%$ lens area/Sv/year ($P = 0.062$).

Central Nervous System Ground/Simulation-Based Study

Possible CNS risks during a space mission include cognitive function (e.g., detriments in short-term memory, reduced motor function, and behavioral changes), while late CNS risks comprise neurological disorders, such as premature aging and Alzheimer's disease or other dementia.

The risks of CNS are of concern for long-term exploration missions to Mars or other destinations, while the possible observation of CNS effects in astronauts participating in the past NASA missions is highly unlikely because in low earth orbit (LEO), the astronauts are partially protected by the magnetic field of the Earth, the lengths of past missions which are relatively short, and the small population size of astronauts (16).

The doses used in experimental studies have been much higher than the annual GCRs dose (~ 0.1 Gy/y at solar maximum and ~ 0.2 Gy/y at solar minimum with $<50\%$ from high charge and energy particles). Several studies have been conducted to simulate the GCR radiation using heavy-ion or proton beams to provide evidence for the CNS health risk for missions outside of LEO. Britten et al. (17) have shown that doses as low as 20 cGy of simulated GCR radiation (1 GeV/u ^{56}Fe particles) can significantly impair learning and memory in a rodent model, while Hienz et al. (18) demonstrated that proton radiation caused marked neurocognitive deficits at doses as low as 25 cGy.

Radiosensitive animals exhibited significant changes in proteins associated with dopamine receptors and transporters in the brain at mission-relevant doses and dose rates. These results indicate that susceptibility should be considered in dose-effect models predicting the radiation-induced CNS changes (19). Further investigation is still mandatory to elucidate the impact of dopamine changes as a predictor for the CNS morbidity of the astronauts. CNS effects depend on multiple mechanisms leading to synapse changes (20), among other effects. The average lifetime of synapses varies in different brain regions and depends on the exposure time. In addition, the microgravity effects are also to be considered.

Space travel may cause cognitive detriments associated with changes in neuron morphology and plasticity. Observations in mice revealed a dependence on radiation quality and absorbed dose, suggesting that microscopic energy deposition plays an important role. Simplified 3D neuron models with properties equivalent to realistic neuron morphology have been developed using GEANT4 to describe the effect observed in rats after a dose from 0.1 to 2 Gy delivered to the hippocampus (21). Of note, the changes to synapses are one aspect to be considered. The papers (22, 23) provide more detailed neuron morphology and track structures.

Radiation-induced impairment of neurogenesis is a concern due to its reported association with cognitive detriments after exposure to low doses of high charge and energy particles. The possible risks to astronauts chronically exposed to space radiation could prevent astronauts from performing complex executive functions (17, 24, 25) which are to be deeply investigated after radiotherapy for brain cancers.

Cacao E and Cucinotta FA in 2016 (26) reported a predictive mathematical model of radiation-induced changes to neurogenesis for various radiation types after acute or fractionated irradiation, extending a mouse model of impaired neurogenesis in the hippocampal dentate gyrus after exposure to low-LET radiation to heavy ion irradiation. Heavy-ion irradiation leads to poor or no recovery from impaired neurogenesis at doses as low as 0.5 Gy in mice.

More recently, the first quantitative meta-analysis of the dose-response for proton and heavy-ion rodent studies has been published based on the widely used novel object recognition test, which estimates detriments in recognition or object memory (27). The log-normal model predicts a heavy-ion dose threshold of ~ 0.01 Gy for novel object recognition-related cognitive detriments.

Cardiovascular Disease Spaceflight-Based Studies

Based on a group of 84 flight astronauts, Delp et al. (28) found no differences in CVD mortality rate between non-flight (9%) and LEO (11%) astronauts, while the CDV risk reported among Apollo lunar astronauts (43%) was 4–5 times higher than in non-flight and LEO astronauts. Unfortunately, Delp et al. (28) did not consider the participation of the Apollo lunar mission crew in other missions, radiation doses, experimental protocols using radioisotopes, and time in space under microgravity conditions. Moreover, the incomplete collection of death certificates was available for only 49%, with the remaining information from newspaper and journal articles (29) raised severe doubt on the above conclusions.

CVD from low-dose radiation exposure represents an important issue for space missions (30) and radiotherapy as experienced in an ever-growing number of cancer survivors (31). There is no demonstrated relationship between CVD risk and low-dose cardiac exposures after a space mission, likely due to the statistical limitations of cohorts of astronauts (30) preselected among health subjects with appropriate life habits. However, associations between CVD and whole-body doses of <1 Gy among atomic bomb survivors and the experience from radiotherapy are of potential clinical importance and provide a foundation for assessing astronaut health.

Ground/Simulation-Based Study

Radiotherapy and recent epidemiological studies have suggested that an increased risk of CVD may also arise from low-level exposure (32). The study of CVD mortality from 1950 to 2003 among the Japanese survivors of the atomic bombings of Hiroshima and Nagasaki (33), showing an increased CVD-related death risk at low doses, raised the attention of the scientific community.

Additional information relied on groups of workers exposed to ionizing radiation. The latest study by Azizova et al. (34) examined hypertension incidence (based on 8,425 cases) in Mayak (nuclear installation in the Southern Urals of Russia) workers concerning external radiation and internal plutonium. They found a significantly positive CVD incidence for external exposure, the excess relative risk (ERR) per sievert of external

radiation dose being 0.13 (95% CI, 0.08–0.19), but not for plutonium exposure.

The International Nuclear Workers Study (INWORKS) has recently investigated CVD mortality among over 300,000 workers from the United States, United Kingdom, and France, reporting a statistically significant increase of ERR per sievert being 0.22 (90% CI, 0.08–0.37), based on the cumulative recorded occupational dose received from external photons (35).

However, the authors highlighted that the significant heterogeneities of workers preclude a reliable interpretation of the CVD ERR results. A 2008 study done by McGeoghegan et al. (36) on a subgroup of workers (i.e., previously operating in the facilities of British Nuclear Fuels plc.) included in the previously cited study reported the same concerns about the reliability of the CVD ERR result.

A study of CVD incidence from 1986 to 2012 using the data derived from the medical examinations of 53,772 Russian liquidators working in the Chernobyl zone during the first year after the accident found highly significant ERR per sievert estimates for the incidence of CVDs (37, 38).

At present, there is an indicative evidence for a link. However, overall, the findings at low-dose exposure are not yet persuasive due to the possible influence of major nonradiation risk factors (concomitant exposure to organic solvents and acids) on the reported associations and possible misclassification of cause of death and various potential selection effects (32, 39).

Cancer Spaceflight-Based Studies

About 3% risk of exposure-induced death is generally used as a basis for setting age- and gender-specific dose limits for astronauts based on the National Council on Radiation Protection and Measurements (NCRP) report no.132 (40). After adjusting US cancer rates to remove smoking effects, radiation risks for lung and other cancers, the radiation mortality risks for never-smokers were reduced compared to the average US population by more than 20% and 50% in the mixture model and multiplicative transfer model, respectively (41).

Ground/Simulation-Based Study

Cancer is a stochastic risk, and for this reason may occur even at shallow doses (defined as doses <100 mGy) which is currently estimated using the Linear-No Threshold model (LNT) according to the United Nations Scientific Committee on the Effects of Atomic Radiation (UNSCEAR) (42), the International Commission on Radiological Protection (ICRP) recommendations (43), and the NCRP commentary (44). However, the debate on the accuracy of the LNT model is still open (45–47). Furthermore, compared to X-rays, multicellular models of tumors and normal tissue due to carbon ions have also been investigated (48).

Of note, the uncertainties of cancer risk predictions to exposure to GCRs have been described within the linear-additivity model using the approach of Monte Carlo sampling from subjective error distributions. One of the sources of uncertainties is related to the behavior of quality factors (QFs) of the particles constituting the GCR at low doses. This issue

represents the central gap of knowledge to quantify the overall uncertainty in risk projections. The function of particle type or charge number and energy of QFs have been intensely investigated using track structure models (41, 49). Moreover, the QF extrapolation to low dose has been verified using the sizeable radiation-induced cancer rates from the UNSCEAR (2008). In addition, the overall probability distribution functions of the NASA QF function for solid cancers and leukemia vs. kinetic energy for iron particles have been recently reviewed (50).

Biomarkers and Chromosomal Aberrations Spaceflight-Based Studies

High-LET radiation is more efficient in producing complex-type chromosome exchanges than sparsely ionizing radiation, and this can potentially be used as a biomarker of radiation quality. Chromosomal aberrations in blood samples of astronauts increase with absorbed doses (51).

The blood lymphocytes of the astronauts were analyzed before and after 3–4 months long duration missions to investigate the complex chromosome exchanges (51). The pooled data for metaphase and premature chromosome condensation analysis for all the four ISS crewmembers revealed 6 complex exchanges preflight in a total of 24,136 cells analyzed, and 12 complex exchanges were detected in 26,065 cells collected after the flight. Chromosome aberrations in the lymphocytes of the crewmembers before and after long-duration permanence on the Mir space station were measured in metaphase cells. The total number of complex exchanges detected was very low; a total of 8 complex exchanges were detected preflight in the 20,910 cells analyzed from all crewmembers combined. After flight, 20 complex exchanges were detected in a total of 30,078 cells from all the astronauts (51).

Similarly, Yang et al. (52) showed that the frequency of chromosomal aberrations increased significantly in postflight samples compared to the samples drawn before the flight and that the frequency of sister chromatid exchanges (SCEs) was similar for both pre- and postflight samples.

Further, they estimated a relative biological effectiveness (RBE) of 2.8 for the Mir-18 mission space radiation environment. To perform the RBE, they calculated the ratio between the estimated equivalent dose from chromosomal aberrations (14.75 cSv) and the measured physical absorbed dose (5.2 cGy). The dose equivalent was derived from a dose-response relationship based on the blood samples of preflight astronauts irradiated at various doses using gamma rays.

Similarly, Cucinotta et al. (53) showed that the chromosome aberration of cosmonauts receiving doses in space ranging from about 0.5 to 15 cGy were in most of the cases 2–5 times higher than the unexposed control samples. The estimated frequency of dicentric aberrations in lymphocytes was in good agreement with the observation in MIR-18 crew members. Moreover, the yield of chromosome aberrations increased after flight for five of the NASA/MIR crew members while two decreases over time, reaching the unirradiated values (i.e., the baseline values observed before the flight) (54). This behavior suggests a non-additive or even infra-additive effect, supporting that a radio-adaptive response could occur (7, 55). The bio-dosimetry based

on the dicentric chromosome aberration analysis has been developed and validated (56–58) and represents a fast and reliable tool for dosimetry assessment of populations exposed to radiological incidents for triage purposes.

Two biological response models were compared to the Mir biodosimetry for chromosome aberration in lymphocyte cells; a track-structure model and the linear-quadratic model with LET-dependent weighting coefficients. Both models are in reasonable agreement with data for aberrations in the lymphocytes of Mir crew members. Of note, the difference in the models is the increased effectiveness predicted by the track model for low charge and energy ions with LET near 10 keV/micrometres, indicating that aluminum shielding, although providing necessary mitigation of the effects of trapped radiation, provides no protective effect from the GCR in LEO (53). No significant increase was observed in the yields of chromosome exchanges in the peripheral lymphocytes of astronauts increased after long-duration missions, indicating that the clearance of aberrations from the blood lymphocytes is negligible up to 240 days after the flight (54).

Gao et al. (59) reported that enhanced radiosensitivity recruits more gene and miRNA involved in DNA damage response under space radiation condition, and the microgravity further enhanced the DNA damage response on the transcriptional level. Similarly, Kaur et al. (60) reported that changes in neutrophil functions are affected by factors associated with space flight, and this relationship may depend on mission duration. Moreover, decreased non-major histocompatibility complex (MHC) restricted killer cell cytotoxicity has also been reported in astronauts after spaceflight (61).

Ground/Simulation-Based Study

Some of the proposed biomarkers to predict the risk of carcinogenesis include complex clustered DNA damage, persistent DNA repair foci, reactive oxygen species, chromosome aberrations, and inflammation. Other biomarkers discussed, often assayed for a longer period of postexposure, include mutations and telomere length changes (62).

Experiments performed at the NASA Space Radiation Laboratory revealed that heavy ions induce expression of the TGF- β 1 isoform, which can modulate late post-radiation changes and increase the risk of tumor development and metastasis even when cells were irradiated with doses as low as 0.1 Gy (63). Further studies are needed to determine whether the chronic exposures received in space may potentiate this process in astronauts, leading to increased cancer risk.

Proteins, microRNAs (miRNAs), and transfer ribonucleic acid (tRNA)-derived fragments in serum showed great potential as early biomarkers of exposure to energetic heavy ions and might be helpful in dose reconstruction and risk assessment of heavy-ion exposure in deep space exploration (64). These biomarkers increase or decrease with the increase of the dose in the range of 10–50 cGy.

Finally, in rats irradiated with 60 cGy using 1 GeV ^{56}Fe -particle, radiation impacts on hippocampal glutamatergic neurotransmissions at 3 and 6 months after exposure, which

might play a critical role in learning and memory, likely causing neurocognitive impairment (65).

Others Risks

Potential induction of mucositis in astronauts after long-term exposure to high LET/high energy particles (such as carbon ions) during extended space flights has been described as related effects (48). The effect in terms of cell density/compactness, double-strand breaks, and induction of NF κ B or interleukins has been investigated using doses ranging from 2 to 10 Gy (66). Activation of the transcription factor NF κ B, carbon ion, and X-rays induced the activation of NF κ B in the mucosa model. Increased secretion of pro-inflammatory cytokines and chemokines is involved in initiating radiation-induced oral exposure mucositis and in linking inflammation to cancer development and progression. Again, the different qualities of radiation appear to affect mucosa cultures in different ways following different kinetics. X-rays induced an early activation of NF κ B already 4 h after treatment, which returned to control levels at 24 h after treatment, while heavy-ion-induced effects reached their maximum of 48 h after treatment (66).

The human skin is exposed in every external radiation scenario, making epithelial tissue an ideal model to study radiation-induced effects, from *in vitro* 3D human organotypic skin tissue model to low doses of high LET oxygen (O), silicon (Si), and iron (Fe) ions to investigate the integrity of the barrier function of the skin, which was maintained at various particles and doses (67).

DISCUSSION

Open Issues

For years, astronauts have been exposed to space radiation comprised of high-energy protons and heavy ions, and secondary particles produced in collisions with spacecraft and tissue. Unfortunately, significant uncertainties exist in projecting risks of late effects from space radiation, such as cancer and cataracts due to the paucity/corrected epidemiological data and levels of absorbed doses.

Interactions of the GCRs with the spacecraft hull will significantly impact the radiation exposure of astronauts. Charged particles traversing the hull or “shielding” of the ship will incur nuclear interactions that depend on the composition and thickness of the hull material. These interactions will result in fragmentation products and particles of reduced energy but higher linear energy transfer (LET) that contribute to the radiation dose within the spacecraft. The average radiation dose for the seven deceased Apollo crew was 0.59 ± 0.15 cGy (range 0.18–1.14 cGy). Using similar assumptions, astronauts in LEO would receive 50–100 mSv over a 6–12 month stay, of which the GCR would account for approximately two-thirds of this total dose. Thus, given their mean mission duration of 15.6 days, the deceased LEO astronauts would receive ~ 0.29 cGy, a GCR dose similar to the Apollo lunar astronauts. The estimated dose for the shortest round-trip to Mars would be in the order of >0.6 Sv (4). This value is close to, or even above, the dose limits proposed by NASA for the entire career of an astronaut (68).

In addition, radiation risk assessment during long-term space flights has an extremely high level of uncertainties due to the space-radiation environment, the solar magnetic field activity, and the presence of shielding with different capabilities of reducing the incident radiation, thus producing heterogeneous secondary radiation particles. Early estimates of the uncertainty on cancer mortality risk due to space radiation ranged from 400 to 1,500%, with more precise estimates showing uncertainties at the 95% confidence level of 4-fold times of the point projection (69).

Eye Flashes

Evidence shows that, at least in part, the eye flashes seen by astronauts are correlated with charged particles traversing the retina, but further studies of the role of the flux of all the GCR particles need to be investigated. Eye flashes have been the first phenomenon suggesting the possible damage to the central nervous system of the astronauts.

Cataract

Cataract risks for astronauts have been reported at doses (8 mSv) lower than ones proposed in the European Directive 53/2013 (15–20 mSv) for workers (70–72). A decreased dose-effect threshold has also been reported for occupational exposure (74). Indeed, the current framework of radiological protection of occupational exposed medical workers reduced the eye-lens equivalent dose from 150 to 15–20 mSv per year (72). The results from systematic investigations of lens opacification based on subjective and no-standardized lens evaluation techniques might represent a limit for the risk prediction, mainly considering that NASA is planning prolonged human-crewed space missions to Moon and Mars. The NASA-funded NASCA (14, 15) study will provide new data for estimating the lens opacification in astronauts using standardized and validated objective techniques. Preliminary data did not reveal any relationship between radiation exposure and progression rates for posterior subcapsular and nuclear cataracts.

However, longer follow-up may be needed to understand better regarding the impact of space radiation on cataract progression rates and characterize visual acuity changes.

Central Nervous System

Space radiobiology studies of CNS effects using particle accelerators simulating space radiation and experimental models attempt to assess the CNS risk relevance relative to doses, dose-rates, and radiation quality expected on a Mars mission (16). However, the definition of clinically significant CNS risks for long-term exploration missions must be fully understood because the doses to the hippocampus of astronauts are under 0.1–0.2 Gy, while in radiotherapy, the mean and maximal doses to the hippocampus are under 10 and 17 Gy, respectively (73) with relevant radiation-induced neurocognitive impairment. CNS and CVDs may affect the health of the astronauts, although the uncertainty of these radiation-induced effects is even higher than cancer induction (44).

One of the most promising ways to prevent and mitigate the acute effects of CNS and the neurocognitive impairment during

long-term spaceflight is based on the use of substances (e.g., Dammarane Sapogenins) (75). These and other possible strategies (76) are not yet included in the actual predictive models.

Cardiovascular Disease

Cardiovascular disease due to the ionizing radiation is of paramount interest for radiotherapy treatment being still one of nowadays the most critical side effects of the treatment, nevertheless the high target conformal capability of modern accelerators. CVD depends on the heart and the lung doses (77) and pretreatment hypertensive heart disease (78).

In spaceflight studies, the correlation between CVD risk and absorbed doses is negative, while in ground-based studies, a relationship between CVD risk and low-level exposure to ionizing radiation is reported (32). One of the most critical uncertainty sources is the limited number of subjects involved in the space missions and the number of astronauts/crews with acute or late effects. This aspect leads to limited statistical power (<6%) for cardiovascular and mortalities (29). Due to the low power, further adjustments for other time-related parameters, such as age at first exposure and latency time were not considered, although these factors could change the risk of damage manifestation. NASA uses a 3% risk of exposure-induced death at the upper 95% CI as a basis for setting age- and gender-specific dose limits for astronauts (79). The actual general population of dose-effect models could be too cautionary, being astronauts preselected for many factors, including cardiovascular performance and vision, lowers risks of cancer, and circulatory and pulmonary diseases (3). Since astronauts are considered as healthy and never-smokers (NS) subjects, the expected cancer risks are 20% and 30% lower for males and females, respectively, for NS compared to the average US population (68). On the other hand, different space missions and irradiation conditions allow for investigating the dose-effect relationship in a wide range of absorbed doses and microgravity conditions. Microgravity and ionizing radiations alter the gene sets when considered separately, while they did not alter the gene sets when used in combination. These indicate a complex interaction between these factors (80).

In conclusion, a comprehensive CVD risk prediction model has not yet been achieved. Further investigation is strongly recommended before long-term exploration of space missions.

Cancer

Galactic cosmic ray spectrum can induce cancer, cognitive deficits, changes associated with premature ageing, and degenerative effects in many organs. Most epidemiologic data results from the astronaut cohort are from exposures incurred on missions during the Space Shuttle era, where <100 mSv was accumulated by an astronaut. Nevertheless, the nominal mission length for astronauts has increased to at least 6 months in duration with exposures of 1 mSv to 1.5 mSv per day, depending on the phase of the solar cycle, the number of spacewalks performed, and the level of solar activity (81).

Even with increasing mission length and radiation exposures, it is noteworthy that no astronaut has been diagnosed with cancer

attributable to space radiation to date. Although the sample size is small, follow-up times for significant exposures are limited, and cancer latency periods are from years to decades. Epidemiology studies from human exposures to gamma radiation may help predict the cancer risks attributed to GCR, but further work is needed to validate these findings. Age- and gender-specific dose limits based on incidence-based risk transfer for NS are used for a more accurate estimation of cancer risk. Gaining knowledge to improve transfer models, which entails knowledge of cancer initiation and promotion effects, could significantly reduce uncertainties in risk projections (68).

In addition, the uncertainties in estimating the risks for late effects (including cancer) from space radiation exposures arise from the variability and complexity of the radiation fields due to multiple interactions with the vehicular spacecraft or human tissues. Moreover, the limited radiobiology data using high energy and high LET particles increase the uncertainty of the radiation quality and the expected dose-rate effects (82, 83). In addition, estimation of the biological risks from space radiation remains a complex problem because of the many radiation types, including protons, heavy ions, and secondary neutrons, with few epidemiology studies for these radiation types (84). In contrast to conventional dosimetric methods (85), the biophysical description of heavy particle tracks has been addressed in the context of the interpretation of both space radiation dosimetry and radiobiology data to provide insights into new approaches to these problems.

Modern instrumentation and detectors operating in space, built for astroparticle measurements (86), allows for the estimation of GCR properties and absorbed dose with a greater accuracy, thanks to the recent availability of the Alpha Magnetic Spectrometer (AMS) detector (87–91), installed on the International Space Station (ISS), that measures charged components of cosmic rays since 2011 and is approved to be operative for all the life cycle of the ISS. *Ad hoc* Monte Carlo calculation tools (92) might validate and better estimate dose-effects relationships. This aspect could be relevant also for the improvement of countermeasure, including shielding evaluation and dosimetry of a specific astronaut irradiation condition. In this concern, a study from NASA (93) outlined greater effectiveness of polyethylene compared to aluminum shielding in terms of annual dose equivalent resulting from the application of various Monte Carlo transport codes and the NASA-developed deterministic code High Z and Energy TRAnsport (HZETRN), based on solutions to the Boltzmann transport equation.

Biomarkers

A chromosomal aberration has been mainly investigated in both space radiobiology (SPRB) and radiotherapy studies. Ionizing radiation produces a significant effect in increasing chromosomal aberrations and chromosome break, and production of dicentric and ring. For this reason, chromosome gaps are very sensitive and act as helpful biomarkers to predict radiation-induced acute and late effects (94–96).

Robust predictive models are essential to managing the risk of radiation-induced carcinogenesis. It is critical to identify early

sensitive and late biomarkers that can unravel how radiation-induced cellular stress alters the risk of carcinogenesis and improves the modeling of individual risk of cancer or other long-term health consequences of exposure (62).

Study on the biological effects after exposure to high LET particles used for radionuclide therapy might further contribute to ground simulation studies and to fully understand the biological effects on radiation-induced chromosome damage in peripheral blood lymphocytes (97).

Auspicious preliminary results have shown that blood cytokine levels, and in general, the alteration of immune system parameters can be considered biomarkers of low doses of radiation exposure.

The identification of predictive biomarkers to determine both the received radiation dose (biodosimetry), as well as the radiosensitivity of individuals, may be an essential aspect for future crew selection (98).

At the state of the art, few models have a reliable and accurate estimation of the dose-effects correlations due to the complexities of the flux of GCR particles and their interactions with the human tissues. Data from radiotherapy might help to improve the risk models for space radiation (99) as for radiological or nuclear attacks due to precise knowledge of absorbed dose and objective determination of effects (100).

Space radiation and microgravity are recognized as primary and inevitable risk factors for humans traveling in space, but the reports regarding their synergistic effects remain inconclusive, and various studies highlight differences in the environmental conditions and intrinsic biological sensitivity (59–61).

The remarkable progress made in cancer research during the last decade indicated that low-dose radiation could lead to various alterations in immune system parameters, including natural killer cell activation modulation of blood cytokine levels, which plays a crucial role in cancer development (101–104) as well as in cancer control (105). This issue needs to be further explored for long-term missions.

The expected absorbed dose range to oral cavity (2–10 Gy) for astronauts is broadly lower than the threshold for the induction of oral mucositis reported for Grade 2 or more toxicity using carbon ion therapy (i.e., 43–54 Gy RBE-corrected (106)) or cumulative doses of 32–42 Gy (107, 108) using photon therapy. In addition, in-flight experimentations on intestinal microbiota showed a significant change without alteration of mucosal integrity (109). These data first reinforce the critical need for further studies exploring the impact of spaceflight on intestinal microbiota to optimize long-term space travel conditions.

Strategies for the Improvement of the Models

Further studies are mandatory to guide the development toward novel medical applications and to protect the astronauts during space exploration.

For this reason, the improvements for health hazards related to space exploration are a unique opportunity for the safe conduction of space missions. The first ground-based GCR

simulator of NASA (110) enables a new era in space radiobiology research due to its capability to generate a spectrum of ion beams that approximates the primary and secondary GCR field experienced at the locations of human organs within a deep-space vehicle. This facility will accelerate our understanding and mitigation of health risks faced by the astronauts.

Ongoing Space Radiobiology Research

Several limitations have been pointed out regarding the capability of the existing accelerator-based test facility to emulate the particle fluxes of spacecraft or planetary atmosphere shielding. The introduced uncertainties are relatively small for the solid cancer risk while they are challenging to estimate for CNS or other hazards (111).

Due to the new interest in human space exploration, the European Space Agency (ESA) is currently expanding its effort in identifying all the necessary research activities to create a European Space Radiation Risk Model (ESRRM) (112) and to obtain a harmonized set of criteria for maximum allowable exposure between all the space agencies (NASA, Jaxa, etc.). The needed research areas to increase the knowledge in the field are recently identified from a team of experts from the ESA Topical Team. Among this area, the development of a new dose-effect model as part of the “missing biology for risk assessment” has a crucial role. In this context, the ESA Topical Team recommends exploring the shape of the dose-effect relationship for radiation-induced health effects and understanding the potential impact of individual susceptibility. Substantial efforts have been made to delineate biological mechanisms and health-related outcomes of low-dose radiation. These include a sizeable Low Dose research program, funded by the US Department of Energy, operated in the 2000s, and the EU funded programs, previously NOTE and DoReMi, and currently MELODI (113). Nevertheless, QFs still demand further investigation to improve the design of the radiobiological dose-effect model. An overview of available dose-effect models for SPRB has been conducted to identify the potential improvements in this expertise field.

CONCLUSION

Cancer and toxicity risks remain not accurately quantified despite the technological developments and conceptual advances of space radiobiology and considerable efforts. In the latest years, significant improvements have been made in the absorbed dose-effect estimation and the construction and development of novel ground-based galactic cosmic ray simulator facilities. Technological advancements might realize the dream of human space exploration, and crewed spaceflights to explore and colonize the Moon and Mars are on the agenda of space agencies. Radiological devices or linear accelerators might help conduct *in vitro* or *in vivo ad hoc* experiments or analyze the available information from the cohort of cancer patients, thus reinforcing our knowledge on cancer and non-cancer space-radiation induced effects. Unfortunately, the number of events helpful in modeling the radiobiological effects is still limited.

Consequently, functional dose-effect models/relationships and their uncertainties need further improvement, and we suggest implementing future research to increase the understanding of biological mechanisms.

AUTHOR CONTRIBUTIONS

AB and LS conceived the manuscript and produced the first draft. AB, SS, and LS contributed to the Pubmed search. All the authors contributed to the critical discussion on the dose-effect models

for space and improved the manuscript. All the authors approved the final version of the manuscript.

ACKNOWLEDGMENTS

The authors gratefully acknowledge the strong support from the AMS collaboration, the National Italian Institute of Nuclear Physics/Scientific Committee 2 (INFN/CSN2) and the Italian Space Agency (ASI) within the agreement ASI-INFN n. 2019-19-HH.0.

REFERENCES

- Dietze G, Bartlett DT, Cool DA, Cucinotta FA, Jia X, McAulay IR, et al. ICRP. 123. Assessment of radiation exposure of astronauts in space. *Ann ICRP*. (2013) 42:1–339. doi: 10.1016/j.icrp.2013.05.004
- Leroy C, Rancoita P. *Principles of Radiation Interaction in Matter and Detection*. Milan, World Scientific Pub Co Inc., (2009). p. 952. doi: 10.1142/6872
- Durante M. Space radiation protection: destination Mars. *Life Sci Space Res*. (2014) 1:2–9. doi: 10.1016/j.lssr.2014.01.002
- Zeitlin C, Hassler D, Cucinotta F, Ehresman B, WimmerSchweingruber R, Brinza D, et al. Measurements of energetic particle radiation in transit to Mars on the Mars science laboratory. *Science*. (2013) 340:1080–4. doi: 10.1126/science.1235989
- Nelson GA. Space Radiation and human exposures, a primer. *Radiat Res*. (2016) 185:349–58. doi: 10.1667/RR14311.1
- Cerri M, Tinganelli W, Negrini M, Helm A, Scifoni E, Tommasino F, et al. Hibernation for space travel: impact on radioprotection. *Life Sci Space Res*. (2016) 11:1–9. doi: 10.1016/j.lssr.2016.09.001
- Maalouf M, Durante M, Foray N. Biological effects of space radiation on human cells: history, advances and outcomes. *J Radiat Res*. (2011) 52:126–46. doi: 10.1269/jrr.10128
- Budinger TF, Tobias CA, Huesman RH, Upham FT, Wieskamp TF, Schott JU, et al. Light flash observations (MA-106). In: Center LBJS editor. *Apollo-Soyuz Test Project Summary Science Report*, (NASA SP-412). Washington, DC: NASA Special Publication (1977). p. 193–209
- Avdeev S, Bidoli V, Casolino M, De grandis E, Furano G, Morselli A, et al. Eye light flashes on the Mir space station. *Acta Astronaut*. (2002) 50:511–25. doi: 10.1016/S0094-5765(01)00190-4
- Narici L, Belli F, Bidoli V, Casolino M, De Pascale MP, Di Fino L, et al. The ALTEA/ALTEINO projects: studying functional effects of microgravity and cosmic radiation. *Adv Space Res*. (2004) 33:1352–7. doi: 10.1016/j.asr.2003.09.052
- Blakely EA, Bjornstad KA, Chang PY, McNamara MP, Chang E, Aragon G, et al. Growth and differentiation of human lens epithelial cells *in vitro* on matrix. *Invest Ophthalmol Vis Sci*. (1999) 41:3898–907.
- Hamada N, Sato T. Cataractogenesis following high-LET radiation exposure. *Mutat Res Rev Mutat Res*. (2016) 770:262–91. doi: 10.1016/j.mrrev.2016.08.005
- Cucinotta FA, Manuel F, Jones J, Iszard G, Murrey J, Djojonegro B, et al. Space radiation and cataracts in astronauts. *Radiat Res*. (2001) 156:460–6. doi: 10.1667/0033-7587(2001)156:0460:SRACIA2.0.CO
- Chylack LT, Peterson LE, Feiveson AH, Wear ML, Keith Manuel F, Tung WH, et al. NASA study of cataract in astronauts (NASCA). Report 1: cross-sectional study of the relationship of exposure to space radiation and risk of lens opacity. *Radiat Res*. (2009) 172:10–20. doi: 10.1667/RR1580.1
- Chylack LT, Feiveson AH, Peterson LE, Tung WH, Wear ML, Marak LJ, et al. NASCA Report 2: longitudinal study of relationship of exposure to space radiation and risk of lens opacity. (2012) 178:25–32. doi: 10.1667/RR2876.1
- Cucinotta FA, Alp M, Sulzman FM, Wang, M. Space radiation risks to the central nervous system. *Life Sci Space Res*. (2014) 2:54–69. doi: 10.1016/j.lssr.2014.06.003
- Britten RA, Davis LK, Johnson AM, Keeney S, Siegel A, Sanford LD, et al. Low (20 cGy) doses of 1 GeV/u ⁵⁶Fe-particle radiation lead to a persistent reduction in the spatial learning ability of rats. *Radiat Res*. (2012) 177:146–51. doi: 10.1667/RR2637.1
- Hienz RD, Davis CM, Weed MR, Guida PM, Gooden VL, Brady JV, et al. Neurobehavioral effects of space radiation on psychomotor vigilance and reaction time tests. In: *Proceedings of the 18th Biannual Meeting of the International Academy of Astronautics Humans in Space Symposium*. Houston, TX (2011) p.11–5.
- Chancellor JC, Scott GB, Sutton JP. Space radiation: the number one risk to astronaut health beyond low earth orbit. *Life*. (2014) 4:491–510. doi: 10.3390/life4030491
- Cucinotta FA, Kim MY, Chappell LJ, Huff JL. How safe is safe enough: radiation risks for a human mission to Mars. *PLoS ONE*. (2013) 8:e74988. doi: 10.1371/journal.pone.0074988
- Batmunkh M, Aksenova SV, Bayarchimeg L, Bugay AN, Lkhagva, O. Optimized neuron models for estimating charged particle energy deposition in hippocampus. *Phys Med*. (2019) 57:88–94. doi: 10.1016/j.ejmp.2019.01.002
- Alp M, Cucinotta FA. Biophysics model of heavy-ion degradation of neuron morphology in mouse hippocampal granular cell layer neurons. *Radiat Res*. (2018) 189:312–25. doi: 10.1667/RR14923.1
- Alp M, Cucinotta FA. Track structure model of microscopic energy deposition by protons and heavy ions in segments of neuronal cell dendrites represented by cylinders or spheres. *Life Sci Space Res*. (2017) 13:27–38. doi: 10.1016/j.lssr.2017.03.004
- Britten RA, Mitcheck S, Johnson AM, Singletary SJ, Keeney SK, Nyalwidhe JO, et al. The identification of serum biomarkers of high-LET radiation exposure and biological sequel. *Health Phys*. (2010) 98:196–203. doi: 10.1097/HP.0b013e3181a1c77c
- Lonart G, Parris B, Johnson AM, Miles S, Sanford LD, Singletary SJ, et al. Executive function in rats is impaired by low (20 cGy) doses of 1 GeV/u ⁵⁶Fe particles. *Radiat Res*. (2012) 178:289–94. doi: 10.1667/RR2862.1
- Cacao E, Cucinotta FA. Modeling heavy-ion impairment of hippocampal neurogenesis after acute and fractionated irradiation. *Radiat Res*. (2016) 186:624–37. doi: 10.1667/RR14569.1
- Cacao E, Cucinotta FA. Meta-analysis of cognitive performance by novel object recognition after proton and heavy ion exposures. *Radiat Res*. (2019) 192:463–72. doi: 10.1667/RR15419.1
- Delp MD, Charvat JM, Limoli C.M., Globus RK, Ghosh, P. Apollo lunar astronauts show higher cardiovascular disease mortality: possible deep space radiation effects on the vascular endothelium. *Sci. Rep*. (2016) 6:29901. doi: 10.1038/srep29901
- Cucinotta FA, Hamada N, Little, MP. No evidence for an increase in circulatory disease mortality in astronauts following space radiation exposures. *Life Sci Space Res*. (2016) 10:53–56. doi: 10.1016/j.lssr.2016.08.002
- Elgart SR, Little MP, Chappell LJ, Caitlin MM, Shavers MR, Huff JL, et al. Radiation exposure and mortality from cardiovascular disease and cancer in early NASA astronauts. *Sci Rep*. (2018) 8:8480. doi: 10.1038/s41598-018-25467-9

31. NCRP. *Second Primary Cancers and Cardiovascular Disease After Radiotherapy*. Bethesda, MD: National Council on Radiation Protection and Measurements (2011). p. 170.
32. Wakeford R. Does low-level exposure to ionizing radiation increase the risk of cardiovascular disease? *Hypertension*. (2019) 73:1170–1. doi: 10.1161/HYPERTENSIONAHA.119.11892
33. Shimizu Y, Kodama K, Nishi N, Kasagi F, Suyama A, Soda M, et al. Radiation exposure and circulatory disease risk: Hiroshima and Nagasaki atomic bomb survivor data, 1950–2003. *BMJ*. (2010) 340:b5349. doi: 10.1136/bmj.b5349
34. Azizova T, Briks K, Bannikova M, Grigorieva E. Hypertension incidence risk in a cohort of Russian workers exposed to radiation at the Mayak Production Association over prolonged periods. *Hypertens*. (2019) 73:1174–84. doi: 10.1161/HYPERTENSIONAHA.118.11719
35. Gillies M, Richardson DB, Cardis E, Daniels RD, O'Hagan JA, Haylock, et al. Mortality from circulatory diseases and other non-cancer outcomes among nuclear workers in France, the United Kingdom and the United States (INWORKS). *Radiat Res*. (2017) 188:276–290. doi: 10.1667/RR14608.1
36. McGeoghegan D, Binks K, Gillies M, Jones S, Whaley S. The non-cancer mortality experience of male workers at British nuclear fuels PLC, 1946–2005. *Int J Epidemiol*. (2008) 37:506–518. doi: 10.1093/ije/dyn018
37. Kashcheev VV, Chekin SY, Maksoutov MA, Tumanov KA, Menyaylo AN, Kochergina EV, et al. Radiation-epidemiological study of cerebrovascular diseases in the cohort of Russian recovery operation workers of the Chernobyl accident. *Health Phys*. (2016) 111:192–7. doi: 10.1097/HP.0000000000000523
38. Kashcheev VV, Chekin SY, Karpenko SV, Maksoutov MA, Menyaylo AN, Tumanov KA, et al. Radiation risk of cardiovascular diseases in the cohort of Russian emergency workers of the Chernobyl accident. *Health Phys*. (2017) 113:23–9. doi: 10.1097/HP.0000000000000670
39. Ozasa K, Takahashi I, Grant EJ, Kodama K. Cardiovascular disease among atomic bomb survivors. *Int J Radiat Biol*. (2017) 93:1145–1150. doi: 10.1080/09553002.2017.1290849
40. NCRP. *Radiation Protection Guidance for Activities in Low-Earth Orbit*. Bethesda, MD: National Council on Radiation Protection and Measurements (2000). p. 132.
41. Cucinotta FA, Kim MY, Chappell, L. *Space Radiation Cancer Risk Projections and Uncertainties*. Washington, DC: National Aeronautics and Space Administration (2012).
42. UNSCEAR. *United Nations Scientific Committee on the Effects of Atomic Radiation Effects of Ionizing Radiation UNSCEAR Report to the General Assembly, With Scientific Annexes*. United Nations, NY. (1993).
43. International Commission on Radiological Protection. ICRP Publication 103: the 2007 recommendations of the international commission on radiological protection. *Ann ICRP*. (2007) 37:1–332. doi: 10.1016/j.icrp.2007.10.003
44. NCRP. *Health Effects of Low Doses of Radiation: Perspectives on Integrating Radiation Biology and Epidemiology*, NCRP Commentary No. 24 (2015).
45. McLean AR, Adlen EK, Cardis E, Elliott A, Goodhead DT, Harms-Ringdahl M, et al. A restatement of the natural science evidence base concerning the health effects of low-level ionizing radiation. *Proc Biol Sci*. (2017) 284:20171070. doi: 10.1098/rspb.2017.1070
46. Weber W, Zanzonico, P. The controversial linear no-threshold model. *J Nucl Med*. (2017) 58:7–8 doi: 10.2967/jnumed.116.182667
47. Scott BR. A critique of recent epidemiologic studies of cancer mortality among nuclear workers. *Dose Response*. (2018) 16:155932581877870. doi: 10.1177/1559325818778702
48. Walenta S, Mueller-Klieser W. Differential superiority of heavy charged-particle irradiation to X-rays: studies on biological effectiveness and side effect mechanisms in multicellular tumour and normal tissue models. *Front Oncol*. (2016) 6:30. doi: 10.3389/fonc.2016.00030
49. Cucinotta FA, To K, Cacao, E. Predictions of space radiation fatality risk for exploration missions. *Life Sci Space Res*. (2017) 13:1–11. doi: 10.1016/j.lssr.2017.01.005
50. Cucinotta FA. Review of NASA approach to space radiation risk assessments for Mars exploration. *Health Phys*. (2015) 108:131–42. doi: 10.1097/HP.0000000000000255
51. George K, Wu H, Willingham V, Cucinotta FA. Analysis of complex-type chromosome exchanges in astronaut's lymphocytes after space flight as a biomarker of high-LET exposure. *J Radiat Res*. (2002) 43:129–32. doi: 10.1269/jrr.43.S129
52. Yang TC, George K, Johnson, AS, Durante M, Fedorenko BS. Biodosimetry results from space flight Mir-18. *Radiat Res*. (1997) 148(Suppl. 5):S17–23. doi: 10.2307/3579712
53. Cucinotta FA, Wilson JW, Williams JR, Dicello JF. Analysis of Mir-18 results for physical and biological dosimetry: radiation shielding effectiveness in LEO. *Radiat Meas*. (2000) 132:181–91. doi: 10.1016/S1350-4487(99)00273-5
54. George K, Durante M, Wu H, Willingham V, Badhwar G, Cucinotta FA. Chromosome aberrations in the blood lymphocytes of astronauts after space flight. *Radiat Res*. (2001) 156:731–8. doi: 10.1667/0033-7587(2001)1560731:CAITBL2.0.CO
55. Olivieri G, Bodycote J, Wolff S. Adaptive response of human lymphocytes to low concentrations of radioactive thymidine. *Science*. (1984) 223:594–7 doi: 10.1126/science.6695170
56. Flegal FN, Devantier Y, McNamee JP, Wilkins RC. Quick scan dicentric chromosome analysis for radiation biodosimetry. *Health Phys*. (2010) 98:276–81. doi: 10.1097/HP.0b013e3181aba9c7
57. IAEA. *Cytogenetic Dosimetry: Applications in Preparedness for and Response to Radiation Emergencies*. IAEA, Vienna, Austria. (2011).
58. Oestreicher U, Samaga D, Ainsbury E, Antunes AC, Baeyens A, Barrios L, et al. RENEB intercomparisons applying the conventional Dicentric Chromosome Assay (DCA). *Int. J. Radiat. Biol*. (2017) 93:20–9 doi: 10.1080/09553002.2016.1233370
59. Gao Y, Xu D, Zhao L, Sun, Y. The DNA damage response of *C. elegans* affected by gravity sensing and radiosensitivity during the Shenzhou-8 spaceflight. *Mutat Res*. (2017) 795:15–26. doi: 10.1016/j.mrfmmm.2017.01.001
60. Kaur I, Simons ER, Castro VA, Ott CM. Changes in neutrophil functions in astronauts. *Brain Behav Immun*. (2003) 18:443–50. doi: 10.1016/j.bbi.2003.10.005
61. Mehta SK, Kaur I, Grimm EA, SMID C, Feedback DL, Pierson D. Decreased non-Mhc-restricted (Cd56+) killer cell cytotoxicity after spaceflight. *J Appl Physiol*. (2001) 91:1814–8. doi: 10.1152/jappl.2001.91.4.1814
62. Sridharan DM, Asaithamby A, Blattnig SR, Costes SV, Doetsch PW, Dynan WS, et al. Evaluating biomarkers to model cancer risk post cosmic ray exposure. *Life Sci Space Res*. (2016) 9:19–47 doi: 10.1016/j.lssr.2016.05.004
63. Wang M, Hada M, Huff J, Pluth JM, Anderson J, O'Neill P, et al. Heavy ions can enhance TGFβ mediated epithelial to mesenchymal transition *J. Radiat Res*. (2012) 53:51–7. doi: 10.1269/jrr.11121
64. Bai H, Zhang T, Wang J, Hua J, Wei W. Identification of novel biomarkers of heavy ion exposure: proteins, miRNAs and tRNA-derived fragments in serum. *Acta Astronautica*. (2021) 186:329–36. doi: 10.1016/j.actaastro.2021.05.047
65. Machida M, Lonart G, Britten RA. Low (60 CGy) Doses of ⁵⁶Fe HZE-particle radiation lead to a persistent reduction in the glutamatergic readily releasable pool in rat hippocampal synaptosomes. *Radiat Res*. (2010) 174:618–23. doi: 10.1667/RR1988.1
66. Tschachojan V, Schroer H, Averbek N, Mueller-Klieser W. Carbon ions and X-rays induce pro-inflammatory effects in 3D oral mucosa models with and without PBMCs. *Oncol Rep*. (2014) 32:1820–8. doi: 10.3892/or.2014.3441
67. von Neubeck C, Geniza MJ, Kauer PM, Robinson RJ, Chrisler WB, Sowa MB. The effect of low dose ionizing radiation on homeostasis and functional integrity in an organotypic human skin model. *Mutat. Res*. (2015) 775:10–8. doi: 10.1016/j.mrfmmm.2015.03.003
68. Cucinotta FA, Chappell LJ. Updates to astronaut radiation limits: radiation risks for never-smokers. *Radiat. Res*. (2011) 176:102–14. doi: 10.1667/RR2540.1
69. Durante M, Cucinotta FA. Heavy ion carcinogenesis and human space exploration. *Nat Rev Cancer*. (2008) 8:465–72. doi: 10.1038/nrc2391
70. Ainsbury EA, Bouffler SD, Dörr W, Graw J, Muirhead CR, Edwards AA, et al. Radiation cataractogenesis: a review of recent studies. *Radiat Res*. (2009) 172:1–9. doi: 10.1667/RR1688.1
71. Shore RE, Neriishi K, Nakashima E. Epidemiological studies of cataract risk at low to moderate radiation doses: (not) seeing is believing. *Radiat Res*. (2010) 174:889–94. doi: 10.1667/RR1884.1

72. Blakely EA, Chang PY, A. review of ground-based heavy ion radiobiology relevant to space radiation risk assessment: cataracts and CNS effects. *Adv Space Res.* (2011) 40:1307–19. doi: 10.1016/j.asr.2007.03.070
73. Kim Y, Kim SH, Lee JH, Kang DG. Verification of Low Risk for Perihippocampal recurrence in patients with brain metastases who received whole-brain radiotherapy with hippocampal avoidance. *Cancer Res Treat.* (2019) 51:568–75. doi: 10.4143/crt.2018.206
74. ICRP. *Statement on Tissue Reactions*. Ottawa, Canada: ICRP (2011).
75. Wu X, Li D, Liu J, Diao L, Ling S, Li Y, et al. Dammarane sapogenins ameliorates neurocognitive functional impairment induced by simulated long-duration spaceflight. *Front. Pharmacol.* (2017) 8:315. doi: 10.3389/fphar.2017.00315
76. Oluwafemi FA, Abdelbaki R, Lai JCY, Mora-Almanza JG, Afolayan EM. A review of astronaut mental health in crewed missions: potential interventions for cognitive and mental health challenges. *Life Sci Space Res.* (2021) 28:26–31 doi: 10.1016/j.lssr.2020.12.002
77. Giuranno L, Ient J, De Ruysscher D, Vooijs MA. Radiation-induced lung injury (RILI). *Front. Oncol.* (2019) 9:877 doi: 10.3389/fonc.2019.00877
78. Schneider U, Ernst M, Hartmann M. The dose-response relationship for cardiovascular disease is not necessarily linear. *Radiat Oncol.* (2017) 12:74. doi: 10.1186/s13014-017-0811-2
79. NASA STD-3001. *National Aeronautics and Space Administration NASA Space Flight Human System Standard Volume I, Crew Health* (2007). National Aeronautics and Space Administration, Washington D.C., USA.
80. Beck M, Moreels M, Quintens R, Abou-El-Ardat K, El-Saghire H, Tabury K, et al. Chronic exposure to simulated space conditions predominantly affects cytoskeleton remodeling and oxidative stress response in mouse fetal fibroblasts. *Int J Mol Med.* (2014) 34:606–15. doi: 10.3892/ijmm.2014.1785
81. Chancellor J, Nowadly C, Williams J, Aunon-Chancellor S, Chesal M, Looper J, et al. Everything you wanted to know about space radiation but were afraid to ask. *J Environ Sci Health C Toxicol Carcinog.* (2021) 39:113–28. doi: 10.1080/26896583.2021.1897273
82. Cucinotta FA. A new approach to reduce uncertainties in space radiation cancer risk predictions. *PLoS ONE.* (2015) 10:e0120717. doi: 10.1371/journal.pone.0120717
83. Cucinotta FA, Schimmerling W, Wilson JW, Peterson LE, Badhwar GD, Saganti PB, et al. Space radiation cancer risks and uncertainties for Mars missions. *Radiat Res.* (2001) 156:682–8. doi: 10.1667/0033-7587(2001)156:0682:SRCRAU2.0.CO;2
84. Hirai Y, Cordova KA, Kodama Y, Hamasaki K, Awa AA, Tomonaga M, et al. Tooth enamel ESR doses and cytogenetic doses of Nagasaki atomic-bomb survivors in comparison with DS02R1 doses. *Int. J. Radiat. Biol.* (2019) 95:321–8. doi: 10.1080/09553002.2019.1552807
85. Cucinotta FA, Wu H, Shavers MR, George K. Radiation dosimetry and biophysical models of space radiation effects. *Gravit Space Biol Bull.* (2003) 16:11–8.
86. Bartoloni A, Strigari L. Can high energy particle detectors be used for improving risk models in space radiobiology? In: *Proceedings of the Global Space Exploration Conference 2021 GLEX2021* (2021). St.Petersburg, Russia. Available online at: <https://iafastro.directory/iaac/paper/id/62186/summary/>
87. Aguilar M, Ali Cavazonza L, Ambrosi G, Arruda L, Attig N, Barao F, et al. The alpha magnetic spectrometer (AMS) on the international space station: results from the first seven years. *Phys Rept.* (2021) 894:1–116. doi: 10.1016/j.physrep.2020.09.003
88. Aguilar M, Ali Cavazonza L, Alpat, B. Ambrosi G, Arruda L, Attig N, et al. Properties of a new group of cosmic nuclei: results from the alpha magnetic spectrometer on sodium, aluminum, and nitrogen. *Phys Rev Lett.* (2021) 127:2 021101. doi: 10.1103/PhysRevLett.127.021101
89. Aguilar M, Ali Cavazonza L, Allen MS, Alpat B, Ambrosi G, Arruda L, et al. Properties of heavy secondary fluorine cosmic rays: results from the alpha magnetic spectrometer. *Phys Rev Lett.* (2021) 126:081102. doi: 10.1103/PhysRevLett.126.081102
90. Aguilar M, Ali Cavazonza L, Allen MS, Alpat B, Ambrosi G, Arruda L, et al. Properties of iron primary cosmic rays: results from the alpha magnetic spectrometer. *Phys Rev Lett.* (2021) 126:041104. doi: 10.1103/PhysRevLett.126.041104
91. Aguilar M, Ali Cavazonza L, Ambrosi G, Arruda L, Attig N, Barao F, et al. Properties of neon, magnesium, and silicon primary cosmic rays results from the alpha magnetic spectrometer. *Phys Rev Lett.* (2021) 124:211102. doi: 10.1103/PhysRevLett.124.211102
92. Norbury JW, Whitman K, Lee K, Slaba TC, Badavi FF. Comparison of space radiation GCR models to recent AMS data. *Life Sci Space Res.* (2018) 18:64–71. doi: 10.1016/j.lssr.2018.05.003
93. Norbury JW, Slaba TC, Aghara S, Badavi FF, et al. Advances in space radiation physics and transport at NASA. *Life Sci Space Res.* (2019) 22:98–124. doi: 10.1016/j.lssr.2019.07.003
94. Bi J, Dai H, Feng J, Bian H, Chen W, Wang Y, et al. Rapid and high-throughput detection of peripheral blood chromosome aberrations in radiation workers. *Dose-Response.* (2019) 17:1559325819840852. doi: 10.1177/1559325819840852
95. Saberi A, Salari E, Latifi SM. Cytogenetic analysis in lymphocytes from radiation workers exposed to low level of ionizing radiation in radiotherapy, CT-scan and angiocardiology units. *Mutat Res.* (2013) 750:92–5. doi: 10.1016/j.mrgentox.2012.10.001
96. Hille A, Hofman-Hüther H, Kühnle E, Wilken B, Rave-Fränk M, Schmidberger H, et al. Spontaneous and radiation-induced chromosomal instability and persistence of chromosome aberrations after radiotherapy in lymphocytes from prostate cancer patients. *Radiat Environ Biophys.* (2010) 49:27–37. doi: 10.1007/s00411-009-0244-x
97. Quintens R, Baatout S, Moreels M. Assessment of radiosensitivity and biomonitoring of exposure to space radiation. In: Choukèr A, editor. *Stress Challenges and Immunity in Space*. Cham, WA: Springer (2020). p.519–33. doi: 10.1007/978-3-030-16996-1_28
98. Sciuto R, Rea S, Ungania S, Testa A, Dini V, Tabocchini MA, et al. The role of physical dosimetry and biological effects in metastatic castration-resistant prostate cancer (mCRPC) patients treated with 223Ra: first in human study. *J Exp Clin Cancer Res.* (2021) 40:281. doi: 10.1186/s13046-021-02056-9
99. Tinganelli W, Luoni, F. Durante, M. What can space radiation protection learn from radiation oncology? *Life Sci Space Res.* (2021) 30:82–95. doi: 10.1016/j.lssr.2021.06.002
100. Giovanetti A, Marconi R, Awad N, Abuzied H, Agamy N, Barakat M, et al. Validation of a biomarker tool capable of measuring the absorbed dose soon after exposure to ionizing radiation. *Sci Rep.* (2021) 11:8118. doi: 10.1038/s41598-021-87173-3
101. Chen DS, Mellman I. Elements of cancer immunity and the cancer-immune set point. *Nature.* (2017) 541:321–30. doi: 10.1038/nature.21349
102. Crucian BE, Choukèr A, Simpson RJ, Mehta S, Marshall G, Smith SM, et al. Immune system dysregulation during spaceflight: potential countermeasures for deep space exploration missions. *Front Immunol.* (2018) 9:1437. doi: 10.3389/fimmu.2018.01437
103. Bigley AB, Agha NH, Baker FL, Spielmann G, Kunz HE, Mylabathula PL, et al. NK cell function is impaired during long-duration spaceflight. *J Appl Physiol.* (2019) 126:842–53. doi: 10.1152/jappphysiol.007.61.2018
104. Crucian B, Stowe RP, Mehta S, Quiarte H, Pierson D, Sams C. Alterations in adaptive immunity persist during long-duration spaceflight. *NPJ Microgravity.* (2015) 1:15013. doi: 10.1038/npjmicrograv.2015.13
105. Van den Boorn JG, Hartmann G. Turning tumors into vaccines: co-opting the innate immune system. *Immunity.* (2013) 39:27–37. doi: 10.1016/j.immuni.2013.07.011
106. Musha A, Shimada H, Shirai K, Saitoh J, Yokoo S, Chikamatsu K, et al. Prediction of acute radiation mucositis using an oral mucosal dose surface model in carbon ion radiotherapy for head and neck tumors. *PLoS ONE.* (2015) 10:e0141734. doi: 10.1371/journal.pone.0141734
107. Dean JA, Welsh LC, Wong KH, Alekscic A, Dunne E, Islam MR, et al. Normal tissue complication probability (NTCP) modelling of severe acute mucositis using a novel oral mucosal surface organ at risk. *Clin Oncol (R Coll Radiol).* (2017) 29:263–73. doi: 10.1016/j.clon.2016.12.001
108. Strigari L, Pedicini P, D'Andrea M, Pinnarò P, Marucci L, Giordano C, et al. A new model for predicting acute mucosal toxicity in head-and-neck cancer patients undergoing radiotherapy with altered schedules. *Int J Radiat Oncol Biol Phys.* (2012) 83:e697–702. doi: 10.1016/j.ijrobp.2012.02.004

109. Alauzet C, Cunat L, Wack, M., Lozniewski A, Busby H, et al. Hypergravity disrupts murine intestinal microbiota. *Sci Rep.* (2019) 9:9410. doi: 10.1038/s41598-019-45153-8
110. Simonsen LC, Slaba TC, Guida P, Rusek, A. NASA's first ground-based galactic cosmic ray simulator: enabling a new era in space radiobiology research. *PLoS Biol.* (2020) 18:e3000669. doi: 10.1371/journal.pbio.3000669
111. Kim MY, Rusek A, Cucinotta FA. Issues for simulation of galactic cosmic ray exposures for radiobiological research at ground-based accelerators. *Front Oncol.* (2015) 5:122. doi: 10.3389/fonc.2015.00122
112. Walsh L, Schneider U, Fogtman A, Kausch C, McKenna-Lawlor S, Narici L, et al. Research plans in Europe for radiation health hazard assessment in exploratory space missions. *Life Sci Space Res.* (2019) 21:73–82. doi: 10.1016/j.lssr.2019.04.002
113. Auerbeck D, Salomaa S, Bouffler S, Ottolenghi A, Smyth V, Sabatier L. Progress in low dose health risk research: novel effects and new concepts in low dose radiobiology. *Mutat Res.* (2018) 776:46–69. doi: 10.1016/j.mrrev.2018.04.001

Conflict of Interest: The authors declare that the research was conducted in the absence of any commercial or financial relationships that could be construed as a potential conflict of interest.

Publisher's Note: All claims expressed in this article are solely those of the authors and do not necessarily represent those of their affiliated organizations, or those of the publisher, the editors and the reviewers. Any product that may be evaluated in this article, or claim that may be made by its manufacturer, is not guaranteed or endorsed by the publisher.

Copyright © 2021 Strigari, Strolin, Morganti and Bartoloni. This is an open-access article distributed under the terms of the Creative Commons Attribution License (CC BY). The use, distribution or reproduction in other forums is permitted, provided the original author(s) and the copyright owner(s) are credited and that the original publication in this journal is cited, in accordance with accepted academic practice. No use, distribution or reproduction is permitted which does not comply with these terms.



Combined Effects of Proton Radiation and Simulated Microgravity on the Cell Viability and ALP Activity of Murine Osteoblast Cells

Liqiu Ma^{1,2}, Fuquan Kong^{1,2}, Yihao Gong^{1,2}, Qiaojuan Wang^{1,2}, Jiancheng Liu^{1,2} and Li Sui^{1,2*}

¹ Department of Nuclear Physics, China Institute of Atomic Energy, Beijing, China, ² National Innovation Center of Radiation Application, Beijing, China

OPEN ACCESS

Edited by:

Fei Ye,
Institute of Modern Physics
(CAS), China

Reviewed by:

Yang Li,
Gunma University Heavy Ion Medical
Center, Japan
Balázs Gergely Madas,
Centre for Energy Research, Hungary

*Correspondence:

Li Sui
lisui@ciae.ac.cn

Specialty section:

This article was submitted to
Radiation and Health,
a section of the journal
Frontiers in Public Health

Received: 16 August 2021

Accepted: 04 November 2021

Published: 30 November 2021

Citation:

Ma L, Kong F, Gong Y, Wang Q, Liu J
and Sui L (2021) Combined Effects of
Proton Radiation and Simulated
Microgravity on the Cell Viability and
ALP Activity of Murine Osteoblast
Cells. *Front. Public Health* 9:759236.
doi: 10.3389/fpubh.2021.759236

Proton radiation (PR) and microgravity (μ G) are two key factors that impact living things in space. This study aimed to explore the combined effects of PR and simulated μ G (S μ G) on bone function. Mouse embryo osteoblast precursor cells (MC3T3-E1) were irradiated with proton beams and immediately treated with S μ G for 2 days using a three-dimensional clinostat. All samples were subjected to cell viability, alkaline phosphatase (ALP) activity and transcriptome assays. The results showed that cell viability decreased with increasing doses of PR. The peak ALP activity after PR or S μ G alone was lower than that obtained with the non-treatment control. No difference in cell viability or ALP activity was found between 1 Gy PR combined with S μ G (PR-S μ G) and PR alone. However, 4 Gy PR-S μ G resulted in decreased cell viability and ALP activity compared with those obtained with PR alone. Furthermore, Gene Ontology analysis revealed the same trend. These results revealed that PR-S μ G may lead to reductions in the proliferation and differentiation capacities of cells in a dose-dependent manner. Our data provide new insights into bone-related hazards caused by multiple factors, such as PR and μ G, in the space environment.

Keywords: proton radiation, microgravity, bone function, transcriptome, combined effects

INTRODUCTION

With the comprehensive development of manned space exploration missions (such as manned missions to the Moon and manned missions to Mars), more astronauts need to be sent into space. Astronauts on space missions will experience space environmental stressors, such as continuous microgravity (μ G) and uninterrupted doses of ionizing radiation (1). The impact of the space environment on astronauts is directly related to their own health and whether the space mission can be successfully completed. Therefore, it is necessary to perform a risk assessment of the space environment for astronauts.

The risks of the μ G environment to astronauts' health cannot be ignored. Long-term space flight causes a variety of physiological and pathological changes in the body of astronauts, such as bone loss, decreased immune function, and muscle atrophy. One of the most obvious is the decrease in bone density caused by space μ G. A recent study conducted a systematic retrospective analysis of the bone density of 148 individuals who had performed space

missions and found that the changes in bone density values caused by space microgravity depend on the skeletal-site position relative to the gravitational vector. For example, compared with the upper limbs and thoracic vertebrae, the bone density of pelvis, lumbar vertebrae and lower limbs has decreased more severely (2). The average bone loss of 1% per month during space flight is a serious threat to the health of astronauts (3), and the main cause of space bone loss is decreased bone formation and not bone resorption (4, 5). In addition to the effects of μ G on astronauts, space radiation also poses a threat to their health. Space agencies have stated that the maximum allowable dose for an astronaut over a lifetime is approximately 1 Sv (6). Radiobiology studies have shown that ionizing radiation damage is divided into physical damage directly caused by charged particles to biologically active molecules and damage indirectly caused by free radicals generated by the reaction of charged ions with water (7). At the molecular level, ionizing radiation can induce gene mutations, gene expression changes, DNA methylation, and protein expression (8–11). At the cellular level, ionizing radiation damage mainly includes decreased cell survival, cell cycle arrest, and chromosomal aberrations (12). At the human level, this damage is not only associated with a higher cancer risk (13) but can also cause temporary or permanent damage to organs such as the cardiovascular system (14), central nervous system (15), and eyes (16) and can even endanger the life of astronauts in severe cases. However, the influence of space radiation on bone remains unclear.

Furthermore, the combined effect of space radiation and μ G has been widely considered. Horneck et al. showed that various organisms are irradiated before space flight to test the influence of μ G on the repair of radiation-induced DNA damage, but again, no significant differences were detected between space and ground (17). It has been reported that the presence of μ G enhances the DNA damage, mutagenic effects and chromosome aberrations induced by radiation (18–20). However, the combined effects of radiation and μ G on bone cells are not well-understood.

Protons are one of the main components of space radiation and exhibit the largest proportion and highest flux (21). In spacecraft and space stations, high-energy protons can directly pass through the shielding layer. The nuclear reaction of high-energy heavy ions in galaxy cosmic rays with the shielding material will also produce a large number of secondary protons (22, 23). Obtaining more basic data based on the combination of proton radiation (PR) and simulated μ G (S μ G) is necessary to reasonably evaluate the effects of the space environment. In this study, we evaluated the viability and alkaline phosphatase (ALP) activity of osteoblast MC3T3-E1 cells to investigate the biological effect of PR combined with S μ G (PR-S μ G).

MATERIALS AND METHODS

Cell Culture

Mouse embryo osteoblast precursor MC3T3-E1 cells were purchased from Institute of Basic Medical Sciences Chinese Academy of Medical Sciences. MC3T3-E1 cells were cultured in α -MEM (HyClone, Logan, UT, USA). All growth media

contained 10% fetal bovine serum (HyClone), penicillin (50 units/ml), and streptomycin (50 μ g/ml). For the examination of ALP activity, untreated control cells and PR- and/or S μ G-treated cells were plated in 12-well plates and incubated in osteogenic medium consisting of growth media supplemented with 50 μ g/ml L-ascorbic acid (vitamin C), 10 mM β -glycerophosphate and 100 nM dexamethasone. All cells were maintained at 37°C in an incubator containing 5% CO₂.

Experimental Design

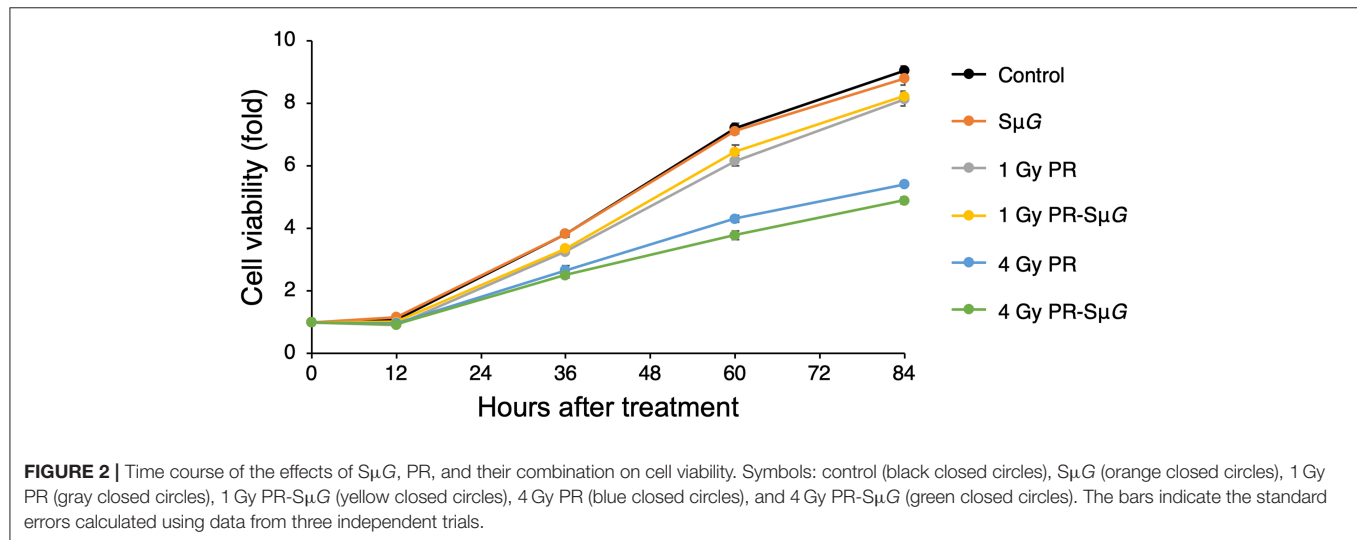
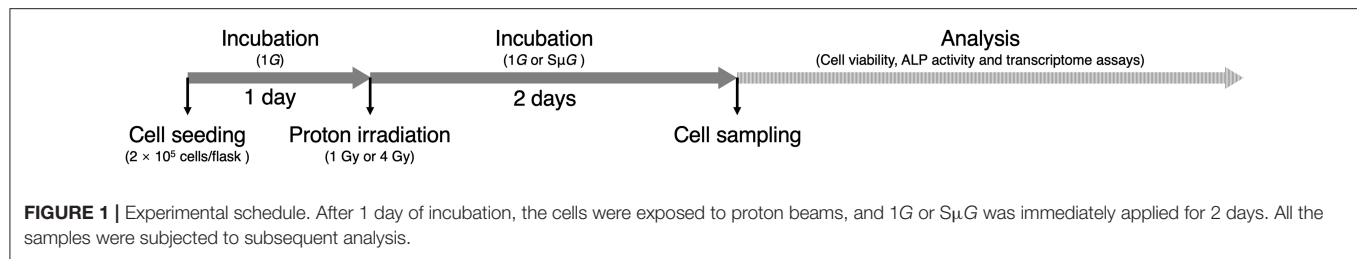
Mouse embryo osteoblast precursor cells (MC3T3-E1) were plated in a T25 flask at a density of 2×10^5 cells/flask. After 24 h of incubation, the cells were exposed to 1 Gy (astronaut career limit dose) (6) or 4 Gy (half lethal dose of bone marrow cells) (24) proton beams (22 MeV, 0.8 Gy/min) at the Beijing Tandem Accelerator Nuclear Physics National Laboratory, and S μ G ($\sim 10^{-3}$ G) was immediately applied for 2 days using a three-dimensional clinostat (Gravite, Space Bio-Laboratories Co., Ltd., Hiroshima, Japan). All the samples were subjected to cell viability, ALP activity and transcriptome assays (Figure 1).

Cell Viability Assay

A Cell Counting Kit-8 (CCK-8) assay (DOJINDO, Kumamoto, Japan) was used to estimate the cell viability of osteoblasts after PR and/or S μ G treatments. Briefly, untreated control cells and PR- and/or S μ G-treated cells were plated in 96-well plates at a density of 4×10^3 cells/well, and 6 replicate wells of each cell group were included in the plates. The cells were cultured for 0, 12, 36, 60, 84 h. At each end point, 10 μ l of CCK-8 reagent was added to the corresponding wells, and the plates were incubated for 2 h at 37°C in an incubator containing 5% CO₂. The absorbance values at 450 nm were read using an automated microplate reader (Beijing Perlong New Technology Co., Ltd., Beijing, China). The cell viability (fold change) of each group at different time points was normalized by the cell viability on Day 0 (0 h).

Cell ALP Activity Assay

Untreated control cells and PR- and/or S μ G-treated cells were plated in 12-well plates at a density of 2×10^4 cells/well and cultured for 4, 7, and 10 days. The medium was changed every 3 days. At each end point, the cells were washed three times with PBS and suspended in 200 μ l of Triton X-100 lysis buffer (Beijing Leagene Biotechnology Co., Ltd., Beijing, China) for 10 s. The homogenate was centrifuged at $12,000 \times g$ for 10 min, and the supernatant was used for subsequent BCA protein and ALP activity assays. Total protein was quantified using a Pierce BCA Protein Assay Kit according to the manufacturer's instructions (Pierce Biotechnology, Rockford, IL, USA). ALP activities in the cultured cells were determined by measuring released *p*-nitrophenyl (FUJIFILM Wako Pure Chemical Co., Osaka, Japan). After 15 min of incubation at 37°C, the absorbance of *p*-nitrophenyl at 405 nm was measured using an automated microplate reader (Beijing Perlong New Technology Co., Ltd., Beijing, China). The relative ALP activity was defined as the concentration of released *p*-nitrophenyl per minute per μ g of protein.



RNA Isolation and Library Preparation

Total RNA was extracted using TRIzol reagent according to the manufacturer's protocol. The RNA purity and quantification were evaluated using a NanoDrop 2000 spectrophotometer (Thermo Scientific, USA). RNA integrity was assessed using the Agilent 2100 Bioanalyzer (Agilent Technologies, Santa Clara, CA, USA). Libraries were then constructed using the TruSeq Stranded mRNA LT Sample Prep Kit (Illumina, San Diego, CA, USA) according to the manufacturer's instructions.

RNA Sequencing and Transcriptome Analysis

The libraries were sequenced on an Illumina HiSeq X Ten platform, and 150-bp paired-end reads were generated. Approximately 50 M raw reads were generated from each sample. The raw data (raw reads) in FASTQ format were first processed using Trimmomatic (25), and the low-quality reads were removed to obtain clean reads. The deep sequencing data from the RNA sequencing analyses have been deposited under accession number PRJNA754381 in the NCBI (National Center for Biotechnology Information) Sequence Read Archive.

The clean reads were mapped to the mouse genome (GRCm38) using HISAT2 (26). The FPKM (27) value of each gene was calculated using Cufflinks (28), and the read counts of each gene were obtained with HTSeq-count (29). Differential expression analysis was performed using

the DESeq (2012) R package. To investigate the profile of genes that exhibit changes in expression, a screening of genes was performed based on a threshold of p -value < 0.05 and a fold change > 2 or fold change < 0.5. A hierarchical cluster analysis of differentially expressed genes (DEGs) was performed to demonstrate the expression pattern of genes in different groups. To gain a general idea of the biological functions of the DEGs, a gene ontology (GO) enrichment analysis was performed using R based on the hypergeometric distribution. A false discovery rate (FDR) < 0.05 served as the threshold to select the GO categories that were significantly enriched.

Statistical Analysis

The statistical significance of the differences was tested using Student's t -test. The differences between the means were considered statistically significant if p < 0.05.

RESULTS

Characterization of MC3T3-E1 Cell Viability After PR-S μ G Treatment

We examined the cell viability of MC3T3-E1 cells after PR-S μ G treatment. MC3T3-E1 cells were irradiated with 1 Gy or 4 Gy proton beams, and S μ G was then immediately applied for 2 days using a three-dimensional clinostat. After these treatments, a cell viability analysis was performed using the CCK-8. No

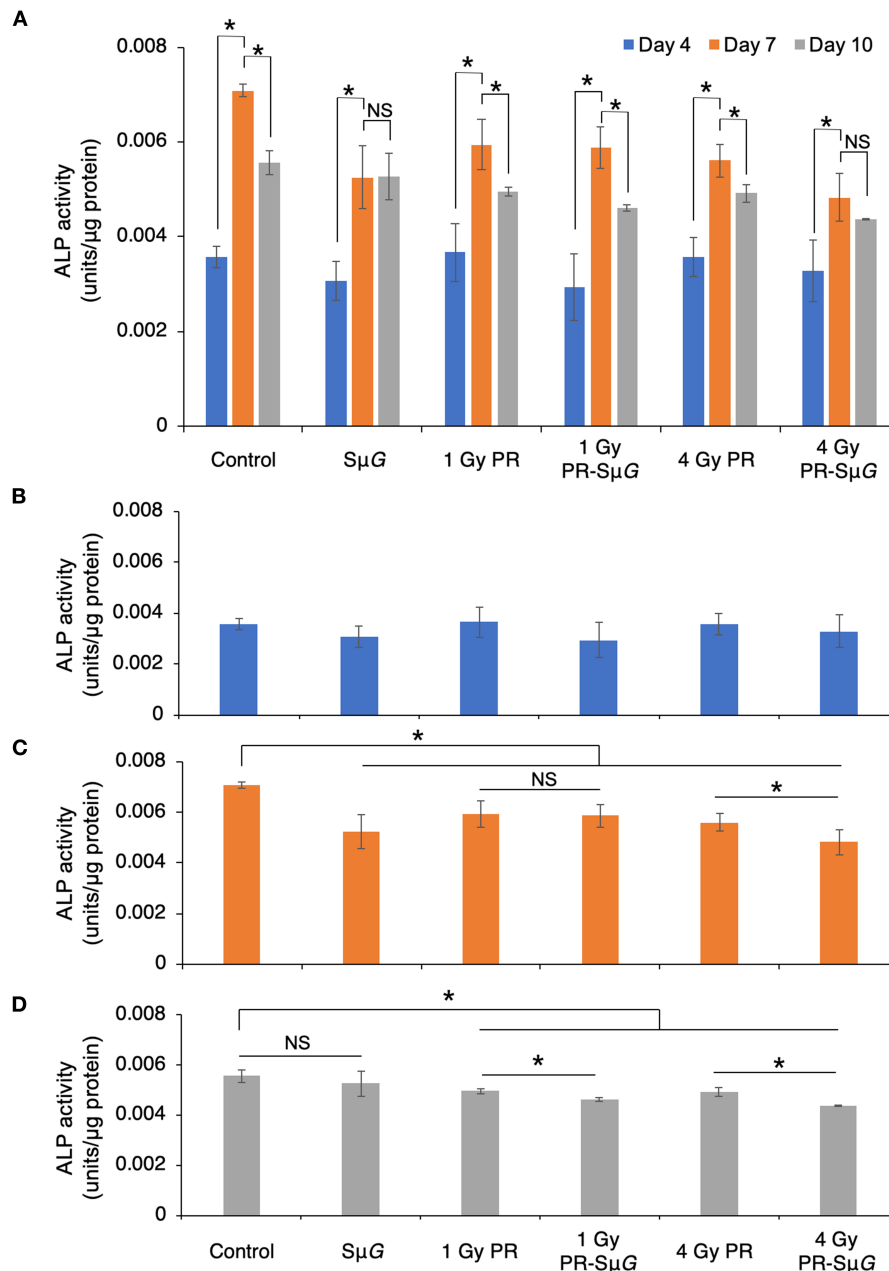


FIGURE 3 | Effects of S μ G, PR, and their combination on ALP activity. **(A)** Time course of ALP activity. ALP activity at day 4 **(B)**, day 7 **(C)**, and day 10 **(D)** posttreatment. The mean values with standard errors are shown. * $p < 0.05$, NS indicates not significant ($p > 0.05$) (Student's t -test). Symbols: day 4 (blue column), day 7 (orange column), and day 10 (gray column). The bars indicate the standard errors calculated using data from three independent trials.

detectable difference in cell viability was found between the control and S μ G groups (Figure 2). Cell viability decreased with increasing doses of PR alone. No difference in cell viability was detected between 1 Gy PR-S μ G and 1 Gy PR alone after 36 hours, whereas the 4 Gy PR-S μ G treatment resulted in significantly lower viability than that obtained with the 4 Gy PR alone ($p < 0.05$).

Evaluation of the ALP Activity of MC3T3-E1 Cells After PR-S μ G Treatment

To further understand the effect of PR-S μ G treatment on the function of osteoblasts, we evaluated the ALP activity of MC3T3-E1 cells on days 4, 7, and 10 after PR and/or S μ G treatment. ALP activity was significantly increased in all the groups from days 4 to 7 after treatment. The highest ALP activity was observed

TABLE 1 | List of gene function annotations related to PR and/or S μ G.

	GO ID	GO term	FDR value
vs. 1 Gy PR-SμG			
1 Gy PR	GO:0060349	Bone morphogenesis	0.020898789
S μ G	N/A	N/A	N/A
vs. 4 Gy PR-SμG			
4 Gy PR	GO:0033690	Positive regulation of osteoblast proliferation	0.029716189
	GO:0045667	Regulation of osteoblast differentiation	0.036043093
	GO:0045779	Negative regulation of bone resorption	0.036043093
S μ G	GO:0030500	Regulation of bone mineralization	0.004557925
	GO:0030282	Bone mineralization	0.007654929
	GO:0060349	Bone morphogenesis	0.008773026
	GO:0045669	Positive regulation of osteoblast differentiation	0.022438056

N/A, not applicable.

at day 7 in all the groups. ALP activity in the S μ G and 4 Gy PR-S μ G groups did not significantly change from day 7 to day 10, but the other four groups showed a significant decrease during this period (**Figure 3A**). At day 4 after treatment, no significant difference in ALP activity was found among the groups (**Figure 3B**). At day 7 after treatment, ALP activity was inhibited in all five treatment groups compared with the control group. Although no significant difference in ALP activity was found between the 1 Gy PR and 1 Gy PR-S μ G groups, that of the 4 Gy PR-S μ G group was significantly lower than that of the 4 Gy PR group (**Figure 3C**). At day 10 after treatment, although no significant difference in ALP activity was found between S μ G alone and the control groups, that of the PR-S μ G group was significantly lower than that of the PR group (**Figure 3D**). Therefore, the S μ G alone and PR alone can each inhibit ALP activity, and the PR-S μ G treatment can further reduce the activity of ALP.

Transcriptome Features of MC3T3-E1 Cells After PR-S μ G Treatment

In this study, 20 samples from the five experimental groups (three independent biological replicates of each group) and the control group (five replicates) were sequenced, and a total of 936,781,862 high-quality reads were obtained from the experimental groups (**Supplementary Table 1**). A nucleotide composition analysis showed that the total GC content of the transcriptome data was 52.40%. The analysis of the base composition and quality showed that the base composition of the original sequencing data was in good condition. For each replicate, 98.28–98.85% of the reads could be mapped to the mouse genome (GRCm38) using HISAT2, and among these mapped reads, 92.11–93.01% achieved a unique match. All sequences covered the reference genes evenly, which showed that the overall quality of the sequences was good and that the sequencing data were random and could be used for subsequent analysis.

To clarify the mechanism underlying the characteristic changes after PR-S μ G treatment, the transcriptome features of PR and/or S μ G treatment were assessed by RNA-seq analysis,

and an osteogenesis-related GO enrichment analysis was performed (**Table 1**). The GO analysis of the DEGs identified from the comparison of 1 Gy PR vs. 1 Gy PR-S μ G resulted in the selection of only the bone morphogenesis-related category (GO:0060349). In contrast, three osteoblast proliferation- or differentiation-related GO categories (GO:0033690, GO:0045667, and GO:0045779) were found to be changed in the comparison of 4 Gy PR vs. 4 Gy PR-S μ G. We did not find any GO category from the comparison of S μ G vs. 1 Gy PR-S μ G, whereas four osteogenesis-related GO categories were found to differ between the S μ G and 4 Gy PR-S μ G groups.

DISCUSSION

The effect of the space environment on cell viability is due to many factors, such as space radiation and μ G. Previous studies have shown that short-duration space travel can cause significant changes in the number and size of osteoblasts (30). Consistently, our experimental data suggest that PR-S μ G also inhibits cell viability (**Figure 2**). Furthermore, treatment with PR alone but not S μ G alone could induce the inhibition of cell activity. Therefore, compared with μ G factors, radiation factors may be an important factor affecting osteoblast viability. In contrast, a large solar proton event (SPE) could be encountered during a long-duration deep-space flight or during long-term missions such as landing on Mars. The risk to astronauts of high-dose proton irradiation in the SPE cannot be ignored. Our experimental results show that a high dose (4 Gy) of PR combined with S μ G has a stronger inhibitory effect on cell viability than PR alone. Although a previous study showed that the radiation-induced DNA damage repair of fibroblasts is not affected by μ G (17), our results suggest that the radiation-induced osteoblast DNA damage repair ability may be affected by μ G. These results indicate that PR combined with S μ G may induce an additional inhibitory effect on osteoblastic viability, and the level of inhibition increases with increasing radiation dose.

ALP is a glycoprotein that can catalyze the hydrolysis of monophosphoric acid in alkaline environments. This protein

can hydrolyse inorganic phosphate, increase the concentration of local inorganic phosphate, promote bone mineralization, and provide conditions for the formation of hydroxyapatite crystallization in bone tissue, which results in initiation of the processes of extracellular matrix mineralization and calcium and phosphorus deposition (31, 32). Therefore, ALP is an important marker of the differentiation and maturation of osteoblasts, and its activity is one of the important indicators of osteocyte function, which can indirectly reflect the function of osteoblasts (33). The effect of the space environment on the bone formation process has been confirmed by space missions (Euromir 95) (34). This study revealed the trends in the change in bone metabolic markers during the 180-day stay on the Mir space station. The results showed that the concentration of the bone formation marker ALP decreased sharply from 0 to 50 days during space flight, whereas the concentration of the bone absorption marker D-pyridinoline increased. The above experimental results prove that the differentiation function of bone cells is reduced in the space environment. Because osteoblasts secrete ALP during differentiation, once osteoblasts differentiate into osteocytes, these cells will not secrete ALP (35). Our results showed that the ALP levels were low 4 days after treatment, which indicated that the cells were in prophase of osteoblastic differentiation (**Figure 3A**). The ALP level reached the highest level after 7 days, which indicated the highest differentiation level of osteoblasts. After 10 days, ALP gradually decreased, indicating that some osteoblasts had differentiated into osteocytes. Our experimental data indicated that PR and/or S μ G inhibited ALP activity at the highest differentiation phase of osteoblasts (day 7, **Figure 3C**). Consistent with the cell viability results, only a high dose (4 Gy) of PR combined with S μ G significantly inhibited ALP activity compared with the results obtained with PR alone. These results suggest that a higher dose of PR combined with S μ G may produce an additional ALP activity inhibitory effect on osteoblasts due to the lower cell viability. At day 10 after treatment, no significant difference in ALP activity was found between the S μ G group and the control group, whereas the ALP activity level in the irradiation groups was significantly lower (**Figure 3D**). The results indicated that the ALP activity of the S μ G alone group recovered completely, and the recovery ability of the other groups was weak. Compared with that in the PR group, the ALP activity in the PR-S μ G group was lower, indicating that the recovery of osteoblast differentiation function was more difficult under the environment induced by the combined effects of PR-S μ G treatment.

The cell viability and function of osteoblasts showed differences between the 4 Gy PR and 4 Gy PR-S μ G groups but not between the 1 Gy PR and 1 Gy PR-S μ G groups. Our transcriptome analysis data strongly support this result (**Table 1**). Only the comparison of 4 Gy PR vs. 4 Gy PR-S μ G revealed a change in GO:0033690, which is related to activating or increasing the rate or extent of osteoblast proliferation, whereas the comparison of 1 Gy PR vs. 1 Gy PR-S μ G showed no significant change in GO:0033690. This result is consistent with

the cell viability results. In addition, only the comparison of 4 Gy PR vs. 4 Gy PR-S μ G showed changes in GO:0045667, which is related to modulating the frequency, rate or extent of osteoblast differentiation, whereas 1 Gy PR vs. 1 Gy PR-S μ G showed no significant changes in GO:0045667. This result was consistent with the results from the analysis of cell ALP activity. Together, these results suggest that PR-S μ G treatment has the ability to alter genes involved in osteoblast proliferation and differentiation and that the expression of these genes ultimately leads to changes in cell viability and ALP activity.

One limitation of this experiment lies in the use of only ALP activity assay to explore the possible effect of PR and/or S μ G on bone function; however, the ALP expression still shows similar trends with GO term among groups. These results provide valuable reference evidence for further studies using other bone functional markers and even the rodent hindlimb unloading model on the combined biological effects of PR-S μ G.

In conclusion, our results suggest that PR-S μ G may exert additional inhibitory effects on the proliferation and differentiation of osteoblasts in a dose-dependent manner. Radiation may be an important factor affecting the recovery of the differentiation ability of osteoblasts, regardless of treatment with PR alone or PR-S μ G. Our data provide new insights for understanding bone-related hazards caused by multiple factors, such as PR and μ G, in the space environment.

DATA AVAILABILITY STATEMENT

The datasets presented in this study can be found in online repositories. The names of the repository/repositories and accession number(s) can be found at: <https://www.ncbi.nlm.nih.gov/>, PRJNA754381.

AUTHOR CONTRIBUTIONS

LM and LS designed research. LM, FK, YG, JL, and QW performed the research. LM analyzed data and drafted the manuscript. LM and LS revised the manuscript. All authors have read and agreed to the final manuscript.

FUNDING

This research was funded by the Continuous Basic Scientific Research Project (grant number WDJC-2019-11).

ACKNOWLEDGMENTS

We thank Joanna G. at AJE (Beijing, China) for editing a draft of this manuscript.

SUPPLEMENTARY MATERIAL

The Supplementary Material for this article can be found online at: <https://www.frontiersin.org/articles/10.3389/fpubh.2021.759236/full#supplementary-material>

REFERENCES

- Moreno-Villanueva M, Wong M, Lu T, Zhang Y, Wu H. Interplay of space radiation and microgravity in DNA damage and DNA damage response. *NPJ Microgravity*. (2017) 3:14. doi: 10.1038/s41526-017-0019-7
- Stavrichuk M, Mikolajewicz N, Corlett T, Morris M, Komarova SV. A systematic review and meta-analysis of bone loss in space travelers. *NPJ Microgravity*. (2020) 6:13. doi: 10.1038/s41526-020-0103-2
- Tilton FE, Degioanni JJ, Schneider vs. long-term follow-up of Skylab bone demineralization. *Aviat Space Environ Med*. (1980) 51:1209-13
- Morey ER, Baylink DJ. Inhibition of bone formation during space flight. *Science*. (1978) 201:1138-41. doi: 10.1126/science.150643
- Vico L, Novikov VE, Very JM, Alexandre C. Bone histomorphometric comparison of rat tibial metaphysis after 7-day tail suspension vs. 7-day spaceflight. *Aviat Space Environ Med*. (1991) 62:26-31
- Zeitlin C, Hassler DM, Cucinotta FA, Ehresmann B, Wimmer-Schweingruber RF, Brinza DE, et al. Measurements of energetic particle radiation in transit to Mars on the Mars Science Laboratory. *Science*. (2013) 340:1080-4. doi: 10.1126/science.1235989
- Surdutovich E, Solov'yov AV. Multiscale physics of ion-induced radiation damage. *Appl Radiat Isot*. (2014) 83:100-4. doi: 10.1016/j.apradiso.2013.01.035
- Adewoye AB, Lindsay SJ, Dubrova YE, Hurler ME. The genome-wide effects of ionizing radiation on mutation induction in the mammalian germline. *Nat Commun*. (2015) 6:6684. doi: 10.1038/ncomms7684
- Long XH, Zhao ZQ, He XP, Wang HP, Xu QZ, An J, et al. Dose-dependent expression changes of early response genes to ionizing radiation in human lymphoblastoid cells. *Int J Mol Med*. (2007) 19:607-15. doi: 10.3892/ijmm.19.4.607
- Prior S, Miosse IR, Nizarushimana E, Pathak R, Skinner C, Kutanzi KR, et al. Densely ionizing radiation affects DNA methylation of selective LINE-1 elements. *Environ Res*. (2016) 150:470-81. doi: 10.1016/j.envres.2016.06.043
- Calaf GM, Hei TK. Ionizing radiation induces alterations in cellular proliferation and c-myc, c-jun and c-fos protein expression in breast epithelial cells. *Int J Oncol*. (2004) 25:1859-66. doi: 10.3892/ijo.25.6.1859
- Little JB. Cellular, molecular, and carcinogenic effects of radiation. *Hematol Oncol Clin North Am*. (1993) 7:337-52. doi: 10.1016/S0889-8588(18)30244-2
- Barcellos-Hoff MH, Blakely EA, Burma S, Fornace AJ, Jr., Gerson S, Hlatky L, et al. Concepts and challenges in cancer risk prediction for the space radiation environment. *Life Sci Space Res*. (2015) 6:92-103. doi: 10.1016/j.lssr.2015.07.006
- Delp MD, Charvat JM, Limoli CL, Globus RK, Ghosh P. Apollo lunar astronauts show higher cardiovascular disease mortality: possible deep space radiation effects on the vascular endothelium. *Sci Rep*. (2016) 6:29901. doi: 10.1038/srep29901
- Cucinotta FA, Alp M, Sulzman FM, Wang M. Space radiation risks to the central nervous system. *Life Sciences in Space Research*. (2014) 2:54-69. doi: 10.1016/j.lssr.2014.06.003
- Cucinotta FA, Schimmerling W, Wilson JW, Peterson LE, Badhwar GD, Saganti PB, et al. Space radiation cancer risks and uncertainties for Mars missions. *Radiat Res*. (2001) 156:682-8. doi: 10.1667/0033-7587(2001)156[0682:SRCRAU]2.0.CO;2
- Horneck G, Rettberg P, Kozubek S, Baumstark-Khan C, Rink H, Schafer M, et al. The influence of microgravity on repair of radiation-induced DNA damage in bacteria and human fibroblasts. *Radiat Res*. (1997) 147:376-84. doi: 10.2307/3579347
- Gao Y, Xu D, Zhao L, Zhang M, Sun Y. Effects of microgravity on DNA damage response in *Caenorhabditis elegans* during Shenzhou-8 spaceflight. *Int J Radiat Biol*. (2015) 91:531-9. doi: 10.3109/09553002.2015.1043754
- Ikenaga M, Yoshikawa I, Kojo M, Ayaki T, Ryo H, Ishizaki K, et al. Mutations induced in *Drosophila* during space flight. *Biol Sci Space*. (1997) 11:346-50. doi: 10.2187/bss.11.346
- Hada M, Ikeda H, Rhone JR, Beitman AJ, Plante I, Souda H, et al. Increased chromosome aberrations in cells exposed simultaneously to simulated microgravity and radiation. *Int J Mol Sci*. (2018) 20:43. doi: 10.3390/ijms20010043
- Meyer P, Ramaty R, Webber WR. Cosmic rays - astronomy with energetic particles. *Phys Today*. (1974) 27:23-32. doi: 10.1063/1.3128914
- Feit J, Milford SN. Secondary protons from cosmic-ray collisions in space. *J Geophys Res*. (1965) 70:5957-60. doi: 10.1029/JZ070i023p05957
- Inozemtsev KO, Kushin VV, Stradi A, Ambrozova I, Kodaira S, Szabo J, et al. Measurement of different components of secondary radiation onboard international space station by means of passive detectors. *Radiat Prot Dosimetry*. (2018) 181:412-7. doi: 10.1093/rpd/ncy043
- ICRP. 1990 Recommendations of the International Commission on Radiological Protection. ICRP Publication 60. *Ann ICRP*. (1991) 21:1-201. doi: 10.1016/0146-6453(91)90066-P
- Bolger AM, Lohse M, Usadel B. Trimmomatic: a flexible trimmer for Illumina sequence data. *Bioinformatics*. (2014) 30:2114-20. doi: 10.1093/bioinformatics/btu170
- Kim D, Langmead B, Salzberg SL. HISAT: a fast spliced aligner with low memory requirements. *Nat Methods*. (2015) 12:357-60. doi: 10.1038/nmeth.3317
- Roberts A, Trapnell C, Donaghey J, Rinn JL, Pachter L. Improving RNA-Seq expression estimates by correcting for fragment bias. *Genome Biol*. (2011) 12:R22. doi: 10.1186/gb-2011-12-3-r22
- Trapnell C, Williams BA, Pertea G, Mortazavi A, Kwan G, van Baren MJ, et al. Transcript assembly and quantification by RNA-Seq reveals unannotated transcripts and isoform switching during cell differentiation. *Nat Biotechnol*. (2010) 28:511-5. doi: 10.1038/nbt.1621
- Anders S, Pyl PT, Huber W. HTSeq—a Python framework to work with high-throughput sequencing data. *Bioinformatics*. (2015) 31:166-9. doi: 10.1093/bioinformatics/btu638
- Hughes-Fulford M, Lewis ML. Effects of microgravity on osteoblast growth activation. *Exp Cell Res*. (1996) 224:103-9. doi: 10.1006/excr.1996.0116
- Whyte MP. Hypophosphatasia and the role of alkaline phosphatase in skeletal mineralization. *Endocr Rev*. (1994) 15:439-61. doi: 10.1210/er.15.4.439
- Orimo H. The mechanism of mineralization and the role of alkaline phosphatase in health and disease. *J Nippon Med Sch*. (2010) 77:4-12. doi: 10.1272/jnms.77.4
- Torii Y, Hitomi K, Yamagishi Y, Tsukagoshi N. Demonstration of alkaline phosphatase participation in the mineralization of osteoblasts by antisense RNA approach. *Cell Biol Int*. (1996) 20:459-64. doi: 10.1006/cbir.1996.0060
- Caillot-Augusseau A, Lafage-Proust MH, Soler C, Pernod J, Dubois F, Alexandre C. Bone formation and resorption biological markers in cosmonauts during and after a 180-day space flight (Euromir 95). *Clin Chem*. (1998) 44:578-85. doi: 10.1093/clinchem/44.3.578
- Tang XK, Cheng W, Xu B, Ying H, Tong PJ, Xiao LW. Experimental study on the isolated culture of osteocytes and identification of osteoblasts in rats. *Zhongguo Gu Shang*. (2013) 26:227-31.

Conflict of Interest: The authors declare that the research was conducted in the absence of any commercial or financial relationships that could be construed as a potential conflict of interest.

Publisher's Note: All claims expressed in this article are solely those of the authors and do not necessarily represent those of their affiliated organizations, or those of the publisher, the editors and the reviewers. Any product that may be evaluated in this article, or claim that may be made by its manufacturer, is not guaranteed or endorsed by the publisher.

Copyright © 2021 Ma, Kong, Gong, Wang, Liu and Sui. This is an open-access article distributed under the terms of the Creative Commons Attribution License (CC BY). The use, distribution or reproduction in other forums is permitted, provided the original author(s) and the copyright owner(s) are credited and that the original publication in this journal is cited, in accordance with accepted academic practice. No use, distribution or reproduction is permitted which does not comply with these terms.



Radioactivity and Space Range of Ultra-Low-Activity for *in vivo* Off-line PET Verification of Proton and Carbon Ion Beam—A Phantom Study

Fuquan Zhang^{1,2,3,4†}, Junyu Zhang^{1,2,3,4†}, Yan Lu⁵, Yixiangzi Sheng⁵, Yun Sun³, Jiangang Zhang³, Jingyi Cheng^{2,3,4} and Rong Zhou^{1*}

¹ College of Physics, Sichuan University, Chengdu, China, ² Shanghai Key Laboratory of Radiation Oncology, Shanghai, China, ³ Department of Nuclear Medicine, Shanghai Proton and Heavy Ion Center, Fudan University Cancer Hospital, Shanghai, China, ⁴ Shanghai Engineering Research Center of Proton and Heavy Ion Radiation Therapy, Shanghai, China, ⁵ Department of Radiotherapy, Shanghai Proton and Heavy Ion Center (SPHIC), Shanghai, China

OPEN ACCESS

Edited by:

Fei Ye,
Institute of Modern Physics
(CAS), China

Reviewed by:

Yidong Yang,
University of Science and Technology
of China, China
Anita Csordás,
University of Pannonia, Hungary

*Correspondence:

Rong Zhou
zhou.rong@scu.edu.cn

[†]These authors share first authorship

Specialty section:

This article was submitted to
Radiation and Health,
a section of the journal
Frontiers in Public Health

Received: 05 September 2021

Accepted: 03 November 2021

Published: 06 December 2021

Citation:

Zhang F, Zhang J, Lu Y, Sheng Y, Sun Y, Zhang J, Cheng J and Zhou R (2021) Radioactivity and Space Range of Ultra-Low-Activity for *in vivo* Off-line PET Verification of Proton and Carbon Ion Beam—A Phantom Study. *Front. Public Health* 9:771017. doi: 10.3389/fpubh.2021.771017

Purpose: The radioactivity induced by proton and heavy ion beam belongs to the ultra-low-activity (ULA). Therefore, the radioactivity and space range of commercial off-line positron emission tomography (PET) acquisition based on ULA should be evaluated accurately to guarantee the reliability of clinical verification. The purpose of this study is to quantify the radioactivity and space range of off-line PET acquisition by simulating the ULA triggered by proton and heavy ion beam.

Methods: PET equipment validation phantom and low activity ¹⁸F-FDG were used to simulate the ULA with radioactivity of 11.1–1480 Bq/mL. The radioactivity of ULA was evaluated by comparing the radioactivity in the images with the values calculated from the decay function with a radioactivity error tolerance of 5%. The space range of ULA was evaluated by comparing the width of the R50 analyzed activity distribution curve with the actual width of the container with a space range error tolerance of 4 mm.

Results: When radioactivity of ULA was >148 Bq/mL, the radioactivity error was <5%. When radioactivity of ULA was >30 Bq/mL, the space range error was below 4 mm.

Conclusions: Off-line PET can be used to quantify the radioactivity of proton and heavy ion beam when the ULA exceeds 148 Bq/mL, both in radioactivity and in space range.

Keywords: ultra-low activity, off-line PET, proton therapy, beam range, PET verification

INTRODUCTION

In vivo biological verification using positron emission tomography (PET) is one of the most important estimation methods in proton or heavy ion precision radiotherapy (1–4). Models of *in vivo* biological verification using PET can be classified into three types: in-beam, in-room and off-line. In-beam and off-line methods are most frequently used in research studies and clinical practice to evaluate the precision of proton or heavy ion beam. The in-beam PET is an

ensemble of PET and particle radiotherapy terminals that can gather the β^+ signal throughout particle beam delivery. In-beam imaging is little influenced by human metabolism and blood flow, and it can increase measurement accuracy (5–7). In-room PET uses a stand-alone and full-ring PET scanner positioned in the treatment room to scan the patient (still in the treatment bed) soon after treatment. In-room PET is a compromise between in-beam and off-line PET (8). The off-line PET is more applicable: patients are transferred to the PET/CT equipment room for gathering of the β^+ signal after particle beam delivery (9, 10).

Compared with the in-beam PET, the off-line PET has several advantages such as much lower cost, shorter treatment time, and increased suitability for clinical practice (11, 12). Off-line PET offers a practical and easy-to-implement method of treatment verification for particle radiotherapy centers with PET/CT scanners located near their treatment rooms. In particle therapy, the detectable activation results from nuclear fragmentation reactions between the projectiles and the target nuclei of the traversed tissue. Proton-induced radioactivity is thus very sensitive to the elemental composition. These sources of uncertainty are reduced in the off-line scenario because of the small number of production channels that yield long-lived positron emitters (13, 14). Because of these two prominent advantages, off-line PET has achieved wide recognition in clinical practice.

In practice, the β^+ signal of acquisition in off-line PET is mainly emitted by ^{11}C (20.39 min). However, there is a 10-min interval between beam delivery and PET acquisition, which can also cause large reductions in radioactivity. PET image quality (radioactivity and beam range) is compromised when the interval time of off-line PET is too long. The radioactivity in the tumor of off-line PET imaging is 37–370 Bq/mL, which is far below the level of conventional ^{18}F FDG (fluorodeoxyglucose) PET/CT imaging (over 7,400 Bq/mL) (15). In clinical practice, the mean radioactivity of 289 Bq/mL in proton radiotherapy for breast cancer has been obtained by calculating the radioactivity of each spot within the target area. The average radioactivity of carbon ion radiotherapy in the anterior gland, liver and head tumors were 90.65, 109.89, and 138.75 Bq/mL, respectively. Hence, whether radioactivity and space range of off-line PET at ultra-low-activity (ULA) is reliable needs further verification.

The radioactivity and space range of commercial off-line PET acquisitions based on ULA should be evaluated accurately to guarantee the reliability of clinical verification. The purpose of this study is to quantify the radioactivity and space range of off-line PET acquisition by simulating the ULA triggered by proton and heavy ion beam using verification phantom.

MATERIALS AND METHODS

Equipment and Verification Phantom

The PET-CT device used in this research was a Biograph mCT PET/CT scanner (Siemens Medical Solutions USA), which has four rings of 192 blocks in total, each of which contains $13 \times$

13 lutetium-oxyorthosilicate (LSO) crystals with dimensions of $4 \times 4 \times 20$ mm. The voltages of the X-ray tube in CT were 80, 100, 120, and 140 kV, respectively. The planar resolution of the reconstruction image was 4×4 mm, and its thickness was 0.6 mm. The PET detection system had four detection rings, each of which contained 48 detection blocks. Each detection block was uniformly divided into 13×13 basic detection units, and the crystal size of each detection unit was $4 \times 4 \times 20$ mm. The aperture of the detector was 78 cm and the field of view of the detector's axial was 21.8 cm. The detector's gating window was 4.1 ns and its energy window was 435–650 keV. We used the Truex image reconstruction algorithm which incorporates OSEM (Ordered Subsets Expectation) iterative algorithm and point-spread-function correction. CT attenuation correction is used in image reconstruction.

Using a PET validation phantom (Flanged Jaszczak ECT Phantom), referring to the National Electrical Manufacturers Association (NEMA) standard, we simulated the ULA of the target after beam delivery. The phantom was cylindrical in shape, its external height was 22.24 cm, its bottom diameter was 19.24 cm, its wall thickness was 3.2 mm, and the material was PTFE. As shown in **Figure 1A**, six cylindrical containers of the same height were arranged in a ring inside the phantom. Their diameters were 8 mm (No. 1), 12 mm (No. 2), 16 mm (No. 3), and 25 mm (Nos. 4, 5, and 6), and their height was 38.1 mm. Thus, the cylinders' volumes were 1.92 ml (No. 1), 4.31 ml (No. 2), 7.66 ml (No. 3), and 18.70 ml (Nos. 4, 5, and 6). During the loading of radiopharmaceuticals into the container, small bubbles often appeared inside the small containers, so we chose the larger containers. The containers (Nos. 4 and 6) were selected as the research objects because of their large volumes and reduced bubble effects.

Experimental Design

The ULA of the experimental design was 11.1–1,480 Bq/mL. Smaller radioactivity would lead to a greater error when measuring activity. Because the measurement error of high-activity radiopharmaceuticals is small, to obtain accurate values for the activity during the measurements, the active compounds were filled into the containers 10 half-lives in advance. The radioactivity of radiopharmaceuticals was measured by the radio activity meter CRC-25R with resolution of 0.01 MBq. The radiopharmaceutical (^{18}F -FDG) at the dose of 27.09 MBq was loaded into each container (Nos. 4 and 2). The radiopharmaceutical at the dose of 95 MBq was loaded into container No. 6 with an error rate lower than one-thousandth. Then, the dye is injected into the container. After freezing, the dye and solution became solid. The container was subsequently full filled with distilled water. The interval between charging radioactive radiopharmaceuticals and scanning is 10 half-lives.

In this experiment, to account for attenuation correction, the phantom was filled with water. PET acquisition was initiated when the radioactivity in the container reached the expected range of radioactivity (**Figure 1B**). The selected parameters were weight of 50 kg, dose of 10 mCi, reconstruction layer thickness of 5 mm and Na element collection for acquisition

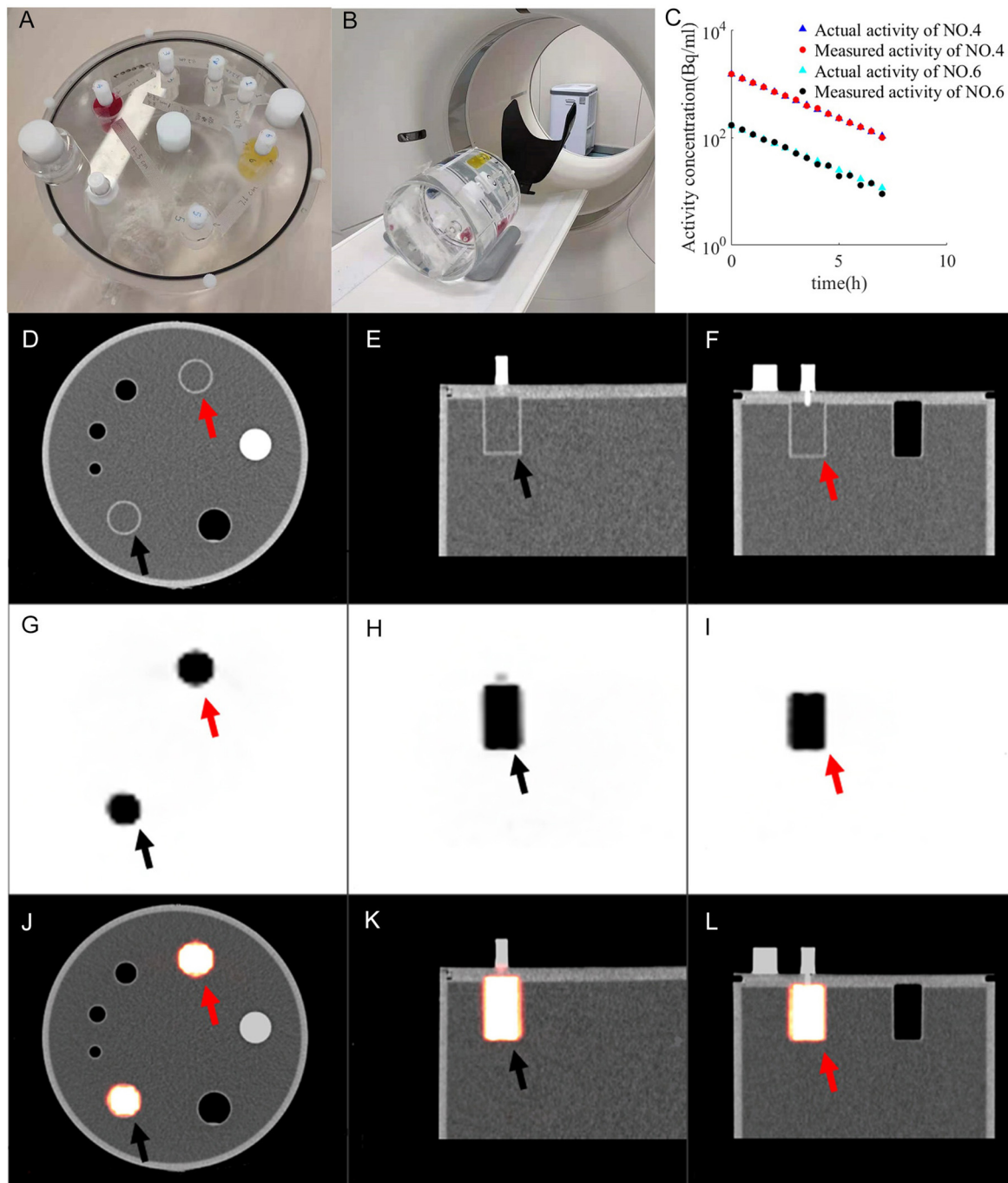


FIGURE 1 | Imaging of PET validation phantom (A) under PET/CT (B). CT images (D–F) and PET images (G–I) form fused images (J–L). The activity of container 4 (red arrow) and container 6 (black arrow) changes with time (C). R_{actu} of container 4 (blue triangle), R_{meas} of container 4 (red dot), R_{actu} of container 6 (green triangles), R_{meas} of container 6 (black dot) are distributed between 11.1 and 1,480 Bq/mL.

(16). The decay parameter was not added in the process of PET reconstruction because the half-life of ^{22}Na is 2 years. Therefore, we set the acquisition method as Na-22 to avoid any decay correction. The phantom was positioned on the

scanner couch and did not moved during acquisitions. Each acquisition time was 15 min, the acquisition interval was 15 min, the total number of scans was 15, and the total acquisition time was 8 h.

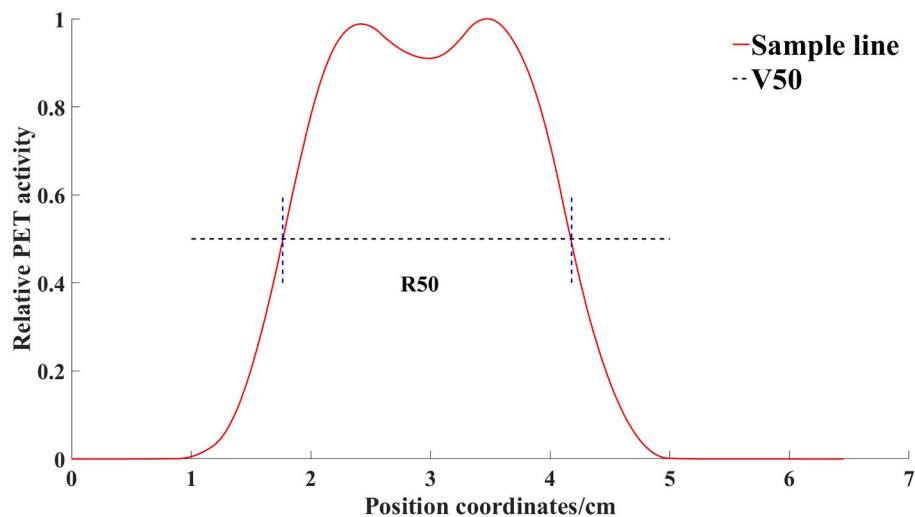


FIGURE 2 | Radioactivity distribution curve of a line through the center of the container obtained by the sampling line. V50 is the horizontal line where half of the maximum value is located. R50 refers to the distance between the points where the anterior and posterior two functional values are equal to half of the peaks, in one peak of the function.

ULA Was Quantitatively Analyzed Based on Comparing Measured and Actual Radioactivity

The radioactivity in the containers was evaluated from the PET images; the methods are according to the half-life formula:

$$A = A_0 \left(\frac{1}{2} \right)^{\frac{t}{T}}$$

where A_0 is the radioactivity before decay, the t is the decay time, and T is the half-life. The variable A would express the activity at time t .

There are two ways to measure the radioactivity in the container: (1) measurement of the radioactivity of the whole container, and then dividing it by the volume of the container to calculate the radioactivity; (2) The radioactivity distributed at the points inside the container (at points above 5 mm from the container wall) was sampled and measured. These two methods are used, respectively, to measure radioactivity.

Comparing the measured radioactivity (R_{meas}) with the actual radioactivity (R_{actu}), R_{actu} was calculated from the decay formula. R_{meas} is compared R_{actu} to obtain the error value according to the following formula:

$$\text{error} = \frac{R_{actu} - R_{meas}}{R_{actu}}$$

An appropriate function of radioactivity was obtained by fitting the error rate, from which the error rate (and its confidence interval) could be calculated. In this study, the measurement error of the radioactivity obtained from the PET images was allowed to be <5% according to the report of The American Association of Physicists in Medicine (AAPM) TG 126 (17).

Space Range of ULA Was Quantitatively Analyzed Using the Method of R50

First, we marked the center points of cylinders Nos. 4 and 6 on each layer of the PET-CT images. Then, across the center of the circle and along the X-axis and Y-axis, we created sampling lines to obtain the radioactivity values of the PET image on their paths. We used the R_{50} method (17) to analyze the width of the radioactivity distribution curve (Figure 2). R_{50} refers to the distance between the points where the anterior and posterior two functional values are equal to half of the peaks, in one peak of the function.

An appropriate function of radioactivity was obtained by fitting the width error, from which the width error (and its confidence interval) could be calculated. According to the report of AAPM Task Group 126 (17), the allowable error in PET/CT joint registration is ± 1 PET voxel, meaning that a 4-mm error is allowed in the space range.

RESULTS

The Model of ULA Was Built Using the Validation Phantom

The change in radioactivity throughout the entire acquisition time is shown in Figure 1C. R_{actu} of container 4 (blue triangle), R_{meas} of container 4 (red dot), R_{actu} of container 6 (green triangles) and R_{meas} of container 6 (black dot) are distributed between 11.1 and 1,480 Bq/mL. R_{actu} is the actual radioactivity. R_{meas} is the measured radioactivity. The resulting PET-CT image is shown in Figures 1D–L. CT images (Figures 1D–F) and PET images (Figures 1G–I) form fused images (Figures 1J–L).

Quantitative Results of ULA

Both method 1 (overall measurements) and method 2 (sampling measurements) analyzed PET images for activity values.

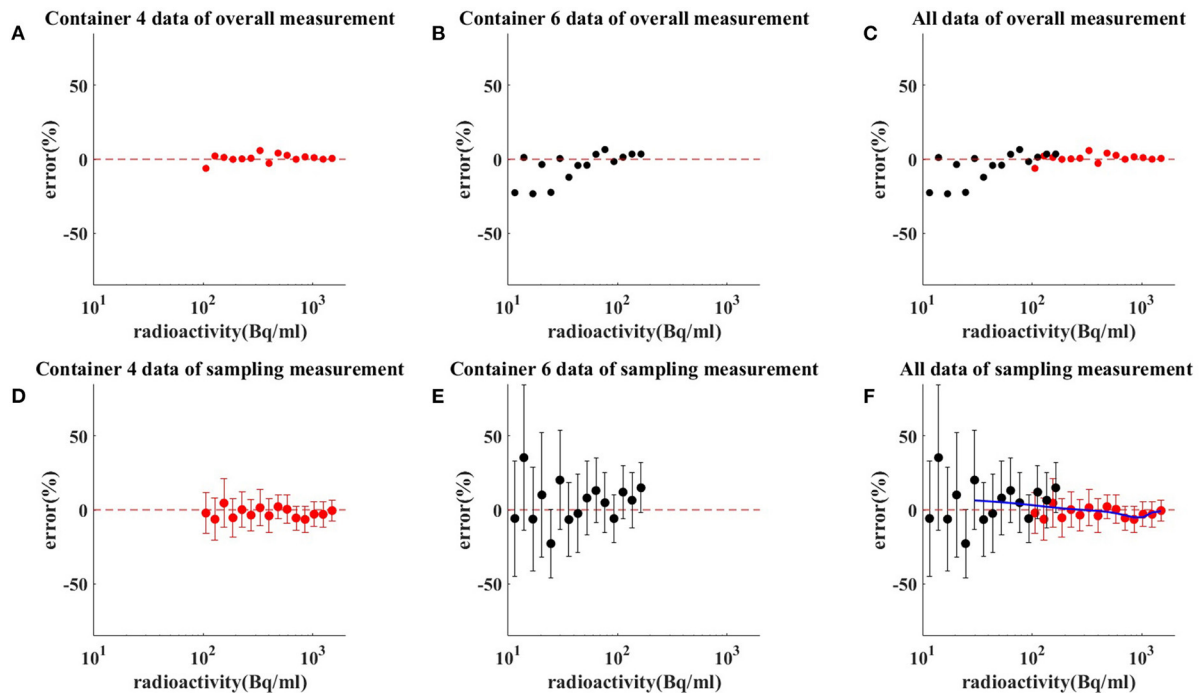


FIGURE 3 | Results of measuring radioactivity by method 1 (C) and method 2 (F). Red dot and red bar represent the mean radioactivity error and the standard error of container 4 (A,D), respectively. Black dot and black bar represent the mean radioactivity error and the standard error of container 6 (B,E), respectively. When radioactivity between 11.1–111, 111–370, and 370–1,480 Bq/mL, the mean activity errors of the overall measurement were 8.83, 2.04, and 1.45%, respectively. When radioactivity between 11.1–111, 111–370, and 370–1,480 Bq/mL, the mean activity errors of sampling measurement were 4.1 ± 26.43 , 2.69 ± 14.6 , and $1.60 \pm 8.73\%$, respectively. The blue line is the radioactivity error fitted curve for ULA.

Depending on measured radioactivity at drug loading, time and decay formula, radioactivity error at different radioactivity from container 4–6 is calculated. The comparison results between the R_{meas} and R_{pred} by method 1 are shown in Figures 3A–C. The comparison results between the R_{meas} and R_{pred} by method 2 are shown in Figures 3D–F. The results of the measure radioactivity error of the overall and sampling measurement are shown in Table 1. When radioactivity between 11.1–111, 111–370, and 370–1,480 Bq/mL, the mean activity errors of the overall measurement were 8.83, 2.04, and 1.45%, respectively, and the mean activity errors of sampling measurement were 4.1 ± 26.43 , 2.69 ± 14.6 , and $1.60 \pm 8.73\%$, respectively. An appropriate function of radioactivity was obtained by fitting the radioactivity error rate, which was calculated to be 2.81%, with a confidence interval of [1.09–4.54%] at 148 Bq/mL. When radioactivity of ULA was >148 Bq/mL, the radioactivity error was <5%.

Quantitative Results of ULA Space Range

The spatial range reliability verification analysis was performed using the R50 method (i.e., active depth curve) to compare container widths. The results are shown in Figure 4. Comparison of container width measured by R50 method with actual width is shown in Table 2. When radioactivity between 11.1–111, 111–370, and 370–1,480 Bq/mL, the average width was 2.189 ± 0.253 , 2.426 ± 0.09 , and 2.521 ± 0.047 cm, respectively. An appropriate function of radioactivity was obtained by fitting the width error. When radioactivity of ULA was 30 Bq/mL, the width error was

TABLE 1 | Radioactivity errors between measured radioactivity and actual radioactivity.

Actual radioactivity concentration (Bq/mL)	Radioactivity errors of overall container measurements (%)	Radioactivity errors of sampling measurements (%)
11.1–111	8.83	4.1 ± 26.43
111–370	2.04	2.69 ± 14.6
370–1,480	1.45	1.60 ± 8.73

3.8 mm [3.66–3.97 mm]. When radioactivity of ULA was 148 Bq/mL, the width error was 0.87 mm [0.84–0.90 mm]. When radioactivity of ULA was 259 Bq/mL, the width error was 0.3 mm [0.12–0.48 mm]. When radioactivity of ULA was >30 Bq/mL, the width error was below 4 mm.

DISCUSSION

The material of the quality control phantom (Flanged Jaszczak ECT the Phantom) is PMMA, which top consists are six containers and a cylindrical PMMA, and the resolution module can be placed inside. The NEMA PET quality control phantom used in this research is one of the most widely accepted standards, which can provide a variety of measurement methods for the quality control of PET scanning. Standards for quality control models were developed with reference to

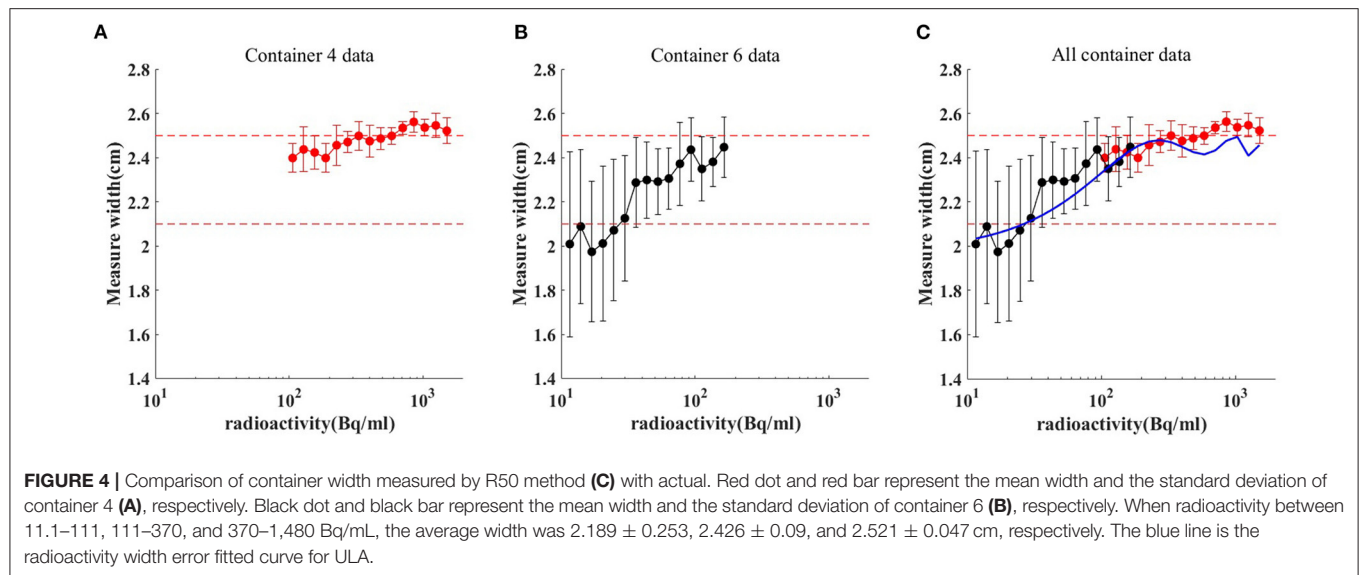


TABLE 2 | Comparison of container width measured by R50 method with actual width (2.5 cm).

Actual radioactivity concentration (Bq/mL)	Average value of width measured (cm)	Error between average width and actual width
11.1–111	2.189 ± 0.253	-3.10 ± 0.253
111–370	2.426 ± 0.091	-0.73 ± 0.091
370–1,480	2.521 ± 0.047	0.21 ± 0.047

the requirements of PET by many institutions, including the Society of Nuclear Medicine and Molecular Imaging (SNMMI), International Electrotechnical Commission (IEC), International Atomic Energy Agency (IAEA), American College of Radiology (ACR), and National Electrical Manufacturers Association (NEMA) (18).

In this study, the ULA of off-line PET was investigated in terms of both radioactivity and space range. When radioactivity of ULA was >148 Bq/mL, the radioactivity error was $<5\%$. This indicates that the off-line PET can meet the radioactivity requirement when the ULA exceeds 148 Bq/mL. When radioactivity of ULA was >30 Bq/mL, the space range error was below 4 mm. This indicates that the off-line PET can meet the space range requirement when the ULA exceeds 30 Bq/mL. Our study complements previous work on off-line PET.

To the best of our knowledge, there have been no reports on quality control for the ULA of off-line PET. Bauer et al. (19) proves the feasibility of the implemented strategy for offline confirmation of scanned carbon ion irradiation. On this basis, Knopf et al. (14) evaluated the impact of the following aspects on the feasibility and accuracy of the off-line PET/CT method by Monte Carlo: (1) biological washout procedure, (2) patient motion, (3) tissue classification based on Hounsfield units (HU) for simulating activity distribution, and (4) tumor site specificity. But the assessment of the reliability of PET imaging at ULA is missing.

Spacer range was set for parameters of beam range and depth verification *in vivo* PET verification (16, 20). Parodi et al. (6, 16) suggested that beam range could be verified within an accuracy of 1–2 mm in head off-line proton verification. Zhang et al. (21) investigated the feasibility of depth verification of off-line PET/CT treatment verification in phantom. The mean radioactivity of 289 Bq/mL in proton radiotherapy for breast cancer has been obtained by calculating the radioactivity of each spot within the target area. When radioactivity of ULA was 259 Bq/mL, the width error was 0.3 mm [0.12–0.48 mm]. This represents that ULA may result in a 0.3 mm error for breast cancer proton off-line PET verification.

Slight errors may lead to unreliable results when operating at low radioactivity, so the accurate filling of quality control phantom determines its reliability for testing. This problem was solved by filling the phantom with radiopharmaceuticals 10 h in advance. The radioactivity was still high when the radiopharmaceuticals were loaded, so the measurement error can be ignored. The position of the quality control phantom was fixed, and the continuous acquisition for a long period ensured not only location registration but also the continuity of the data. The assessment of radioactivity was greatly affected by the leakage of liquid. In practical operation, liquid leakage is very easy to occur in the process of removing air bubbles. Therefore, we used dye in solution to observe if leakage of fluid occurred. A method of freezing radiopharmaceuticals was used to reduce the effect caused by leakage of fluid during dilution. Therefore, we could solve the problem of radioactive liquid leakage by freezing and dyeing, which could facilitate more accurate comparisons of the radioactive values.

CONCLUSIONS

PET equipment validation phantom with ultra-low activity ^{18}F -FDG can be used to simulate the radioactivity of ULA. When radioactivity of ULA was >148 Bq/mL, the radioactivity error was $<5\%$. When radioactivity of ULA was >30 Bq/mL, the space

range error was below 4 mm. Off-line PET can be used to quantify the radioactivity based on proton and heavy ion beam when the ULA exceeds 148 Bq/mL, both in radioactivity and in space range.

DATA AVAILABILITY STATEMENT

The original contributions presented in the study are included in the article/supplementary material, further inquiries can be directed to the corresponding author/s.

AUTHOR CONTRIBUTIONS

JuZ and YL contributed to the conception of the study. JuZ and YSh contributed significantly to analysis and manuscript

preparation. FZ performed the data analyses and wrote the manuscript. JiZ and YSu helped perform the analysis with constructive discussions. RZ and JC are responsible for ensuring that the descriptions are accurate and agreed by all authors. All authors contributed to the article and approved the submitted version.

ACKNOWLEDGMENTS

This project was supported by Shanghai Municipal Health Commission (Grant No. 202040279), Pudong New Area Science and Technology Development Foundation (No. PKJ 2020-Y56), and Natural Science Foundation of Shanghai (21ZR460300).

REFERENCES

- Zhu X, Fakhri GE. Proton therapy verification with PET imaging. *Theranostics*. (2013) 3:731–40. doi: 10.7150/thno.5162
- Yang M, Zhu XR, Park PC, Titt U, Mohan R, Virshup G, et al. Comprehensive analysis of proton range uncertainties related to patient stopping-power-ratio estimation using the stoichiometric calibration. *Phys Med Biol*. (2012) 57:4095–115. doi: 10.1088/0031-9155/57/13/4095
- Gensheimer ME, Yock TI, Liebsch NJ, Sharp GC, Paganetti H, Madan N, et al. *In vivo* proton beam range verification using spine MRI changes. *Int J Radiat Oncol Biol Phys*. (2010) 78:268–75. doi: 10.1016/j.ijrobp.2009.11.060
- Min CH, Lee HR, Kim CH, Lee SB. Development of array-type prompt gamma measurement system for *in vivo* range verification in proton therapy. *Med Phys*. (2012) 39:2100–7. doi: 10.1118/1.3694098
- Crespo P, Shakirin G, Enghardt W. On the detector arrangement for in-beam PET for hadron therapy monitoring. *Phys Med Biol*. (2006) 51:2143–63. doi: 10.1088/0031-9155/51/9/002
- Parodi K, Enghardt W, Haberer T. In-beam PET measurements of β^+ radioactivity induced by proton beams. *Phys Med Biol*. (2001) 47:21–36. doi: 10.1088/0031-9155/47/1/302
- Ferrero V, Fiorina E, Morrocchi M, Pennazio F, Baroni G, Battistoni G, et al. Online proton therapy monitoring: clinical test of a Silicon-photodetector-based in-beam PET. *Sci Rep*. (2018) 8:4100. doi: 10.1038/s41598-018-22325-6
- Knopp MU, Binzel K, Wright CL, Zhang J, Knopp MV. Enhancing the patient experience with IP addressable digital LED lighting in imaging environments: a phase I feasibility study. *J Med Internet Res*. (2018) 22:e11839. doi: 10.2196/preprints.11839
- Wood D, Cottrell A, Baker SC. The role of offline PET-CT imaging in evaluating the particle beam range and beam stop for prostate cancer treated with heavy ion therapy. *Oncology*. (2015) 29:205039. doi: 10.1111/j.1464-410X.2010.10031.x
- Wuerl M. *Towards Offline PET Monitoring at a Cyclotron-Based Proton Therapy Facility*. Experiments and Monte Carlo simulations. Bestmasters (2016). doi: 10.1007/978-3-658-13168-5
- Parodi K, Bortfeld T, Haberer T. Comparison between in-beam and offline positron emission tomography imaging of proton and carbon ion therapeutic irradiation at synchrotron- and cyclotron-based facilities. *Int J Radiat Oncol Biol Phys*. (2008) 71:945–56. doi: 10.1016/j.ijrobp.2008.02.033
- Remmele S, Hesser J, Paganetti H, Bortfeld T. A deconvolution approach for PET-based dose reconstruction in proton radiotherapy. *Phys Med Biol*. (2011) 56:7601–19. doi: 10.1088/0031-9155/56/23/017
- Knopf A, Parodi K, Bortfeld T, Shih HA, Paganetti H. Systematic analysis of biological and physical limitations of proton beam range verification with offline PET/CT scans. *Phys Med Biol*. (2009) 54:4477–95. doi: 10.1088/0031-9155/54/14/008
- Knopf A, Parodi K, Paganetti H, Cascio E, Bonab A, Bortfeld T. Quantitative assessment of the physical potential of proton beam range verification with PET/CT. *Phys Med Phys*. (2007) 53:4137–51. doi: 10.1118/1.2761186
- Fletcher JW, Kinahan PE. PET/CT Standardized Uptake Values (SUVs) in clinical practice and assessing response to therapy. *Semin Ultrasound CT MR*. (2010) 31:496–505. doi: 10.1053/j.sult.2010.10.001
- Parodi K, Paganetti H, Shih HA, Michaud S, Loeffler JS, DeLaney TF, et al. Patient study of *in vivo* verification of beam delivery and range, using positron emission tomography and computed tomography imaging after proton therapy. *Int J Radiat Oncol Biol Phys*. (2007) 68:920–34. doi: 10.1016/j.ijrobp.2007.01.063
- Lopez BP, Jordan DW, Kemp BJ, Kinahan PE, Schmittdlein CR, Mawlawi OR. PET/CT acceptance testing and quality assurance: executive summary of AAPM task group 126 report. *Med Phys*. (2020) 48:e31–5. doi: 10.1002/mp.14656
- Prenosil GA, Hentschel M, Fürstner M, Sari H, Rominger A, editors. NEMA NU 2–2018 performance measurements of Biograph Vision Quadra PET/CT system. *NuklearMedizin 2021 – digital*. (2021) 60:152. doi: 10.1055/s-0041-1726744
- Bauer J, Unholtz D, Sommerer F, Kurz C, Haberer T, Herfarth K, et al. Implementation and initial clinical experience of offline PET/CT-based verification of scanned carbon ion treatment. *Radiother Oncol*. (2013) 107:218–26. doi: 10.1016/j.radonc.2013.02.018
- Parodi K, Paganetti H, Cascio E, Flanz JB, Bonab AA, Alpert NM, et al. PET/CT imaging for treatment verification after proton therapy: a study with plastic phantoms and metallic implants. *Med Phys*. (2007) 34:419–35. doi: 10.1118/1.2401042
- Zhang J, Lu Y, Hsi W, Zhang J, Sheng Y, Shi L, et al. Evaluation of proton therapy accuracy using a PMMA phantom and PET prediction module. *Front Oncol*. (2018) 8:523. doi: 10.3389/fonc.2018.00523

Conflict of Interest: The authors declare that the research was conducted in the absence of any commercial or financial relationships that could be construed as a potential conflict of interest.

Publisher's Note: All claims expressed in this article are solely those of the authors and do not necessarily represent those of their affiliated organizations, or those of the publisher, the editors and the reviewers. Any product that may be evaluated in this article, or claim that may be made by its manufacturer, is not guaranteed or endorsed by the publisher.

Copyright © 2021 Zhang, Zhang, Lu, Sheng, Sun, Zhang, Cheng and Zhou. This is an open-access article distributed under the terms of the Creative Commons Attribution License (CC BY). The use, distribution or reproduction in other forums is permitted, provided the original author(s) and the copyright owner(s) are credited and that the original publication in this journal is cited, in accordance with accepted academic practice. No use, distribution or reproduction is permitted which does not comply with these terms.



Carbon Ion Radiotherapy Evokes a Metabolic Reprogramming and Individualized Response in Prostate Cancer

Renli Ning^{1,2,3†}, Yulei Pei^{2,3,4†}, Ping Li^{2,3,5}, Wei Hu^{2,3,4}, Yong Deng^{2,3,6}, Zhengshan Hong^{2,3,5}, Yun Sun^{1,2,3*}, Qing Zhang^{2,3,4*} and Xiaomao Guo^{1,2,3*}

¹ Department of Research and Development, Shanghai Proton and Heavy Ion Center, Fudan University Cancer Hospital, Shanghai, China, ² Shanghai Key Laboratory of Radiation Oncology (20dz2261000), Shanghai, China, ³ Shanghai Engineering Research Center of Proton and Heavy Ion Radiation Therapy, Shanghai, China, ⁴ Department of Radiation Oncology, Shanghai Proton and Heavy Ion Center, Fudan University Cancer Hospital, Shanghai, China, ⁵ Department of Radiation Oncology, Shanghai Proton and Heavy Ion Center, Shanghai, China, ⁶ Department of Research and Development, Shanghai Proton and Heavy Ion Center, Shanghai, China

OPEN ACCESS

Edited by:

Fei Ye,
Institute of Modern Physics
(CAS), China

Reviewed by:

Walter Tinganelli,
GSI Helmholtz Center for Heavy Ion
Research, Germany
Narongchai Autavapromporn,
Chiang Mai University, Thailand

*Correspondence:

Xiaomao Guo
guoxm1800@126.com
Qing Zhang
qing.zhang@sphic.org.cn
Yun Sun
yun.sun@sphic.org.cn

[†]These authors have contributed
equally to this study

Specialty section:

This article was submitted to
Radiation and Health,
a section of the journal
Frontiers in Public Health

Received: 15 September 2021

Accepted: 03 November 2021

Published: 07 December 2021

Citation:

Ning R, Pei Y, Li P, Hu W, Deng Y,
Hong Z, Sun Y, Zhang Q and Guo X
(2021) Carbon Ion Radiotherapy
Evokes a Metabolic Reprogramming
and Individualized Response in
Prostate Cancer.
Front. Public Health 9:777160.
doi: 10.3389/fpubh.2021.777160

Introduction: Carbon ion radiotherapy (CIRT) is a novel treatment for prostate cancer (PCa). However, the underlying mechanism for the individualized response to CIRT is still not clear. Metabolic reprogramming is essential for tumor growth and proliferation. Although changes in metabolite profiles have been detected in patients with cancer treated with photon radiotherapy, there is limited data regarding CIRT-induced metabolic changes in PCa. Therefore, the study aimed to investigate the impact of metabolic reprogramming on individualized response to CIRT in patients with PCa.

Materials and Methods: Urine samples were collected from pathologically confirmed patients with PCa before and after CIRT. A UPLC-MS/MS system was used for metabolite detection. XCMS online, MetDNA, and MS-DIAL were used for peak detection and identification of metabolites. Statistical analysis and metabolic pathway analysis were performed on MetaboAnalyst.

Results: A total of 1,701 metabolites were monitored in this research. Principal component analysis (PCA) revealed a change in the patient's urine metabolite profiles following CIRT. Thirty-five metabolites were significantly altered, with the majority of them being amino acids. The arginine biosynthesis and histidine metabolism pathways were the most significantly altered pathways. Hierarchical cluster analysis (HCA) showed that after CIRT, the patients could be clustered into two groups according to their metabolite profiles. The arginine biosynthesis and phenylalanine, tyrosine, and tryptophan biosynthesis pathways are the most significantly discriminated pathways.

Conclusion: Our preliminary findings indicate that metabolic reprogramming and inhibition are important mechanisms involved in response to CIRT in patients with PCa. Therefore, changes in urine metabolites could be used to timely assess the individualized response to CIRT.

Keywords: prostate cancer, metabolites, carbon ion radiotherapy, metabolic reprogramming, individualized response, metabolite profiles

INTRODUCTION

Carbon ion radiotherapy (CIRT) is a novel and powerful tool to treat prostate cancer (PCa). Studies have shown an excellent five-year biochemical disease-free survival (bDFS) and low levels of late gastrointestinal and genitourinary toxicities (1, 2). This benefit has been attributed to the physical and biological advantages of CIRT that limits dose to normal tissue while allowing for safe dose escalation. In the past 7 years, our center has treated 162 pathologically confirmed patients with PCa with CIRT, and the three-year bDFS reached 93%. However, these patients with PCa showed an individualized treatment response after CIRT. Yet, the underlying mechanism is still not clear. Moreover, there are still no effective indicators that could be used to timely predict treatment response. Patients might have to wait several months for serum total prostate-specific antigen (PSA) and magnetic resonance imaging (MRI) results after the completion of CIRT, which adversely impacts decision-making. Therefore, there is a need to understand the underlying mechanism involved in response to CIRT in patients with PCa, so as to facilitate the identification of suitable treatment response makers and to evaluate the treatment prognosis.

Metabolic reprogramming is one of the main hallmarks of malignancy, in which tumor cells alter their metabolism, microenvironment, and immune cell function to promote their growth, proliferation, and immune evasion (3). Significant changes in the serum metabolite profiles were detected after photon radiotherapy in different malignancies such as hepatocarcinoma and breast cancer (4, 5). However, it has been shown that carbon ion is associated with a different metabolic response toward photon (6). Meanwhile, the impact of CIRT-induced metabolic changes on PCa treatment response is still not known.

A pilot study conducted in Poland evaluated the free serum and urine amino acid profiles in patients with PCa (7). The results of the study indicate that these metabolite parameters might have great performance for PCa detection. Several metabolites have already shown similar or even better performance for PCa detection when compared with PSA (AUC ranging from 0.53 to 0.83) (8). Therefore, metabolites could potentially be used to evaluate early treatment response following CIRT. Nalbantoglu evaluated the PCa treatment response to radiotherapy and showed that the most significant alterations after photon irradiation were linked with the nitrogen, pyrimidine, purine, porphyrin, alanine, aspartate, glutamate, and glycerophospholipid metabolic pathways (9). Cheema found a correlation between individualized radiation toxicities and

TABLE 1 | Patients' demographic and clinical characteristics.

Characteristics	Statistics	No of patients (n = 15)	(%)
Age (years)	73 (50–82)		
T	T1	1	6.7
	T2	9	60
	T3	4	26.7
	Tx	1	6.7
N	M0	15	100
M	N0	14	93.3
	N1	1	6.7
Gleason score	6	7	46.7
	7	4	26.7
	≥8	4	26.7
Risk group for	Low	2	13.3
Localized PCa	Intermediate	6	40
	High	5	33.3
	Very high	1	6.7

Data are expressed as numbers (n) and percentages (%). T, tumor; N, lymph node; M, metastasis.

metabolite profiles (10). However, these studies were based on photon radiotherapy, highlighting the need to evaluate the impact of CIRT on metabolic reprogramming and individualized treatment response in patients with PCa.

As urine contains over 2,500 metabolites, it can be easily used to evaluate global metabolic changes in patients with cancer (11). Therefore, the study aimed to perform a preliminary investigation to assess the impact of metabolic reprogramming on individualized CIRT response in patients with PCa by measuring variations in urine metabolites following CIRT. We expect this primary investigation of CIRT metabolic reprogramming and the individualized response will further step up the PCa CIRT and will also add value to either CIRT or photon radiotherapy for other malignancies.

MATERIALS AND METHODS

Study Samples and Population

From July 2020 to December 2020, 15 patients with pathologically confirmed prostate adenocarcinoma were enrolled in this study. CIRT was delivered using the Siemens IONTRIS particle therapy device. The clinical target volume (CTV) included prostate with or without proximal seminal vesicles based on different risk group types. The median CIRT dose to the prostate was 60.4 GyE (range 55.2–65.6 GyE) in 12–16 fractions and was prescribed to the 99% isodose line. Risk stratification was based on NCCN guidelines version 2.2020. The demographic and clinical characteristics of enrolled patients are summarized in Table 1.

Sample Collection and Preparation

The patients' urine samples were collected in the 4 h before receiving the first fraction and 4 h after finishing the last

Abbreviations: PCa, Prostate cancer; CIRT, carbon ion radiotherapy; bDFS, biochemical disease-free survival; UPLC-MS/MS, high-performance liquid chromatography, coupled to tandem mass spectrometry; CTV, clinical target volume; T, tumor; N, lymph node; M, metastasis; QC, quality control; ESI, electrospray ionization; MetDNA, Metabolite identification and Dysregulated Network Analysis (<http://metdna.zhulab.cn/>); MS-DIAL software, <http://prime.psc.riken.jp/>; FC, fold change; FDR, false discovery rates; PCA, principal component analysis; PLS-DA, partial least-squares discriminant analysis; sPLS-DA, sparse partial least-squares discriminant analysis; HCA, hierarchical cluster analysis.

fraction and then stored at 4°C immediately after collection. A 0.22- μ m membrane filter was used to remove contaminated bacteria, and 800 μ l of chilled methanol/acetonitrile (1:1, v/v) solution was added to 200 μ l of the thawed samples. The supernatant was extracted from the centrifuged mixture, transferred into a new Eppendorf tube, and evaporated into a dry solid. The dry supernatant was redissolved into 200 μ L chilled acetonitrile/water (1:1, v/v) and transferred into smaller sample vials. Quality control (QC)

samples were prepared by mixing equal amounts (50 μ L) of each sample.

High-Throughput UPLC-MS/MS Analysis

High-throughput UPLC-MS/MS (high-performance liquid chromatography, coupled to tandem mass spectrometry) analysis of urine samples was performed on an AB SCIEX ExionLCY system combined with AB SCIEX 500R QTOF. The urinary metabolites were separated in an ACQUITY UPLC BEH

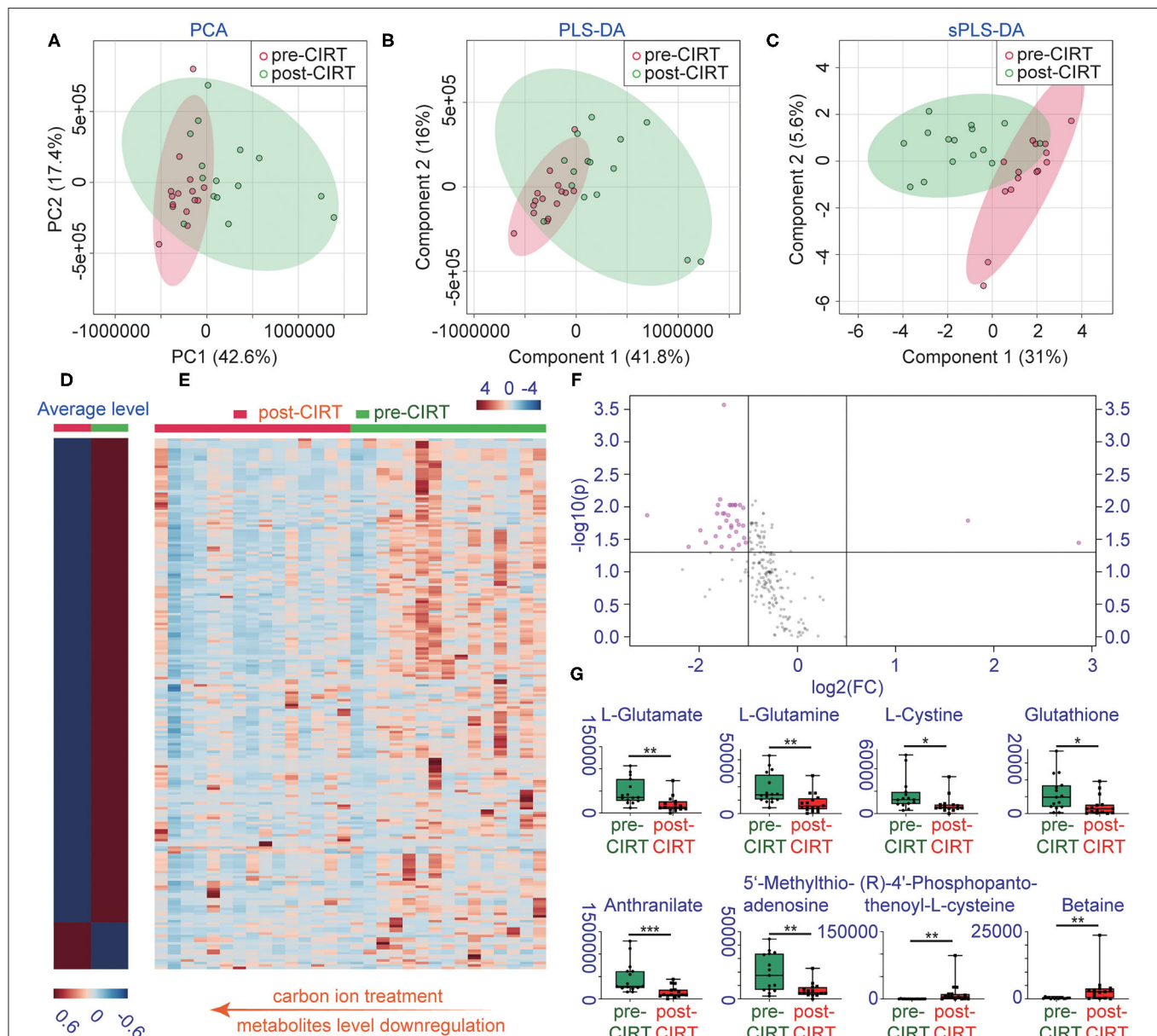


FIGURE 1 | Changes in metabolite profiles before and after CIRT. (A) PCA scores, (B) partial least squares-discriminant analysis (PLS-DA), (C) sparse partial least squares-discriminant analysis (sPLS-DA), (D) heat map of the average level of metabolite concentrations in pre-CIRT and post-CIRT urine samples, and (E) heat map of the metabolite concentrations in pre-CIRT and post-CIRT urine samples. Upregulated metabolites are shown in red and downregulated in blue. The intensity of the color estimates the magnitude of the change. (F) Volcano plot of pre-CIRT samples and post-CIRT samples. Significantly altered metabolites ($FDR < 0.05$, $FC > 2$) are indicated in pink; nonsignificantly altered metabolites are indicated in gray. (G) Boxplots of L-glutamate, L-glutamine, L-cystine, glutathione, anthranilate, 5'-methylthioadenosine, (R)-4'-phosphopantothienoyl-L-cysteine, betaine.

Amide 1.7 μm (2.1×100 mm) column. Two mobile phases were prepared. Mobile phase A contained water with 10 mM NH_4FA and 0.1%FA, and mobile phase B was acetonitrile: water = 95:5 (V/V) with 10 mM NH_4FA and 0.1%FA. A 17-min gradient was applied as follows: 2 min, 100% B; 11 min, 45% B; 12 min, 45% B; 12.1 min, 100% B; and 17 min, 100% B. Electrospray ionization mode was performed in the mass spectrometry analysis. Three blanks and six replicates of the QC samples were injected at the beginning of the batch for column conditioning, and the QC sample was analyzed every ten injections. Auto-calibrations were performed every five analyses.

Data Collection and Metabolite Identification

A UPLC-MS/MS was used to acquire the raw data, and XCMS online was used for peak detection and dataset alignment. MetDNA and MS-DIAL software were used for the identification of metabolites. The acquired peak tables were then uploaded onto the MetaboAnalyst for statistical analysis and metabolic pathway analysis. Concentrations of metabolites were represented by peak area and normalized according to the creatinine levels.

Data Analysis

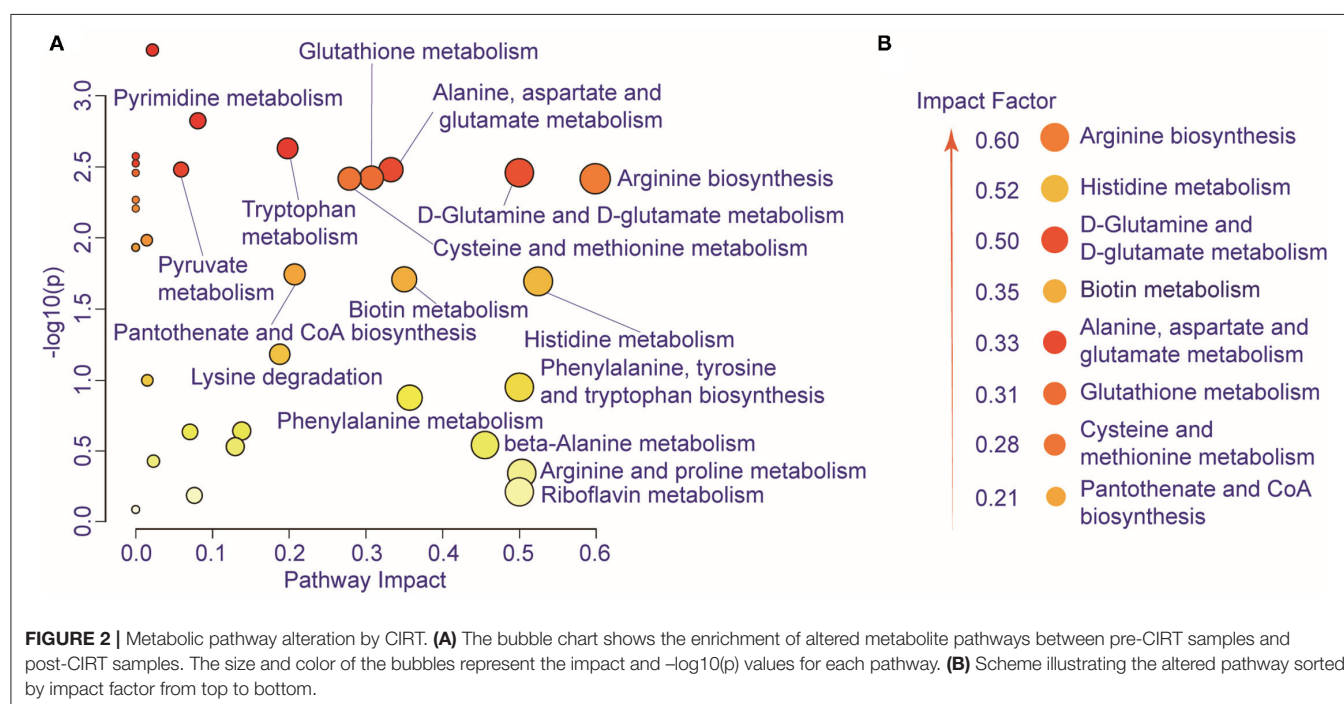
MetaboAnalyst 5.0 was used to analyze data. A volcano plot consisting of a combination of fold change (FC) analysis and non-parametric tests was used to identify any statistically significant differences in the metabolites between the pre-CIRT samples and post-CIRT samples. The unsupervised principal component analysis (PCA) was performed to detect the significant separation shift between compared groups. Supervised multivariate analysis and partial least-squares discriminant analysis (PLS-DA) were performed to achieve maximum separation among the groups.

The sparse PLS-DA (sPLS-DA) algorithm was used to reduce the number of variables (metabolites) to produce robust and easy-to-interpret models. Hierarchical cluster analysis (HCA) was used to separate the metabolite profiles between compared groups. Boxplots showed the minimum, lower quartile, median, upper quartile, and maximum values of metabolite concentrations. Error bars stood for the minimum values to the maximum.

RESULTS

The Impact of CIRT on Urine Metabolite Profiles in Patients With PCa

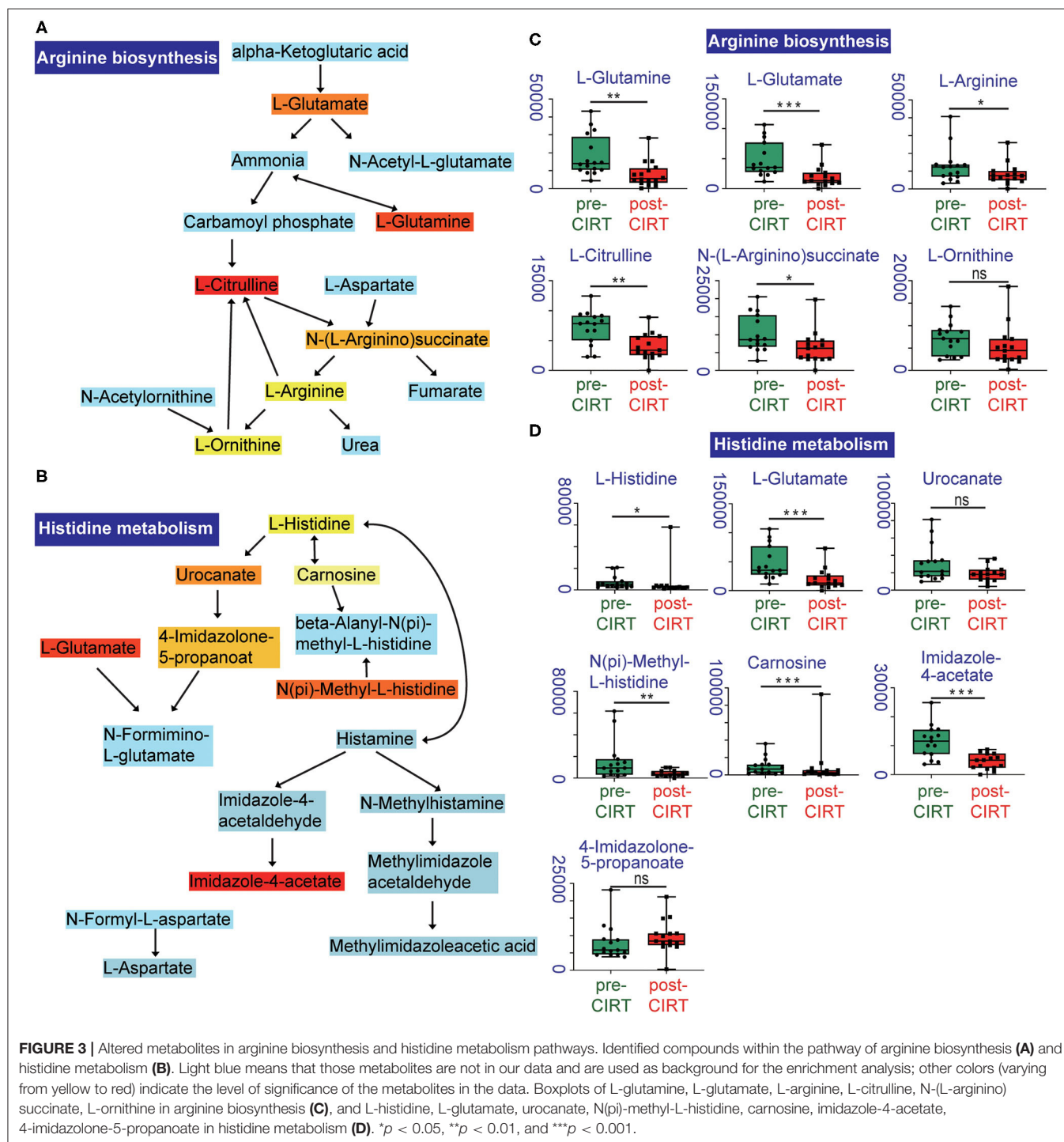
A total of 1,701 metabolites were monitored by UPLC-MS/MS. Multivariate analysis was performed using PCA, PLS-DA, and sPLS-DA (Figures 1A–C). All samples were analyzed with the unsupervised model PCA to examine possible sample group separations and sample clustering behavior. The PCA score plot revealed significant variations in the patient's urine metabolite profiles before and after CIRT. The pre-CIRT sample clusters are located on the left side of the score plot, and the post-CIRT sample clusters are located on the right side. The small overlap between the two demonstrates the significant difference in the metabolite profiles before and after CIRT. Moreover, the metabolite HCA can clearly discriminate the majority of pre-CIRT samples from the post-CIRT samples (Supplementary Figure 1). The heat map shown in (Figures 1D,E) further confirms that the concentration of metabolites in the urine sample experienced downregulation in most patients after CIRT. The volcano plot identified 35 significantly altered metabolites after CIRT (Figure 1F),

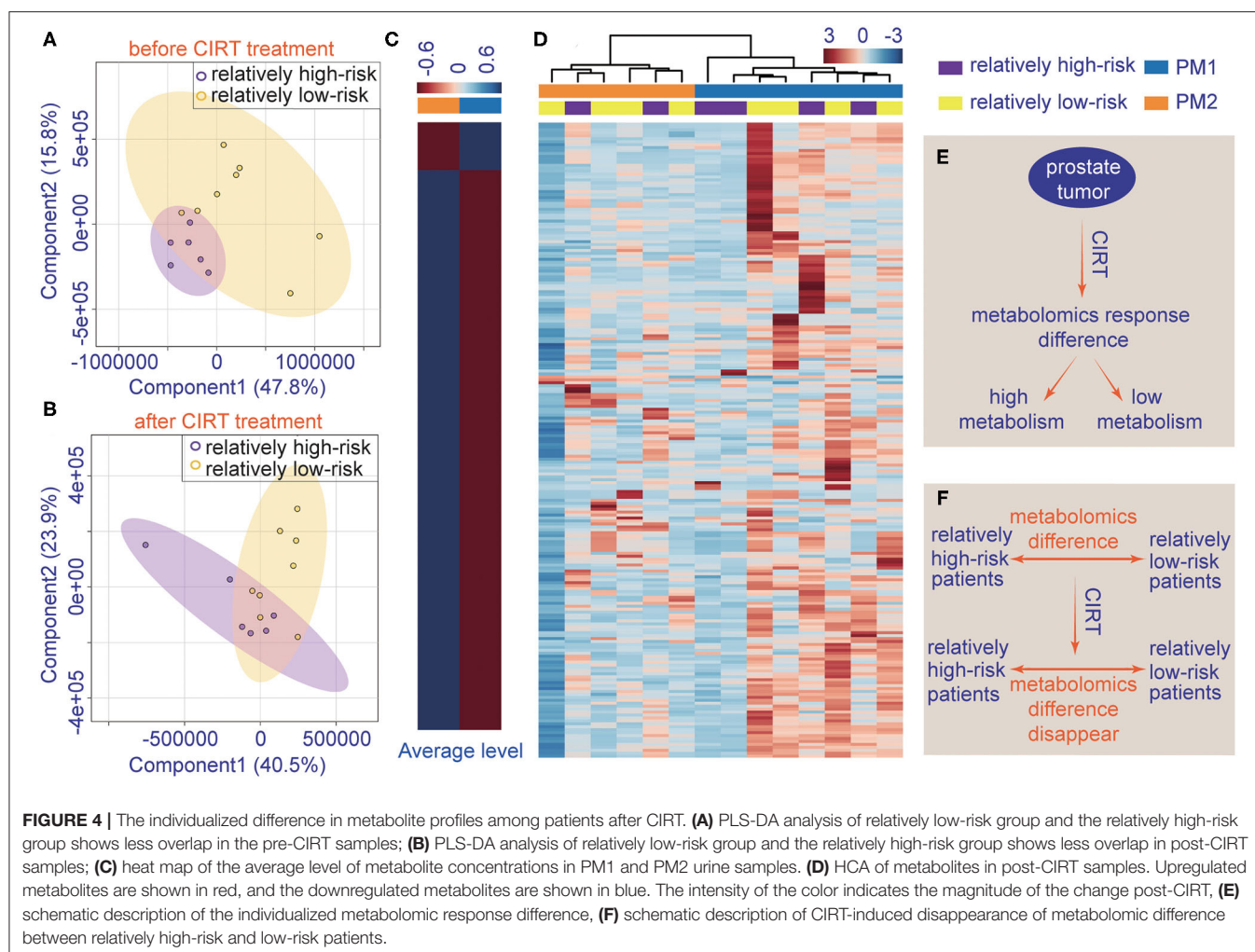


with 33 of these metabolites were downregulated after CIRT after CIRT including L-glutamate, L-glutamine, L-cystine, glutathione, anthranilate, 5'-methylthioadenosine, and two were upregulated, including (R)-4'-phosphopantothenoyl-L-cysteine and betaine (**Figure 1G**). The above results indicate that CIRT can significantly alter the PCa metabolism, mainly by decreasing the amino acid metabolism in urine.

CIRT-Induced Metabolic Pathway Changes

We further performed pathway enrichment analysis of the identified metabolites, and we found that these metabolites could be enriched in eight pathways (FDR < 0.05, impact > 2), including histidine metabolism, arginine biosynthesis, glutathione metabolism, cysteine and methionine metabolism, pantothenate, and CoA biosynthesis, biotin metabolism, alanine,





aspartate and glutamate metabolism, D-glutamine and D-glutamate metabolism. These metabolic pathways are part of amino acid metabolism, carbohydrate metabolism, and also vitamins and cofactors metabolism. The bubble plot shown in **Figure 2A** demonstrates the significance and the impact of each pathway. **Figure 2B** demonstrates the altered pathway sorted by impact factor from top to bottom. **Figures 3A,B** shows the metabolites in arginine biosynthesis and histidine metabolism. **Supplementary Figures 2, 3** demonstrate the details of the other six pathways that were significantly altered. **Supplementary Table 1** shows the FDR and the impact of the enriched metabolite pathways before and after CIRT. The alterations of the arginine biosynthesis and histidine metabolism pathways by CIRT are the most significant. L-glutamine, L-glutamate, L-arginine, L-citrulline, N-(L-arginino) succinate, and L-ornithine in arginine biosynthesis are all downregulated (**Figure 3C**), and L-histidine, L-glutamate, urocanate, N(pi)-methyl-L-histidine, carnosine, and imidazole-4-acetate in the histidine metabolism are downregulated as well (**Figure 3D**).

Potential Metabolite Profile Response Indicators for CIRT

The relation of metabolic clustering with different risk classifications was further explored. Patient risk stratification was performed under the NCCN guidelines. The low-risk and medium-risk patients were considered as a relatively low-risk group, and the high-risk and very high-risk patients were considered as a relatively high-risk group (**Supplementary Table 2**).

The patient's urine metabolites in pre-CIRT were further analyzed by PLS-DA and were clustered into two groups. The results were matched with the risk subtype (**Figure 4A**). However, the PLS-DA analysis of post-CIRT urine metabolites shows more overlap (**Figure 4B**), indicating that patients assessed as the same risk subtype no longer represented similar urine metabolite profiles, which means CIRT could significantly decrease the discrimination of the risk stratification.

The HCA also revealed that after CIRT, the patients could be clustered into two groups, PM1 and PM2, according to their

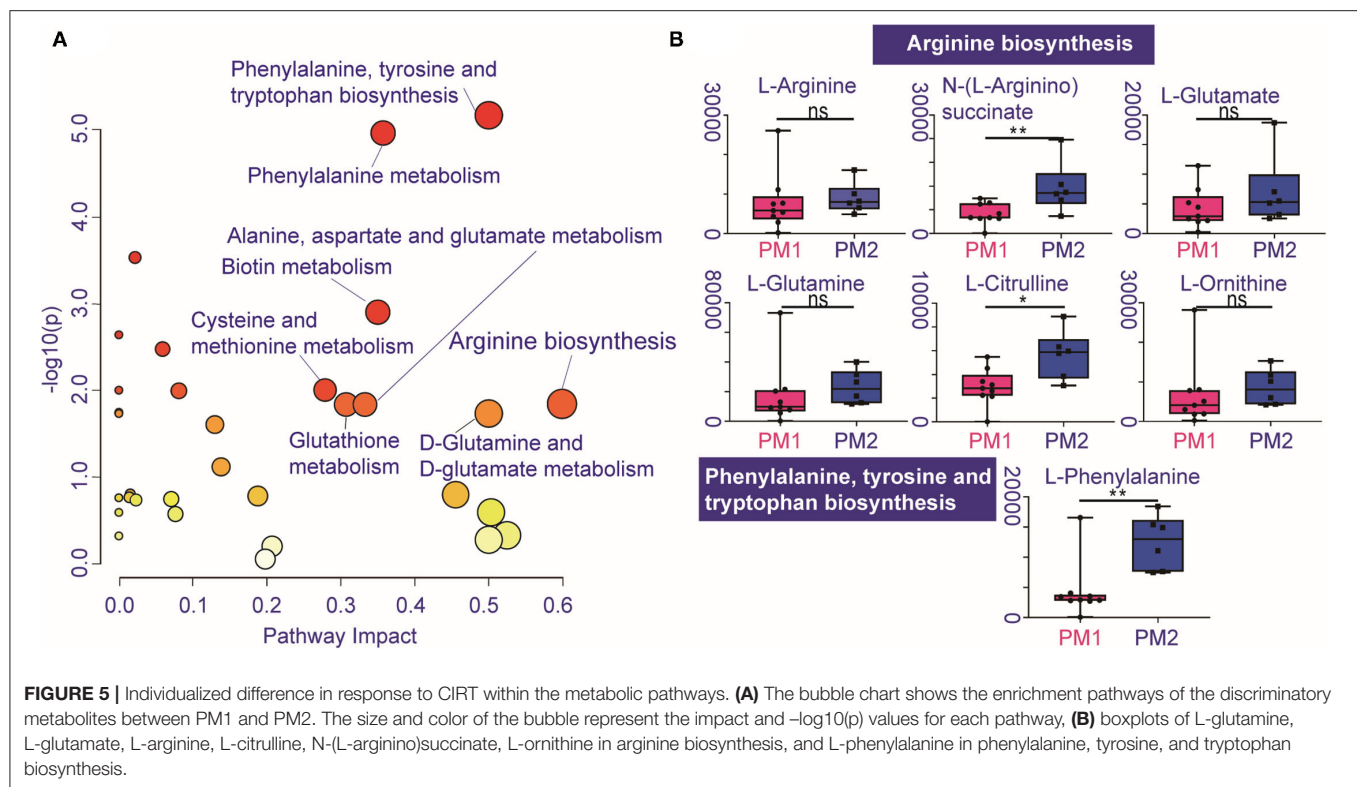


FIGURE 5 | Individualized difference in response to CIRT within the metabolic pathways. **(A)** The bubble chart shows the enrichment pathways of the discriminatory metabolites between PM1 and PM2. The size and color of the bubble represent the impact and $-\log_{10}(p)$ values for each pathway, **(B)** boxplots of L-glutamine, L-glutamate, L-arginine, L-citrulline, N-(L-arginino)succinate, L-ornithine in arginine biosynthesis, and L-phenylalanine in phenylalanine, tyrosine, and tryptophan biosynthesis.

metabolic profiles (Figure 4D). This clustering was different from the risk subtype. The PCa patients in the PM2 group had a higher level of urine metabolite concentrations than PM1 group (Figure 4C), which means the patients in the two groups may have different responses to CIRT. Figures 4E,F illustrate the schematic diagrams of this process.

Metabolic Pathways Enrichment Analysis After CIRT

Pathway enrichment shows the response diversity of PCa to CIRT. The bubble chart of the discriminatory metabolic pathway is shown in Figure 5A. Supplementary Table 3 demonstrates the FDR and the impact of the enriched pathways in discriminating between metabolites in post-CIRT urine samples. Discriminatory metabolites are mainly enriched in eight pathways ($FDR < 0.05$, impact > 2), including phenylalanine, tyrosine, and tryptophan biosynthesis, phenylalanine metabolism, biotin metabolism, cysteine and methionine metabolism, glutathione metabolism, arginine biosynthesis, alanine, aspartate, and glutamate metabolism, D-glutamine and D-glutamate metabolism. The arginine biosynthesis and the phenylalanine, tyrosine, and tryptophan biosynthesis pathways are the most significant. Figure 5B shows that the concentration of L-glutamine, L-glutamate, L-arginine, L-citrulline, N-(L-arginino)succinate, L-ornithine in the arginine biosynthesis, and L-phenylalanine in phenylalanine, tyrosine, and tryptophan biosynthesis are higher in PM2 when compared with PM1.

DISCUSSION

Carbon ion radiotherapy is a relatively new radiotherapy technique, and few studies have evaluated the impact of CIRT on cancer metabolism, especially PCa. Therefore, in this study, we evaluated the impact of this new technology on PCa metabolism.

Carbon ion radiotherapy showed a strong ability to inhibit metabolism in PCa. Compared to the concentrations of the metabolites in untreated patients' urine samples, almost all discriminated metabolites (33/35) were downregulated after CIRT. This result demonstrates the ability of CIRT to inhibit tumor metabolism. Moreover, CIRT could generally inhibit most of the metabolic processes involved in the proliferation, metastasis, and finally the progression of PCa. The results in this study primarily suggest that CIRT has the ability to significantly downregulate metabolism in patients with PCa.

Carbon ion radiotherapy inhibited the production of metabolites that are mainly enriched in the arginine biosynthesis and histidine metabolism pathways. The main alteration of amino acid in the process of prostate tumorigenicity involves histidine and arginine metabolism, and also the metabolism of alanine, aspartate, and glutamate, and some aromatic amino acid metabolism (12). The arginine biosynthesis pathway plays a key role, and it is known to be upregulated in PCa progression (13, 14). The deprivation of arginine in cancer cells can lead to dysfunction of mitochondria, reprogramming of transcription, and result in cell death (15). Arginine deprivation therapy for PCa has been found to be an effective treatment (16) and

has a strong radiosensitizing impact (17). Moreover, increased metabolism of L-arginine by myeloid cells can result in an impaired lymphocyte response to antigens and tumor growth (18). Therefore, the downregulation of arginine metabolism will inhibit PCa progression and also has the potential to promote antitumor immune effects. Histidine metabolism is another pathway that is significantly inhibited after CIRT. Histidine metabolism has been found elevated in men with T2 PCa, and its metabolite 4-imidazoleacetate shows cumulative effect in serum from T2 to T4 PCa (19). Herein, through a high-resolution metabolomic technique based on UPLC-MS/MS, we found carbon ion downregulated almost all of the amino acid metabolism, especially the histidine, arginine, and glutamine, presenting the unique inhibition effects of the carbon ion beam on PCa. This effect was significantly different from the reported photon radiation effects (20). Considering the role of these amino acids in PCa progression, further exploring the effects of the carbon ion beam on PCa metabolism was necessary for the future.

Interestingly, we found the urine metabolites of these patients with PCa have different responses to CIRT. All patients could be clustered into two groups, PM1 and PM2. PM2 showed relatively higher concentrations of metabolites after CIRT. The clustered result was different from the clinical risk stratification. Therefore, the difference in the concentrations of metabolites between PM1 and PM2 can be attributed to tumor sensitivity to CIRT. PCa in the PM2 group patients seemed to be less sensitive to CIRT when compared with the PCa in the PM1 group. However, long-term follow-up is necessary to confirm the role of urine metabolites as treatment response markers for CIRT in PCa.

The metabolic results also confirm the response to CIRT of PCa in the PM2 group, shown by the higher levels of metabolites related to arginine biosynthesis and also phenylalanine, tyrosine, and tryptophan biosynthesis. These results further confirm that arginine biosynthesis is important for PCa and may play a central role in response to CIRT.

CONCLUSION

In this study, CIRT showed its strong ability to inhibit metabolism pathways in PCa. CIRT-induced changes in the metabolite profiles mainly enriched in arginine biosynthesis and histidine metabolism. Urine metabolites of patients with PCa had different responses to CIRT. More sensitive PCa showed lower

levels of metabolites in urine samples, especially the arginine biosynthesis and also phenylalanine, tyrosine, and tryptophan biosynthesis pathway. CIRT-evoked metabolic reprogramming seems to be one of the most important underlying mechanisms of CIRT to inhibit PCa. Our preliminary results indicate that some urine metabolites could potentially be used to identify the individualized response to CIRT in patients with PCa. However, further longitudinal studies with a larger sample size are recommended to confirm these results.

DATA AVAILABILITY STATEMENT

The raw data supporting the conclusions of this article will be made available by the authors, without undue reservation.

ETHICS STATEMENT

The studies involving human participants were reviewed and approved by Shanghai Proton and Heavy Ion Center Institutional Review Board. The patients/participants provided their written informed consent to participate in this study.

AUTHOR CONTRIBUTIONS

YP, QZ, and RN finished study design. QZ and YP finished experimental studies. YP and YS finished data analysis. QZ, PL, ZH, YP, WH, and YD collected and proceeded patients' samples and clinical information. YS, QZ, and YP finished manuscript editing. QZ, XG, and YS supervised the study. All authors read and approved the final manuscript.

FUNDING

This article was supported by the Science and Technology Development Fund of Shanghai Pudong New Area (PKJ2019-Y07, PKJ2020-Y52, PKJ2019-Y06), the Natural Science Foundation of Shanghai (21ZR1481800).

SUPPLEMENTARY MATERIAL

The Supplementary Material for this article can be found online at: <https://www.frontiersin.org/articles/10.3389/fpubh.2021.777160/full#supplementary-material>

REFERENCES

- Nomiya T, Tsuji H, Kawamura H, Ohno T, Toyama S, Shioyama Y, et al. A multi-institutional analysis of prospective studies of carbon ion radiotherapy for prostate cancer: a report from the Japan Carbon ion Radiation Oncology Study Group (J-CROS). *Radiother Oncol.* (2016) 121:288–93. doi: 10.1016/j.radonc.2016.10.009
- Zhang Y, Li P, Yu Q, Wu S, Chen X, Zhang Q, et al. Preliminary exploration of clinical factors affecting acute toxicity and quality of life after carbon ion therapy for prostate cancer. *Radiat Oncol.* (2019) 14:94. doi: 10.1186/s13014-019-1303-3
- Peitzsch C, Gorodetska I, Klusa D, Shi Q, Alves TC, Pantel K, et al. *Metabolic regulation of prostate cancer heterogeneity and plasticity.* In: *Semin Cancer Biology.* (2020). doi: 10.1016/j.semcancer.2020.12.002
- Ng SSW, Jang GH, Kurland IJ, Qiu Y, Guha C, Dawson LA. Plasma metabolomic profiles in liver cancer patients following stereotactic body radiotherapy. *EBioMedicine.* (2020) 59:102973. doi: 10.1016/j.ebiom.2020.102973
- Arenas M, Rodríguez E, García-Heredia A, Fernández-Arroyo S, Sabater S, Robaina R, et al. Metabolite normalization with local radiotherapy following breast tumor resection. *PLoS ONE.* (2018) 13:e0207474. doi: 10.1371/journal.pone.0207474

6. Hanot M, Boivin A, Malésys C, Beuve M, Colliaux A, Foray N, et al. Glutathione depletion and carbon ion radiation potentiate clustered DNA lesions, cell death and prevent chromosomal changes in cancer cells progeny. *PLoS ONE*. (2012) 7:e44367. doi: 10.1371/journal.pone.0044367
7. Dereziński P, Klupczynska A, Sawicki W, Palka JA, Kokot ZJ. Amino acid profiles of serum and urine in search for prostate cancer biomarkers: a pilot study. *Int J Med Sci*. (2017) 14:1–12. doi: 10.7150/ijms.15783
8. Lima AR, Pinto J, Amaro F, Bastos ML, Carvalho M, Guedes de, Pinho P. Advances and perspectives in prostate cancer biomarker discovery in the last 5 years through tissue and urine metabolomics. *Metabolites*. (2021) 11:181. doi: 10.3390/metabo11030181
9. Nalbantoglu S, Abu-Asab M, Suy S, Collins S, Amri H. Metabolomics-based biosignatures of prostate cancer in patients following radiotherapy. *Omic*. (2019) 23:214–23. doi: 10.1089/omi.2019.0006
10. Cheema AK, Grindrod S, Zhong X, Jain S, Menon SS, Mehta KY, et al. Discovery of metabolic biomarkers predicting radiation therapy late effects in prostate cancer patients. *Adv Exp Med Biol*. (2019) 1164:141–50. doi: 10.1007/978-3-030-22254-3_11
11. Lee B, Mahmud I, Marchica J, Dereziński P, Qi F, Wang F, et al. Integrated RNA and metabolite profiling of urine liquid biopsies for prostate cancer biomarker discovery. *Sci Rep*. (2020) 10:3716. doi: 10.1038/s41598-020-60616-z
12. Fernández-Peralbo MA, Gómez-Gómez E, Calderón-Santiago M, Carrasco-Valiente J, Ruiz-García J, Requena-Tapia MJ, et al. Prostate cancer patients-negative biopsy controls discrimination by untargeted metabolomics analysis of urine by LC-QTOF: upstream information on other omics. *Sci Rep*. (2016) 6:38243. doi: 10.1038/srep38243
13. Qiu F, Huang J, Sui M. Targeting arginine metabolism pathway to treat arginine-dependent cancers. *Cancer Lett*. (2015) 364:1–7. doi: 10.1016/j.canlet.2015.04.020
14. Kelly RS, Vander Heiden MG, Giovannucci E, Mucci LA. Metabolomic biomarkers of prostate cancer: prediction, diagnosis, progression, prognosis, and recurrence. *Cancer Epidemiol Biomarkers Prev*. (2016) 25:887–906. doi: 10.1158/1055-9965.EPI-15-1223
15. Chen CL, Hsu SC, Chung TY, Chu CY, Wang HJ, Hsiao PW, et al. Arginine is an epigenetic regulator targeting TEAD4 to modulate OXPHOS in prostate cancer cells. *Nat Commun*. (2021) 12:2398. doi: 10.1038/s41467-021-22652-9
16. Kim RH, Coates JM, Bowles TL, McNerney GP, Sutcliffe J, Jung JU, et al. Arginine deiminase as a novel therapy for prostate cancer induces autophagy and caspase-independent apoptosis. *Cancer Res*. (2009) 69:700–8. doi: 10.1158/0008-5472.CAN-08-3157
17. Vynnytska-Myronovska B, Bobak Y, Garbe Y, Dittfeld C, Stasyk O, Kunz-Schughart LA. Single amino acid arginine starvation efficiently sensitizes cancer cells to canavanine treatment and irradiation. *Int J Cancer*. (2012) 130:2164–75. doi: 10.1002/ijc.26221
18. Bronte V, Zanovello P. Regulation of immune responses by L-arginine metabolism. *Nat Rev Immunol*. (2005) 5:641–54. doi: 10.1038/nri1668
19. Huang J, Mondul AM, Weinstein SJ, Karoly ED, Sampson JN, Albanes D. Prospective serum metabolomic profile of prostate cancer by size and extent of primary tumor. *Oncotarget*. (2017) 8:45190–9. doi: 10.18632/oncotarget.16775
20. Ferreira MR, Sands CJ, Li JV, Andreyev JN, Chekmeneva E, Gulliford S, et al. Impact of pelvic radiation therapy for prostate cancer on global metabolic profiles and microbiota-driven gastrointestinal late side effects: a longitudinal observational study. *Int J Radiat Oncol Biol Phys*. (2021) 111:1204–13. doi: 10.1016/j.ijrobp.2021.07.1713

Conflict of Interest: The authors declare that the research was conducted in the absence of any commercial or financial relationships that could be construed as a potential conflict of interest.

Publisher's Note: All claims expressed in this article are solely those of the authors and do not necessarily represent those of their affiliated organizations, or those of the publisher, the editors and the reviewers. Any product that may be evaluated in this article, or claim that may be made by its manufacturer, is not guaranteed or endorsed by the publisher.

Copyright © 2021 Ning, Pei, Li, Hu, Deng, Hong, Sun, Zhang and Guo. This is an open-access article distributed under the terms of the Creative Commons Attribution License (CC BY). The use, distribution or reproduction in other forums is permitted, provided the original author(s) and the copyright owner(s) are credited and that the original publication in this journal is cited, in accordance with accepted academic practice. No use, distribution or reproduction is permitted which does not comply with these terms.



Carbon Ion Radiotherapy Acts as the Optimal Treatment Strategy for Unresectable Liver Cancer During the Coronavirus Disease 2019 Crisis

Zheng Li^{1,2,3,4†}, Qiang Li^{1,2,3,5*†}, Xiaohu Wang^{1,4}, Sha Li⁶, Weiqiang Chen^{1,2,3,5}, Xiaodong Jin^{1,2,3,5}, Xinguo Liu^{1,2,3,5}, Zhongying Dai^{1,2,3,5}, Xiongxiang Liu^{1,2,3,5}, Xiaogang Zheng^{1,2,3,5}, Ping Li^{1,2,3,5}, Hui Zhang^{1,2,3,5}, Qiuning Zhang^{1,4}, Hongtao Luo^{1,4} and Ruifeng Liu^{1,4}

¹ Institute of Modern Physics, Chinese Academy of Sciences (CAS), Lanzhou, China, ² Key Laboratory of Heavy Ion Radiation Biology and Medicine of Chinese Academy of Sciences, Lanzhou, China, ³ Gansu Provincial Key Laboratory of Basic Research on Heavy Ion Radiation Application in Medicine, Lanzhou, China, ⁴ Lanzhou Heavy Ion Hospital, Lanzhou, China, ⁵ University of Chinese Academy of Sciences, Beijing, China, ⁶ The 940th Hospital of Joint Logistics Support Force of Chinese People's Liberation Army, Lanzhou, China

OPEN ACCESS

Edited by:

Lu Cai,
University of Louisville, United States

Reviewed by:

Silva Bortolussi,
University of Pavia, Italy
Ming Chen,
Sun Yat-sen University, China

*Correspondence:

Qiang Li
liqiang@impcas.ac.cn

[†]These authors have contributed
equally to this work

Specialty section:

This article was submitted to
Radiation and Health,
a section of the journal
Frontiers in Public Health

Received: 31 August 2021

Accepted: 05 November 2021

Published: 09 December 2021

Citation:

Li Z, Li Q, Wang X, Li S, Chen W, Jin X, Liu X, Dai Z, Liu X, Zheng X, Li P, Zhang H, Zhang Q, Luo H and Liu R (2021) Carbon Ion Radiotherapy Acts as the Optimal Treatment Strategy for Unresectable Liver Cancer During the Coronavirus Disease 2019 Crisis. *Front. Public Health* 9:767617. doi: 10.3389/fpubh.2021.767617

The coronavirus disease 2019 (COVID-19) pandemic has greatly disrupted the normal treatment of patients with liver cancer and increased their risk of death. The weight of therapeutic safety was significantly amplified for decision-making to minimize the risk of severe acute respiratory syndrome coronavirus 2 (SARS-CoV-2) infection. Herein, the safety and effectiveness of carbon ion radiotherapy (CIRT) for unresectable liver cancer (ULC) were evaluated, and Chinese experiences were shared to solve the predicament of ULC treatment caused by SARS-CoV-2. Worldwide studies were collected to evaluate CIRT for ULC as the world has become a community due to the COVID-19 pandemic. We not only searched five international databases including the Cochrane Library, Web of Science, PubMed, Embase, and Scopus but also performed supplementary retrieval with other sources. Chinese experiences of fighting against COVID-19 were introduced based on the advancements of CIRT in China and a prospective clinical trial of CIRT for treating ULC. A total of 19 studies involving 813 patients with ULC were included in the systematic review. The qualitative synthetic evaluation showed that compared with transarterial chemoembolization (TACE), CIRT could achieve superior overall survival, local control, and relative hepatic protection. The systematic results indicated that non-invasive CIRT could significantly minimize harms to patients with ULC and concurrently obtain superior anti-cancer effectiveness. According to the Chinese experience, CIRT allows telemedicine within the hospital (TMIH) to keep a sufficient person-to-person physical distance in the whole process of treatment for ULC, which is significant for cutting off the transmission route of SARS-CoV-2. Additionally, CIRT could maximize the utilization rate of hospitalization and outpatient care (UHO). Collectively, CIRT for ULC patients not only allows TMIH and the maximized UHO but also has the compatible advantages of safety and effectiveness. Therefore, CIRT should be identified as the

optimal strategy for treating appropriate ULC when we need to minimize the risk of SARS-CoV-2 infection and to improve the capacity of medical service in the context of the unprecedented COVID-19 crisis.

Keywords: liver neoplasms, carbon ion radiotherapy, telemedicine, COVID-19, SARS-CoV-2, medical resource

INTRODUCTION

The coronavirus disease 2019 (COVID-19) pandemic, an infectious disease caused by a novel coronavirus named severe acute respiratory syndrome coronavirus 2 (SARS-CoV-2) (1, 2), was declared a pandemic by the WHO on March 11, 2020 (3). COVID-19 has been spreading around the world and bringing unprecedented catastrophe to humans (2–4). The figures released by WHO on November 23, 2021 showed that SARS-CoV-2 had infected more than 257.46 million people and caused more than 5.15 million deaths in over 220 countries and regions worldwide (4). The COVID-19 pandemic has impacted every aspect of human life, especially in the health care of all countries (5, 6). Patients with cancer are susceptible to being infected by it because of the poor systemic immunosuppressive state caused by the malignancy and conventional anticancer treatments, such as surgery or chemotherapy (7–12). Moreover, cancer and its conventional treatments are associated with deteriorating conditions and a worse prognosis of patients with COVID-19 concomitant (7–12). In order to reduce the risk of SARS-CoV-2 infection, postponing treatment was proposed in some guidelines to adjust cancer management (13); however, it is becoming increasingly inapplicable because of the increasing cancer malignant death (5, 14, 15). What is the solution for this dilemmatic predicament caused by the COVID-19 pandemic (16)? Obviously, we should find a way of fighting against cancer and SARS-CoV-2 synchronously (4, 14, 15). Some evidence has indicated that the optimization of anti-cancer safety is a realistic and feasible solution for the predicament during the COVID-19 crisis (7–12). What is the revised optimal treatment strategy for unresectable liver cancer (ULC) in the context of the COVID-19 crisis?

The weight of therapeutic safety is enlarged due to SARS-CoV-2 (7–12). Therefore, non-invasiveness and telemedicine within the hospital (TMIH) should be the crucial considerations for anti-cancer treatment during the COVID-19 crisis, especially for patients in the worst-hit areas (7–12). The principles of non-invasiveness and TMIH are necessary to get the optimal risk-benefit results in the fighting against SARS-CoV-2 and liver cancer synchronously (7–12, 17–19). There are unique superiorities of non-invasive carbon ion radiotherapy (CIRT) (20, 21), especially when it comes to the ability of TMIH concerning the controllable risk of SARS-CoV-2 infection, as well as preserving the patient's systemic function (including immunity) at relatively good levels to reduce the risk of SARS-CoV-2 infection (21–30). Several similar studies are helpful to fully understand the unique potentiality of CIRT in preserving cancer patients from the SARS-CoV-2 infection (31–35). Therefore, non-invasive CIRT seems to be the optimal strategy among multifarious therapies for treating ULC during

the COVID-19 crisis when an oncologist needs to minimize the risk of SARS-CoV-2 infection (7–12, 21–30). However, the evidence for decision-making is lacking in terms of CIRT for ULC. Accordingly, the safety and effectiveness of CIRT for treating ULC were comprehensively evaluated by this systematic review to give evidence-based references in decision-makings and the advancements of CIRT in China together with clinical experiences were shared to provide references for other countries struggling with SARS-CoV-2 and liver cancer.

MATERIALS AND METHODS

A pre-retrieval procedure was implemented to ensure that the best results of literature retrieval could be obtained, which started on March 11, 2020. A preliminary and rapid systematic review was conducted before this study to ascertain how to design this study scientifically and accurately.

Inclusion and Exclusion Criteria of Study Selection

Studies were included if they matched the following criteria based on the pilot study of a systematic review. (1) Participants: patients were diagnosed with liver cancer by histopathology and imageological examination, ineligible or infeasible for resection; regardless of primary liver cancer or metastatic liver cancer. (2) Intervention and comparison: there were few studies with a control group for the assessment of CIRT in treating patients with liver cancer on the basis of pre-retrieval. Therefore, a study should be included if CIRT was evaluated with effectiveness and/or adverse effects in treating liver cancer, whether there was a comparison group or not. (3) Outcomes: the outcomes of evaluation included overall survival (OS), local control, short-term effects, adverse effects, and complications. (4) The study type was unrestricted due to the development stage of CIRT. All study types of clinical research were included to evaluate CIRT for liver cancer on the basis of the pre-retrieval and preliminary systematic review. Publications were excluded if they had inappropriate research designs including cellular or animal experiments, letters, editorials, commentaries, protocols, reviews, systematic reviews, or meta-analyses.

Search Strategy and Study Screening

The pre-retrieval was performed on March 11, 2020 and the comprehensive retrieval was started on April 15, 2020, following the pilot systematic review. The retrieval was updated every month during the research process in order to acquire the latest data of reports. The final retrieval time was May 31, 2021.

We searched five international databases including the Cochrane Library, Web of Science, PubMed, Embase, and Scopus from the database inception to May 31, 2021. We also

searched other supplementary resources, such as Google Scholar, Medical Matrix, reference lists of relevant reviews and included papers, COVID-19 Open Research Dataset Challenge (CORD-19), COVID-19 Research Database (WHO), and the WHO International Clinical Trials Registry Platform. The search terms contained the target disease group and intervention groups, such as liver neoplasms, CIRT, SARS-CoV-2, and COVID-19. No restrictions were set for the study language, publication date, and publication status. All relevant clinical trials were collected to evaluate CIRT for patients with liver cancer.

All records were imported into the EndNote software of the X9 version (Clarivate Analytics, Clarivate, London, England) for further management and screening. Studies were selected according to the inclusion and exclusion criteria. The articles were reviewed by the researchers independently in two stages for the study screening: the first stage was an evaluation of the titles and abstracts, followed by a full-text review as the second stage. The researchers discussed the discrepancies and re-evaluated the articles until a consensus was reached.

Data Extraction and Data Analysis

Data were extracted from each included article using standardized forms. The subset of interventions that satisfied the inclusion criteria was kept in the analysis after having discarded the groups that did not satisfy the inclusion criteria when the trials have multiple groups. The list of the collected data included: (1) the basic characteristics of the included studies; (2) the outcomes from the research results. All data were extracted from the text, tables, or figures of the included papers. CIRT was assessed using the method of qualitative synthetic analyses due to its development stage. The data of CIRT were synthesized in both tabular and narrative formats according to the qualitative analysis method of the systematic review.

Chinese Experience of Fighting Against SARS-CoV-2 and Liver Cancer

The experiences of fighting against SARS-CoV-2 from different countries are necessary due to the unprecedented crisis worldwide. We explored the optimal strategy for treating ULC in the context of the COVID-19 crisis *via* the included studies combined with the experience of Chinese citizens. No ethical approval or patient consent was required for the systematic review as the data originated from previously published studies online. The clinical trial of the first Chinese carbon ion therapy system (CITS) in Wuwei, China was conducted in accordance with the Good Clinical Practice Guidelines and the Declaration of Helsinki, and this trial was approved by the ethics committee of the research institute. All patients provided written informed consent.

RESULTS

Results of Study Search and Screening

From our systematized search, a total of 1,065 records were imported into the EndNote software for further identification, including 1,049 records identified through traditional database searching and 16 records identified through

additional sources. A total of 575 reduplicative records were removed because of the repeats included by the different databases. After the elimination of duplicates, 490 records were screened for eligibility by their titles and abstracts at the first stage and by full-text screening at the second stage. A total of 19 eligible studies (36–54) were finally included (Figure 1).

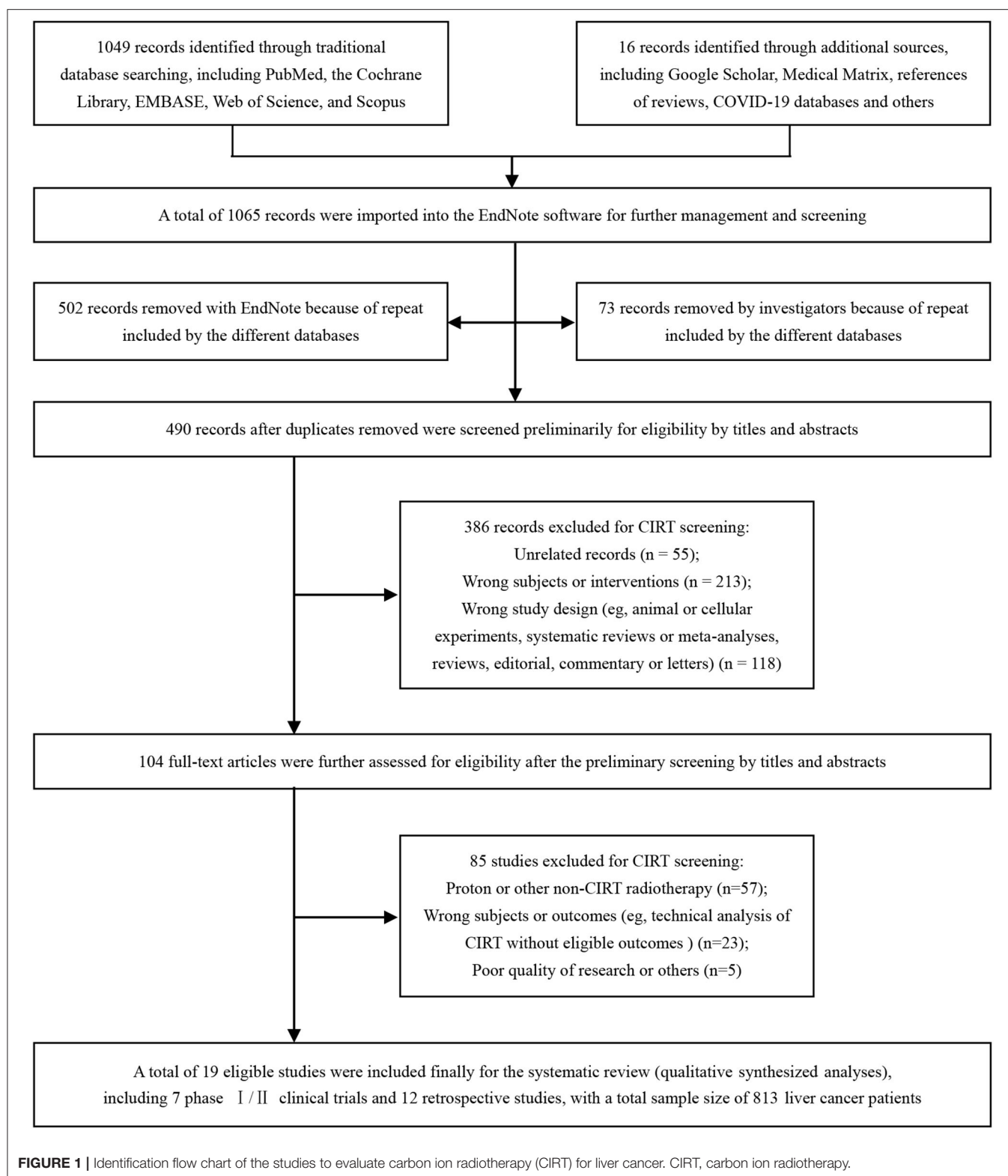
Characteristics of the Included Studies

All of the included studies (36–54) were published in Science Citation Index (SCI) journals and included in the Web of Science with good quality reports. The main features of the 19 included studies (36–54) are presented in Table 1. One propensity-score matching study (43) compared CIRT with transarterial chemoembolization (TACE) for liver cancer, while the other studies (36–42, 44–54) have a single-arm design for the evaluation of CIRT with measurements of safety and efficacy. There were seven phase I/II clinical trials (41, 42, 48, 50, 52–54) and 12 retrospective studies (36–40, 43–47, 49, 51). One study (50) was done in Germany, while the other studies all came from Japan (36–49, 51–54). The total sample size was 813 patients at a rough estimate, which contained 807 patients from Japan. We could not calculate the total sample size accurately because of the existence of overlapping populations, however, the bias of data analysis was low risk because CIRT was assessed using the method of qualitative analyses instead of meta-analyses (Table 1).

Qualitative Synthetic Analysis for CIRT

A total of 19 studies (36–54) were eligible for the qualitative synthetic analysis of CIRT for liver cancer. The main clinical outcome data after CIRT have been summarized in Table 2. Both prospective and retrospective studies from Japan and Germany have demonstrated encouragingly high rates of OS and local control and low rates of hepatotoxicity with CIRT for treating patients with liver cancer. The reported actuarial OS rates ranged from 90 to 100% at 1 year, from 50 to 88% at 3 years, and from 22 to 48.9% at 5 years, respectively. The local control rates ranged from 81 to 93% at 5 years. A total of four patients with grade 3 adverse events of the hepatotoxicity of transaminase level elevation were reported among the 813 patients included in this qualitative analysis. All studies (36–54) affirmed that severe radiation morbidities were uncommon, and no treatment-related deaths of CIRT were observed (Table 2).

Shiba et al. (43) reported a propensity-score matching (PSM) study that compared CIRT with TACE for patients with single hepatocellular carcinoma. Seventeen matched pairs of patients from each group were included for further analyses after PSM. The results demonstrated that CIRT significantly improved the clinical outcomes over TACE with regard to the 3-year OS rate (88% with CIRT vs. 58% with TACE, $p < 0.05$), 3-year local control rate (80% with CIRT vs. 26% with TACE, $p < 0.01$), and 3-year progression-free survival rate (51% with CIRT vs. 15% with TACE, $p < 0.05$), respectively. Compared with TACE, CIRT was associated with a significant reduction regarding the number of patients whose liver function progressed to a worse Child-Pugh class within 3 months from the initiation of treatment ($p < 0.01$).



There were two studies (41, 49) regarding single fraction CIRT for metastatic liver cancer, and the results showed that single fraction CIRT was safe and effective. As a special case, a woman with a

6 cm chemo-resistant metastatic liver tumor from breast cancer was successfully cured with a single shot of 36-GyE CIRT, and the woman survived more than 8 years without local recurrence (49).

TABLE 1 | Assessment of the basic characteristics of the 19 included studies.

References	Treatment	Nation	Study design	Research year range	Cases (n)	Age (years)	M/F (n)	Child-Pugh A/B/C (n)	Diameter (cm)
Shiba et al. (36)	CIRT	Japan	SRS	2013.10–2020.3	11	65 ^Δ (47–76) [#]	8/3	Unclear	3.1 ^Δ (1.5–6.5) [#]
Okazaki et al. (37)	CIRT	Japan	SRS	2011.1–2018.12	9	80 ^Δ (56–85) [#]	7/2	6/3/0	3.4 ^Δ (1.0–4.7) [#]
Takakusagi et al. (38)	CIRT	Japan	CR	Unclear	2	Case 1: 75; Case 2: 76	Case 1: male; Case 2: male	Case 1: A; Case 2: A	Case 1: 1.3; Case 2: 2.9
Shiba et al. (39)	CIRT	Japan	SRS	2011.7–2018.8	11	76 ^Δ (57–86) [#]	9/2	10/1/0	5.3 ^Δ (2.7–11.9) [#]
Yasuda et al. (40)	CIRT	Japan	SRS	2008.12–2013.3	57	75 ^Δ (49–89) [#]	33/24	51/6/0	3.3 ^Δ (1.3–9.5) [#]
Makishima et al. (41)	CIRT	Japan	CTI	Unclear	29	69 ^Δ (46–84) [#]	20/9	Unclear	2.5 ^Δ (1.2–10.2) [#]
Shibuya et al. (42)	CIRT	Japan	CTI	2012.10–2016.4	21	7 [§] (<70) [#] , 14 [§] (≥70) [#]	14/7	21/0/0	4.8 [*] (3.0–7.8) [#] ; 11 [§] (<5) [#] , 10 [§] (≥5) [#]
Shiba et al. (43)	CIRT vs. TACE	Japan	PSMS	2007.4–2016.9	Total: 34; CIRT: 17, TACE: 17	CIRT: 75 ^Δ (45–85) [#] ; TACE: 78 ^Δ (59–90) [#]	CIRT: 8/9; TACE: 9/8	CIRT: 15/2/0; TACE: 14/3/0	CIRT: 3.0 ^Δ (1.1–6.4) [#] ; TACE: 3.0 ^Δ (0.8–6.0) [#]
Shibuya et al. (44)	CIRT	Japan	SRS, MS	2005.4–2014.11	174	73 ^Δ (37–95) [#] , 67 [§] (<70) [#] , 107 [§] (≥70) [#]	114/60	153/20/0	3.0 ^Δ (0.8–10.3) [#] ; 84 [§] (<3) [#] , 90 [§] (≥3) [#]
Shiba et al. (45)	CIRT	Japan	SRS	2010.9–2016.12	68	Sarcopenia: 77 ^Δ (57–95) [#] ; Non-sarcopenia: 74 ^Δ (45–90) [#]	41/27	57/11/0	Sarcopenia: 3.3 ^Δ (1.2–9.0) [#] ; Non-sarcopenia: 3.6 ^Δ (0.9–7.7) [#]
Toyama et al. (46)	CIRT	Japan	CR	2014.9–2016.2	1	50	Female	A	5 cm
Shiba et al. (47)	CIRT	Japan	SRS	2011.3–2015.11	31	≥80 [#]	22/9	27/4/0	4.5 ^Δ (1.5–9.3) [#]
Kasuya et al. (48)	CIRT	Japan	CTI, CTII	1997–2003	126	68 ^Δ (37–84) [#]	90/36	97/29/0	4.0 ^Δ (1.0–12.0) [#] ; 39 [§] (≤3.0) [#] , 56 [§] (>3.0, ≤5.0) [#] , 38 [§] (>5.0) [#]
Harada et al. (49)	CIRT	Japan	CR	Unclear	1	54	Female	Unclear	6 cm
Habermehl et al. (50)	CIRT	Germany	CTI	Unclear	6	69 ^Δ (53–78) [#] ; 3 [§] (<70) [#] , 3 [§] (≥70) [#]	3/3	4/1/0	3.5 ^Δ (0.9–4.5) [#]
Komatsu et al. (51)	CIRT	Japan	SRS	2001.5–2009.1	101	55 [§] (<70) [#] , 46 [§] (≥70) [#]	73/28	78/20/3	81 [§] (<5.0) [#] , 22 [§] (5.0–10.0) [#] , 5 [§] (>10.0) [#]
Imada et al. (52)	CIRT	Japan	CTI, CTII	2000.4–2003.3	64	69 ^Δ (37–84) [#]	48/16	49/15/0	4.0 ^Δ (1.2–12.0) [#]
Imada et al. (53)	CIRT	Japan	CTI, CTII	1995.4–2000.3	43	66 ^Δ (45–83) [#]	29/14	35/8/0	Unclear
Kato et al. (54)	CIRT	Japan	CTI, CTII	1995.6–1997.2	24	64 ^Δ (54–77) [#] ; 4 [§] (54–60) [#] , 15 [§] (61–70) [#] , 5 [§] (71–77) [#]	13/11	16/8/0	5.0 ^Δ (2.1–8.5) [#] ; 5 [§] (≤3.0) [#] , 9 [§] (>3.0, ≤5.0) [#] , 10 [§] (>5.0) [#]

CIRT, carbon ion radiotherapy; TACE, transarterial chemoembolization; PSMS, propensity-score matching study; CTI, clinical trial, Phase I; CTII, clinical trial, phase II; SRS, single-arm retrospective study; MS, multicenter study; CR, case report; M, male; F, female; ^Δ median; [#] range; ^{*} average; [§] number of people.

Chinese Experience of Fighting Against SARS-CoV-2 and Liver Cancer

The CITS in Wuwei, China, which was independently developed by the Institute of Modern Physics (IMP), Chinese Academy of Sciences in 1993, successfully completed the treatment of 46 cancerous cases as a clinical trial and was officially registered as a medical device of Class 3 in China on September 29, 2019. The CITS in Wuwei is the first Chinese CIRT equipment with the serial number 20193050713 and the type specification HIMM-01-GS-WW-1, and several CITSs in other areas of China

are now under construction. A total of 47 cancer cases were enrolled into the clinical trial for the medical device registration of CITS in Wuwei. One patient withdrew from the trial after enrolment, and 46 subjects completed the trial finally. There were a total of seven patients with ULC in the trial, including six cases with primary hepatocellular carcinoma and one case with hepatic metastasis from rectal cancer. All of these patients were advanced and intractable cancer cases. No severe radiation morbidities and treatment-related deaths of CIRT were observed during the treatment and follow-up. The data acquired from the

TABLE 2 | Clinical outcomes of the included CIRT studies for patients with liver cancer.

References	Dose/# Fx/BED10	OS	LC	RILD Definition	RILD Rate	RILD Deaths
Shiba et al. (36)	60.0 GyE/4/150 GyE; 60.0 GyE/12/90 GyE 64.8 GyE/12/99.79 GyE	2-year 100%	2-year 61%	CTCAEv4.0; CP Class progression	0%	0%
Okazaki et al. (37)	52.8 GyE/4/122.5 GyE; 52.8 GyE/12/76.03 GyE; 60 GyE/4/150 GyE 60 GyE/12/90 GyE	MST 18.3 months	1-year 100%	Change in CP score	Acute phase CP+1: 44% Late phase CP+1: 33% CP+2: 11%	0%
Takakusagi et al. (38)	48 GyE/2/163.2 GyE; 60 GyE/4/150 GyE	1-year 100%	1-year 100%	CP Class progression	0%	0%
Shiba et al. (39)	52.8 GyE/4/122.5 GyE; 60 GyE/4/150 GyE 60 GyE/12/90 GyE	3-year 64%	3-year 78%	CP Class progression	3 months CP-A→ B 18% 6 months CP-A→ B 30%	0%
Yasuda et al. (40)	45 GyE/2/146.25 GyE	1-year 97% 3-year 67% 5-year 45%	1-year 98% 3-year 91% 5-year 91%	CTCAEv4.0; Change in CP score	≥G3: 0%; ≥CP+2: 0%	0%
Makishima et al. (41)	36–58 GyE/1/165.6–394.4 GyE	3-year 78%	3-year 82%, high doses; 3-year 28%, lower doses	NCI-CTC/RTOG- ARMSS/EORTC- LRMSS	Acute toxicities G1: 17% G2: 3% Late toxicities G1: 21% G3: 7%	0%
Shibuya et al. (42)	60 GyE/4/150 GyE	1-year 100% 2-year 92.3%	1-year 90.5% 2-year 80.0%	CTCAEv4.0: GGT, AST	Within 90 days ≤G1: 86% G2: 14% After 90 days ≤G1: 90% G2: 10%	0%
Shiba et al. (43)	52.8 GyE /4/122.5 GyE; 60 GyE /4/150 GyE; 60 GyE /12/90 GyE	3-year 88%	3-year 80%	CP Class progression	0%	0%
Shibuya et al. (44)	48.0 GyE /2/163.2 GyE; 52.8–60.0 GyE /4/122.5–150 GyE	1-year 95.4% 2-year 82.5% 3-year 73.3%	1-year 94.6% 2-year 87.7% 3-year 81.0%	CTCAEv4.0: AST, ALT	1.7%; one case with G3 ALT elevation	0%
Shiba et al. (45)	52.8, 60 GyE/4/122.5, 150 GyE	Sarcopenia: 3-year 66% Non-sarcopenia: 3-year 77%	Sarcopenia: 3-year 81% Non-sarcopenia: 3-year 72%	CTCAEv4.0: AST, ALT	Acute toxicities G1: 7% G2: 3% Late toxicities G1: 4% G2: 4%	0%
Toyama et al. (46)	60 GyE/4/150 GyE	1-year 100%	1-year 100%	NR	0%	0%
Shiba et al. (47)	Close-GI-tract: 60 GyE/12/90 GyE Others: 52.8–60 GyE/4/122.5–150 GyE	2-year 82%	2-year 89%	CP score and Class progression	3 months CP+1: 13% CP+2: 3% 6 months CP+1: 16% CP+2: 3% CP-A→ B 3%	0%
Kasuya et al. (48)	Phase I: 54, 48, 48 GyE/12, 8, 4/78.3, 76.8 GyE/105.6 GyE Phase II: 52.8 GyE/4/122.5 GyE	1-year 90% 3-year 50% 5-year 25%	1-year 95% 3-year 91% 5-year 90%	CP score and Class progression	3 months CP+1: 29% CP+2: 3% CP+3: 1% 6 months CP+1: 22% CP+2: 5% CP-A→ B 13%	0%

(Continued)

TABLE 2 | Continued

References	Dose/# Fx/BED10	OS	LC	RILD Definition	RILD Rate	RILD Deaths
Harada et al. (49)	36 GyE/1/165.6 GyE	8-year 100%	8-year 100%	NR	0%	0%
Habermehl et al. (50)	40 GyE/4/80 GyE	MST 11 months	Crude 100%	CTCAEv4.03: AST, ALT	≥G2: 40%	0%
Komatsu et al. (51)	52.8–76.0 GyE/4–20/87.6–122.5 GyE	5-year 36%	5-year 93%	CTCAEv2: AST, ALT	≥G2: 3% G3: 1%	0%
Imada et al. (52)	52.8 GyE/4/122.5 GyE	5-year 22%	5-year 88%	Change in CP score	CP+1: 84% CP+2: 16%	0%
Imada et al. (53)	48.0–79.5 GyE/4–15/65.8–122.5 GyE	Larger enlargement group 3-year 80.0% 5-year 48.9% Smaller enlargement group 3-year 52.2% 5-year 29.4%	NR	NR	NR	0%
Kato et al. (54)	49.5–79.5 GyE/15/65.8–121.6 GyE	1-year 92% 3-year 50% 5-year 25%	1-year 92% 3-year 81% 5-year 81%	Change in CP score	CP+1: 30% CP+2: 22%	0%

Fx, fraction; BED10, biologic equivalent dose with α/β of 10; OS, overall survival; LC, local control; RILD, radiation-induced liver disease; NR, not reported; CP, Child-Pugh score; MST, median survival time; GGT, Gamma-glutamyltransferase; AST, Aspartate aminotransferase; ALT, Alanine aminotransferase; NCI-CTC, National Cancer Institute – Common Toxicity Criteria; RTOG-ARMSS, Radiation Therapy Oncology Group, Acute Radiation Morbidity Scoring System; EORTC-LRMSS, European Organization for Research and Treatment of Cancer, Late Radiation Morbidity Scoring System; CTCAE, Common Terminology Criteria for Adverse Events; *2 temporary grade 3 liver toxicity cases due to biliary obstruction were observed at 9 and 21 months after the treatment as late toxicity at 53 Gy (RBE), but both fully recovered.

clinical trial in Wuwei, China demonstrated that the Chinese CITS encouraged safety and anti-cancer effectiveness in treating liver cancer (Table 3).

According to the experience of Chinese citizens, compared with other locoregional treatment (LRT) (including surgical resection, thermal ablation, transarterial chemoembolization, percutaneous ethanol injection, and so on), CIRT allows TMIH with controllable risk of SARS-CoV-2 infection in the whole process of treatment for ULC. Compared with photon (or proton) radiotherapy modalities, CIRT could achieve the optimal utilization rate of hospitalization and outpatient care (UHO). Therefore, non-invasive CIRT is identified as the optimal treatment strategy for appropriate patients with ULC concerning the need to cut off the transmission route of SARS-CoV-2 and to improve the capacity of healthcare service in the context of the unprecedented COVID-19 crisis. Based on Chinese foundations, ultramodern projects of CIRT have been planning and preparing to bring its superiorities into full play. A schematic diagram for the development planning of the CIRT center is exhibited in Figure 2. As shown in Figure 2, the new-style CIRT center has the excellent ability of TMIH and is non-contact. In addition, the burgeoning digital medicine of CIRT possesses many other superiorities including non-invasion, precision, automation, multimedia, and multi-discipline, which is beneficial to protect vulnerable cancer groups from SARS-CoV-2 infection by minimizing toxicities to cancer patients (especially for immune-system). Therefore, the Chinese CITSs will play a crucial role in pulling the appropriate patients with liver cancer through crises such as the COVID-19 pandemic.

DISCUSSION

Globally, COVID-19 has caused unprecedented social turmoil, triggering a comprehensive transformation of global healthcare systems (3–6, 13, 55–59). From the perspective of cancer patients, any policy or strategy that neglects their benefit due to the COVID-19 pandemic, such as delaying treatment in some guidelines after the COVID-19 outbreak as a typical example, has immensely increased the risk of cancerous malignant death (13, 60–62). Based on fully respecting the interests of patients with ULC worldwide, herein, we put forward a kind of brand new perspective and method to fight against SARS-CoV-2 and ULC simultaneously by optimizing the treatment strategy of ULC.

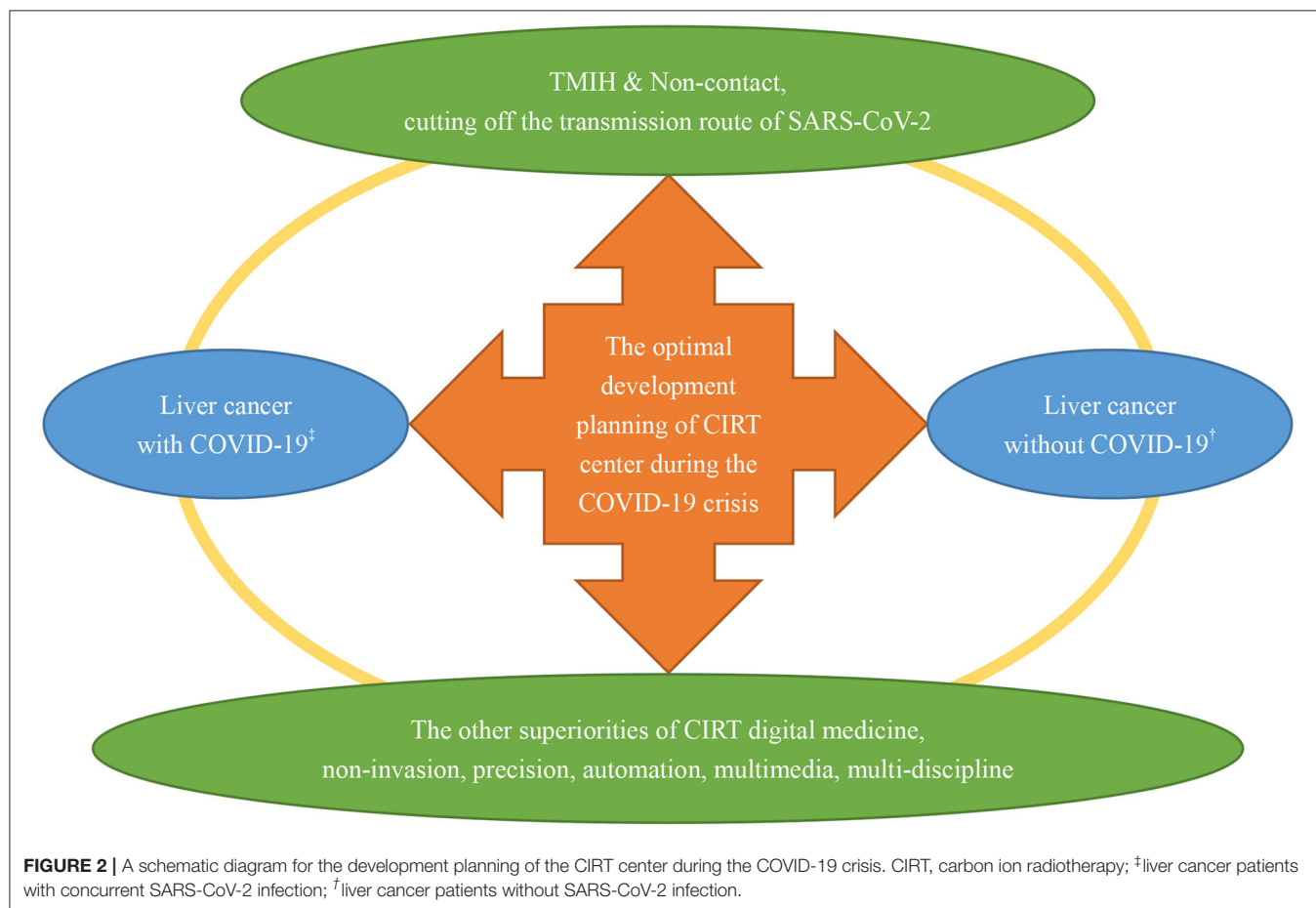
CIRT for Liver Cancer During the COVID-19 Crisis

Aitken et al. (32) suggested that photon-based stereotactic ablative radiotherapy (SABR) could be considered as an effective and feasible alternative to surgery for patients with liver cancer because of the unprecedented impacts of the COVID-19 pandemic on the United Kingdom cancer services. Maybe the COVID-19 pandemic is primetime for the application of SABR in cancer treatment and the single fraction SABR has been further placed great expectations (31, 34). Why was CIRT identified as the optimal strategy for ULC in the context of the COVID-19 crisis? Primarily, TMIH and non-invasiveness are the crucial considerations for decision-making (7–12). What is more, CIRT possesses multidimensional superiorities compared with either photon or proton radiotherapy (21, 29, 63, 64). CIRT is

TABLE 3 | Clinical outcomes of CIRT with the first Chinese carbon ion therapy system (CITS) for patients with liver cancer.

Items classification	Case 1	Case 2	Case 3	Case 4	Case 5	Case 6	Case 7
Age (years)	72	49	63	68	49	44	72
Gender	Male	Male	Male	Male	Male	Male	Female
Pathological type	Primary HCC	Primary HCC	Primary HCC	Primary HCC	Primary HCC	Primary HCC	Hepatic metastasis of rectal cancer
Treatment-related deaths	No	No	No	No	No	No	No
Severe radiation morbidities	No	No	No	No	No	No	No
Efficacy at 3 mon	PR	SD	SD	SD	PR	PR	SD
Efficacy at 6 mon	PR	PR	SD	SD	SD	CR	SD
Survival at 0.5 year	Yes	Yes	Yes	Yes	Yes	Yes	Yes
Survival at 1 year	Yes	Yes	Yes	Yes	Yes	Yes	Yes

HCC, hepatocellular carcinoma; mon, months post-treatment; CR, complete response; PR, partial response; SD, stable disease; CIRT, carbon ion radiotherapy; CITS, carbon ion therapy system; ULC, unresectable liver cancer.



superior to SABR for treating patients with liver cancer due to its unique advantages in terms of target conformity and normal liver tissue sparing, relative biological effectiveness (RBE), duration of treatment, risk of subsequent primary cancers, and so on (20, 21, 29, 30, 35, 63–68). Additionally, CIRT is beneficial to protect the immune system and activate specific anti-cancer immunity by triggering the immunoreaction on account of its excellent superiorities in the aspects of dose localization and RBE (21–28),

which is extremely significant for patients to fight against cancer and SARS-CoV-2 synchronously (7–12).

The qualitative synthetic analyses results of CIRT for liver cancer demonstrated encouragingly high rates of OS and local control and low rates of hepatotoxicity. One of the most limiting factors of the use of radiotherapy for liver cancer is the significantly poor radiation tolerance of the normal liver tissues, especially when the liver function is

impaired by some chronic liver disease (50, 51). CIRT is the optimal radiation modality for maximizing anti-cancer effectiveness while minimizing radiation-induced hepatotoxicity due to its inherently physical and biological superiorities (65, 66). A propensity-score matching (PSM) study (43), a method that could minimize potential selection bias of patients in retrospective studies by mimicking some characteristics of RCT, has manifested that CIRT possesses significantly more effectiveness and less toxicity than TACE in the treatment of liver cancer. A synthetical study by Zhang et al. indicated that CIRT is more therapeutically beneficial with adequate safety than the radiotherapy modality of proton or photon (20). Based on the evidence, CIRT was identified as the optimal strategy for appropriate patients with ULC during the COVID-19 crisis, especially the single fraction CIRT for specific ULC patients concerning the need to minimize the risk of SARS-CoV-2 infection.

China's Experience in Combating COVID-19 and Liver Cancer

The statistics showed that liver cancer was the third leading cause of cancer death worldwide in 2020, with about 906,000 new cases and 830,000 deaths annually (69). In addition, nearly half of the world's morbidity and mortality of liver cancers are distributed in China (69, 70). There exists a dilemmatic predicament with regards to conventional therapies for liver cancer in the context of the COVID-19 crisis, which is significantly different from the real world before the COVID-19 pandemic (7–12). Protecting patients from the SARS-CoV-2 infection generally results in delaying (even giving up) conventional treatment for liver cancer patients on account of the high risk of SARS-CoV-2 infection caused by conventional treatment (7–13). But on the other hand, what is the optimal alternative strategy for the conventional treatment for reducing the risk of cancer malignant death? In order to find the way out of this unprecedented predicament, we have identified CIRT as the optimal treatment strategy for applicative patients with ULC after a comprehensive investigation.

The IMP of China has started to develop CITS independently since 1993, and now, we have many original innovations not only in the equipment and clinical technology but also in the supporting theoretical basis, such as the relative biological effectiveness (RBE) modeling for CIRT (71). Why was CIRT identified as the optimal strategy for ULC concerning the need to minimize the risk of SARS-CoV-2 infection? Based on the Chinese CITS foundations and the successful experiences in fighting COVID-19, the reasons could be summarized as follows. (1) The first reason is with respect to cutting off transmission routes. CIRT has the excellent ability of TMIH and non-contact in the whole process of treatment for ULC, thereby allowing quarantine and keeping a sufficient person-to-person physical distance between patients and others. This peculiarity of CIRT is crucial to realize cutting off the transmission route of SARS-CoV-2. (2) The second reason is with respect to protecting vulnerable populations. (a) CIRT is a non-invasive and precision treatment modality for ULC. Therefore,

CIRT could minimize toxicities to patients (especially for the immune system) and concurrently obtain excellent anti-cancer effectiveness, which is significant to preserve patients with ULC in a relatively good systemic and immune condition for fighting against SARS-CoV-2 and cancer in the context of the COVID-19 crisis. (b) Compared with photon (or proton) radiotherapy modalities, CIRT is associated with significantly fewer fractions and a shorter duration of hospitalization, which is beneficial to reduce the risk of nosocomial cross-infection of SARS-CoV-2, as well as to increase the turnover rate of hospitalization. Accelerating the turnover rate of hospitalization is necessary for healthcare systems in the context of the COVID-19 crisis because of the widespread shortage of medical resources. (c) All the advantages of CIRT, especially the unique capacity of a single fraction regimen for completing the treatment, make it feasible to offer an outpatient ablative approach with minimal hospital footfall and duration, which is significant to minimize the risk of SARS-CoV-2 infection by minimizing the exposure frequency of nosocomial SARS-CoV-2 sources. Therefore, single fraction CIRT would be the optimal choice of radiotherapy during the COVID-19 crisis for specific patients with liver cancer. As a response to this pandemic, the use of CIRT will become more and more important due to the increasing need to offer optimal risk-benefit results. We propose that personalized treatment recommendations should be addressed to minimize the risk of SARS-CoV-2 infection and malignant death synchronously along with meticulous personal protective protocols for liver cancer patients.

In the summer of 2021, the SARS-CoV-2 Delta Variant surge has caused a new wave of the epidemic peak in America and other countries (4, 59, 72, 73). As a matter of fact, there has been an unprecedented shortage of hospital beds and other medical resources due to the severe COVID-19 epidemic, causing the increasing death of both patients with and without COVID-19 (4, 5, 16, 59). Therefore, it is imperative to accelerate the turnover rate of hospitalization and increase the capacity of outpatient care in the context of the COVID-19 crisis (5, 16, 32, 59). CIRT could maximize the UHO of ULC patients on account of the shortened hospital stay (due to shortened treatment course) and the excellent capacity of the outpatient approach. Consequently, CIRT is helpful not only to improve the capacity of medical service but also to minimize the risk of nosocomial cross-infection of SARS-CoV-2 by reducing the exposure frequency and total duration in the SARS-CoV-2 environment.

Study Limitations

The present study has a few limitations. With the exception of a PSM study (43) for CIRT in comparison with TACE, the other studies (36–42, 44–54) for the CIRT assessment were all case reports or single-arm studies lacking a contrastive control group. This is mainly due to the growing stage of CIRT. While the evidential strength of the CIRT assessment is limited, the evidence of CIRT is urgently needed and important for global oncologists to fight against SARS-CoV-2 and liver cancer concurrently in the context of the COVID-19 pandemic because of its unique superiorities. All of this evidence and

experiences are necessary for decision-making because timely life-saving is the foremost principle in the unprecedented crisis worldwide.

CONCLUSIONS AND FUTURE PROSPECTS

In order to optimize the treatment strategy of patients with ULC due to the COVID-19 crisis worldwide, multi-angle methods were implemented to evaluate the non-invasive CIRT for treating ULC, from which we concluded that CIRT could obtain favorable anti-cancer effectiveness and concurrently, minimize toxicities to patients for preserving patients in a relatively good systemic and immune condition. In addition, CIRT has the ability of TMIH with the controllable risk of SARS-CoV-2 infection exposure, as well as the optimal utilization rate of both hospitalization and outpatient care concurrently. Therefore, we have definitively judged CIRT as the optimal treatment strategy for appropriate patients with ULC when we need to minimize the risk of SARS-CoV-2 infection and improve the capacity of medical service in the COVID-19 crisis. We believe that CIRT will be greatly helpful to reduce the risk of SARS-CoV-2 infection and cancer malignant death concurrently during the COVID-19 pandemic. We also firmly believe that the trajectory of this unprecedented pandemic caused by SARS-CoV-2 will become better and better worldwide with international cooperation and mutual assistance, innovation, and sharing.

DATA AVAILABILITY STATEMENT

The original contributions presented in the study are included in the article/supplementary material, further inquiries can be directed to the corresponding author.

REFERENCES

1. Zhou P, Yang XL, Wang XG, Hu B, Zhang L, Zhang W, et al. A pneumonia outbreak associated with a new coronavirus of probable bat origin. *Nature*. (2020) 579:270–3. doi: 10.1038/s41586-020-2012-7
2. Lu R, Zhao X, Li J, Niu P, Yang B, Wu H, et al. Genomic characterisation and epidemiology of 2019 novel coronavirus: implications for virus origins and receptor binding. *Lancet*. (2020) 395:565–74. doi: 10.1016/s0140-6736(20)30251-8
3. World Health Organisation. *WHO Time-Line COVID-19*. Available online at: <https://www.who.int/emergencies/diseases/novel-coronavirus-2019/events-as-they-happen> (accessed March 11, 2020).
4. World Health Organisation. *WHO Coronavirus Disease (COVID-19) Dashboard*. Available online at: <https://covid19.who.int/> (accessed November 23, 2021).
5. Rosenbaum L. The untold toll - the pandemic's effects on patients without Covid-19. *N Engl J Med*. (2020) 382:2368–71. doi: 10.1056/NEJMms2009984
6. Tuech JJ, Gangloff A, Di Fiore F, Benyoucef A, Michel P, Schwarz L. The day after tomorrow: how should we address health system organization to treat cancer patients after the peak of the COVID-19 epidemic? *Oncology*. (2020) 98:827–35. doi: 10.1159/000509650
7. Liang W, Guan W, Chen R, Wang W, Li J, Xu K, et al. Cancer patients in SARS-CoV-2 infection: a nationwide analysis in China. *Lancet Oncol*. (2020) 21:335–7. doi: 10.1016/s1470-2045(20)30096-6

ETHICS STATEMENT

The studies involving human participants were reviewed and approved by the Ethics Committee of Gansu Provincial Cancer Hospital and the Ethics Committee of Gansu Wuwei Tumor Hospital. The patients/participants provided their written informed consent to participate in this study.

AUTHOR CONTRIBUTIONS

ZL and QL developed the study conception and design. ZL, QL, and XW supervised the whole study process and coordinated all the work. ZL, QL, XW, SL, and WC collected the data and prepared the figures and tables. ZL, QL, XJ, and XGL contributed to selecting the analytical tools and methods. ZL, QL, ZD, XXL, XZ, PL, HZ, QZ, HL, and RL analyzed, interpreted, reviewed, and cross-checked the data. ZL and QL wrote and revised the manuscript. All authors critically reviewed and approved the final manuscript.

FUNDING

This work was jointly supported by the China Postdoctoral Science Foundation (Grant No. 2019M663860), the National Natural Science Foundation of China (Grant No. 11875299), the Key Deployment Project of the Chinese Academy of Sciences (Grant No. KFZD-SW-222), and the West Light Foundation of Chinese Academy of Sciences (Grant No. 29Y86205).

ACKNOWLEDGMENTS

We thank all authors for their contributions to this study.

8. Tang IV, Hu Y. Poor clinical outcomes for patients with cancer during the COVID-19 pandemic. *Lancet Oncol*. (2020) 21:862–4. doi: 10.1016/s1470-2045(20)30311-9
9. Zhang L, Zhu F, Xie L, Wang C, Wang J, Chen R, et al. Clinical characteristics of COVID-19-infected cancer patients: a retrospective case study in three hospitals within Wuhan, China. *Ann Oncol*. (2020) 31:894–901. doi: 10.1016/j.annonc.2020.03.296
10. Tian J, Yuan X, Xiao J, Zhong Q, Yang C, Liu B, et al. Clinical characteristics and risk factors associated with COVID-19 disease severity in patients with cancer in Wuhan, China: a multicentre, retrospective, cohort study. *Lancet Oncol*. (2020) 21:893–903. doi: 10.1016/s1470-2045(20)30309-0
11. Yang K, Sheng Y, Huang C, Jin Y, Xiong N, Jiang K, et al. Clinical characteristics, outcomes, and risk factors for mortality in patients with cancer and COVID-19 in Hubei, China: a multicentre, retrospective, cohort study. *Lancet Oncol*. (2020) 21:904–13. doi: 10.1016/s1470-2045(20)30310-7
12. Yarza R, Bover M, Paredes D, López-López F, Jara-Casas D, Castelo-Loureiro A, et al. SARS-CoV-2 infection in cancer patients undergoing active treatment: analysis of clinical features and predictive factors for severe respiratory failure and death. *Eur J Cancer*. (2020) 135:242–50. doi: 10.1016/j.ejca.2020.06.001
13. Garg PK, Kaul P, Choudhary D, Turaga KK, Singh MP, Tiwari AR, et al. Discordance of COVID-19 guidelines for patients with cancer: a systematic review. *J Surg Oncol*. (2020). 122:579–93. doi: 10.1002/jso.26110
14. Omarini C, Maur M, Luppi G, Narni F, Luppi M, Dominici M, et al. Cancer treatment during the coronavirus disease 2019 pandemic: do not

- postpone. *do it! Eur J Cancer.* (2020) 133:29–32. doi: 10.1016/j.ejca.2020.04.034
15. Huillard O, Goldwasser F. Cancer treatment during the coronavirus disease 2019 pandemic: do not postpone but decide wisely. *Eur J Cancer.* (2020) 135:51. doi: 10.1016/j.ejca.2020.05.024
 16. Kutikov A, Weinberg DS, Edelman MJ, Horwitz EM, Uzzo RG, Fisher RI, et al. War on two fronts: cancer care in the time of COVID-19. *Ann Intern Med.* (2020) 172:756–8. doi: 10.7326/m20-1133
 17. Moraliyage H, De Silva D, Ranasinghe W, Adikari A, Alahakoon D, Prasad R, et al. Cancer in lockdown: impact of the COVID-19 pandemic on patients with cancer. *Oncologist.* (2021) 26:e342–4. doi: 10.1002/onco.13604
 18. Hasson SP, Waissengrin B, Shachar E, Hodruj M, Fayngor R, Brezis M, et al. Rapid implementation of telemedicine during the COVID-19 pandemic: perspectives and preferences of patients with cancer. *Oncologist.* (2021) 26:e679–85. doi: 10.1002/onco.13676
 19. Royce TJ, Sanoff HK, Rewari A. Telemedicine for cancer care in the time of COVID-19. *JAMA Oncol.* (2020) 6:1698–9. doi: 10.1001/jamaoncol.2020.2684
 20. Zhang W, Hu W, Hu J, Gao J, Yang J, Kong L, et al. Carbon ion radiation therapy for sinonasal malignancies: promising results from 2282 cases from the real world. *Cancer Sci.* (2020) 111:4465–79. doi: 10.1111/cas.14650
 21. Kamada T, Tsujii H, Blakely EA, Debus J, De Neve W, Durante M, et al. Carbon ion radiotherapy in Japan: an assessment of 20 years of clinical experience. *Lancet Oncol.* (2015) 16:e93–e100. doi: 10.1016/s1470-2045(14)70412-7
 22. Durante M, Brenner DJ, Formenti SC. Does heavy ion therapy work through the immune system? *Int J Radiat Oncol Biol Phys.* (2016) 96:934–6. doi: 10.1016/j.ijrobp.2016.08.037
 23. Durante M, Formenti S. Harnessing radiation to improve immunotherapy: better with particles? *Br J Radiol.* (2020) 93:20190224. doi: 10.1259/bjr.20190224
 24. Matsunaga A, Ueda Y, Yamada S, Harada Y, Shimada H, Hasegawa M, et al. Carbon-ion beam treatment induces systemic antitumor immunity against murine squamous cell carcinoma. *Cancer.* (2010) 116:3740–8. doi: 10.1002/cncr.25134
 25. Durante M, Yamada S, Ando K, Furusawa Y, Kawata T, Majima H, et al. X-rays vs. carbon-ion tumor therapy: cytogenetic damage in lymphocytes. *Int J Radiat Oncol Biol Phys.* (2000) 47:793–8. doi: 10.1016/s0360-3016(00)00455-7
 26. Liu Y, Dong Y, Kong L, Shi F, Zhu H, Yu J. Abscopal effect of radiotherapy combined with immune checkpoint inhibitors. *J Hematol Oncol.* (2018) 11:104. doi: 10.1186/s13045-018-0647-8
 27. Demaria S, Golden EB, Formenti SC. Role of local radiation therapy in cancer immunotherapy. *JAMA Oncol.* (2015) 1:1325–32. doi: 10.1001/jamaoncol.2015.2756
 28. Lippitz BE, Harris RA. A translational concept of immuno-radiobiology. *Radiation Oncol.* (2019) 140:116–24. doi: 10.1016/j.radonc.2019.06.001
 29. Shiba S, Shibuya K, Kawashima M, Okano N, Kaminuma T, Okamoto M, et al. Comparison of dose distributions when using carbon ion radiotherapy versus intensity-modulated radiotherapy for hepatocellular carcinoma with macroscopic vascular invasion: a retrospective analysis. *Anticancer Res.* (2020) 40:459–64. doi: 10.21873/anticancer.13974
 30. Abe T, Saitoh J, Kobayashi D, Shibuya K, Koyama Y, Shimada H, et al. Dosimetric comparison of carbon ion radiotherapy and stereotactic body radiotherapy with photon beams for the treatment of hepatocellular carcinoma. *Radiat Oncol.* (2015) 10:187. doi: 10.1186/s13014-015-0491-8
 31. Ng SSW, Ning MS, Lee P, McMahon RA, Siva S, Chuong MD. Single-fraction stereotactic body radiation therapy: a paradigm during the coronavirus disease 2019 (COVID-19) pandemic and beyond? *Adv Radiat Oncol.* (2020) 5:761–73. doi: 10.1016/j.adro.2020.06.011
 32. Aitken K, Good J, Hawkins M, Grose D, Mukherjee S, Harrison M, et al. Liver stereotactic ablative radiotherapy: an effective and feasible alternative to surgery during the COVID-19 pandemic. *Clin Oncol.* (2020) 32:477. doi: 10.1016/j.clon.2020.04.012
 33. Mou B, Hyde D, Araujo C, Bartha L, Bergman A, Liu M. Implementation of single-fraction lung stereotactic ablative radiotherapy in a multicenter provincial cancer program during the COVID-19 pandemic. *Cureus.* (2021) 13:e15598. doi: 10.7759/cureus.15598
 34. Scorsetti M, Goodman KA, Seong J, Loi M, Huguet F, Dawson LA. Hepatocellular carcinoma in the COVID-19 era: primetime for stereotactic body radiotherapy and a lesson for the future? *Oncologist.* (2020) 25:e1249–50. doi: 10.1634/theoncologist.2020-0416
 35. Barcellini A, Vitolo V, Cobianchi L, Valvo F, Vischioni B, Bonora M, et al. Pancreatic cancer: does a short course of carbon ion radiotherapy worth during COVID-19 outbreak? *Pancreatol.* (2020) 20:1004–5. doi: 10.1016/j.pan.2020.05.007
 36. Shiba S, Shibuya K, Okamoto M, Okano N, Kubo N, Kaminuma T, et al. Carbon-ion radiotherapy for oligometastatic colorectal cancer in the liver or lung. *Anticancer Res.* (2021) 41:1997–2005. doi: 10.21873/anticancer.14967
 37. Okazaki S, Shibuya K, Shiba S, Okamoto M, Miyasaka Y, Osu N, et al. Carbon ion radiotherapy for patients with hepatocellular carcinoma in the caudate lobe carbon ion radiotherapy for hepatocellular carcinoma in caudate lobe. *Hepatol Res.* (2021) 51:303–12. doi: 10.1111/hepr.13606
 38. Takakusagi S, Takagi H, Shibuya K, Kosone T, Sato K, Kakizaki S, et al. Two elder cases of hepatocellular carcinoma adjacent to intrahepatic vessels successfully treated by carbon ion radiotherapy. *Clin J Gastroenterol.* (2020) 13:920–6. doi: 10.1007/s12328-020-01151-2
 39. Shiba S, Shibuya K, Okamoto M, Okazaki S, Komatsu S, Kubota Y, et al. Clinical impact of Hypofractionated carbon ion radiotherapy on locally advanced hepatocellular carcinoma. *Radiat Oncol.* (2020) 15:195. doi: 10.1186/s13014-020-01634-z
 40. Yasuda S, Kato H, Imada H, Isozaki Y, Kasuya G, Makishima H, et al. Long-Term results of high-dose 2-fraction carbon ion radiation therapy for hepatocellular carcinoma. *Adv Radiat Oncol.* (2020) 5:196–203. doi: 10.1016/j.adro.2019.09.007
 41. Makishima H, Yasuda S, Isozaki Y, Kasuya G, Okada N, Miyazaki M, et al. Single fraction carbon ion radiotherapy for colorectal cancer liver metastasis: a dose escalation study. *Cancer Sci.* (2019) 110:303–9. doi: 10.1111/cas.13872
 42. Shibuya K, Ohno T, Katoh H, Okamoto M, Shiba S, Koyama Y, et al. A feasibility study of high-dose hypofractionated carbon ion radiation therapy using four fractions for localized hepatocellular carcinoma measuring 3 cm or larger. *Radiation Oncol.* (2019) 132:230–5. doi: 10.1016/j.radonc.2018.10.009
 43. Shiba S, Shibuya K, Katoh H, Kaminuma T, Miyazaki M, Kakizaki S, et al. A comparison of carbon ion radiotherapy and transarterial chemoembolization treatment outcomes for single hepatocellular carcinoma: a propensity score matching study. *Radiat Oncol.* (2019) 14:137. doi: 10.1186/s13014-019-1347-4
 44. Shibuya K, Ohno T, Terashima K, Toyama S, Yasuda S, Tsuji H, et al. Short-course carbon-ion radiotherapy for hepatocellular carcinoma: a multi-institutional retrospective study. *Liver Int.* (2018) 38:2239–47. doi: 10.1111/liv.13969
 45. Shiba S, Shibuya K, Katoh H, Koyama Y, Okamoto M, Abe T, et al. No deterioration in clinical outcomes of carbon ion radiotherapy for sarcopenia patients with hepatocellular carcinoma. *Anticancer Res.* (2018) 38:3579–86. doi: 10.21873/anticancer.12631
 46. Toyama S, Shioyama Y, Suefuji H, Shinoto M, Matsumoto K, Terashima K, et al. A case of the cirrhotic patient performed living donor liver transplantation after carbon-ion radiotherapy for hepatocellular carcinoma. *Int Cancer Conf J.* (2018) 7:65–70. doi: 10.1007/s13691-018-0322-5
 47. Shiba S, Abe T, Shibuya K, Katoh H, Koyama Y, Shimada H, et al. Carbon ion radiotherapy for 80 years or older patients with hepatocellular carcinoma. *BMC Cancer.* (2017) 17:721. doi: 10.1186/s12885-017-3724-4
 48. Kasuya G, Kato H, Yasuda S, Tsuji H, Yamada S, Haruyama Y, et al. Progressive hypofractionated carbon-ion radiotherapy for hepatocellular carcinoma: combined analyses of 2 prospective trials. *Cancer.* (2017) 123:3955–65. doi: 10.1002/cncr.30816
 49. Harada M, Karasawa K, Yasuda S, Kamada T, Nemoto K. One shot of carbon-ion radiotherapy cured a 6-cm chemo-resistant metastatic liver tumor: a case of breast cancer. *Jpn J Radiol.* (2015) 33:598–602. doi: 10.1007/s11604-015-0462-x
 50. Habermehl D, Debus J, Ganten T, Ganten MK, Bauer J, Brecht IC, et al. Hypofractionated carbon ion therapy delivered with scanned ion beams for patients with hepatocellular carcinoma - feasibility and clinical response. *Radiat Oncol.* (2013) 8:59. doi: 10.1186/1748-717x-8-59
 51. Komatsu S, Fukumoto T, Demizu Y, Miyawaki D, Terashima K, Sasaki R, et al. Clinical results and risk factors of proton and carbon ion therapy for hepatocellular carcinoma. *Cancer.* (2011) 117:4890–904. doi: 10.1002/cncr.26134

52. Imada H, Kato H, Yasuda S, Yamada S, Yanagi T, Kishimoto R, et al. Comparison of efficacy and toxicity of short-course carbon ion radiotherapy for hepatocellular carcinoma depending on their proximity to the porta hepatis. *Radiother Oncol.* (2010) 96:231–5. doi: 10.1016/j.radonc.2010.05.019
53. Imada H, Kato H, Yasuda S, Yamada S, Yanagi T, Hara R, et al. Compensatory enlargement of the liver after treatment of hepatocellular carcinoma with carbon ion radiotherapy - relation to prognosis and liver function. *Radiother Oncol.* (2010) 96:236–42. doi: 10.1016/j.radonc.2010.03.025
54. Kato H, Tsujii H, Miyamoto T, Mizoe JE, Kamada T, Tsuji H, et al. Results of the first prospective study of carbon ion radiotherapy for hepatocellular carcinoma with liver cirrhosis. *Int J Radiat Oncol Biol Phys.* (2004) 59:1468–76. doi: 10.1016/j.ijrobp.2004.01.032
55. Dhawan G, Kapoor R, Dhawan R, Singh R, Monga B, Giordano J, et al. Low dose radiation therapy as a potential life saving treatment for COVID-19-induced acute respiratory distress syndrome (ARDS). *Radiother Oncol.* (2020) 147:212–6. doi: 10.1016/j.radonc.2020.05.002
56. Paules CI, Marston HD, Fauci AS. Coronavirus infections-more than just the common cold. *Jama.* (2020) 323:707–8. doi: 10.1001/jama.2020.0757
57. Chatterjee P. Is India missing COVID-19 deaths? *Lancet.* (2020) 396:657. doi: 10.1016/s0140-6736(20)31857-2
58. The Lancet. COVID-19 in India: the dangers of false optimism. *Lancet.* (2020) 396:867. doi: 10.1016/s0140-6736(20)32001-8
59. Kadri SS, Simpson SQ. Potential implications of SARS-CoV-2 delta variant surges for rural areas and hospitals. *Jama.* (2021) 326:1003–4. doi: 10.1001/jama.2021.13941
60. de Joode K, Dumoulin DW, Engelen V, Bloemendal HJ, Verheij M, van Laarhoven HWM, et al. Impact of the coronavirus disease 2019 pandemic on cancer treatment: the patients' perspective. *Eur J Cancer.* (2020) 136:132–9. doi: 10.1016/j.ejca.2020.06.019
61. Dai M, Liu D, Liu M, Zhou F, Li G, Chen Z, et al. Patients with cancer appear more vulnerable to SARS-CoV-2: a multicenter study during the COVID-19 outbreak. *Cancer Discov.* (2020) 10:783–91. doi: 10.1158/2159-8290.CD-20-0422
62. Yu J, Ouyang W, Chua MLK, Xie C. SARS-CoV-2 transmission in patients with cancer at a tertiary care hospital in Wuhan, China. *JAMA Oncol.* (2020) 6:1108–10. doi: 10.1001/jamaoncol.2020.0980
63. Tinganelli W, Durante M. Carbon ion radiobiology. *Cancers.* (2020) 12:1–37. doi: 10.3390/cancers12103022
64. Mohamad O, Tabuchi T, Nitta Y, Nomoto A, Sato A, Kasuya G, et al. Risk of subsequent primary cancers after carbon ion radiotherapy, photon radiotherapy, or surgery for localised prostate cancer: a propensity score-weighted, retrospective, cohort study. *Lancet Oncol.* (2019) 20:674–85. doi: 10.1016/s1470-2045(18)30931-8
65. Mohamad O, Yamada S, Durante M. Clinical indications for carbon ion radiotherapy. *Clin Oncol.* (2018) 30:317–29. doi: 10.1016/j.clon.2018.01.006
66. Kirkby KJ, Kirkby NF, Burnet NG, Owen H, Mackay RI, Crellin A, et al. Heavy charged particle beam therapy and related new radiotherapy technologies: the clinical potential, physics and technical developments required to deliver benefit for patients with cancer. *Br J Radiol.* (2020) 93:20200247. doi: 10.1259/bjr.20200247
67. Qi WX, Fu S, Zhang Q, Guo XM. Charged particle therapy versus photon therapy for patients with hepatocellular carcinoma: a systematic review and meta-analysis. *Radiother Oncol.* (2015) 114:289–95. doi: 10.1016/j.radonc.2014.11.033
68. Igaki H, Mizumoto M, Okumura T, Hasegawa K, Kokudo N, Sakurai H, et al. systematic review of publications on charged particle therapy for hepatocellular carcinoma. *Int J Clin Oncol.* (2018) 23:423–33. doi: 10.1007/s10147-017-1190-2
69. Sung H, Ferlay J, Siegel RL, Laversanne M, Soerjomataram I, Jemal A, et al. Global cancer statistics 2020: GLOBOCAN estimates of incidence and mortality worldwide for 36 cancers in 185 countries. *CA Cancer J Clin.* (2021) 71:209–49. doi: 10.3322/caac.21660
70. Cao W, Chen HD, Yu YW, Li N, Chen WQ. Changing profiles of cancer burden worldwide and in China: a secondary analysis of the global cancer statistics 2020. *Chin Med J.* (2021) 134:783–91. doi: 10.1097/cm9.0000000000001474
71. Dai T, Li Q, Liu X, Dai Z, He P, Ma Y, et al. Nanodosimetric quantities and RBE of a clinically relevant carbon-ion beam. *Med Phys.* (2020) 47:772–80. doi: 10.1002/mp.13914
72. Sheikh A, McMenamin J, Taylor B, Robertson C. SARS-CoV-2 Delta VOC in Scotland: demographics, risk of hospital admission, and vaccine effectiveness. *Lancet.* (2021) 397:2461–2. doi: 10.1016/s0140-6736(21)01358-1
73. Mlcochova P, Kemp S, Dhar MS, Papa G, Meng B, Ferreira Iatm, et al. SARS-CoV-2 B.1.617.2 Delta variant replication and immune evasion. *Nature.* (2021) 599:114–9. doi: 10.1038/s41586-021-03944-y

Conflict of Interest: The authors declare that the research was conducted in the absence of any commercial or financial relationships that could be construed as a potential conflict of interest.

Publisher's Note: All claims expressed in this article are solely those of the authors and do not necessarily represent those of their affiliated organizations, or those of the publisher, the editors and the reviewers. Any product that may be evaluated in this article, or claim that may be made by its manufacturer, is not guaranteed or endorsed by the publisher.

Copyright © 2021 Li, Li, Wang, Li, Chen, Jin, Liu, Dai, Liu, Zheng, Li, Zhang, Zhang, Luo and Liu. This is an open-access article distributed under the terms of the Creative Commons Attribution License (CC BY). The use, distribution or reproduction in other forums is permitted, provided the original author(s) and the copyright owner(s) are credited and that the original publication in this journal is cited, in accordance with accepted academic practice. No use, distribution or reproduction is permitted which does not comply with these terms.



From Classical Radiation to Modern Radiation: Past, Present, and Future of Radiation Mutation Breeding

Liqiu Ma^{1,2*}, Fuquan Kong^{1,2}, Kai Sun³, Ting Wang^{4*} and Tao Guo^{3*}

¹ Department of Nuclear Physics, China Institute of Atomic Energy, Beijing, China, ² National Innovation Center of Radiation Application, Beijing, China, ³ National Engineering Research Center of Plant Space Breeding, South China Agricultural University, Guangdong, China, ⁴ Key Laboratory of High Magnetic Field and Ion Beam Physical Biology, Hefei Institutes of Physical Science, Chinese Academy of Sciences, Hefei, China

OPEN ACCESS

Edited by:

Fai Ye,
Institute of Modern Physics
(CAS), China

Reviewed by:

Kun Wu,
Institute of Genetics and
Developmental Biology (CAS), China
Yi Xie,
Institute of Modern Physics
(CAS), China

*Correspondence:

Liqiu Ma
maliqui@ciae.ac.cn
Ting Wang
wangting@ipp.ac.cn
Tao Guo
guoguo@scau.edu.cn

Specialty section:

This article was submitted to
Radiation and Health,
a section of the journal
Frontiers in Public Health

Received: 31 August 2021

Accepted: 15 November 2021

Published: 21 December 2021

Citation:

Ma L, Kong F, Sun K, Wang T and
Guo T (2021) From Classical Radiation
to Modern Radiation: Past, Present,
and Future of Radiation Mutation
Breeding.
Front. Public Health 9:768071.
doi: 10.3389/fpubh.2021.768071

Radiation mutation breeding has been used for nearly 100 years and has successfully improved crops by increasing genetic variation. Global food production is facing a series of challenges, such as rapid population growth, environmental pollution and climate change. How to feed the world's enormous human population poses great challenges to breeders. Although advanced technologies, such as gene editing, have provided effective ways to breed varieties, by editing a single or multiple specific target genes, enhancing germplasm diversity through mutation is still indispensable in modern and classical radiation breeding because it is more likely to produce random mutations in the whole genome. In this short review, the current status of classical radiation, accelerated particle and space radiation mutation breeding is discussed, and the molecular mechanisms of radiation-induced mutation are demonstrated. This review also looks into the future development of radiation mutation breeding, hoping to deepen our understanding and provide new vitality for the further development of radiation mutation breeding.

Keywords: mutation breeding, classical radiation, particle radiation, space radiation, mutagenesis

INTRODUCTION

Crops provide the most basic guarantee for human survival on Earth, its domestication plays an important role in developing wild plants to produce cultivated crops through the long-term screening of desirable characteristics caused by gene mutations (1, 2). However, spontaneous mutation appears at an extremely low frequency in nature ($\sim 10^{-6}$), rendering the process of excellent variety cultivation screening tedious. How to accelerate the frequency of mutation has always been a key problem in crop variety development, with a long history from natural evolution to cross breeding and mutation breeding in crop breeding.

Mutation breeding refers to the method of using artificial mutagenesis to obtain new biological cultivars, mainly through chemical or radiation mutagenesis. Chemical mutagenesis refers to the biochemical reaction between chemical agents and genetic material, and the result is mostly point mutations in genes. Although chemical mutagenesis is effective, its environmental optimization and biological safety need to be improved. Comparatively, radiation mutagenesis has the characteristics of more complex genetic mutations and more beneficial mutant phenotypes.

Radiation mutation breeding is generally divided into classical radiation mutation breeding, particle mutation breeding and space radiation mutation breeding. Classical radiation mutation breeding methods mainly include X-ray and gamma ray applications. As a commonly used method, classical radiation mutation breeding has been proven to be useful for crop

variation, which mainly refers to the process of using various rays to induce a large number of genomic mutations and speed up the production of mutant traits through energy deposition directly or indirectly onto DNA. This approach offers the possibility of inducing desirable attributes that either cannot be expressed in nature or have been lost during evolution, and a large number of new varieties widely used in production have been bred by classical radiation mutation technology (3).

Particle mutation breeding mainly uses accelerated particles, such as heavy-ions or protons. They have unique physical properties, such as diversified radiation parameters, complex track structure and depth-dose distribution. Accelerated particle has been considered a powerful mutagen for crop breeding because it induces excellent biological mutagenic effectiveness at relatively low radiation doses (4). A notable feature of the particle radiation mutagenesis technology is that it can produce novel cultivars with good traits without affecting other phenotypes (5).

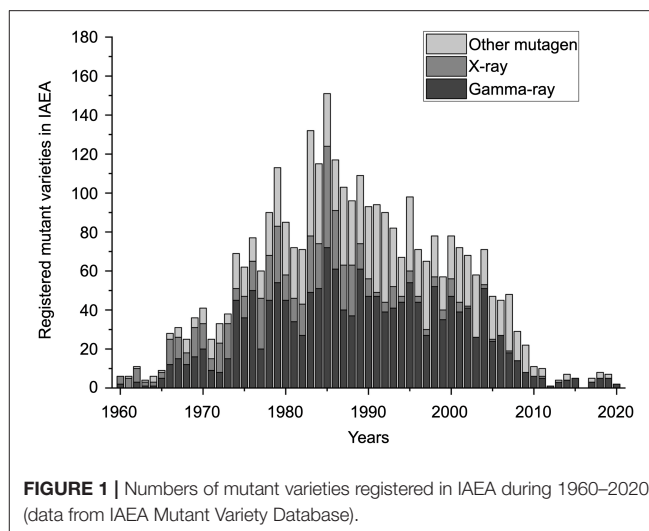
With the steady advancement of manned space projects, space exploration activities will become more frequent in the future. The space environment refers to the outer space outside the atmosphere accompanied by radiation, microgravity, and alternating magnetic fields. This special and complex environment brings new opportunities for mutation breeding. Compared with traditional radiation, space breeding has the characteristics of a high mutation frequency and multiple directions; its mutation rate can reach 10% (6), and a series of new plant varieties have been developed in this way (7, 8).

Radiation mutation breeding has played an important role in the cultivation of new crop varieties. In this review, we first briefly discuss achievements through radiation breeding in recent decades as well as some concerns on the process and mechanism of classical radiation, accelerated particle and space radiation mutagenesis. This review will deepen our knowledge and provide a theoretical foundation for improving the efficiency of future crop radiation mutation breeding and promoting improvement under the challenge of other newly emerging breeding methods.

DEVELOPMENT AND MECHANISM OF CLASSICAL RADIATION MUTATION BREEDING

Past and Present of Classical Radiation Mutation Breeding

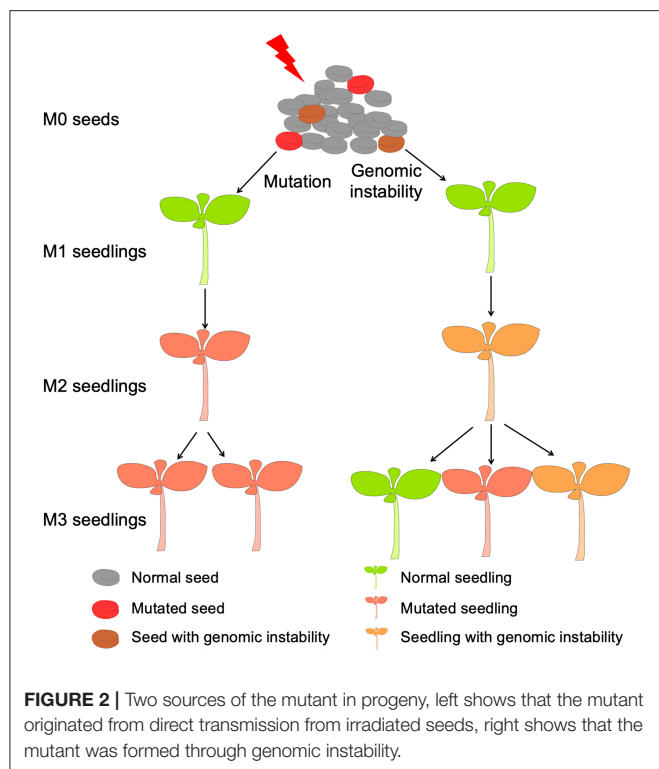
Radiation was suggested as a mutagen since Muller demonstrated that exposure to X-rays can cause genetic mutations in 1928 (9). After Stadler first published papers on mutations induced by irradiation in maize and barley (10, 11), radiation has been widely applied to develop new cultivars used for crop production and as genetic resources. Compared to other breeding methods, such as cross-breeding and chemical mutagenesis, radiation mutation breeding has incomparable advantages, with a wide mutation spectrum and high mutation efficiency (12). To date, 3,365 mutant varieties have been registered in the Mutant Variety Database of the International Atomic Energy Agency (IAEA), and more than 1,000 new varieties have been used and promoted worldwide. Here, we analyse the varieties bred by mutation in the



past 60 years from 1960 to 2020 (13). **Figure 1** shows that most of the registered varieties bred by various mutation approaches were concentrated before 2010, with a peak in the 1980s. Seventy percentage of the overall registered varieties were produced by classical gamma rays and X-rays irradiation, which laid a crucial foundation for the agriculture development. However, great challenges have been brought to traditional breeding methods with the development of advanced mutation technology, such as targeted gene editing represented by CRISPR (clustered regularly interspaced short palindromic repeat) technology in recent years (14), which might explain the steep decline in the number of varieties registered in Mutant Variety Database of IAEA after 2010. Of course, it is possible that many new varieties might have been bred by traditional radiation during this period without being registered. Nevertheless, the downward trend suggests that after years of continuous breeding, variation traits have been basically saturated from a macroscopic view, especially in some important crop varieties, and it is difficult to obtain new breakthrough variation traits under current knowledge on radiation mutation. Therefore, more research should be performed to elucidate the mechanism of radiation mutagenesis.

The Mutagenesis Mechanism Under Classical Radiation Mutation Breeding Radiation-Induced DNA Damage

The process of radiation mutation breeding begins with interactions between radiation and DNA, including direct structural and functional changes to DNA molecules via radiation energy and indirect damage by free radicals generated through interactions between water molecules and ionizing radiation (15). To maintain genomic integrity, cells have evolved a set of repair mechanisms to address DNA damage. Indeed, the repair method is invoked according to the type of DNA damage incurred (16). DNA damage can be divided into two categories: single-strand break (SSB) and double-strand break (DSB). The SSB repair pathways are mainly base excision repair (BER), nucleotide excision repair (NER) and mismatch repair (MMR).



In contrast, DSBs are mainly repaired by non-homologous end-joining (NHEJ) and homologous recombination (HR) (16, 17). However, DNA damage is not equivalent to mutation. If DNA damage is repaired correctly, no mutation will remain. Gene mutation is the result of “errors” in the process of DNA damage repair. Some of these errors are accidental, such as replication errors caused by some single-strand breaks not being detected before DNA replication, unstable DNA single strands in the process of repair, and the participation of low-fidelity polymerase, among others; the mutation type is basically a point mutation with base substitution (18). For severe DSBs, deletion and translocation of fragments are introduced in the repair process (19). If these mutations are retained in subsequent cell division and inherited by progeny, they become the source of mutant traits, as shown in **Figure 2**.

Radiation-Induced Genomic Instability

In addition to the direct inheritance of DNA damage caused by radiation to progeny, there is another method of inheritance that can result in mutant traits in offspring, as shown in **Figure 2**. As mentioned above, the genetic stability of the genome is key to maintaining normal cell proliferation and differentiation. Normal cells have efficient DNA damage monitoring and response mechanisms to deal with the pressure on the genome caused by internal and external stress, and maintain genome damage and repair in a relatively balanced state. When this balance is broken, however, cells enter a DNA mutation susceptibility state called genomic instability, which can be caused by genetic mutation or epigenetic modification

(20). Radiation-induced genomic instability is a concept that describes delayed and persistent genetic alterations in progeny of the irradiated cells, which was first detected in *in vitro* cell system experiments in the 1950s (21). Subsequent studies have found that gamma rays, neutrons, protons and α particles can induce genomic instability in cells, which manifests as an increase in various types of mutations, such as single-nucleotide mutations, an increase or decrease in genomic copy number, gene amplification, rearrangement and deletion (22, 23). Using a homologous recombination reporter system, radiation-induced genomic instability has also been confirmed in plant systems, with increased frequencies of homologous recombination persisting in subsequent generations (24–26).

DEVELOPMENT AND MECHANISM OF PARTICLE RADIATION MUTATION BREEDING

The New Generation Particle Radiation Mutagenesis Technology

Unlike classical gamma rays and X-rays, which are essentially electromagnetic waves, the emerging mutagens represented by accelerated heavy-ions or protons are essentially charged particles. Compared with classical radiation, accelerated particle irradiation can deposit more energy along the ion track and can maintain a higher mutation frequency and mutation spectrum at a relatively low dose (4). This is because accelerated particles with high linear energy transfer (LET) cause high-density ionization along the ion track, causing a large amount of damage to DNA in a small area, which is termed clustered DNA damage (27–29). Such clustered DNA damage is difficult to repair effectively and correctly, leading to the generation of free DNA fragments, which contribute to the formation of chromosome rearrangements and large deletions (30–32). These rearrangements and large deletions can generate more combinations of gene mutation sites, thereby breaking the linkage inheritance of traits, and it is expected that more mutants with excellent traits will be obtained.

The technology of particle radiation mutagenesis based on advanced particle accelerators originated in Japan in the 1990s (4). Although there are many particle accelerator facilities in the world, most of them are used for nuclear physics research, and there are few irradiation facilities that can be used for crop breeding. Particle accelerators can be divided into medium- and high-energy (MeV or GeV level) particle accelerators and low-energy (KeV level) particle accelerators according to the energy of the accelerated particles. In general, medium- and high-energy particles are considered to penetrate the target material, whereas low-energy particle cannot penetrate the target material, which is commonly referred to as ion implantation. To date, the medium- and high-energy particle accelerator facilities used for particle radiation mutation breeding include RIBF of the Institute of Physical and Chemical Research (RIKEN, Japan), TIARA of the National Institutes for Quantum Science and Technology (QST, Japan), W-MAST of the Wakasa Wan Energy Research Center (WERC, Japan), LNS of the National Institute for Nuclear Physics (INFN, Italy), HIRFL of the Institute of Modern

TABLE 1 | Particle accelerator facilities that can be used for radiation breeding.

Medium- and High-energy facility	Institute	Ion species	Energy (MeV)	LET (keV/μm)	Range in water (mm)
RIBF	RIKEN, Japan	C, N, Ne, Ar, Fe	1,620–5,040	23–640	4–40
TIARA	QST, Japan	He, C, Ne	100–350	9–441	6–16
W-MAST	WERC, Japan	H, C	200~500.4	0.5–52	5–256
LNS	INFN, Italy	C	960	31	17
HIRFL	CAS-IMP, China	C, Ar	960–2,760	31–327	5–17
CYCIAE100	CIAE, China	H	100	0.7	76

Physics, Chinese Academy of Sciences (CAS-IMP, China), and CYCIAE100 of the Chinese Institute of Atomic Energy (CIAE, China) (Table 1). In the field of low-energy particle mutagenesis, the most representative research facilities are the IBBe-Device of the Hefei Institute of Physical Science, Chinese Academy of Sciences (CAS-HIPS, China), IBBT of Chiang Mai University (CMU, Thailand)..

In the early stage of the development of particle radiation mutagenesis, the technology was used for the improvement of ornamental plants, and most of the new cultivars created were exported all over the world, demonstrating its excellent cultivar improvement ability (33). Since the early twenty-first century, research on the variety improvement and mutagenesis mechanism of food crops has been successively carried out (5). More than 30 years of experience in particle radiation mutagenesis shows that the frequency of new traits in crops induced by this technology is relatively high, that the mutation trait is relatively stable and that the breeding period is greatly shortened. Mutants of food crops and ornamental plants with excellent traits generated by this technology can directly launch new cultivars or as parental materials for cross-breeding, contributing to solutions for food and environmental problems. Therefore, particle radiation mutagenesis technology has broad economic benefits and important social significance, and it is a breeding method worthy of promotion.

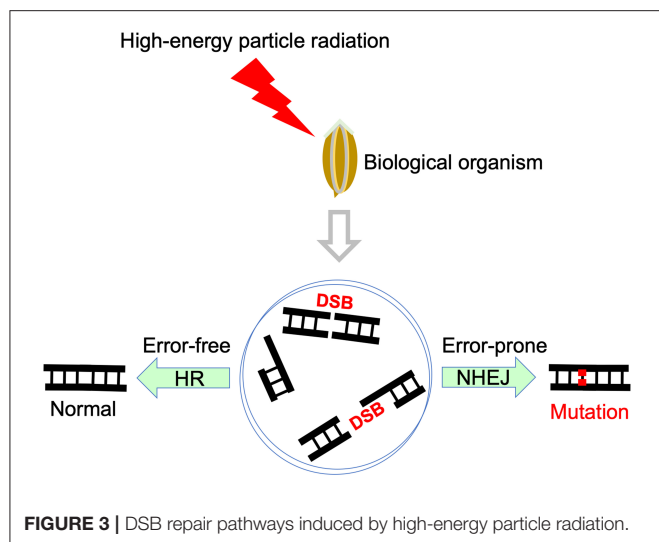
Application and Mutagenesis Mechanism of High-Energy Particle Mutation Breeding

High-energy particle mutation breeding has a history of nearly 30 years thus far. The earliest high-energy particle radiation mutagenesis was used to improve the phenotype of ornamental plants, including sterility and flower color and shape. Since 2002, new flower cultivars, including the new sterile cultivar verbena and new color or shape cultivars chrysanthemum, dahlia and rose, have been developed (34). High-energy particles have also been widely used in the development of agricultural products with excellent traits, such as dwarfed buckwheat, barley and pepper (34), tearless and non-pungent onion (35), lettuce with low browning characteristics (36), rice with a stay-green phenotype (37). High-energy particle radiation mutagenesis technology also plays an important role in the field of biofuels, such as the successful mutagenesis of lipid-rich *Parachlorella kessleri* (38) and *Euglena gracilis* (39).

The successful mutagenesis of the abovementioned variants promoted the development of basic research related to particle

radiation mutagenesis. To make particle radiation mutagenesis technology more efficient, it is necessary to find the most suitable physical radiation parameters, such as radiation dose and LET, which are important parameters to be considered in particle radiation mutagenesis. The survival rate of both model plants and model microbes decreases with increasing dose, and the radiation physical parameters most suitable for mutagenesis must balance survival and mutation. For example, a study by Kazama et al. using the model plant *Arabidopsis thaliana* showed that a 300–400 Gy irradiation dose and a 30 keV/μm LET carbon ion beam can generate the maximum number of mutants (40). Further mechanistic studies at the genomic level in both model plants and model microbes showed that a smaller LET is better at inducing small deletions but that larger LET radiation would lead to large deletions (41–43). In addition, through whole-genome sequencing, Kazama et al. found that relatively high LET Ar ions can cause more complicated rearrangement errors in *Arabidopsis thaliana* than C-ion irradiation technology (44). In general, mutations are generated on the basis of the damage being repaired incorrectly, and the nature of DNA damage caused by high-energy particle radiation is mainly a large number of SSBs and DSBs. SSBs are easily repaired in a short period of time, whereas DSBs constitute damage that has the greatest impact on DNA and usually requires more time to repair (45). DSB damage is mainly repaired competitively through HR or NHEJ pathways (46, 47), as shown in Figure 3. The HR is highly accurate while the NHEJ is error prone. For example, a study by Ma et al. using the model microbe *Neurospora crassa* reported that compared with the NHEJ-deficient strain, the HR-deficient strain results in higher mutation frequency after high-energy particle irradiation (48). Another study based on rice transcriptome sequencing suggested that alternative NHEJ (aNHEJ) may be involved in the DNA repair of complex damage induced by high-LET irradiation (49). These studies revealed that NHEJ has a greater contribution to mutagenesis, and NHEJ enhancement and/or HR suppression strategies may significantly increase the mutagenic efficiency of high-energy particle irradiation.

Furthermore, the new trait mutants obtained by particle radiation mutagenesis are suitable for gene function mining, gene mapping, and even the creation of elite alleles. Several mutants of *Arabidopsis thaliana*, wheat, buckwheat, and rice have been isolated following particle irradiation based on gene mutations formed through error-prone DSB repair pathways such as canonical NHEJ and aNHEJ. These mutants can help us to understand the function of affected genes; for example, FRL1



impacts sepal development (50), *VRN1* influences flowering (51), *S-ELF3* is associated with a dwarf phenotype (52), *CSV1* is related to chloroplast development (53), and *LIN1* controls rice grain length (54). In addition, the Y chromosome genes of *Silene latifolia* have been physically mapped using sex chromosome mutants induced by particle irradiation (55). A recent study showed that particle radiation has the ability to create neutral alleles at the rice *S1* locus, making it possible to cross distantly related species and broadening crop breeding (56).

Application and Mutagenesis Mechanism of Low-Energy Particle Mutation Breeding

The biological effect of particle irradiation has always been an important part of radiobiology. However, for a long time, low-energy particles (10–200 KeV) have been underestimated due to their extremely short penetration depth in matter, which leads to the hypothesis that it is impossible to induce high-level biological effects via their interaction with organisms. In the early 1980s, Yu et al. first confirmed the genetic effect of low-energy particle implantation on rice (57, 58). After years of application in breeding, low-energy particle has been proven to be a high-efficiency mutagenic source for genetic modification, leading to great achievements (59, 60) and promoting the formation of a new interdisciplinary of low-energy particle biology (61). Nevertheless, the debate regarding the mutagenesis mechanism of low-energy particle implantation remains. In the 1990s, Yu et al. proposed the four-factor theory of energy absorption, mass deposition, momentum transfer and charge neutralization, whereby energetic ions are transferred into organisms to cause serious etching to cells and physical damage to biological macromolecules (61). Combining the following ion channel and soft X-ray theory provided an explanation of the physical interaction process. Then, the mutagenesis mechanism of low-energy particle implantation was further elucidated from the biological process. Considering that the theoretical range for low-energy particles in water is $<1\ \mu\text{m}$, which could hardly penetrate

the seed coat, the possibility of inducing biological genetic effects might be due to the radiation-induced bystander effect (RIBE). RIBEs are the phenomenon in which non-irradiated cells exhibit biological effects as a result of signals received from nearby irradiated cells (62). To test this hypothesis, the shoot apical meristem (SAM) and root apical meristem (RAM) of *Arabidopsis* seeds were shielded, and only the middle of each seed was irradiated. After 30 KeV ^{40}Ar irradiation, various postembryonic development endpoints of SAM and RAM were inhibited (63). In another study, different parts of *Arabidopsis* R3L66 seeds (SAM-, RAM-, cotyledon-, and radicle-oriented) were irradiated, and significant increases in genetic changes (HR frequency and HR-related gene expression) were observed in the non-irradiated aerial parts of the irradiated plants (26). These results confirmed that long-distance bystander effects occur in plants. The temporal and spatial characteristics as well as the molecular mechanism of radiation bystander signals in plants have also been elucidated (64–67), and such mechanistic studies have provided strong evidence for clarifying the biological effects induced by low-energy particle irradiation. Currently, big data analysis technology is used to associate the radiation parameters of low-energy particles with the trait variation induced. It is expected that adjusting radiation parameters, such as the type of irradiated particles, dose or energy, will overcome the randomness of mutation and promote further development in the field of low-energy particle mutation breeding.

RESEARCH ON SPACE BREEDING OF PLANTS

Continuous Low-Dose and Combined Irradiation of Different Radiation Sources in a Space Environment May Be Important Factors Inducing Genetic Variation

Compared with on Earth, radiation and microgravity are two important factors that affect living organisms in space (68). Radiation is mainly produced by solar cosmic rays (SCRs) and galactic cosmic rays (GCRs). The radiation in low-Earth orbit also includes particles captured by the Earth's radiation belt, such as high-energy protons, heavy-ions, electrons, neutrons, and gamma rays (69). Among them, high atomic number and high energy particles in the heavy ion component, typically referred to as HZE particles, which are able to penetrate the spacecraft cabin and produce many secondary particles (70) in the spacecraft cabin, including gamma rays, electrons, protons, neutrons, and other heavy ions with different LET values. Long-term space flight test results show that the overall average absorbed dose rate in a low-Earth orbit spacecraft cabin is generally 0.1 to 0.5 mGy/d (71).

Although the space radiation dose rate and total absorbed dose are very low, the peak energy of HZE particles can reach $10^3\ \text{MeV}$, and LET can reach more than $100\ \text{keV}/\mu\text{m}$, which has strong penetrability and ionization ability. Studies have shown that clustered DNA damage and DSBs induced by high-LET radiation are often difficult to accurately repair, especially in heterochromatin areas, and may even be irreparable

(72). In addition, cells exhibit hyper-radiosensitivity (HRS) (73) and inverse dose rate effects (IDREs) (74). Therefore, long-term continuous exposure to low-dose composite radiation from different radiation sources in the space environment may produce considerable mutagenic effects. After short-term space flight, the mutation frequency of specific genes in yeast and *Caenorhabditis elegans* is 2 to 3 times higher than that of the ground control (75). The measurement results of rice seeds by the nuclear track radiation detection device carried by “Shenzhou 3” spaceship showed that 7 seeds directly bombarded by HZE particles introduced 10–15% molecular polymorphisms vs. contemporary control plants (76). Sun et al. also reported that space radiation induces epigenetic changes in plants and produces high-frequency mutations (77).

The microgravity of the space environment is another potential mutagenic factor. Anikeeva et al. found that microgravity can interfere with the DNA damage repair system, hinder or inhibit the repair of DNA damage, increase the sensitivity of plants to other mutagenic factors, and have a synergistic effect with radiation to aggravate biological mutations and increase the mutation rate (78). However, some studies have shown that the microgravity environment will not interfere with the biological effects of radiation (79). At present, it remains controversial whether there is a joint effect between radiation and microgravity (80).

A Series of New Plant Varieties Derived From Space Mutation Have Been Released and Widely Applied in China

Many germplasm resources have been created using space breeding technology, and a large number of new plant varieties have been released in China. For example, in 1987, the Institute of Genetics of the Chinese Academy of Sciences cooperated with Guangxi Agricultural University to breed a new indica-japonica intersubspecific hybrid rice variety with strong hybridization, high seed-setting rate and full-filled grains (81). Xie et al. bred the restoration lines “Hang 1” and “Hang 2” by using space-based mutagenesis technology and developed a series of superhybrid rice varieties for large-scale production and application (82). Wang et al. obtained space-induced materials such as “Hanghui 1173”, “Hanghui 1179”, and highly rice blast-resistant “H4” and bred more than 50 rice varieties, including “Huahang 1” (83). In addition, stable and excellent varieties of wheat and sorghum developed by researchers from the Chinese Academy of Sciences and Chinese Academy of Agricultural Sciences have been obtained, such as wheat “Luyuan 502” (84). The Horticulture Branch of the Heilongjiang Academy of Agricultural Sciences and the Chinese Academy of Sciences have sent green pepper and tomato seeds on returnable satellites many times and selected high-yield, disease-resistant and good-quality space varieties “Yufan 1” and “Yufan 2” (85). The new space danshen variety “Tiandan No. 1” cultivated by the Tasly group has a single-plant quality three times that of ordinary danshen, and its active ingredient content is significantly higher than that of the control (86). Yuan et al. studied the variation frequency of mutated offspring derived from *Robinia pseudoacacia* seeds carried by the

“Shijian 8” recoverable satellite and cultivated the new variety “hangci 4,” which showed a non-thorn trait (87).

THE COMBINATION OF THE NEXT-GENERATION EFFECTIVE PARTICLE RADIATION AND A HIGH-THROUGHPUT SCREENING METHOD WILL FURTHER IMPROVE THE EFFICIENCY OF RADIATION BREEDING

Direct or indirect DNA damage caused by ionizing radiation is the most important factor in the introduction of genetic variation. Therefore, constantly developing radiation sources with higher ionization capacity and then controlling the precise release of ionization energy at biogenetically active sites of organisms, such as the shoot apical meristem (SAM) cells of seed embryos (88), through physical parameter adjustment can induce high-density DNA damage at the genome-wide level and introduce more genetic variation. Modern particle radiation technology that can efficiently induce DNA damage is the basis for the future development of radiation breeding. In addition, single-cell radiation treatment can avoid the chimaerism phenomenon of multicellular tissue after radiation, so gamete cells are potential radiation objects. Furthermore, the identification and screening of genetic variation induced by radiation is key in breeding protocols. Identification methods of genetic variation include phenotypic identification (89), cytological identification (90), and molecular identification (91). In recent years, the development of modern high-throughput instruments and their combination with molecular labeling technology have resulted in a variety of efficient, accurate, and systematic breeding techniques, which can be used for high-throughput identification of genotypes and phenotypes of mutagenized populations for multiple consecutive generations. Multispectral machine vision technology and image processing technology improve the efficiency and dimension of phenotype identification and help breeders find potential mutations more quickly (92). The effective combination of the abovementioned technologies and drones will break the bottleneck of phenotype identification and realize high-throughput scanning of yield and stress resistance. For starch, protein, oil and other chemical materials highly related to crop quality, near-infrared technology can realize non-destructive identification at the single seed level and pre-planting screening of seed populations, so identification could be advanced by one genetic generation (93). The screening of specific genomic sequences is the key to mining elite alleles. The combination of a mixed sample strategy, high-throughput targeted sequencing and DNA labeling technology can significantly reduce the identification cost of targeted sequences and greatly improve the efficiency of DNA variation identification (94). Furthermore, the germplasm identified by phenotype and genotype should be closely combined with classical and modern biotechnology breeding procedures to improve the utilization efficiency of germplasm. The mutant germplasm identified can be directly cultivated into new varieties

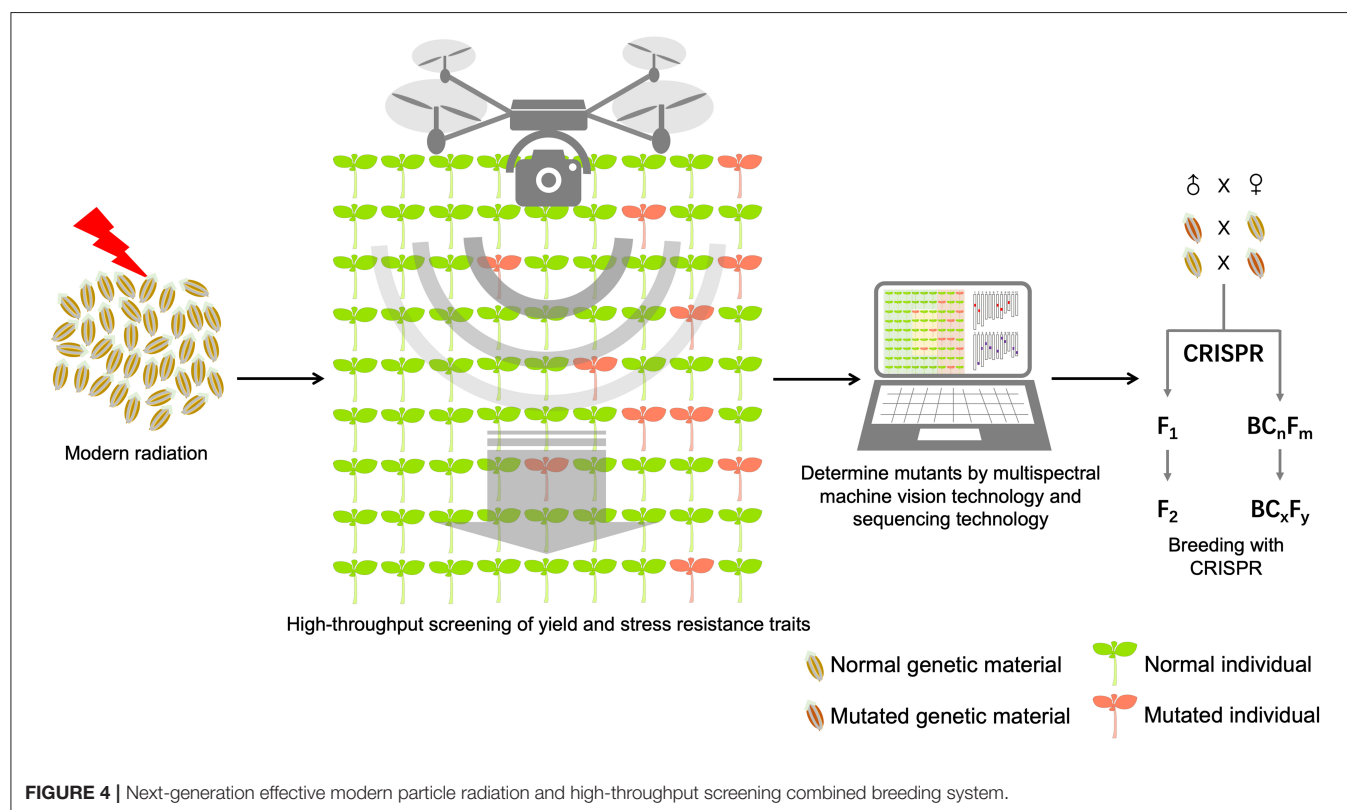
or used as important parental material to indirectly produce new varieties, improving mutagenesis breeding efficiency and offering new germplasm (95). Wang Ping proposed a method combining three factors: the mutagenesis materials as the core, molecular marker screening as an aid, and field identification as a supplement. Based on the above method, a series of new rice varieties were cultivated (96). How to efficiently pyramid and utilize multiple superior mutation sites is an important challenge. The rapid development of genome editing technology provides a new way to solve this problem (97). Breeders can obtain enhanced germplasms harboring multiple elite mutation sites by recombining mutation fragments or accurately replacement mutation sites through genome editing technology. We summarize the next-generation effective modern particle and high-throughput screening combined breeding system, as shown in **Figure 4**.

DISCUSSION

During the past 60 years, radiation mutation breeding together with other mutation breeding methods has been widely used to improve several crops and determine gene functions, even though it is facing a bottleneck in the development process, and the booming gene-editing technology has also brought great challenges. Nonetheless, with the increasing human population, decreasing in arable farmland area and deterioration of climate and the environment (drought, extreme temperature), there are strong requirements for stress-tolerant crop breeding. Under such circumstances, we should emphasize the mutual

development and joint use of multiple breeding approaches to further shorten the crop breeding cycle and improve breeding efficiency (98). A large number of breeding traits are complex quantitative traits, and gene editing or molecular breeding techniques based on a few genes are not ideal for the improvement of quantitative traits. Therefore, it is necessary to strengthen research on mutation breeding. However, similar to other breeding techniques, radiation mutation breeding has limitations, such as beneficial mutant frequency being relatively low and the direction and nature of variation being difficult to predict. Indeed, producing more useful varieties and elucidating radiation mutagenesis mechanisms remain scientific problems worthy of attention. Overall, our understanding of the mutagenesis mechanism of radiation breeding is still insufficient, and in-depth research needs to be conducted, including regarding the origin of mutations in progeny plants. As indicated above, genomic instability also leads to mutations, constituting a double-edged sword for crop breeding: it can not only increase the variation rate of progeny but also result in the instability of mutant traits. Thus, the role of genomic instability in plant mutagenesis needs to be uncovered. Relying on the development of advanced radiation devices and combining high-throughput gene sequencing and other advanced molecular biotechnology, it is expected that the mutagenic effect of radiation might eventually be predictable, allowing research to develop toward directional mutagenesis.

The establishment of an accelerated particle radiation device provides a fundamental guarantee for the application of modern radiation mutation breeding, and its diversified parameter



combinations might allow for directional mutagenesis in plant breeding. As a new generation of radiation mutagenesis sources, particle radiation represented by heavy-ions has further improved mutation frequency and the mutation spectrum compared with classical radiation mutagenesis, such as gamma rays and X-rays. This new generation breeding technology can generate more combinations of gene mutation sites, thereby breaking the linkage inheritance of traits, and it is expected that more mutants with excellent traits can be obtained, offering a breakthrough in the creation of new crop cultivars. Although particle radiation mutagenesis has been widely used in crop breeding and molecular genetic mechanism research, the mutagenesis mechanism is very complicated, and the mutagenesis effects of different radiation physical parameters of particles varied. Therefore, the key to the efficient creation of mutants is to select the appropriate types of accelerated particles and their radiation physical parameters. Several screening strategies for optimizing radiation parameters at the phenotypic and molecular levels have emerged (40, 99, 100). These studies provide valuable experience and new ideas for the formulation of optimal radiation conditions in the future particle radiation mutation breeding process. With the continuous development of sequencing technology, the combination of accelerated particle radiation with whole-genome resequencing, transcriptome sequencing, and other technologies can be employed to deeply explore changes in the genome and transcriptome levels in crops after accelerated particle irradiation and to further clarify the mutagenic mechanism of particle radiation. Furthermore, the further upgrade of particle radiation mutagenesis technology is of great significance to improve the efficiency of mutagenesis breeding.

Space radiation further expands the scope of radiation breeding, and the study of mutagenic effects in the space environment involves multiple disciplines, such as space biology,

genetics, mutagenesis, and breeding. Although many studies have confirmed the mutagenic effects of the space environment and a series of varieties have been selected through space mutation, there is still a lack of research on the molecular characteristics, molecular spectrum and genetic mechanisms of mutations induced by the space environment. The following aspects are worthy of in-depth discussion: (1) analysis of the synergistic mutagenic effects of microgravity and space radiation; (2) single-factor analysis and ground simulation of space radiation mutagenic factors; (3) single-cell mutation mapping of space radiation-induced mutation and genetic network construction; and (4) high-efficiency identification of space-induced variation and development of rapid fixation technology. The development of single-cell sequencing, high-throughput sequencing, and high-throughput detection technologies provides favorable conditions for studying the effects of space environmental mutagenesis and accelerating the utilization of genetic variation at the whole-genome level.

AUTHOR CONTRIBUTIONS

LM, TW, and TG jointly drafted the manuscript. All authors contributed to the literature search and analysis, and reviewed and approved the final manuscript.

FUNDING

This research was supported by the fund of innovation center of radiation application (No. KFZC2021010401).

ACKNOWLEDGMENTS

We thank Alyson M. at AJE (Beijing, China) for editing a draft of this manuscript.

REFERENCES

1. Doebley JF, Gaut BS, Smith BD. The molecular genetics of crop domestication. *Cell*. (2006) 127:1309–21. doi: 10.1016/j.cell.2006.12.006
2. Larson G, Piperno DR, Allaby RG, Purugganan MD, Andersson L, Arroyo-Kalin M, et al. Current perspectives and the future of domestication studies. *Proc Natl Acad Sci USA*. (2014) 111:6139–46. doi: 10.1073/pnas.1323964111
3. Brunner H. Radiation induced mutations for plant selection. *Appl Radiat Isotopes*. (1995) 46:589–94. doi: 10.1016/0969-8043(95)00096-8
4. Tanaka A, Shikazono N, Hase Y. Studies on biological effects of ion beams on lethality, molecular nature of mutation, mutation rate, and spectrum of mutation phenotype for mutation breeding in higher plants. *J Radiat Res*. (2010) 51:223–33. doi: 10.1269/jrr.09143
5. Abe T, Kazama Y, Hirano T. Ion beam breeding and gene discovery for function analyses using mutants. *Nucl Phys News*. (2015) 25:30–4. doi: 10.1080/10619127.2015.1104130
6. Liang X, Huang X, Mo M. Feasibility analysis of mulberry breeding by aerospace mutation. *Guangxi Sericult*. (2009) 46:32–6.
7. Chen Z, Wang H. Peiza Taifeng and Huahang No. 1. *Crop Res*. (2004) 4:283. doi: 10.16848/j.cnki.issn.1001-5280.2004.04.086
8. Zhao H, Guo H, Zhao L, Gu J, Zhao S, Li J, et al. A temperature-sensitive winter wheat chlorophyll mutant derived from space mutated. *J Nucl Agric*. (2010) 24:1110–6.
9. Muller HJ. The measurement of gene mutation rate in *Drosophila*, its high variability, and its dependence upon temperature. *Genetics*. (1928) 13:279–357. doi: 10.1093/genetics/13.4.279
10. Stadler LJ. Mutations in Barley induced by x-rays and radium. *Science*. (1928) 68:186–7. doi: 10.1126/science.68.1756.186
11. Stadler LJ. Genetic effects of x-rays in maize. *Proc Natl Acad Sci USA*. (1928) 14:69–75. doi: 10.1073/pnas.14.1.69
12. Shirasawa K, Hirakawa H, Nunome T, Tabata S, Isobe S. Genome-wide survey of artificial mutations induced by ethyl methanesulfonate and gamma rays in tomato. *Plant Biotechnol J*. (2016) 14:51–60. doi: 10.1111/pbi.12348
13. IAEA. *IAEA Mutant Variety Database*. Available online at: <http://mvd.iaea.org> (accessed July 28, 2021).
14. Gao C. Genome engineering for crop improvement and future agriculture. *Cell*. (2021) 184:1621–35. doi: 10.1016/j.cell.2021.01.005
15. Lomax ME, Folkes LK, O'Neill P. Biological consequences of radiation-induced DNA damage: relevance to radiotherapy. *Clin Oncol*. (2013) 25:578–85. doi: 10.1016/j.clon.2013.06.007
16. Santivasi WL, Xia F. Ionizing radiation-induced DNA damage, response, and repair. *Antioxid Redox Signal*. (2014) 21:251–9. doi: 10.1089/ars.2013.5668
17. Kavanagh JN, Redmond KM, Schettino G, Prise KM. DNA double strand break repair: a radiation perspective. *Antioxid Redox Signal*. (2013) 18:2458–72. doi: 10.1089/ars.2012.5151

18. Guirouilh-Barbat J, Lambert S, Bertrand P, Lopez BS. Is homologous recombination really an error-free process? *Front Genet.* (2014) 5:175. doi: 10.3389/fgene.2014.00175
19. Vu GT, Cao HX, Watanabe K, Hensel G, Blattner FR, Kumlehn J, et al. Repair of site-specific DNA double-strand breaks in Barley occurs via diverse pathways primarily involving the sister chromatid. *Plant Cell.* (2014) 26:2156–67. doi: 10.1105/tpc.114.126607
20. Aguilera A, Gomez-Gonzalez B. Genome instability: a mechanistic view of its causes and consequences. *Nat Rev Genet.* (2008) 9:204–17. doi: 10.1038/nrg2268
21. Puck TT, Marcus PI. Action of x-rays on mammalian cells. *J Exp Med.* (1956) 103:653–66. doi: 10.1084/jem.103.5.653
22. Sinclair WK. X-Ray-induced heritable damage (small-colony formation) in cultured mammalian cells. *Radiat Res.* (1964) 21:584–611. doi: 10.2307/3571653
23. Morgan WF. Non-targeted and delayed effects of exposure to ionizing radiation: I. Radiation-induced genomic instability and bystander effects *in vitro*. *Radiat Res.* (2003) 159:567–80. doi: 10.1667/0033-7587(2003)159[0567:NADEOE]2.0.CO;2
24. Molinier J, Ries G, Zipfel C, Hohn B. Transgeneration memory of stress in plants. *Nature.* (2006) 442:1046–9. doi: 10.1038/nature05022
25. Wang T, Li F, Liu Q, Bian P, Wang J, Wu Y, et al. Homologous recombination in Arabidopsis seeds along the track of energetic carbon ions. *Mutat Res.* (2012) 737:51–7. doi: 10.1016/j.mrfmmm.2012.05.006
26. Li F, Wang T, Xu S, Yuan H, Bian P, Wu Y, et al. Abscopal mutagenic effect of low-energy-ions in *Arabidopsis thaliana* seeds. *Int J Radiat Biol.* (2011) 87:984–92. doi: 10.3109/09553002.2011.574780
27. Goodhead DT. Initial events in the cellular effects of ionizing radiations: clustered damage in DNA. *Int J Radiat Biol.* (1994) 65:7–17. doi: 10.1080/09553009414550021
28. Asaithamby A, Chen DJ. Mechanism of cluster DNA damage repair in response to high-atomic number and energy particles radiation. *Mutat Res.* (2011) 711:87–99. doi: 10.1016/j.mrfmmm.2010.11.002
29. Surdutovich E, Solov'yov AV. Multiscale physics of ion-induced radiation damage. *Appl Radiat Isot.* (2014) 83(Pt. B):100–4. doi: 10.1016/j.apradiso.2013.01.035
30. Pastwa E, Neumann RD, Mezhevaya K, Winters TA. Repair of radiation-induced DNA double-strand breaks is dependent upon radiation quality and the structural complexity of double-strand breaks. *Radiat Res.* (2003) 159:251–61. doi: 10.1667/0033-7587(2003)159[0251:RORIDD]2.0.CO;2
31. Tsuruoka C, Suzuki M, Hande MP, Furusawa Y, Anzai K, Okayasu R. The difference in LET and ion species dependence for induction of initially measured and non-rejoined chromatin breaks in normal human fibroblasts. *Radiat Res.* (2008) 170:163–71. doi: 10.1667/RR1279.1
32. Hirano T, Kazama Y, Ishii K, Ohbu S, Shirakawa Y, Abe T. Comprehensive identification of mutations induced by heavy-ion beam irradiation in *Arabidopsis thaliana*. *Plant J.* (2015) 82:93–104. doi: 10.1111/tpj.12793
33. Tanaka A. Targeted mutation breeding of flower color by taking advantage of ion-beam irradiation and genomic information Preface. *Plant Biotechnol.* (2012) 29:191–2. doi: 10.5511/plantbiotechnology.12.0002p
34. Abe T, Ryuto H, Fukunishi N. Ion beam radiation mutagenesis. In: Shu QY, Forster BP, Nakagawa H, editors. *Plant Mutation Breeding and Biotechnology*. Vienna: Joint FAO/IAEA (2012). p. 99–106.
35. Kato M, Masamura N, Shono J, Okamoto D, Abe T, Imai S. Production and characterization of tearless and non-pungent onion. *Sci Rep.* (2016) 6:23779. doi: 10.1038/srep23779
36. Sawada R, Hirano T, Iimure K, Abe T, Ozaki Y. Low polyphenol oxidase mutant induced by 12c6+ ion beam irradiation to protoplasts of lettuce (*Lactuca sativa* L). *Hortic Res.* (2016) 15:347–53. doi: 10.2503/hrj.15.347
37. Yamatani H, Kohzuma K, Nakano M, Takami T, Kato Y, Hayashi Y, et al. Impairment of Lhca4, a subunit of LHCI, causes high accumulation of chlorophyll and the stay-green phenotype in rice. *J Exp Bot.* (2018) 69:1027–35. doi: 10.1093/jxb/erx468
38. Takeshita T, Ivanov IN, Oshima K, Ishii K, Kawamoto H, Ota S, et al. Comparison of lipid productivity of *Parachlorella kessleri* heavy-ion beam irradiation mutant PK4 in laboratory and 150-L mass bioreactor, identification and characterization of its genetic variation. *Algal Res.* (2018) 35:416–26. doi: 10.1016/j.algal.2018.09.005
39. Yamada K, Suzuki H, Takeuchi T, Kazama Y, Mitra S, Abe T, et al. Efficient selective breeding of live oil-rich *Euglena gracilis* with fluorescence-activated cell sorting. *Sci Rep.* (2016) 6:26327. doi: 10.1038/srep26327
40. Kazama Y, Ma L, Hirano T, Ohbu S, Abe T. Rapid evaluation of effective linear energy transfer in heavy-ion mutagenesis of *Arabidopsis thaliana*. *Plant Biotechnol.* (2012) 29:441–5. doi: 10.5511/plantbiotechnology.12.0921a
41. Ichida H, Matsuyama T, Ryuto H, Hayashi Y, Fukunishi N, Abe T, et al. Molecular characterization of microbial mutations induced by ion beam irradiation. *Mutat Res.* (2008) 639:101–7. doi: 10.1016/j.mrfmmm.2007.10.009
42. Hirano T, Kazama Y, Ohbu S, Shirakawa Y, Liu Y, Kambara T, et al. Molecular nature of mutations induced by high-LET irradiation with argon and carbon ions in *Arabidopsis thaliana*. *Mutat Res.* (2012) 735:19–31. doi: 10.1016/j.mrfmmm.2012.04.010
43. Ma L, Kazama Y, Hirano T, Morita R, Tanaka S, Abe T, et al. LET dependence on killing effect and mutagenicity in the model filamentous fungus *Neurospora crassa*. *Int J Radiat Biol.* (2018) 94:1125–33. doi: 10.1080/09553002.2019.1524940
44. Kazama Y, Ishii K, Hirano T, Wakana T, Yamada M, Ohbu S, et al. Different mutational function of low- and high-linear energy transfer heavy-ion irradiation demonstrated by whole-genome resequencing of Arabidopsis mutants. *Plant J.* (2017) 92:1020–30. doi: 10.1111/tpj.13738
45. Nikjoo H, Taleei R, Liamsuwan T, Liljequist D, Emfietzoglou D. Perspectives in radiation biophysics: from radiation track structure simulation to mechanistic models of DNA damage and repair. *Radiat Phys Chem.* (2016) 128:3–10. doi: 10.1016/j.radphyschem.2016.05.005
46. McVey M, Lee SE. MMEJ repair of double-strand breaks (director's cut): deleted sequences and alternative endings. *Trends Genet.* (2008) 24:529–38. doi: 10.1016/j.tig.2008.08.007
47. Lieber MR. The mechanism of double-strand DNA break repair by the nonhomologous DNA end-joining pathway. *Annu Rev Biochem.* (2010) 79:181–211. doi: 10.1146/annurev.biochem.052308.093131
48. Ma L, Kazama Y, Inoue H, Abe T, Hatakeyama S, Tanaka S. The type of mutations induced by carbon-ion-beam irradiation of the filamentous fungus *Neurospora crassa*. *Fungal Biol.* (2013) 117:227–38. doi: 10.1016/j.funbio.2013.01.002
49. Ishii K, Kazama Y, Morita R, Hirano T, Ikeda T, Usuda S, et al. Linear energy transfer-dependent change in rice gene expression profile after heavy-ion beam irradiation. *PLoS ONE.* (2016) 11:e0160061. doi: 10.1371/journal.pone.0160061
50. Hase Y, Tanaka A, Baba T, Watanabe H. FRL1 is required for petal and sepal development in Arabidopsis. *Plant J.* (2000) 24:21–32. doi: 10.1046/j.1365-313x.2000.00851.x
51. Shimada S, Ogawa T, Kitagawa S, Suzuki T, Ikari C, Shitsukawa N, et al. A genetic network of flowering-time genes in wheat leaves, in which an APETALA1/FRUITFULL-like gene, VRN1, is upstream of FLOWERING LOCUS T. *Plant J.* (2009) 58:668–81. doi: 10.1111/j.1365-313X.2009.03806.x
52. Yasui Y, Mori M, Aii J, Abe T, Matsumoto D, Sato S, et al. S-LOCUS EARLY FLOWERING 3 is exclusively present in the genomes of short-styled buckwheat plants that exhibit heteromorphic self-incompatibility. *PLoS ONE.* (2012) 7:e31264. doi: 10.1371/journal.pone.0031264
53. Morita R, Nakagawa M, Takehisa H, Hayashi Y, Ichida H, Usuda S, et al. Heavy-ion beam mutagenesis identified an essential gene for chloroplast development under cold stress conditions during both early growth and tillering stages in rice. *Biosci Biotechnol Biochem.* (2017) 81:271–82. doi: 10.1080/09168451.2016.1249452
54. Morita R, Ichida H, Ishii K, Hayashi Y, Abe H, Shirakawa Y, et al. LONG GRAIN 1: a novel gene that regulates grain length in rice. *Mol Breed.* (2019) 39:135. doi: 10.1007/s11032-019-1032-1
55. Kazama Y, Ishii K, Aonuma W, Ikeda T, Kawamoto H, Koizumi A, et al. A new physical mapping approach refines the sex-determining gene positions on the *Silene latifolia* Y-chromosome. *Sci Rep.* (2016) 6:18917. doi: 10.1038/srep18917
56. Koide Y, Ogino A, Yoshikawa T, Kitashima Y, Saito N, Kanaoka Y, et al. Lineage-specific gene acquisition or loss is involved in interspecific hybrid sterility in rice. *Proc Natl Acad Sci USA.* (2018) 115:E1955–62. doi: 10.1073/pnas.1711656115

57. Yu Z. *Introduction to Ion Beam Biotechnology*. New York: Springer Press (2006). p. 8–10, 183–207, 63–71.
58. Yu Z, Deng J, He J, Huo Y, Wu Y, Wang X, et al. Mutation breeding by ion implantation. *Nucl Instruments Methods Phys Res.* (1991) 59–60:705–8. doi: 10.1016/0168-583X(91)95307-Y
59. Khitka B, Phanchaisri B, Sutipatanasomboon A, Nuangmek W, Yu LD, Techarang J. Low-energy heavy-ion-beam-induced mutation of novel high-yielding drought-tolerant Thai Jasmine rice. *Nucl Instruments Methods Phys Res Sect B Beam Interact Mater Atoms.* (2021) 492:34–42. doi: 10.1016/j.nimb.2021.02.003
60. Gu SB, Li SC, Fe Ng HY, Wu Y, Yu ZL. A novel approach to microbial breeding—low-energy ion implantation. *Appl Microbiol Biotechnol.* (2008) 78:201–9. doi: 10.1007/s00253-007-1312-2
61. Feng H, Yu Z, Chu PK. Ion implantation of organisms. *Mater Sci Eng R.* (2006) 54:49–120. doi: 10.1016/j.mser.2006.11.001
62. Lorimore SA, Coates PJ, Wright EG. Radiation-induced genomic instability and bystander effects: inter-related nontargeted effects of exposure to ionizing radiation. *Oncogene.* (2003) 22:7058–69. doi: 10.1038/sj.onc.1207044
63. Yang G, Mei T, Yuan H, Zhang W, Chen L, Xue J, et al. Bystander/abscopal effects induced in intact *Arabidopsis* seeds by low-energy heavy-ion radiation. *Radiat Res.* (2008) 170:372–80. doi: 10.1667/RR1324.1
64. Li F, Liu P, Wang T, Bian P, Yu Z. The induction of bystander mutagenic effects *in vivo* by alpha-particle irradiation in whole *Arabidopsis thaliana* plants. *Radiat Res.* (2010) 174:228–37. doi: 10.1667/RR2052.1
65. Wang T, Li F, Xu S, Bian P, Wu Y, Wu L, et al. The Time course of long-distance signaling in radiation-induced bystander effect *in vivo* in *Arabidopsis thaliana* demonstrated using root micro-grafting. *Radiat Res.* (2011) 176:234–43. doi: 10.1667/rr2486.1
66. Xu W, Wang T, Xu S, Xu S, Wu L, Wu Y, et al. Radiation-induced epigenetic bystander effects demonstrated in *Arabidopsis thaliana*. *Radiat Res.* (2015) 183:511–24. doi: 10.1667/RR13909.1
67. Deng C, Wu J, Wang T, Hong G, Wu L, Wu Y, et al. Negative modulation of bystander DNA repair potential by x-ray targeted tissue volume in *Arabidopsis thaliana*. *Radiat Res.* (2019) 191:556–65. doi: 10.1667/RR15314.1
68. Wu H, Huff J, Casey R, Kim M, Cucinotta F. *Risk of Acute Radiation Syndromes Due to Solar Particle Events, Human Health and Performance Risks of Space Exploration Missions*. NASA SP-2009-3405 (2009).
69. Hada M, Ikeda H, Rhone JR, Beitman AJ, Plante I, Souda H, et al. Increased chromosome aberrations in cells exposed simultaneously to simulated microgravity and radiation. *Int J Mol Sci.* (2018) 20:43. doi: 10.3390/ijms20010043
70. Ding N, Pei H, Hu W, He J, Li H, Wang J, et al. Cancer risk of high-charge and -energy ions and the biological effects of the induced secondary particles in space. *Rendiconti Lincei.* (2014) 25:59–63. doi: 10.1007/s12210-014-0288-y
71. Rabbow E, Rettberg P, Barczyk S, Bohmeier M, Parpart A, Panitz C, et al. The astrobiological mission EXPOSE-R on board of the International Space Station. *Int J Astrobiol.* (2015) 14:3–16. doi: 10.1017/S1473550414000202
72. Lorat Y, Brunner CU, Schanz S, Jakob B, Taucher-Scholz G, Rube CE. Nanoscale analysis of clustered DNA damage after high-LET irradiation by quantitative electron microscopy—the heavy burden to repair. *DNA Repair.* (2015) 28:93–106. doi: 10.1016/j.dnarep.2015.01.007
73. Martin LM, Marples B, Lynch TH, Hollywood D, Marignol L. Exposure to low dose ionising radiation: molecular and clinical consequences. *Cancer Lett.* (2014) 349:98–106. doi: 10.1016/j.canlet.2013.12.015
74. Leonard BE, Lucas AC, LDR. brachytherapy: can low dose rate hypersensitivity from the “inverse” dose rate effect cause excessive cell killing to peripheral connective tissues and organs? *Br J Radiol.* (2009) 82:131–9. doi: 10.1259/bjr/66381835
75. Hartman PS, Hlavacek A, Wilde H, Lewicki D, Schubert W, Kern RG, et al. A comparison of mutations induced by accelerated iron particles *versus* those induced by low earth orbit space radiation in the FEM-3 gene of *Caenorhabditis elegans*. *Mutat Res.* (2001) 474:47–55. doi: 10.1016/S0027-5107(00)00154-8
76. Luo Y, Wang X, Mei M, Zhuang C, Zhou F, Wei Z, et al. Genomic polymorphism in consecutive generation rice plants from seeds on board spaceship and their relationship with space HZE particles. *Acta Biophys Sin.* (2006) 22:131–8. doi: 10.1007/s11515-007-0043-1
77. Sun Y, Li Y, Chen Y, Guo Y, Deng L. “Study on the Genetic Mutagenesis of Green Pepper and Tomato in Space Environment.” *Plant Res.* (1997) 2:64–9.
78. Anikeeva ID, Kostina LN, Vaulina EN. Experiments with air-dried seeds of *Arabidopsis thaliana* (L) Heynh. and *Crepis capillaris* (L) Wallr. aboard Salyut 6. *Adv Space Res.* (1983) 3:129–33. doi: 10.1016/0273-1177(83)90182-5
79. de Serres FJ, Smith DB. The Gemini-XI S-4 spaceflight-radiation interaction experiment. III. comparison of the spectra of recessive lethal mutations at specific loci in the ad-3 region in *Neurospora crassa*. *Radiat Res.* (1970) 42:471–87. doi: 10.2307/3572963
80. Yatagai F, Honma M, Dohmae N, Ishioka N. Biological effects of space environmental factors: a possible interaction between space radiation and microgravity. *Life Sci Space Res.* (2019) 20:113–23. doi: 10.1016/j.lssr.2018.10.004
81. Jiang X. Progress and prospects of 863-2 space mutation breeding. *J Space Sci.* (1996) 16:77–82.
82. Xie H, Wang W, Chen B, Zhang J, Zheng JTH, et al. Breeding and application of the restorer line “Hang No1” in super-high-yielding hybrid rice. *Chin Agric Sci.* (2004) 11:1688–92.
83. Wang H, Chen Z, Yang Q, Li L, Hong Y, Zhang J, et al. Variation of major agronomic characters and resistance to blast of mutant lines by space mutation in *Oryza sativa*. *J South China Agric Univ.* (2004) 4:1–5. doi: 10.3969/j.issn.1001-411X.2004.04.001
84. Zhao Y, Zhao Q, Bai Z, Wang C, Li Z, Cui Q. Study on Sorghum mutant induced by space flight. *Bot Bull.* (2001) 1:81–9.
85. Li J, Liu M, Wang P, Zhang J, Xue H, Guo Y. Effects of space conditions on mutation and inheritance of tomato. *Aerospace Med Med Eng.* (2000) 2:114–8.
86. Liu H. Space breeding: creating the myth of Chinese herbal medicine planting. *China News Trad Chin Med.* (2012) 7.
87. Yuan CQ, Li YF, Sun P, Sun YH, Zhang GJ, Yang MS, et al. Assessment of genetic diversity and variation of *Robinia pseudoacacia* seeds induced by short-term spaceflight based on two molecular marker systems and morphological traits. *Genet Mol Res.* (2012) 11:4268–77. doi: 10.4238/2012.December.17.2
88. Mahajan M, Yadav RK. Labeling and sorting of *Arabidopsis* SAM cell populations to capture their transcriptome profile. *Methods Mol Biol.* (2020) 2094:39–47. doi: 10.1007/978-1-0716-0183-9_5
89. Long T, An B, Li X, Zhang W, Li J, Yang Y, et al. Construction and screening of an irradiation-induced mutant library of indica rice 93-11. *Chinese Journal of Rice Science* (2016) 30:44–52. doi: 10.16819/j.1001-7216.2016.5126
90. Yang M, Fu S, Chen X, Zhang H, Tang Z, Ren Z. Creation of wheat-rye small-fragment translocation using fast neutron irradiation. *J Triticeae Crops.* (2014) 5:609–14. doi: 10.7606/j.issn.1009-1041.2014.05.006
91. Mao D, Guan H, Wang Z, Chen Z, Pan M, Pan R, et al. Improvement of rice blast resistance of restorer line N175 by marker-assisted selection. *J Fujian Agric Forestry Univ.* (2017) 46:241–6. doi: 10.13323/j.cnki.j.fafu(nat.sci.).2017.03.001
92. Forero MG, Mambucay CL, Monroy MF, Miranda SL, Méndez D, Valencia MO, et al. Comparative analysis of detectors and feature descriptors for multispectral image matching in rice crops. *Plants.* (2021) 10:1791. doi: 10.3390/plants10091791
93. Min TG, Kang WS. Nondestructive classification between normal and artificially aged corn (*Zea mays* L) seeds using near infrared spectroscopy. *Korean J Crop Sci.* (2008) 53:314–9. doi: 10.1007/978-1-4020-8804-9_25
94. Guo Z, Yang Q, Huang F, Zheng H, Sang Z, Xu Y, et al. Development of high-resolution multiple-SNP arrays for genetic analyses and molecular breeding through genotyping by target sequencing and liquid chip. *Plant Commun.* (2021) 2:100230. doi: 10.1016/j.xplc.2021.100230
95. Chen Z, Zhou D, Guo T, Wang H. Research progress of rice space mutation bio-breeding. *J South China Agric Univ.* (2019) 40:195–202. doi: 10.7671/j.issn.1001-411X.201905073
96. Wang P. The results of rice aerospace breeding passed the identification. *Plant Doctor.* (2016) 29:27.
97. Zhu XG, Zhu JK. Precision genome editing heralds rapid *de novo* domestication for new crops. *Cell.* (2021) 184:1133–4. doi: 10.1016/j.cell.2021.02.004
98. Das P, Mishra M, Lakra N, Singla-Pareek SL, Pareek A. 1. Mutation breeding: a powerful approach for obtaining abiotic stress tolerant crops and upgrading food security for human nutrition. In: Tomlekova N, Kojgar I, and Wani R editors, *Mutagenesis: Exploring Novel Genes and*

- Pathways*. Wageningen: Wageningen Academic Publisher (2014). p. 15–36. doi: 10.3920/978-90-8686-787-5_1
99. Hase Y, Akita Y, Kitamura S, Narumi I, Tanaka A. Development of an efficient mutagenesis technique using ion beams: Toward more controlled mutation breeding. *Plant Biotechnol.* (2012) 29:193–200. doi: 10.5511/plantbiotechnology.12.0106a
 100. Ichida H, Morita R, Shirakawa Y, Hayashi Y, Abe T. Targeted exome sequencing of unselected heavy-ion beam-irradiated populations reveals less-biased mutation characteristics in the rice genome. *Plant J.* (2019) 98:301–14. doi: 10.1111/tpj.14213

Conflict of Interest: The authors declare that the research was conducted in the absence of any commercial or financial relationships that could be construed as a potential conflict of interest.

Publisher's Note: All claims expressed in this article are solely those of the authors and do not necessarily represent those of their affiliated organizations, or those of the publisher, the editors and the reviewers. Any product that may be evaluated in this article, or claim that may be made by its manufacturer, is not guaranteed or endorsed by the publisher.

Copyright © 2021 Ma, Kong, Sun, Wang and Guo. This is an open-access article distributed under the terms of the Creative Commons Attribution License (CC BY). The use, distribution or reproduction in other forums is permitted, provided the original author(s) and the copyright owner(s) are credited and that the original publication in this journal is cited, in accordance with accepted academic practice. No use, distribution or reproduction is permitted which does not comply with these terms.



From Photon Beam to Accelerated Particle Beam: Antimetastasis Effect of Combining Radiotherapy With Immunotherapy

Liqiu Ma ^{1,2*}

¹ Department of Nuclear Physics, China Institute of Atomic Energy, Beijing, China, ² National Innovation Center of Radiation Application, Beijing, China

OPEN ACCESS

Edited by:

Yi Xie,
Institute of Modern Physics,
(CAS), China

Reviewed by:

Walter Tinganelli,
Helmholtz Association of German
Research Centres (HZ), Germany

*Correspondence:

Liqiu Ma
maliqiu@ciae.ac.cn

Specialty section:

This article was submitted to
Radiation and Health,
a section of the journal
Frontiers in Public Health

Received: 01 January 2022

Accepted: 25 February 2022

Published: 29 March 2022

Citation:

Ma L (2022) From Photon Beam to
Accelerated Particle Beam:
Antimetastasis Effect of Combining
Radiotherapy With Immunotherapy.
Front. Public Health 10:847119.
doi: 10.3389/fpubh.2022.847119

Cancer is one of the major diseases that seriously threaten the human health. Radiotherapy is a common treatment for cancer. It is noninvasive and retains the functions of the organ where the tumor is located. Radiotherapy includes photon beam radiotherapy, which uses X-rays or gamma rays, and particle beam radiotherapy, using beams of protons and heavy ions. Compared with photon beam radiotherapy, particle beam radiotherapy has excellent dose distribution, which enables it to kill the primary tumor cells more effectively and simultaneously minimize the radiation-induced damage to normal tissues and organs surrounding the tumor. Despite the excellent therapeutic effect of particle beam radiotherapy on the irradiated tumors, it is not an effective treatment for metastatic cancers. Therefore, developing novel and effective treatment strategies for cancer is urgently needed to save patients with distant cancer metastasis. Immunotherapy enhances the body's own immune system to fight cancer by activating the immune cells, and consequently, to achieve the systemic anticancer effects, and it is considered to be an adjuvant therapy that can enhance the efficacy of particle beam radiotherapy. This review highlights the research progress of the antimetastasis effect and the mechanism of the photon beam or particle beam radiotherapy combined with immunotherapy and predicts the development prospects of this research area.

Keywords: accelerated particle beam, photon beam, metastasis, radiotherapy, immunotherapy, abscopal effect

INTRODUCTION

Cancer is one of the leading causes of death worldwide (1). About 10 million people died of cancer in 2020 (2). Approximately 90% of cancer-related deaths are caused by distant metastasis (3). Early-stage cancer can be cured by surgery, chemotherapy, and radiotherapy. However, once the cancer has progressed to the advanced stage, the cancer cells spread to other organs; hence, even if the primary tumor can be effectively treated, distant metastasis becomes the key problem affecting the patient's survival and quality of life. Therefore, the development of novel and effective treatment strategies for cancer is urgently needed to treat patients with distant metastasis.

Considerable progress has been achieved in cancer treatment research in recent years (4). With the development of nuclear science and technology, the emerging concept of "precise treatment

of tumors by nuclear technology” has gradually been recognized, and the most representative treatment concept is particle beam radiotherapy based on protons and heavy ions (5). Particle beam radiotherapy differs from traditional radiotherapy in terms of its physical and biological characteristics. It possesses excellent depth-dose distribution, which accurately and efficiently induces cancer cell death with limited effect on the surrounding healthy tissue (5), thereby avoiding or reducing the occurrence of complications during the treatment. However, as cancer progresses, the cancer cells are able to enhance their metastatic capacity and escape from immune surveillance, eventually leading to the formation of metastatic cancers in distal organs (6, 7). Particle beam radiotherapy has a excellent therapeutic effect on the irradiated tumors, but this treatment is ineffective for micrometastatic cancer, which is not diagnosed by CT and PET (8–11). Therefore, scientific studies, which are designed to suppress or even cure metastatic cancer, are imperative for enhancing the efficacy of particle beam radiotherapy.

The probability of the induction of the abscopal effect during radiotherapy in clinical practice is negligible. Usually, it can bring survival benefit to patients who have already developed distant metastatic cancer. The abscopal effect was first proposed by Mole in 1953 (12). This phenomenon refers to the regression of distant tumor lesions that have not received radiotherapy following local radiation exposure to the tumor. Presently, the primary manner of deepening one’s understanding of abscopal effect is via a small number of published clinical case reports and preclinical studies about the induction mechanism of this effect. Most of the early case reports focused on the abscopal effect that was induced only by local photon radiotherapy (13–17). Some recent case reports have confirmed that both proton beam and heavy ion beam radiotherapy are also able to induce the abscopal effect (18, 19). However, studies on the induction mechanism of the abscopal effect remain limited. For instance, the study conducted by Camphausen et al. using the Trp53-deficient mice suggested that, at the molecular level, the induction of the abscopal effect was dependent on the tumor suppressor gene p53 (20). Overall, the abscopal effect is a very rare phenomenon in clinical practice, and its induction mechanism remains unclear.

Immunotherapy is considered as an auxiliary mean to enhance the efficacy of radiotherapy. The most representative types of immunotherapy include the “dendritic cell (DC)-based vaccine therapy”, advocated by Nobel Prize winner Ralph M. Steinman (21), and the “immune checkpoint inhibitor therapy” (22, 23) developed based on the “immunotherapy targets PD-1 and CTLA-4” discovered by Nobel Prize winners Tasuku Honjo and James P. Allison. Immunotherapy is dependent on the patient’s immune system to fight cancer cells; thus, it is a systemic cancer treatment, and it is expected to bring hope to patients with cancer metastasis.

This review discusses the research progress of the antimetastasis effect and its mechanism of photon beam or particle beam radiotherapy combined with immunotherapy, and predicts the future developmental trend.

PHOTON BEAM RADIOTHERAPY COMBINED WITH IMMUNOTHERAPY

Once immunotherapy is combined with other cancer treatments, its remarkable synergy improves therapeutic effects significantly (24–26). The combination of radiotherapy and immunotherapy has become a research focus in tumor treatment, including photon beam radiotherapy combined with DCs or immune checkpoint inhibitors. DCs are a type of antigen-presenting cells that possess the function of antigen internalization and presentation, wherein they present antigens to T cells, which triggers the systemic antitumor immune response in the body (27). The antitumor and antimetastasis effects have been shown in preclinical studies regarding photon beam radiotherapy combined with DCs (28, 29). On the other hand, attention has also been paid to photon beam radiotherapy combined with immune checkpoint inhibitors (30–33). Immune checkpoint molecules, like PD-1 and CTLA-4, can negatively regulate the antitumor immune responses in the body by inducing a decrease in the activation level of killer T cells, which enables cancer cells to escape the attack of immune cells. The treatment with immune checkpoint inhibitors blocks the signal transduction of the immune checkpoint molecules on the surface of the T cell membrane, releasing the anticancer “brake” of the immune system, which is expected to produce effective and lasting activation of antitumor immunity in the body. The *New England Journal of Medicine* reported a successful case of combining conventional radiotherapy with CTLA-4 immune checkpoint inhibitor for the treatment of pleural-based paraspinal metastatic melanoma, wherein the regression of hilar lymphadenopathy and splenic metastatic lesions was observed (30). This report also found an increase in the proportion of immune-activating CD4⁺ICOS^{high} lymphocytes in the blood but a decrease in the proportion of immunosuppressive myeloid-derived suppressor cells following radiotherapy. A similar case showed that the combination therapy, which was used to treat liver metastatic lung adenocarcinoma, led to the regression of liver, lung, and sacrum metastatic lesions and caused significant changes in the proportion of immune cells in the blood and carcinoembryonic antigen concentration after treatment (31). In addition to a few clinical cases, there have also been some basic studies of radiotherapy combined with immune checkpoints. For instance, when photon beam radiotherapy was used in combination with the dual immune checkpoint inhibitors (anti-CTLA-4 and anti-PD-L1), the effects of these two immune checkpoint inhibitors did not cause redundancy, but instead they complemented each other through different immune activation mechanisms, thereby inhibiting the growth of the unirradiated distant metastatic tumor and improving survival (32). Another study revealed that the photon beam radiotherapy combined with the dual immune checkpoint inhibitors (anti-CTLA-4 and anti-PD-L1) had a better antimetastasis efficacy than radiotherapy combined with either CTLA-4 or PD-L1 immune checkpoint inhibitor alone (33). In summary, the combination of photon beam radiotherapy and immunotherapy can potentially inhibit cancer metastasis.

Although radiotherapy combined with immune checkpoint inhibitors brings excellent antitumor and antimetastasis effects, the side effects caused by immune checkpoint inhibitors cannot be underestimated. The CTLA-4 and PD-1/PD-L1 inhibitors lead to side effects such as rash, diarrhea, hepatotoxicity, and endocrine disorders and an overall incidence of adverse drug events of above 50% (34, 35). Apart from the abovementioned side effects of immune checkpoint inhibitors, when they are used in combination with radiotherapy, some other side effects have also been reported. The journal of *JAMA Oncology* reported that in the treatment of brain metastasis, which comes from primary melanoma, non-small-cell lung cancer, and renal cell carcinoma, symptomatic radiation necrosis of the brain occurred in approximately 20% of the patients who received radiotherapy combined with immune checkpoint inhibitors, whereas, this occurred in only 6.8% of the patients who only received radiotherapy (36). Another report indicated that a history of radiation pneumonitis prior to PD-1 immune checkpoint inhibitor treatment can increase the risk of interstitial lung disease (37). Therefore, to ensure both the safe use and antimetastasis effect of the combination therapy in more patients, safety studies for the combination therapy need to be conducted from a novel perspective.

PARTICLE BEAM RADIOTHERAPY COMBINED WITH IMMUNOTHERAPY

With the development of nuclear science and technology, preclinical studies regarding particle beam radiotherapy combined with immunotherapy for metastasis suppression have also been conducted. Particularly, much attention has been given to the preclinical study of particle beam radiotherapy combined with DC-based immunotherapy, performed by the research team of the National Institute of Radiological Sciences (Japan). In 2010, this team reported that combining particle beam radiotherapy with α -galactosylceramide (α -GalCer) pulsed DC-based immunotherapy could effectively inhibit the formation of metastatic cancer (38). Later on, this team reported that in particle beam radiotherapy combined with DC-based immunotherapy, metastatic cancer suppression could be achieved by intravenous injection of the immature DC amplified *in vitro*, without the need of loading the DC with α -GalCer. This finding revealed that the killing effect of natural killer T (NKT) cells might not be involved in the primary mechanism of the antimetastasis effect of the combination therapy (39). This study also demonstrated that DC-based immunotherapy combined with particle beam radiotherapy was more effective in suppressing cancer metastasis than when combined with photon beam therapy at equivalent biological effect doses of photon beam or particle beam irradiation. In a recent study conducted by this team, the universality of the abovementioned combination therapy was verified using mice with different genetic backgrounds and their syngeneic types of cancer (40). The results demonstrated that the combination therapy effectively inhibited lung metastasis in Th1-dominant mice but not in Th2-dominant mice. Further analysis of the

activation level of DCs suggested that the Th balance-related host genetic background rather than the tumor affected the antimetastasis effect of particle beam radiotherapy combined with DC-based immunotherapy. These results have provided a basis for the clinical screening of patients who are suitable for receiving combination therapy, ensuring that combination therapy is performed on the appropriate patients to achieve better treatment outcomes and its usage is avoided for patients who are not suitable for it.

Moreover, preclinical studies of particle beam radiotherapy combined with immune checkpoint inhibitors have been conducted. For instance, a preclinical study performed by the team of Osaka University (Japan) reported that particle beam radiotherapy combined with dual immune checkpoint inhibitors (anti-CTLA-4 and anti-PD-L1) effectively suppressed both the proliferation of primary tumors and unirradiated distant tumors (41). According to the study jointly conducted by GSI Helmholtzzentrum für Schwerionenforschung GmbH (Germany) and National Institute of Radiological Sciences (Japan), particle beam combined with dual immune checkpoint inhibitors (anti-CTLA-4 and anti-PD-1) induced a higher antimetastasis effect compared with photon beam at the equivalent dose of same primary tumor control level (42). The above two studies have revealed that particle beam radiotherapy combined with dual immune checkpoint inhibitors exhibit potential sensitized antitumor and antimetastasis effects, and may be more effective than the combination of photon beam and dual immune checkpoint inhibitors.

The abovementioned studies have suggested that particle beam radiotherapy combined with immunotherapy is a novel and effective treatment strategy for patients with cancer metastasis, but its universality and safety data are limited and need to be further investigated in preclinical studies and clinical settings in the future.

INDUCTION OF THE ABCOPAL EFFECT BY RADIOTHERAPY COMBINED WITH IMMUNOTHERAPY

Immunotherapy is a new method of cancer treatment that has been developing in recent years. Local radiotherapy combined with immunotherapy has been performed to induce the abscopal effect in an increasing number of clinical cases. For instance, several clinical cases have reported that the abscopal effect is induced by combining radiotherapy with immune checkpoint inhibitors (30, 31). Furthermore, a clinical trial showed that local radiotherapy combined with the subcutaneous injection of granulocyte-macrophage colony-stimulating factor (GM-CSF) demonstrated a higher probability of inducing the abscopal effect on non-small cell lung cancer, breast cancer, and thymic cancer. Moreover, the cases with induced abscopal effect showed a longer overall survival in most patients (43).

Most of the preclinical studies have focused on the induction of the abscopal effect by combining radiotherapy with immunotherapy. For instance, photon beam radiation

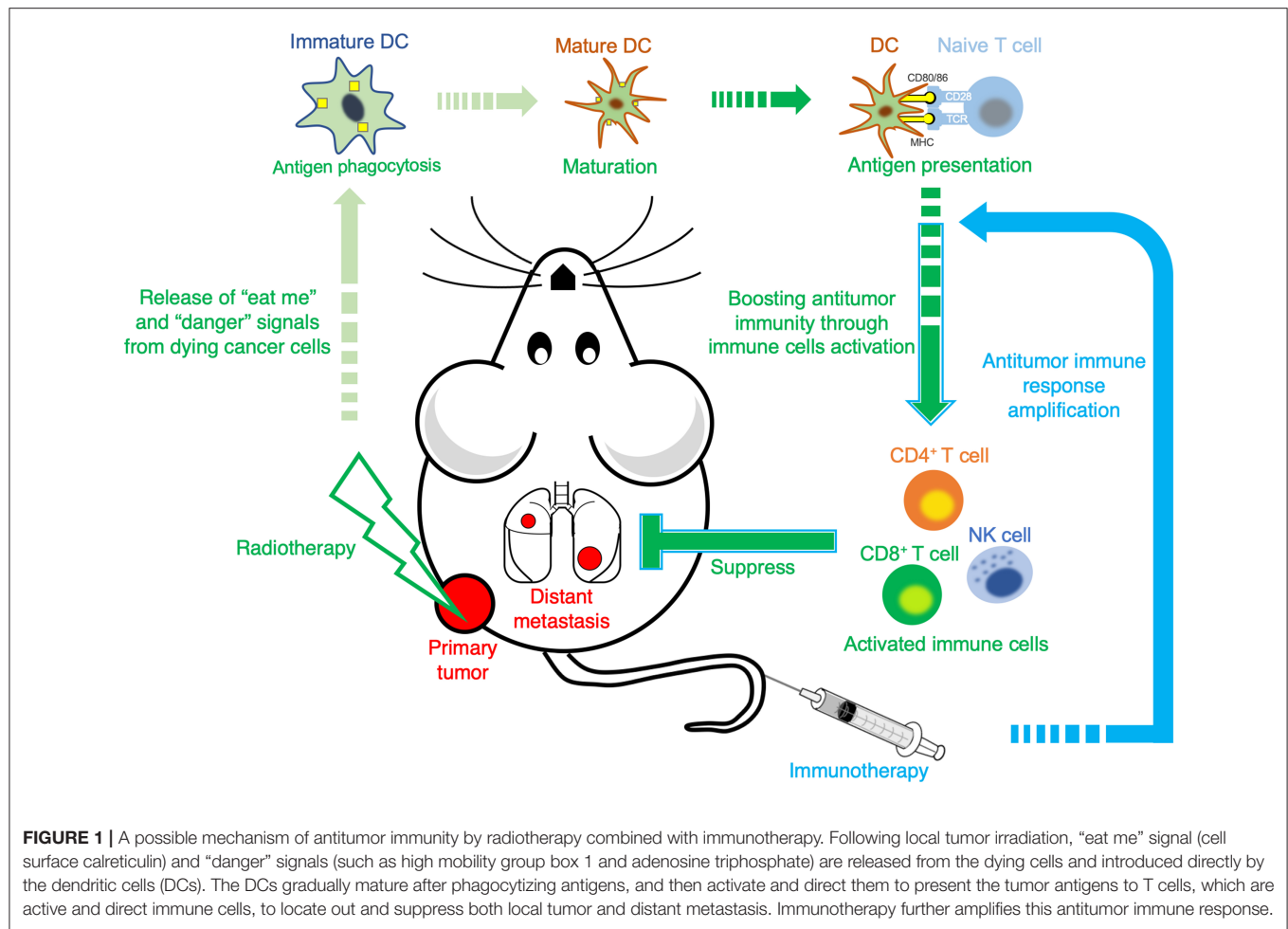


FIGURE 1 | A possible mechanism of antitumor immunity by radiotherapy combined with immunotherapy. Following local tumor irradiation, "eat me" signal (cell surface calreticulin) and "danger" signals (such as high mobility group box 1 and adenosine triphosphate) are released from the dying cells and introduced directly by the dendritic cells (DCs). The DCs gradually mature after phagocytizing antigens, and then activate and direct them to present the tumor antigens to T cells, which are active and direct immune cells, to locate out and suppress both local tumor and distant metastasis. Immunotherapy further amplifies this antitumor immune response.

exposure combined with FMS-like tyrosine kinase 3 ligand (Flt3-L) on mice bearing 67NR breast cancer induces the abscopal effect (44). Another study showed that radiotherapy combined with tumor-associated antigen specific vaccine induced the regression of unirradiated distant tumors and pulmonary metastases (45). A series studies reported that 6 MeV electron beam therapy combined with chemokine CCL3 variant (eMIP) could also significantly induce the regression of unirradiated distant tumors, and the subsequent study showed that following the implementation of this combination therapy, eMIP combines with the radiation-induced damage-associated molecular patterns *in vivo* to activate CD8⁺ and CD4⁺ T cells and natural killer (NK) cells, which are then involved in inducing the abscopal effect (46–48). Recently, multiple studies by using dual tumors-bearing mouse model regarding immune checkpoint inhibitors have been reported, and their findings suggested that radiotherapy combined with immune checkpoint inhibitors can also induce the abscopal effect. For instance, melanoma B16-F10 tumor-bearing mice were treated with photon beam radiotherapy combined with anti-CTLA-4 antibody immunotherapy. After 3 weeks of radiotherapy, 17% of the mice showed complete response (CR) (32). In

addition, photon beam combined with dual immune checkpoint inhibitors (anti-CTLA-4 and anti-PD-L1) applied to mice bearing LM8 osteosarcoma showed more than 40% of the mice with CR (33). Furthermore, compared with photon beam, particle beam combined with dual immune checkpoint inhibitors (anti-CTLA-4 and anti-PD-1/PD-L1) immunotherapy showed an increased proportion of mice with CR (41) and an enhanced inhibition of lung metastasis (42). Some studies on the underlying mechanism for antitumor immunity indicated that particle beam radiation has the ability to induce immunogenic cell death in cancer cells, releasing "eat me" and "danger" signals, such as calreticulin (CALR) and high mobility group box 1 (HMGB1) (49, 50), respectively, thereby promoting the activation of DCs, which ultimately activates antitumor immunity (39). Therefore, immunotherapy is expected to enhance particle beam radiation-induced antitumor immunity, thereby increasing the induction efficiency of the abscopal effect.

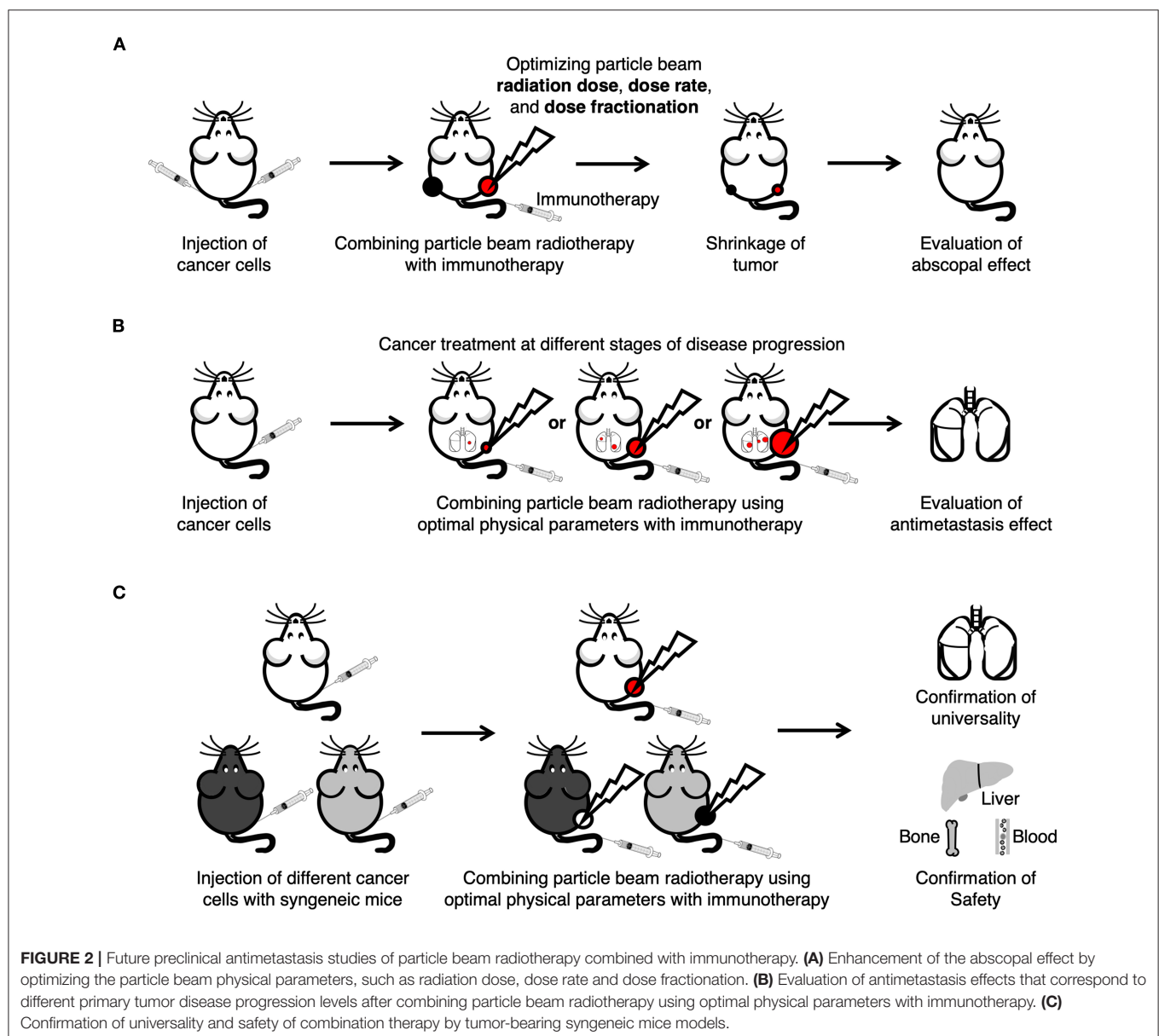
In summary, the radiation-induced activation of antitumor immunity may be a key factor in inducing the abscopal effect and immunotherapy further amplifies this immune response and enhances the systemic anticancer effect (Figure 1). The

stable induction and deep-level mechanism of the abscopal effect can be studied by using the combination of radiotherapy and immunotherapy. Through these studies, it is expected that the abscopal effect can be turned from a rare phenomenon into a stable and effective tool for antimetastasis therapy in the near future.

DISCUSSION

Optimizing the radiation parameters of radiotherapy combined with immunotherapy is expected to engender better treatment outcomes. A recent study of radiotherapy combined with anti-CTLA-4 antibody immunotherapy showed that the relatively large total radiation dose that can almost eradicate the primary tumor not only significantly improved the treatment outcomes of

the irradiated primary tumor but also inhibited the proliferation of the unirradiated distant tumor (51). Another study showed that combining multifractionated radiotherapy with CTLA-4 immune checkpoint inhibitor induced the abscopal effect better than combining single-fractionated radiotherapy with CTLA-4 immune checkpoint inhibitor (52). Additionally, optimizing the physical parameters of radiotherapy has the potential of reducing the risk of side effects caused by the combination therapies. A mice study conducted by the University of Pennsylvania found that the radiation dose in proton therapy was an important factor affecting hematologic toxicity (53). Vozenin et al. have proven that ultra-high dose rate (FLASH) radiotherapy could significantly reduce acute skin reactions in an animal study using cats (54). Whole abdominal proton FLASH radiotherapy was performed on mice by Diffenderfer et al., and it significantly



inhibited intestinal fibrosis compared with standard proton radiotherapy (55). Although there are no current reports on FLASH radiotherapy combined with immunotherapy, the advantages of local tumor control and lower toxic side effects of FLASH radiotherapy indicate that this combination therapy may play a more important role in the future of cancer treatment. Therefore, optimizing the physical parameters of radiotherapy, such as radiation dose, dose rate, and dose fractionation, in combination therapy is associated with both antitumor and antimetastasis effects, as well as the toxic side effects on healthy tissues and organs. The best therapeutic effect of combination therapy is essentially the maximization of the anticancer effect and the minimization of the toxic side effects.

In both photon beam radiotherapy and particle beam radiotherapy, a significant shrinkage or even regression of unirradiated distant metastatic tumor has been observed in some individual patients after local irradiation of the tumor, and this phenomenon is called the abscopal effect (18, 19, 30). An increasing number of evidence has suggested that the abscopal effect is mediated by the immune system after radiation (30, 44, 56). However, abscopal effect is extremely rare, and current studies mainly focus on the very few clinical case reports and induction mechanism of the effect. To date, although irradiation of cancer cells by particle beam can activate the antitumor immune response (39), no evidence has been found that particle beam radiotherapy alone can stably induce the abscopal effect. Particle beam radiotherapy combined with immunotherapy opens novel perspectives regarding the stable induction of the abscopal effect. For future preclinical studies of particle beam radiotherapy

combined with immunotherapy, the following prospects are proposed (Figure 2). First, the efficiency of inducing the abscopal effect should be improved by optimizing the physical parameters of radiation in the combination therapy. Second, the antimetastasis effect should be evaluated after combining particle beam radiotherapy using optimal physical parameters with immunotherapy. Finally, the universality and safety of the combination therapy should be researched to provide a theoretical basis and data support for conducting future clinical trials. Once the combination therapy that can stably induce the abscopal effect has been found, cancer patients with distant metastasis may be eventually cured by receiving particle beam radiation to kill the primary tumor, and then inducing the abscopal effect with the appropriate methods to eliminate the metastatic cancer.

AUTHOR CONTRIBUTIONS

LM drafted the manuscript, contributed to the literature search and analysis, and reviewed and approved the final manuscript.

FUNDING

This research was supported by the CIAE President's Strategic Grant (No. YZ212404000801).

ACKNOWLEDGMENTS

The author thanks Jialing Wen and Wangcai Ren for proof reading the manuscript.

REFERENCES

1. WHO. *Cancer-Key Facts*. (2021):Available at: <http://www.who.int/news-room/fact-sheets/detail/cancer> (Accessed December 31, 2021).
2. Sung H, Ferlay J, Siegel RL, Laversanne M, Soerjomataram I, Jemal A, et al. Global cancer statistics 2020: GLOBOCAN estimates of incidence and mortality worldwide for 36 cancers in 185 countries. *CA Cancer J Clin*. (2021). doi: 10.3322/caac.21660
3. Mehlen P, Puisieux A. Metastasis: a question of life or death. *Nat Rev Cancer*. (2006) 6:449–58. doi: 10.1038/nrc1886
4. Heymach J, Krilov L, Alberg A, Baxter N, Chang SM, Corcoran RB, et al. Clinical cancer advances 2018: annual report on progress against cancer from the american society of clinical oncology. *J Clin Oncol*. (2018) 36:1020–44. doi: 10.1200/JCO.2017.77.0446
5. Durante M, Flanz J. Charged particle beams to cure cancer: atrengths and challenges. *Semin Oncol*. (2019) 46:219–25. doi: 10.1053/j.seminoncol.2019.07.007
6. Hanahan D, Weinberg RA. Hallmarks of cancer: the next generation. *Cell*. (2011) 144:646–74. doi: 10.1016/j.cell.2011.02.013
7. Ma L, Sakamoto Y, Kanai A, Otsuka H, Takahashi A, Kakimi K, et al. Characterization of a novel murine colon carcinoma subline with high-metastatic activity established by *in vivo* selection method. *Int J Mol Sci*. (2020) 21:2829. doi: 10.3390/ijms21082829
8. Glynn RJ, Seddon JM, Gragoudas ES, Egan KM, Hart LJ. Evaluation of tumor regression and other prognostic factors for early and late metastasis after proton irradiation of uveal melanoma. *Ophthalmology*. (1989) 96:1566–73. doi: 10.1016/S0161-6420(89)32685-6
9. Gragoudas ES, Seddon JM, Egan KM, Glynn RJ, Goitein M, Munzenrider J, et al. Metastasis from uveal melanoma after proton beam irradiation. *Ophthalmology*. (1988) 95:992–9. doi: 10.1016/S0161-6420(88)33091-5
10. Gragoudas ES, Seddon JM, Egan KM, Polivogianis L, Hsieh CC, Goitein M, et al. Prognostic factors for metastasis following proton beam irradiation of uveal melanomas. *Ophthalmology*. (1986) 93:675–80. doi: 10.1016/S0161-6420(86)33699-6
11. Koutsandrea C, Moschos MM, Dimissianos M, Georgopoulos G, Ladas I, Apostolopoulos M. Metastasis rates and sites after treatment for choroidal melanoma by proton beam irradiation or by enucleation. *Clin Ophthalmol*. (2008) 2:989–95. doi: 10.2147/OPHTH.S4006
12. Mole RH. Whole body irradiation; radiobiology or medicine? *Br J Radiol*. (1953) 26:234–41. doi: 10.1259/0007-1285-26-305-234
13. Lakshmanagowda PB, Viswanath L, Thimmaiah N, Dasappa L, Supre SS, Kallur P. Abscopal effect in a patient with chronic lymphocytic leukemia during radiation therapy: a case report. *Cases J*. (2009) 2:204. doi: 10.1186/1757-1626-2-204
14. Cotter SE, Dunn GP, Collins KM, Sahni D, Zukotynski KA, Hansen JL, et al. Abscopal effect in a patient with metastatic Merkel cell carcinoma following radiation therapy: potential role of induced antitumor immunity. *Arch Dermatol*. (2011) 147:870–2. doi: 10.1001/archdermatol.2011.176
15. Okuma K, Yamashita H, Niibe Y, Hayakawa K, Nakagawa K. Abscopal effect of radiation on lung metastases of hepatocellular carcinoma: a case report. *J Med Case Rep*. (2011) 5:111. doi: 10.1186/1752-1947-5-111
16. Ishiyama H, Teh BS, Ren H, Chiang S, Tann A, Blanco AI, et al. Spontaneous regression of thoracic metastases while progression of brain metastases after stereotactic radiosurgery and stereotactic body radiotherapy for metastatic renal cell carcinoma: abscopal effect prevented by the blood-brain

- barrier? *Clin Genitourin Cancer*. (2012) 10:196–8. doi: 10.1016/j.clgc.2012.01.004
17. Siva S, Callahan J, MacManus MP, Martin O, Hicks RJ, Ball DL. Abscopal [corrected] effects after conventional and stereotactic lung irradiation of non-small-cell lung cancer. *J Thorac Oncol*. (2013) 8:e71–2. doi: 10.1097/JTO.0b013e318292c55a
 18. Ebner DK, Kamada T, Yamada S. Abscopal effect in recurrent colorectal cancer treated with carbon-ion radiation therapy: 2 case reports. *Adv Radiat Oncol*. (2017) 2:333–8. doi: 10.1016/j.adro.2017.06.001
 19. Brennenman RJ, Sharifai N, Fischer-Valuck B, Hassanzadeh C, Guzelian J, Chrisinger JSA, et al. Abscopal effect following proton beam radiotherapy in a patient with inoperable metastatic retroperitoneal sarcoma. *Front Oncol*. (2019) 9:922. doi: 10.3389/fonc.2019.00922
 20. Camphausen K, Moses MA, Menard C, Sproull M, Beecken WD, Folkman J, et al. Radiation abscopal antitumor effect is mediated through p53. *Cancer Res*. (2003) 63:1990–3. doi: 10.1016/S0360-3016(02)03449-1
 21. Steinman RM. Dendritic cells *in vivo*: A key target for a new vaccine science. *Immunity*. (2008) 29:319–24. doi: 10.1016/j.immuni.2008.08.001
 22. Ishida Y, Agata Y, Shibahara K, Honjo T. Induced expression of PD-1, a novel member of the immunoglobulin gene superfamily, upon programmed cell death. *EMBO J*. (1992) 11:3887–95. doi: 10.1002/j.1460-2075.1992.tb05481.x
 23. Leach DR, Krummel MF, Allison JP. Enhancement of antitumor immunity by CTLA-4 blockade. *Science*. (1996) 271:1734–6. doi: 10.1126/science.271.5256.1734
 24. Mahmood J, Shukla HD, Soman S, Samanta S, Singh P, Kamlapurkar S, et al. Immunotherapy, radiotherapy, and hyperthermia: a combined therapeutic approach in Pancreatic cancer treatment. *Cancers (Basel)*. (2018) 10:469. doi: 10.3390/cancers10120469
 25. Hiniker SM, Maecker HT, Knox SJ. Predictors of clinical response to immunotherapy with or without radiotherapy. *J Radiat Oncol*. (2015) 4:339–45. doi: 10.1007/s13566-015-0219-2
 26. van der Burg SH, Arens R, Ossendorp F, van Hall T, Melief CJ. Vaccines for established cancer: overcoming the challenges posed by immune evasion. *Nat Rev Cancer*. (2016) 16:219–33. doi: 10.1038/nrc.2016.16
 27. Kambayashi T, Laufer TM. Atypical MHC class II-expressing antigen-presenting cells: can anything replace a dendritic cell? *Nat Rev Immunol*. (2014) 14:719–30. doi: 10.1038/nri3754
 28. Nikitina EY, Gabrilovich DI. Combination of gamma-irradiation and dendritic cell administration induces a potent antitumor response in tumor-bearing mice: approach to treatment of advanced stage cancer. *Int J Cancer*. (2001) 94:825–33. doi: 10.1002/1097-0215(20011215)94:6<825::AID-IJC1545>3.0.CO;2-5
 29. Teitz-Tennenbaum S, Li Q, Rynkiewicz S, Ito F, Davis MA, McGinn CJ, et al. Radiotherapy potentiates the therapeutic efficacy of intratumoral dendritic cell administration. *Cancer Res*. (2003) 63:8466–75.
 30. Postow MA, Callahan MK, Barker CA, Yamada Y, Yuan J, Kitano S, et al. Immunologic correlates of the abscopal effect in a patient with melanoma. *N Engl J Med*. (2012) 366:925–31. doi: 10.1056/NEJMoa1112824
 31. Golden EB, Demaria S, Schiff PB, Chachoua A, Formenti SC. An abscopal response to radiation and ipilimumab in a patient with metastatic non-small cell lung cancer. *Cancer Immunol Res*. (2013) 1:365–72. doi: 10.1158/2326-6066.CIR-13-0115
 32. Twyman-Saint Victor C, Rech AJ, Maity A, Rengan R, Pauken KE, Stelekati E, et al. Radiation and dual checkpoint blockade activate non-redundant immune mechanisms in cancer. *Nature*. (2015) 520:373–7. doi: 10.1038/nature14292
 33. Takahashi Y, Yasui T, Tamari K, Minami K, Otani K, Isohashi F, et al. Radiation enhanced the local and distant anti-tumor efficacy in dual immune checkpoint blockade therapy in osteosarcoma. *PLoS ONE*. (2017) 12:e0189697. doi: 10.1371/journal.pone.0189697
 34. Puzanov I, Diab A, Abdallah K, Bingham CO. 3rd, Brogdon C, Dadu R, et al. Managing toxicities associated with immune checkpoint inhibitors: consensus recommendations from the Society for Immunotherapy of Cancer (SITC) Toxicity Management Working Group. *J Immunother Cancer*. (2017) 5:95. doi: 10.1186/s40425-017-0300-z
 35. Wang Y, Zhou S, Yang F, Qi X, Wang X, Guan X, et al. Treatment-related adverse events of PD-1 and PD-L1 inhibitors in clinical trials: a systematic review and meta-analysis. *JAMA Oncol*. (2019) 5:1008–19. doi: 10.1001/jamaoncol.2019.0393
 36. Martin AM, Cagney DN, Catalano PJ, Alexander BM, Redig AJ, Schoenfeld JD, et al. Immunotherapy and symptomatic radiation necrosis in patients with brain metastases treated with stereotactic radiation. *JAMA Oncol*. (2018) 4:1123–4. doi: 10.1001/jamaoncol.2017.3993
 37. Tamiya A, Tamiya M, Nakahama K, Taniguchi Y, Shiroyama T, Isa SI, et al. Correlation of radiation pneumonitis history before nivolumab with onset of interstitial lung disease and progression-free survival of patients with pre-treated advanced non-small cell lung cancer. *Anticancer Res*. (2017) 37:5199–205. doi: 10.21873/anticancer.11943
 38. Ohkubo Y, Iwakawa M, Seino K, Nakawata M, Wada H, Kamijuku H, et al. Combining carbon ion radiotherapy and local injection of alpha-galactosylceramide-pulsed dendritic cells inhibits lung metastases in an *in vivo* murine model. *Int J Radiat Oncol Biol Phys*. (2010) 78:1524–31. doi: 10.1016/j.ijrobp.2010.06.048
 39. Ando K, Fujita H, Hosoi A, Ma L, Wakatsuki M, Seino KI, et al. Intravenous dendritic cell administration enhances suppression of lung metastasis induced by carbon-ion irradiation. *J Radiat Res*. (2017) 58:446–55. doi: 10.1093/jrr/rxx005
 40. Ma L, Sakamoto Y, Ando K, Fujita H, Takahashi A, Takeshima T, et al. Th balance-related host genetic background affects the therapeutic effects of combining carbon-ion radiation therapy with dendritic cell immunotherapy. *Int J Radiat Oncol Biol Phys*. (2021) 112:780–9. doi: 10.1016/j.ijrobp.2021.10.141
 41. Takahashi Y, Yasui T, Minami K, Tamari K, Hayashi K, Otani K, et al. Carbon ion irradiation enhances the antitumor efficacy of dual immune checkpoint blockade therapy both for local and distant sites in murine osteosarcoma. *Oncotarget*. (2019) 10:633–46. doi: 10.18632/oncotarget.26551
 42. Helm A, Tinganelli W, Simonello P, Kurosawa F, Fournier C, Shimokawa T, et al. Reduction of lung metastases in a mouse osteosarcoma model treated with carbon ions and immune checkpoint inhibitors. *Int J Radiat Oncol Biol Phys*. (2021) 109:594–602. doi: 10.1016/j.ijrobp.2020.09.041
 43. Golden EB, Chhabra A, Chachoua A, Adams S, Donach M, Fenton-Kerimian M, et al. Local radiotherapy and granulocyte-macrophage colony-stimulating factor to generate abscopal responses in patients with metastatic solid tumours: a proof-of-principle trial. *Lancet Oncol*. (2015) 16:795–803. doi: 10.1016/S1470-2045(15)00054-6
 44. Demaria S, Ng B, Devitt ML, Babb JS, Kawashima N, Liebes L, et al. Ionizing radiation inhibition of distant untreated tumors (abscopal effect) is immune mediated. *Int J Radiat Oncol Biol Phys*. (2004) 58:862–70. doi: 10.1016/j.ijrobp.2003.09.012
 45. Hodge JW, Sharp HJ, Gameiro SR. Abscopal regression of antigen disparate tumors by antigen cascade after systemic tumor vaccination in combination with local tumor radiation. *Cancer Biother Radiopharm*. (2012) 27:12–22. doi: 10.1089/cbr.2012.1202
 46. Shiraishi K, Ishiwata Y, Nakagawa K, Yokochi S, Taruki C, Akuta T, et al. Enhancement of antitumor radiation efficacy and consistent induction of the abscopal effect in mice by ECI301, an active variant of macrophage inflammatory protein-1alpha. *Clin Cancer Res*. (2008) 14:1159–66. doi: 10.1158/1078-0432.CCR-07-4485
 47. Kanegasaki S, Matsushima K, Shiraishi K, Nakagawa K, Tsuchiya T. Macrophage inflammatory protein derivative ECI301 enhances the alarmin-associated abscopal benefits of tumor radiotherapy. *Cancer Res*. (2014) 74:5070–8. doi: 10.1158/0008-5472.CAN-14-0551
 48. Kanegasaki S, Tsuchiya T. Alarmins released during local antitumor treatments play an essential role in enhancing tumor growth inhibition at treated and non-treated sites via a derivative of CCL3. *Oncoimmunology*. (2014) 3:e958956. doi: 10.4161/21624011.2014.958956
 49. Huang Y, Dong Y, Zhao J, Zhang L, Kong L, Lu JJ. Comparison of the effects of photon, proton and carbon-ion radiation on the ectocalreticulin exposure in various tumor cell lines. *Ann Transl Med*. (2019) 7:542. doi: 10.21037/atm.2019.09.128
 50. Ran J, Wang J, Dai Z, Miao Y, Gan J, Zhao C, et al. Irradiation-induced changes in the immunogenicity of lung cancer cell lines: Based

- on comparison of X-rays and carbon ions. *Front Public Health*. (2021) 9:666282. doi: 10.3389/fpubh.2021.666282
51. Takenaka W, Takahashi Y, Tamari K, Minami K, Katsuki S, Seo Y, et al. Radiation dose escalation is crucial in anti-CTLA-4 antibody therapy to enhance local and distant antitumor effect in murine osteosarcoma. *Cancers (Basel)*. (2020) 12:1546. doi: 10.3390/cancers12061546
 52. Dewan MZ, Galloway AE, Kawashima N, Dewyngaert JK, Babb JS, Formenti SC, et al. Fractionated but not single-dose radiotherapy induces an immune-mediated abscopal effect when combined with anti-CTLA-4 antibody. *Clin Cancer Res*. (2009) 15:5379–88. doi: 10.1158/1078-0432.CCR-09-0265
 53. Ware JH, Sanzari J, Avery S, Sayers C, Krigsfeld G, Nuth M, et al. Effects of proton radiation dose, dose rate and dose fractionation on hematopoietic cells in mice. *Radiat Res*. (2010) 174:325–30. doi: 10.1667/RR1979.1
 54. Vozenin MC, De Fornel P, Petersson K, Favaudon V, Jaccard M, Germond JF, et al. The advantage of FLASH radiotherapy confirmed in mini-pig and cat-cancer patients. *Clin Cancer Res*. (2019) 25:35–42. doi: 10.1158/1078-0432.CCR-17-3375
 55. Diffenderfer ES, Verginadis II, Kim MM, Shoniyozov K, Velalopoulou A, Goia D, et al. Design, implementation, and *in vivo* validation of a novel proton FLASH radiation therapy system. *Int J Radiat Oncol Biol Phys*. (2020) 106:440–8. doi: 10.1016/j.ijrobp.2019.10.049
 56. Grass GD, Krishna N, Kim S. The immune mechanisms of abscopal effect in radiation therapy. *Curr Probl Cancer*. (2016) 40:10–24. doi: 10.1016/j.cupr.2015.10.003

Conflict of Interest: The author declares that the research was conducted in the absence of any commercial or financial relationships that could be construed as a potential conflict of interest.

Publisher's Note: All claims expressed in this article are solely those of the authors and do not necessarily represent those of their affiliated organizations, or those of the publisher, the editors and the reviewers. Any product that may be evaluated in this article, or claim that may be made by its manufacturer, is not guaranteed or endorsed by the publisher.

Copyright © 2022 Ma. This is an open-access article distributed under the terms of the Creative Commons Attribution License (CC BY). The use, distribution or reproduction in other forums is permitted, provided the original author(s) and the copyright owner(s) are credited and that the original publication in this journal is cited, in accordance with accepted academic practice. No use, distribution or reproduction is permitted which does not comply with these terms.



Artificial Intelligence Radiotherapy Planning: Automatic Segmentation of Human Organs in CT Images Based on a Modified Convolutional Neural Network

Guosheng Shen^{1,2,3,4}, Xiaodong Jin^{1,2,3,4}, Chao Sun^{1,2,3,4} and Qiang Li^{1,2,3,4*}

¹ Institute of Modern Physics, Chinese Academy of Sciences, Lanzhou, China, ² Key Laboratory of Basic Research on Heavy Ion Radiation Application in Medicine, Lanzhou, China, ³ Key Laboratory of Heavy Ion Radiation Biology and Medicine of Chinese Academy of Sciences, Lanzhou, China, ⁴ University of Chinese Academy of Sciences, Beijing, China

OPEN ACCESS

Edited by:

Dariusz Leszczynski,
University of Helsinki, Finland

Reviewed by:

Yu-Dong Zhang,
University of Leicester,
United Kingdom
Zhonghong Xin,
First Hospital of Lanzhou
University, China

*Correspondence:

Qiang Li
liqiang@impcas.ac.cn

Specialty section:

This article was submitted to
Radiation and Health,
a section of the journal
Frontiers in Public Health

Received: 11 November 2021

Accepted: 24 March 2022

Published: 15 April 2022

Citation:

Shen G, Jin X, Sun C and Li Q (2022)
Artificial Intelligence Radiotherapy
Planning: Automatic Segmentation of
Human Organs in CT Images Based
on a Modified Convolutional Neural
Network.
Front. Public Health 10:813135.
doi: 10.3389/fpubh.2022.813135

Objective: Precise segmentation of human organs and anatomic structures (especially organs at risk, OARs) is the basis and prerequisite for the treatment planning of radiation therapy. In order to ensure rapid and accurate design of radiotherapy treatment planning, an automatic organ segmentation technique was investigated based on deep learning convolutional neural network.

Method: A deep learning convolutional neural network (CNN) algorithm called BCDU-Net has been modified and developed further by us. Twenty two thousand CT images and the corresponding organ contours of 17 types delineated manually by experienced physicians from 329 patients were used to train and validate the algorithm. The CT images randomly selected were employed to test the modified BCDU-Net algorithm. The weight parameters of the algorithm model were acquired from the training of the convolutional neural network.

Result: The average Dice similarity coefficient (DSC) of the automatic segmentation and manual segmentation of the human organs of 17 types reached 0.8376, and the best coefficient reached up to 0.9676. It took 1.5–2 s and about 1 h to automatically segment the contours of an organ in an image of the CT dataset for a patient and the 17 organs for the CT dataset with the method developed by us, respectively.

Conclusion: The modified deep neural network algorithm could be used to automatically segment human organs of 17 types quickly and accurately. The accuracy and speed of the method meet the requirements of its application in radiotherapy.

Keywords: convolutional neural network (CNN), human organs, CT images, automatic segmentation, Dice similarity coefficient (DSC)

INTRODUCTION

Radiation therapy, which deliver lethal doses to a target volume while sparing the surrounding normal tissues as much as possible, has been a key modality of cancer treatments. So, accurate and rapid identification and delineation of normal organs and target volumes are the basis for precision radiotherapy (1–5). In the conventional workflow of radiation therapy, medical doctors spend too

much time dealing with CT images manually and the accuracy of organs segmentation depends heavily on the professional skills of medical doctors (6). An amateurish job of human organ contour segmentation could seriously influence the curative effect of radiotherapy.

The common organ segmentation algorithms with conventional automaticity and semi-automaticity are based on gray value, texture, template setting, and other features of CT images. Therefore, these methods are often apt to failure in identifying all organs in CT images and delineating the contours (7–9).

With the rapid development of artificial intelligence (AI) technologies, especially in the application of fundamental convolutional neural networks (CNN), the medical image recognition and segmentation are getting more and more higher reliability and accuracy, and this is also a hot issue in current research (10–15), a lot of new CNN net (such as BDR-CNN-GCN) were designed to classified the cancer and achieve a significantly effective (16). The appearance of semantic-based full convolutional network and U-Net enables AI technology to achieve pixel-to-pixel prediction, which had a wide impact on the field of computer vision as soon as they appeared. It has been widely used in the image segmentation, object detection, object recognition, and so on. In the field of biomedical images, CNN is widely used in automatic detection and classification of diseases, prediction of therapeutic effects, segmentation and recognition of special tissues and organs, etc. (15, 17–21). The medical data which has been annotated by experienced physicians was used to train and validate the CNN net, so the CNN can be used to predict and extracts the features from new medical data. Based on these features which obtained from the designed CNNs, the algorithm can accurately predict and segment the medical images (22–26).

In order to achieve the precision radiotherapy, automatic and accurate identification, and segmentation of human organs in medical images are absolutely necessary. Therefore, we designed and modified a U network of CNNs (BCDU-Net: Bi-Directional ConvLSTM U-Net with Dense Connected Convolutions) (27–29), and CT images and corresponding organs (RT-structure) data set from 339 patients were applied to train, validate, and test the network in our work. The method of automatic and accurate segmentation of human organs in medical image definitely can provide support for decreasing the workload of physicians and the development of precision radiotherapy in the future.

MATERIALS AND METHODS

Test Data

In this study, the data were randomly selected from more than 22,000 CT images and corresponding tissue and organ contours from 339 patients who received radiotherapy in a tumor hospital in 2018. All of these tissue and organ contours which had been used in radiotherapy were generated and verified by several experienced physicians using the conventional commercial treatment planning system in the hospital.

The CT images and corresponding tissue and organ contours used in the experiment are outlined as follows: 984 bladder images, 451 brainstem images, 451 left eye (eye-L) images, 359

right eye (eye-R) images, 1,778 left femur (femur-L) images, 1,603 right femur (femur-R) images, 2,059 heart images, 699 intestine images, 964 left kidney images, 908 right kidney images, 2,890 liver images, 1,491 left lung images, 3,397 right lung images, and 754 mandible images, 1,673 rectum images, 550 spleen images, and 890 stomach images.

In this study, 70% of the images of each organ contours and corresponding CT images were randomly selected for training, 20% were selected for verification and 10% were selected for testing.

Deep CNN Algorithm

In order to realize automatic segmentation of organs with CT images, a new U-Net algorithm based on the deep CNN algorithm was designed and developed using python language, in which a BCDU-Net network algorithm of deep neural network which has been published by Azad et al. (27) was referred and improved by us in the present work. In the BCDU-net algorithm the authors included BN after each up-convolutional layer to speed up the network learning process. And BN can help the network to improve the performance. Also the network with dense connections could improve the accuracy. The key idea of dense convolutions is sharing feature maps between blocks through direct connection between convolutional block. Consequently, each dense block receives all preceding layers as input, and therefore, produces more diversified and richer features. So the BCDU-net has a better preference (28, 29).

The schematic diagram of the modified algorithm is shown in **Figure 1**. In the conventional U-Net algorithm, input images are directly copied and added into the deconvolution decoder part from the code part of network, so that the automatic segmentation prediction could be realized. The Bi-Directional ConvLSTM algorithm (28, 29) is used to extract features in the BCDU-Net network compared with the conventional U-Net one. In this work, several conventional U-Net network algorithms were tested and the BCDU-Net model showed an excellent performance in automatic organ recognition with CT images. Therefore, the BCDU-Net model algorithm was modified for use in this work.

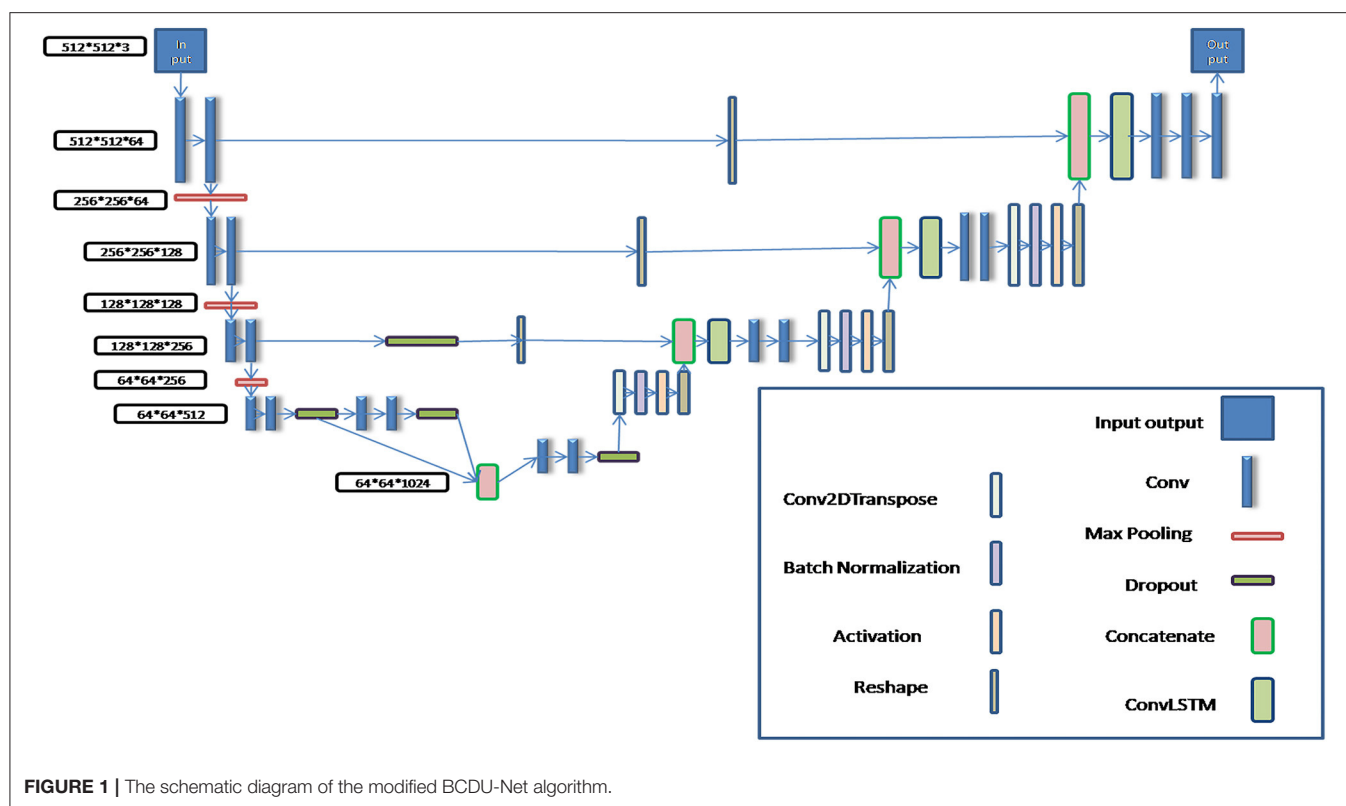
In the process of algorithm development, in order to make the BCDU-Net network model suitable for the input of $512 \times 512 \times 3$ CT images and the output of $512 \times 512 \times 3$ tissue and organ contour sets, it was modified by adding two convolution computations behind the deconvolution computing layer so as to obtain multi-channel segmentation images. Then, the predicted contours of organs were automatically output.

Assessment Method

Accuracy, Precision, and Dice similarity coefficient (DSC) were used to evaluate the algorithm effectiveness in this paper.

Recall: the proportion of correct prediction results in all test data. The threshold range of accuracy is $[0,1]$, the larger the value of accuracy is, the better the results are.

Precision: the proportion of correct prediction. The threshold range of precision is $[0,1]$, the larger the value of accuracy is, the better the results are.



DSC: an important parameter to evaluate the effect of network prediction. Its calculation formula is as follows:

$$DSC = 2 * (Precision * Recall) / (Precision + Recall) \quad (1)$$

The threshold range of DSC is [0,1], the closer it is to 1, the more accurate the prediction results will be.

In this paper, all of the mentioned evaluation parameters were used to evaluate the prediction results of each organ contours.

Testing Platform

The hardware platform used in this work is as follows: Dell T5820/P5820X (tower workstation); CPU: I7-7800x 6-core 3.5 ghz Core X series; Graphics GPU: Nvidia Titan RTX-24G; Memory: DDR4 32 GB; Hard disk: solid state 1T+mechanical 4T.

Operating system: Ubuntu Linux 16.04; Development tools: Spyder + Tensorflow + Keras; Development language: Python.

RESULTS

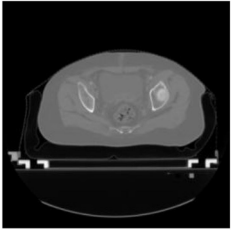
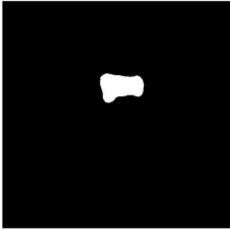

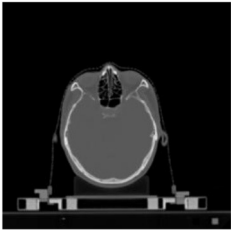
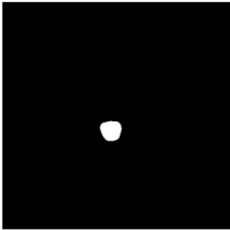
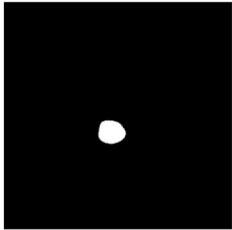
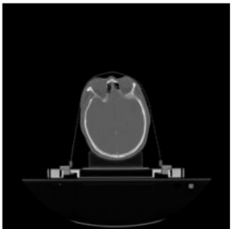
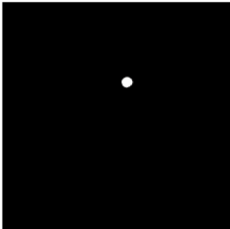
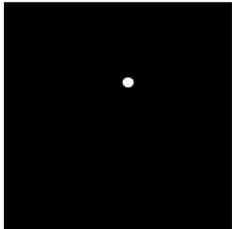

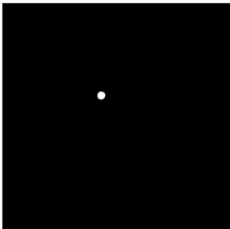
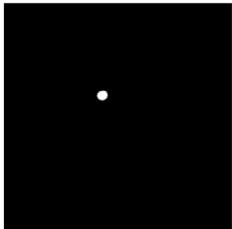
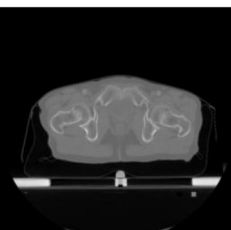
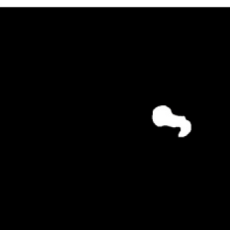
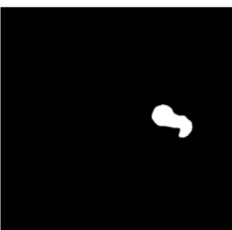
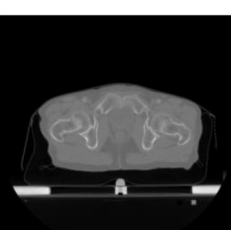

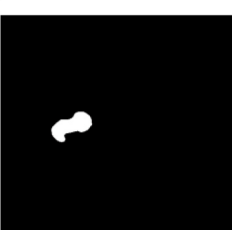
More than 22,000 CT images and corresponded organ contours from 329 patients were randomly extracted, in which 70% was for training set, 20% for validation set and 10% for testing set. The labeled CT images and corresponded organ contour images were used to train and validate the algorithm modified in this paper. And then the weight parameters of the modified BCDU-Net algorithm model were obtained.

According to the acquired model parameters mentioned above, the testing set was calculated and examined. The performance of the modified algorithm for automatic organ segmentation in CT images is shown in **Table 1**. The organ contours segmented automatically by the algorithm were similar to those delineated by physicians manually. The model parameters including DSC, Accuracy, Recall, and Precision evaluation ones were served to evaluate the segmentation effectiveness of each organ in the validation and testing sets. In our work, the BCDU-Net CNN algorithm model was used to automatically segment different organs with the different training parameters such as epoch learning rate. The CT images which were randomly selected from the patients were put into the network model for training, and then the contours of different organs which were delineated automatically by the AI technology and manually by medical doctors were evaluated with the similarity coefficients, respectively. The results are given in **Table 2**. Most of the DSC values were better than 0.85 and among them the best even reached up to 0.9676. Generally, the automatic segmentation results met the requirements of clinical practice.

DISCUSSION

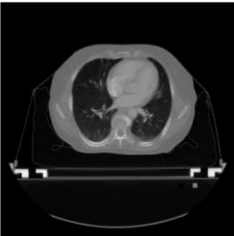
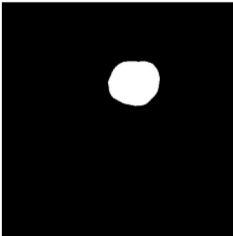
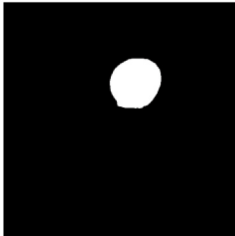
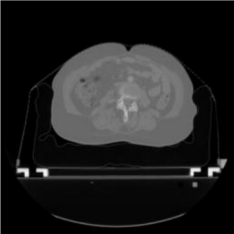
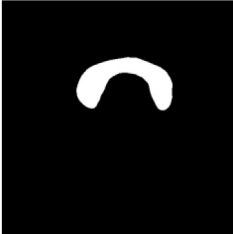
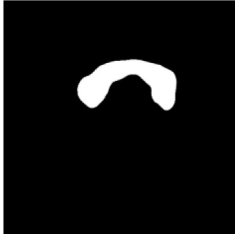
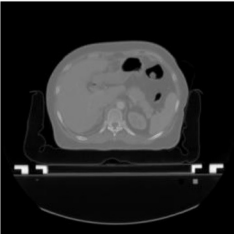
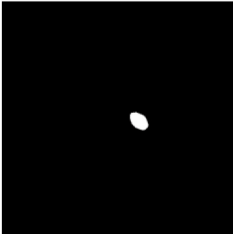
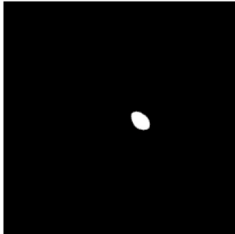
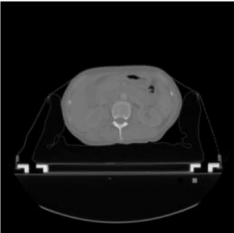
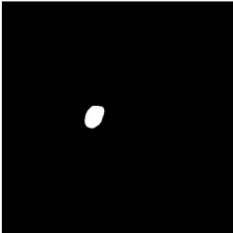
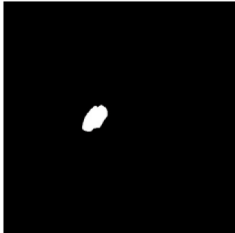
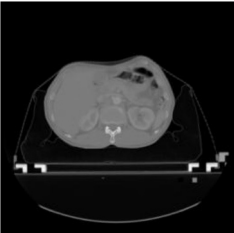
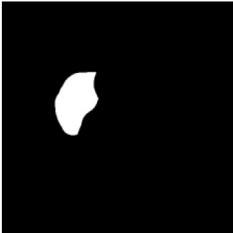

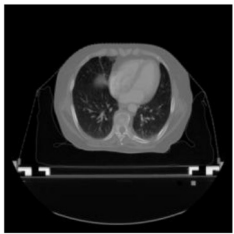
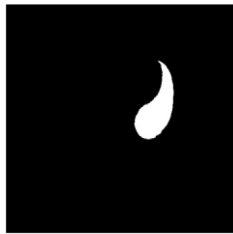

At present, it takes medical doctors a lot of time and energy to identify and delineate human organs in CT images for radiotherapy treatment planning. High accuracy and efficiency of manual segmentation is always a big challenge for medical doctors. With the development of AI technology, the

TABLE 1 | The result of manual and automatic organ segmentation.

	Input CT image	Organs with manual segmentation	Organ with automatic segmentation
Bladder			
Brainstem			
Eye-L			
Eye-R			
Femur-L			
Femur-R			

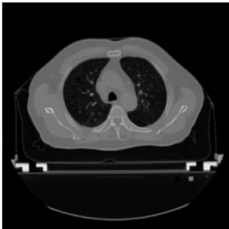
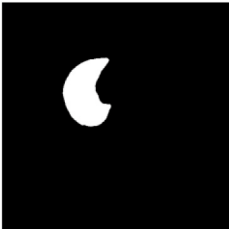

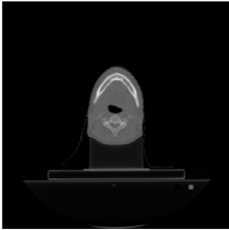
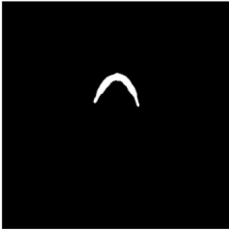
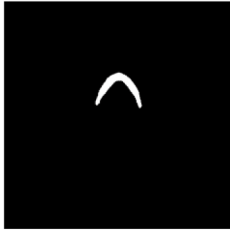
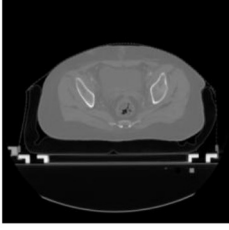
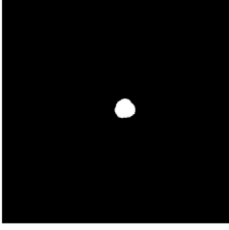
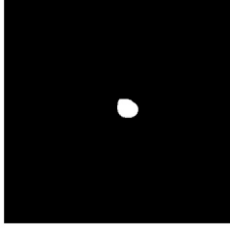
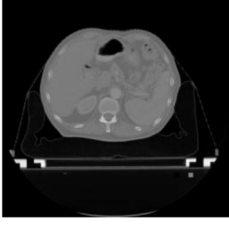
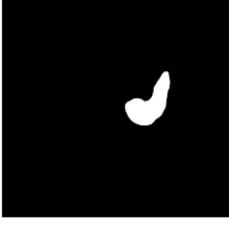
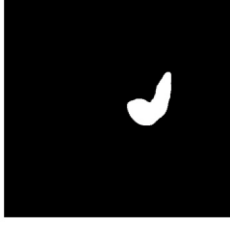
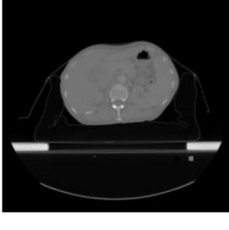
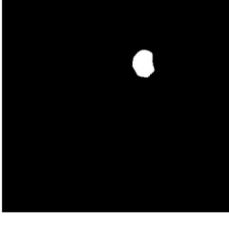
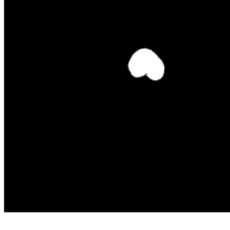
(Continued)

TABLE 1 | Continued

	Input CT image	Organs with manual segmentation	Organ with automatic segmentation
Heart			
Intestine			
Kidney-L			
Kidney-R			
Liver			
Lung-L			

(Continued)

TABLE 1 | Continued

	Input CT image	Organs with manual segmentation	Organ with automatic segmentation
Lung-R			
Mandible			
Rectum			
Spleen			
Stomach			

performance of the deep learning CNN algorithm which is used in image processing becomes better, and the CNN algorithm gets more applications in medical images processing for automatic detection of diseases and delineation of specific tissues and organs (malignant and benign). New BDR-CNN-GCN algorithm had been designed and used to classify breast cancer and achieved a better results (16). Also some new AI algorithms were designed and applied in different aspects of healthcare which strongly support the development of healthcare automation technology (2–4, 7–9). In our work, the BCDU-Net deep learning CNN model was modified and used for training and validation via

22,000 CT images and corresponding human organs 17 type from 339 patients. Compared with the manual segmentation, the average DSC value of the modified algorithm for the automatic segmentation of 17 type human organs was 0.8376, and the best DSC coefficient was up to 0.9676. Moreover, the DSC coefficient of 13 in 17 organs was better than 0.82. Obviously, the effectiveness of the algorithm after modification was improved.

The number of the images for each human organ in the 17 type, which were employed for training and validation, was different. So various epoch values were set when we trained for the different organs. The results are given in **Table 3**. The epoch

TABLE 2 | Evaluation for the automatic organ segmentation.

	DSC	Accuracy	Recall	Precision
Bladder	0.8403	0.9977	0.6826	0.9981
Brainstem	0.6786	0.9987	0.6934	0.9925
Eye-L	0.8839	0.9996	0.9537	0.9997
Eye-R	0.8690	0.9995	0.9147	0.9997
Femur-L	0.9357	0.9991	0.9668	0.9993
Femur-R	0.9405	0.9991	0.9586	0.9994
Heart	0.9086	0.9948	0.9727	0.9954
Intestine	0.5084	0.9745	0.8340	0.9767
Kidney-L	0.9313	0.9992	0.9650	0.9994
Kidney-R	0.8822	0.9987	0.9728	0.9988
Liver	0.9221	0.9948	0.9071	0.9979
Lung-L	0.8879	0.9960	0.8434	0.9989
Lung-R	0.9676	0.9977	0.9741	0.9986
Mandible	0.8252	0.9982	0.8976	0.9987
Rectum	0.6782	0.9981	0.5585	0.9997
Spleen	0.9082	0.9978	0.9087	0.9989
Stomach	0.6717	0.9950	0.5289	0.6563

TABLE 3 | The training epoch and CT image numbers for the different organs.

Organ	Number of images	Epoch
Bladder	1,467	80
Brainstem	984	100
Eye-L	451	120
Eye-R	359	120
Femur-L	1,778	60
Femur-R	1,603	60
Heart	2,059	60
Intestine	699	100
Kidney-L	964	100
Kidney-R	908	100
Liver	2,890	50
Lung-L	1,491	80
Lung-R	3,397	40
Mandible	754	100
Rectum	1,673	60
Spleen	550	120
Stomach	890	100

value was set small when the number of the training images was large. Conversely, the epoch value was set large when the number of the training images was small. So, the accuracy of the automatic organ segmentation was improved, and the DSC value became better.

In this work, the DSC values of four organs (intestine, stomach, rectum, and brainstem) were lower than those of the other organs. The reason probably was that it was difficult to split these four organs accurately by medical doctors. So, the labeling quality of the images which were used to train

and validate the network was poor. It took 6–8 h to train and validate the modified BCDU-Net algorithm model parameters for each organ. However, the contour of an organ could be segmented automatically in about 1.5–2 s from CT image. Clearly, the automatic organ segmentation with the modified algorithm is much higher efficient than manual delineation by medical doctors.

Even so, we will improve the precision of the modified model through cooperating closely with more experienced medical doctors, making the proposed method to be applied in clinical practice as early as possible.

CONCLUSION

To achieve accurate automatic organ segmentation in CT images, the structure of the BCDU-Net CNN algorithm model was designed and improved. More than 22,000 CT images and the contours of human organs of 17 types from 339 patients were applied to train and validate the CNN algorithm model. So, the parameters of the algorithm model were obtained. The performance of the algorithm with an average DSC coefficient of 0.8376 and time consumption of about 1.5–2 s was obtained. Thus, the algorithm could be used to segment human organs of 17 types in CT images automatically and efficiently. More cooperation with experienced medical doctors definitely makes the modified model more suitable for clinical use.

DATA AVAILABILITY STATEMENT

The datasets presented in this study can be found in online repositories. The names of the repository/repositories and accession number(s) can be found at: <https://pan.cstcloud.cn/s/gO5MpMG9TNQ>.

ETHICS STATEMENT

The studies involving human participants were reviewed and approved by the Academic Committee of the Institute of Modern Physics, Chinese Academy of Sciences. The patients/participants provided their written informed consent to participate in this study.

AUTHOR CONTRIBUTIONS

GS and QL: conception, design, and experimental testing. XJ and CS: administrative support and data interpretation. All authors contributed to the article and approved the submitted version.

FUNDING

This work was jointly supported by the Key Deployment Project of Chinese Academy of Sciences (Grant No. KFZD-SW-222) and the West Light Foundation of Chinese Academy of Sciences [Grant No. (2019)90].

REFERENCES

- Wang SH, Sun J, Phillips P, Zhao G, Zhang YD. Polarimetric synthetic aperture radar image segmentation by convolutional neural network using graphical processing units. *J. Real Time Image Process.* (2018) 15:631–42. doi: 10.1007/s11554-017-0717-0
- Wang SH, Tang C, Sun J, Yang J, Huang C, Phillips P, et al. Multiple sclerosis identification by 14-layer convolutional neural network with batch normalization, dropout, and stochastic pooling. *Front Neurosci.* (2018) 12: 818. doi: 10.3389/fnins.2018.00818
- Zhang YD, Pan C, Sun J, Tang C. Multiple sclerosis identification by convolutional neural network with dropout and parametric ReLU. *J Comput Sci.* (2018) 28:1–10. doi: 10.1016/j.jocs.2018.07.003
- Chen L, Shen C, Zhou Z, Maquilan G, Albuquerque K, Folkert MR, et al. Automatic PET cervical tumor segmentation by combining deep learning and anatomic prior. *Phys Med Biol.* (2019) 64:085019. doi: 10.1088/1361-6560/ab0b64
- Bi WL, Hosny A, Schabath MB, Giger ML, Birkbak NJ, Mehrtash A, et al. Artificial intelligence in cancer imaging: clinical challenges and applications. *CA Cancer J Clin.* (2019) 69:127–57. doi: 10.3322/caac.21552
- James C, Luis S, Issam EN. Big data analytics for prostate radiotherapy. *Front Oncol.* (2016) 6:149. doi: 10.3389/fonc.2016.00149
- Ibragimov B, Xing L. Segmentation of organs-at-risks in head and neck CT images using convolutional neural networks. *Med Phys.* (2017) 44:547–57. doi: 10.1002/mp.12045
- Babier A, Boutilier JJ, McNiven AL, Chan T. Knowledge-based automated planning for oropharyngeal cancer. *Med Phys.* (2018) 45:2875–83. doi: 10.1002/mp.12930
- Meyer P, Noblet V, Mazzara C, Lallement A. Survey on deep learning for radiotherapy. *Comput Biol Med.* (2018) 98:126–46. doi: 10.1016/j.compbiomed.2018.05.018
- Xing L, Krupinski EA, Cai J. Artificial intelligence will soon change the landscape of medical physics research and practice. *Med Phys.* (2018) 45:1791–3. doi: 10.1002/mp.12831
- Le MH, Chen J, Wang L, Wang Z, Liu W, Cheng KT, et al. Automated diagnosis of prostate cancer in multi-parametric MRI based on multimodal convolutional neural networks. *Phys. Med. Biol.* (2017) 62:6497–14. doi: 10.1088/1361-6560/aa7731
- Basheera S, Satya SRM. Classification of brain tumors using deep features extracted using CNN. *J. Phys. Conf.* (2019) 1172:012016. doi: 10.1088/1742-6596/1172/1/012016
- Junyoung P, Donghui H, Yun KK, Kang SK, Kyeong KY, Sung LJ. Computed tomography super-resolution using deep convolutional neural network. *Phys. Med. Biol.* (2018) 63:145011. doi: 10.1088/1361-6560/aacdd4
- Liang H, Tsui B, Ni H, Valentim C, Baxter SL, Liu G, et al. Evaluation and accurate diagnoses of pediatric diseases using artificial intelligence. *Nat Med.* (2019) 25:433–8. doi: 10.1038/s41591-018-0335-9
- Jochims A, Deist TM, Naqa IE, Kessler M, Mayo C, Reeves J, et al. Developing and validating a survival prediction model for NSCLC patients through distributed learning across 3 countries. *Int J Radiat Oncol Biol Phys.* (2017) 99:344–52. doi: 10.1016/j.ijrobp.2017.04.021
- Zhang YD, Satapathy SC, Guttry DS, Górriz JM, Wang SH. Improved breast cancer classification through combining graph convolutional network and convolutional neural network. *Inform Process Manag.* (2021) 58:102439. doi: 10.1016/j.ipm.2020.102439
- Lustberg T, Van Soest J, Gooding M, Peressutti D, Aljabar P, Van der Stoep J, et al. Clinical evaluation of atlas and deep learning based automatic contouring for lung cancer. *Radiother. Oncol.* (2017) 126:312–7. doi: 10.1016/j.radonc.2017.11.012
- Zhen X, Chen J, Zhong Z, Hrycushko BA, Zhou L, Jiang SB, et al. Deep convolutional neural network with transfer learning for rectum toxicity prediction in cervical cancer radiotherapy: a feasibility study. *Phys Med Biol.* (2017) 62:8246–63. doi: 10.1088/1361-6560/aa8d09
- Zhang K, Zuo W, Chen Y, Meng D, Zhang L. Beyond a Gaussian denoiser: residual learning of deep CNN for image denoising. *IEEE Trans Image Process.* (2017) 26:3142–55. doi: 10.1515/9783110524116
- Xu M, Qi S, Yue Y, Teng Y, Wei Q. Segmentation of lung parenchyma in CT images using CNN trained with the clustering algorithm generated dataset. *Biomed Eng Online.* (2019) 18:2. doi: 10.1186/s12938-018-0619-9
- Chen X, Men K, Li Y, Yi J, Dai J. A feasibility study on an automated method to generate patient-specific dose distributions for radiotherapy using deep learning. *Med Phys.* (2019) 46:56–64. doi: 10.1002/mp.13262
- Komatsu S, Oike T, Komatsu Y, Kubota Y, Nakano T. Deep learning-assisted literature mining for *in vitro* radiosensitivity data. *Radiother Oncol.* (2019) 139:87–93. doi: 10.1016/j.radonc.2019.07.003
- Sun Y, Shi H, Zhang S, Wang P, Zhao W, Zhou X, et al. Accurate and rapid CT image segmentation of the eyes and surrounding organs for precise radiotherapy. *Med Phys.* (2019) 46:2214–22. doi: 10.1002/mp.13463
- Cardenas CE, McCarroll R, Court LE, Elgohari BA, Elhalawani H, Fuller CD, et al. Deep learning algorithm for auto-delineation of high-risk oropharyngeal clinical target volumes with built-in dice similarity coefficient parameter optimization function. *Int J Radiat Oncol Biol Phys.* (2018) 101:468–78. doi: 10.1016/j.ijrobp.2018.01.114
- Der Veen JV, Willems S, Deschuymer S, Drb C, Wc A, Fm B, et al. Benefits of deep learning for delineation of organs at risk in head and neck cancer. *Radiother Oncol.* (2019) 138:68–74. doi: 10.1016/j.radonc.2019.05.010
- Dolensek N, Gehrlach DA, Klein AS, Nadine G. Facial expressions of emotion states and their neuronal correlates in mice. *Science.* (2020) 368:89–94. doi: 10.1126/science.aaz9468
- Azad R, Asadiaghbolaghi M, Fathy M, Escalera S. Bi-directional ConvLSTM U-Net with Densley connected convolutions. In: *IEEE/CVF International Conference on Computer Vision Workshop (ICCVW)*. Seoul. (2019). doi: 10.1109/ICCVW.2019.00052
- Song H, Wang W, Zhao S, Shen J, Lam KM. Pyramid dilated deeper ConvLSTM for video salient object detection. In: *European Conference on Computer Vision*. Munich (2018). p. 744–60. doi: 10.1007/978-3-030-01252-6_44
- Shi X, Chen Z, Wang H, Yeung DY, Wong WK, Woo WC. Convolutional LSTM network: a machine learning approach for precipitation nowcasting. *Neural Information Processing Systems*. Montreal, QC (2015). p. 802–10.

Conflict of Interest: The authors declare that the research was conducted in the absence of any commercial or financial relationships that could be construed as a potential conflict of interest.

Publisher's Note: All claims expressed in this article are solely those of the authors and do not necessarily represent those of their affiliated organizations, or those of the publisher, the editors and the reviewers. Any product that may be evaluated in this article, or claim that may be made by its manufacturer, is not guaranteed or endorsed by the publisher.

Copyright © 2022 Shen, Jin, Sun and Li. This is an open-access article distributed under the terms of the Creative Commons Attribution License (CC BY). The use, distribution or reproduction in other forums is permitted, provided the original author(s) and the copyright owner(s) are credited and that the original publication in this journal is cited, in accordance with accepted academic practice. No use, distribution or reproduction is permitted which does not comply with these terms.

Advantages of publishing in Frontiers



OPEN ACCESS

Articles are free to read
for greatest visibility
and readership



FAST PUBLICATION

Around 90 days
from submission
to decision



HIGH QUALITY PEER-REVIEW

Rigorous, collaborative,
and constructive
peer-review



TRANSPARENT PEER-REVIEW

Editors and reviewers
acknowledged by name
on published articles

Frontiers

Avenue du Tribunal-Fédéral 34
1005 Lausanne | Switzerland

Visit us: www.frontiersin.org

Contact us: frontiersin.org/about/contact



REPRODUCIBILITY OF RESEARCH

Support open data
and methods to enhance
research reproducibility



DIGITAL PUBLISHING

Articles designed
for optimal readership
across devices



FOLLOW US

@frontiersin



IMPACT METRICS

Advanced article metrics
track visibility across
digital media



EXTENSIVE PROMOTION

Marketing
and promotion
of impactful research



LOOP RESEARCH NETWORK

Our network
increases your
article's readership